

THE FORMATION
OF
MASSIVE STARS

Dissertation

zur Erlangung des Grades

Doktor der Naturwissenschaften

Fakultät für Physik und Astronomie

Ruhr-Universität Bochum

von

Vera H. Hoffmeister

Oberhausen

Bochum 2008

1. Gutachter: Prof. Dr. Rolf Chini
 2. Gutachter: Prof. Dr. Ralph Neuhäuser
- Mündliche Prüfung: 27. Mai 2008

THE FORMATION
OF
MASSIVE STARS

PhD Thesis

Faculty of Physics and Astronomy

Ruhr-University Bochum

Vera H. Hoffmeister

Oberhausen

Bochum 2008

First referee: Prof. Dr. Rolf Chini
Second referee: Prof. Dr. Ralph Neuhäuser
Oral examination: 27th of May 2008

UB 24445

Contents

1	Introduction & Overview	1
1.1	Star Formation	1
1.1.1	Cluster Formation	1
1.1.2	High-Mass Stars	2
1.2	The Omega Nebula	3
1.3	This Thesis	4
2	Observations & Data Reduction	5
2.1	Optical Imaging	5
2.2	<i>JHK</i> imaging	6
2.3	<i>L</i> Band Imaging	9
2.4	Adaptive Optics <i>JHKsL'M'</i> Imaging	10
2.5	Optical Spectroscopy	11
2.5.1	Spectroscopy of the Cluster	11
2.5.2	Spectroscopy of the Large Silhouette Disk	12
2.6	Infrared Spectroscopy	13
2.7	Intrinsic Colors	14
2.7.1	Dwarf Stars	14
2.7.2	T Tauri Stars	14
2.8	Color Transformations	15
2.9	Transformed Near Infrared Reddening Paths	16
3	Results	17
3.1	Color-Color Diagrams	17
3.1.1	Diagrams of the Form $V - \lambda$ vs. $B - V$	17
3.1.2	Diagrams of the Form $I - \lambda$ vs. $V - I$	18
3.1.3	The $J - H$ vs. $H - K$ Diagram	18
3.1.4	The $J - H$ vs. $H - L$ Diagram	21
3.1.5	The $J - H$ vs. $K - L$ Diagram	22
3.1.6	The $J - K$ vs. $K - L$ Diagram	23
3.1.7	The $H - K$ vs. $K - L$ diagram	24
3.1.8	Determination of IRE from NIR TCDs	25
3.2	Color-Magnitude Diagrams	26
3.2.1	The V vs. $B - V$ Diagram	27
3.2.2	The I vs. $B - I$ Diagram	27
3.2.3	The J vs. $J - H$ Diagram	28

3.2.4	The H vs. $H - K$ Diagram	29
3.3	Spectra	31
3.3.1	Optical Spectra	31
3.3.2	Infrared Spectra	31
4	Discussion	33
4.1	The Young Cluster	33
4.1.1	Optical Surveys	33
4.1.2	X-ray Sources	33
4.1.3	Infrared Surveys	36
4.1.4	Spectroscopic Surveys	42
4.1.5	The Extinction toward M 17	42
4.1.6	The Distance toward M 17	45
4.1.7	High-Mass Stars and Energy Balance	49
4.1.8	Low-Mass Stars	52
4.1.9	IR Excess Objects	52
4.1.10	CO Band Head Sources	54
4.1.11	Cluster Age	59
4.2	Objects of Special Interest	60
4.2.1	The Major Exciting Binary CEN 1 a and b	60
4.2.2	M 17-UC1	61
4.2.3	IRS 5	65
4.2.4	IRS 15	67
4.2.5	The Silhouette Disk	69
4.2.6	Extremely Red Objects	72
4.2.7	The KW Object	75
4.3	Sequential Star Formation?	76
4.4	Structure of the Complex	76
5	Summary and Perspectives	79
5.1	Summary	79
5.2	Perspectives	80
A	Spectroscopic Results	81
A.1	Optical Spectroscopy	87
A.2	J Band Spectroscopy	93
A.3	K Band Spectroscopy	98
B	Abbreviations	111
	Bibliography	113
	Curriculum Vitae	121

List of Figures

1.1	The giant H II region M 17 in visual light	3
2.1	<i>Vri</i> image of the cluster region in M 17	5
2.2	<i>JHKs</i> mosaic of the cluster region	6
2.3	Histogram of apparent magnitudes in <i>JHK</i>	7
2.4	Photometric error versus apparent magnitudes for <i>JHK</i>	8
2.5	Location of sky fields	8
2.6	<i>L</i> -band mosaic of the cluster region	10
3.1	TCDs of the form $V - \lambda$ vs. $B - V$	18
3.2	TCDs of the form $I - \lambda$ vs. $V - I$	19
3.3	TCD $J - H$ vs. $H - K$	20
3.4	TCD $J - H$ vs. $H - L$	21
3.5	TCD $J - H$ vs. $K - L$	22
3.6	TCD $J - K$ vs. $K - L$	23
3.7	TCD $H - K$ vs. $K - L$	24
3.8	Determination of IRE from NIR TCDs	25
3.9	CMD V vs. $B - V$	26
3.10	CMD I vs. $B - I$	27
3.11	CMD J vs. $J - H$	28
3.12	CMD H vs. $H - K$	29
3.13	CMD H vs. $H - K$ - stars without J -band detection	30
4.1	Large scale optical view of the M 17 region	34
4.2	<i>Chandra</i> ACIS-I binned image of M 17 with 886 source extraction regions	35
4.3	<i>JHK</i> diagram of 4330 stars toward M 17	38
4.4	Spatial distribution of stars toward M 17	39
4.5	<i>HKL</i> diagram of 2967 stars toward M 17	41
4.6	Distance modulus vs. color excess	44
4.7	J vs. $J - H$ color-magnitude diagram	47
4.8	Dereddened CMD VBV for 318 spectroscopically classified stars	51
4.9	H -band luminosity function	57
4.10	P 11 and P δ line for CEN 1 a	60
4.11	M 17-UC1 as seen by NACO and VISIR	62
4.12	K -band spectrum of M 17-UC1	63
4.13	SED of M 17-UC1	64
4.14	IRS 5 and its neighbors as seen by NACO and VISIR	65

4.15	<i>K</i> -band spectrum of IRS 5	66
4.16	SED of IRS5	66
4.17	Optical and NIR spectra of IRS 15	67
4.18	<i>KLN</i> image of IRS 15	68
4.19	Silhouette of the 20.000 AU accretion disk	69
4.20	Multi-wavelength sequence of the hourglass-shaped reflection nebula	70
4.21	Optical spectrum of the bipolar nebula	71
4.22	Distribution of extremely red objects	72
4.23	<i>K – L</i> color distribution of extremely red objects	74
4.24	<i>IJK</i> imaging of the KW object	75
4.25	The M 17 region at 1200 μ m as seen by SIMBA	78
A.1	Optical spectra	88
A.2	<i>J</i> band spectra	94
A.3	<i>K</i> band spectra	99

List of Tables

2.1	Selected technical details of the NIR imaging	7
2.2	Photometric Standard Stars	9
2.3	Selected technical details of the NIR spectroscopy	13
2.4	Reddening Law	16
4.1	Statistics of sources from the <i>JHK</i> diagram	40
4.2	High-mass stars in M 17	50
4.3	Statistics of the <i>K</i> -band spectra	55
4.4	Photometry of the IRS 5 group	65
4.5	Statistics of extremely red sources	73
A.1	Spectroscopic results	87

Chapter 1

Introduction & Overview

This chapter describes particular aspects of star formation (SF), the Omega Nebula (M17), and the contents of this thesis.

1.1 Star Formation

In the following two aspects of SF are discussed. In particular the formation of star clusters and high-mass stars including their importance for SF in general.

1.1.1 Cluster Formation

Starting from a pre-existing giant molecular cloud, the sequence of events is likely as follows:

Compression

Formation of cold dense molecular cores or filaments, induced by gravoturbulent cloud fragmentation (Mac Low & Klessen 2004). This means that supersonic turbulence rapidly produces localized compressed pockets of gas, some of which remain gravitationally bound and provide the initial conditions for collapse (Padoan & Nordlund 2002; Klessen et al. 2005). A characteristic density of about 10^5 cm^{-3} and a temperature of 10–15 K result from the equation of state of dusty molecular gas with solar abundances (Jappsen et al. 2005; Larson 2005).

Collapse

Non-homologous gravitational collapse of portions of the cores into optically thick, pressure-supported protostellar embryos with initial masses of the order of $10^{-3} M_{\odot}$ (Larson 1969; Bate 2000). The term non-homologous collapse refers to the fact that the relative distribution of material changes, as opposed to a homologous or self-similar collapse.

Accretion

Accretion of material onto protostellar objects as they evolve toward the main sequence. For low-mass objects the accretion stops well before hydrogen burning commences. These pre main-sequence (PMS) objects of fixed mass then slowly and quasi-hydrostatically contract to the main sequence (Palla & Stahler 1993; Baraffe et al. 2002). However, high-mass objects

eventually start burning hydrogen and develop radiation-driven winds as they continue to accrete and evolve up the main sequence to hotter and more luminous states (Kudritzki 2002).

Disruption

Disruption of the birth cloud, as the first high-mass stars strongly influence their environment by their winds, outflows, and UV radiation, and eventually become supernovae. The most massive stars go supernova after ~ 3 Myr. When the remnant molecular cloud has been dissipated, the result is mostly a cluster of OB stars or an OB association, with an associated cospatial population of lower mass stars (Zinnecker et al. 1993). Often, several evolutionary stages of star formation can be found side by side .

1.1.2 High-Mass Stars

Formation

The most massive stars form in the densest environments by processes that are not well understood. Low occurrences, large distances, high extinction, quick evolution, and short timescales of critical evolutionary phases make observations of the formation of massive stars challenging. Finally, massive stars are seldomly (if at all) formed in isolation; the proximity of other high-mass stars compounds the complex influence of the forming star on its local environment via gravitational interactions, powerful outflows and winds, ionizing radiation, and supernovae. The low number statistics of young or forming high-mass stars is only partially offset by their higher luminosities, which allow us to study them at greater distances than their low-mass counterparts. However, insufficient spatial resolution is an issue. Lacking a better observational guidance, theoretical models have remained controversial. So far there are three competing concepts of massive star formation:

1. monolithic collapse in isolated cores
2. competitive accretion in a protocluster environment
3. stellar collisions and mergers in very dense systems

General Importance

Massive stars play a key role in the evolution of the Universe. They are the principal source of heavy elements and UV radiation. Through a combination of winds, massive outflows, expanding H II regions, and supernova explosions they provide an important source of mixing and turbulence in the interstellar medium (ISM) of galaxies. Turbulence in combination with differential rotation drives galactic dynamos. Galactic magnetic fields are generated, interacting with supernova shock fronts that accelerate cosmic rays. Cosmic rays, UV radiation, and dissipation of turbulence are the principal sources of heating in the ISM, whereas heavy elements found in dust and molecules and in atomic/ionic form ultimately are responsible for its cooling. Massive stars thus profoundly affect the star and planet formation process (Bally et al. 2005) as well as the physical, chemical, and morphological structure of galaxies (Kennicutt 1998, 2005). In spite of the dominant role that massive stars play in shaping galactic structure and evolution, our understanding of their formation and early evolution is still sketchy.

1.2 The Omega Nebula

The Omega Nebula was first mentioned in 1745 by the Swiss astronomer Jean Phillippe Loys de Chéseaux in his list of 21 nebulae but remained fairly unknown. Two decades later Charles Messier independently rediscovered the nebula on June 3rd 1764 and included it in his famous catalog as entry No.17. Since then M17 has been known under various other names such as Swan or Horseshoe Nebula but also appeared in several catalogs as W38, S45, G15.0-0.7 and NGC 6618. M17 is a complex region of ongoing star formation where a young cluster of high-mass stars ionizes a luminous H II region. The H II region and the stellar winds of the most massive stars interact with adjacent molecular clouds leading to all sorts of interference as witnessed by numerous trunks, pillars and photodissociation regions (PDRs). Likewise, there is compelling evidence for triggered SF with new generations of young objects occurring at the interface between the H II region and the surrounding molecular clouds. While the gaseous and dusty components of M17 have been well investigated there is only limited observational material on the properties of the embedded stellar population. This is mainly a consequence of the large extinction in the optical regime and the confusion due to high stellar densities in the infrared (IR).

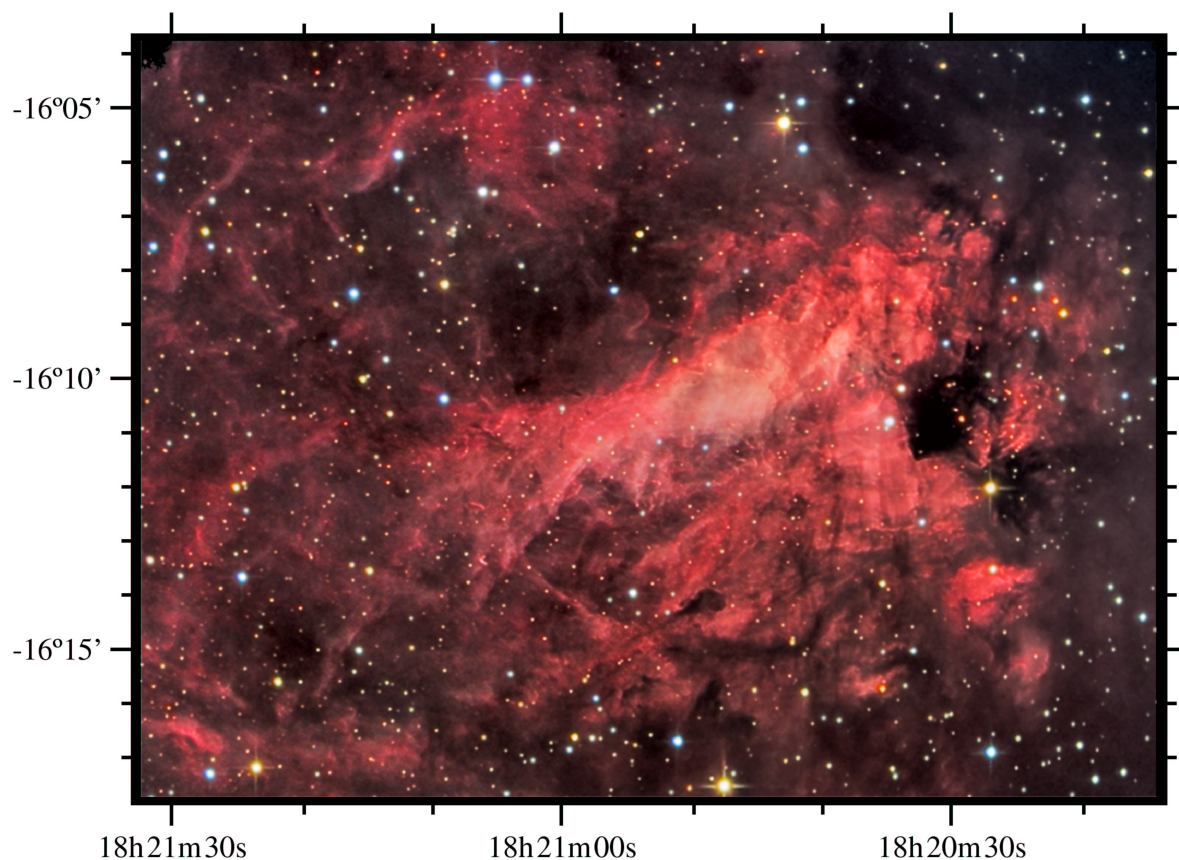


Figure 1.1: The giant H II region M17 in visual light. (Courtesy: W. Ries and S. Heutz)

1.3 This Thesis

The motivation for the present work was to readdress the questions of distance, reddening, stellar content and evolutionary stage of M 17 by means of data with unprecedented sensitivity and spatial resolution. It was the aim to investigate the star forming process in this unique area both in detail for particular regions and objects but also globally to check whether triggered star formation plays a role and whether different generations of stars can be distinguished.

The outline of this thesis is the following: First the huge amount of observational data and the corresponding reduction and calibration procedures are presented in Chapter 2. In Chapter 3 various results are displayed in form of color-color and color-magnitude diagrams. These new results, which are based on an unprecedented large number of faint cluster members will be discussed in Chapter 4. Finally, Chapter 5 puts the new results into a common context and provides an outlook on future observations that ought to be performed in order to extend our knowledge on the formation of massive stars. Individual spectra are displayed in the Appendix.

Chapter 2

Observations & Data Reduction

The observational material of the present work consists of various data sets which will be described in the following sections. Likewise, for each observing mode the corresponding reduction and calibration procedures are explained.

2.1 Optical Imaging

The *BVRI* data have been obtained in July 2003 by the courtesy of S. Kimeswenger. The ESO New Technology Telescope (NTT) and EMMI (Dekker et al. 1986) have been used. The central position was RA = 18:20:28.9 and DEC = -16:10:30 (J2000) with a field of view (FoV) of $9'.1 \times 10'.1$. All images have been obtained in RILD mode using *Bb*, *V*, Gunn *r* and *i* filters. The pixel resolution and the effective spatial resolution was $0''.33$ and $1''.1$ (FWHM), respectively. To cover a large range in stellar brightness various integration times have been used (*Bb*: 10, 300 sec; *V*: 5, 300 sec; *r*: 3, 20, 300 sec; *i*: 2, 20, 300 sec). However, a few of the brightest sources are still saturated. The photometrical calibration has been established by the standard star group PG1633+099 (Landolt 1992).

Color-color diagrams (hereafter referred to as TCDs, i.e. Two-Color-Diagrams) have been used to determine transformation equations from Gunn *r* and *i* to Johnson *R* and *I* (Sec. 2.8). Limiting magnitudes are $B = 22.4$ mag, $V = 23.0$ mag, $R = 21.4$ mag, $I = 19.3$ mag; the completeness limits have been estimated to be $B = 18.0$ mag, $V = 17.5$ mag, $R = 17.0$ mag, $I = 16.0$ mag. The number of stars with photometry ranges from 547 stars in *B* to about 2000 in *i*. The data have been reduced with IRAF¹ v.2.11.3a; point spread function (PSF) photometry was achieved with IRAF/DAOPHOT. Complementary information about EMMI² is available in the Internet.

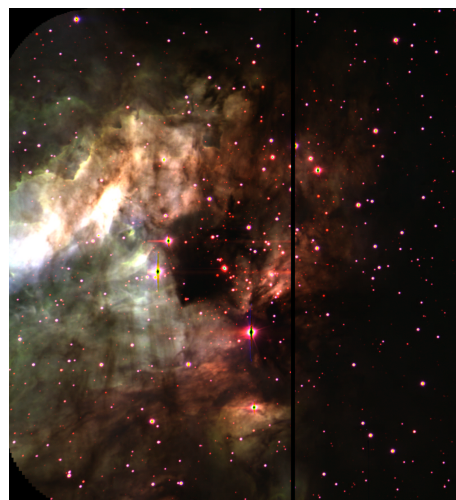


Figure 2.1: EMMI *Vri* image of the cluster region in M17. North is at the top and east to the left.

¹Image Reduction and Analysis Facility

²<http://www.ls.eso.org/lasilla/Telescopes/NEWNT/emmi/>

2.2 *JHK* imaging

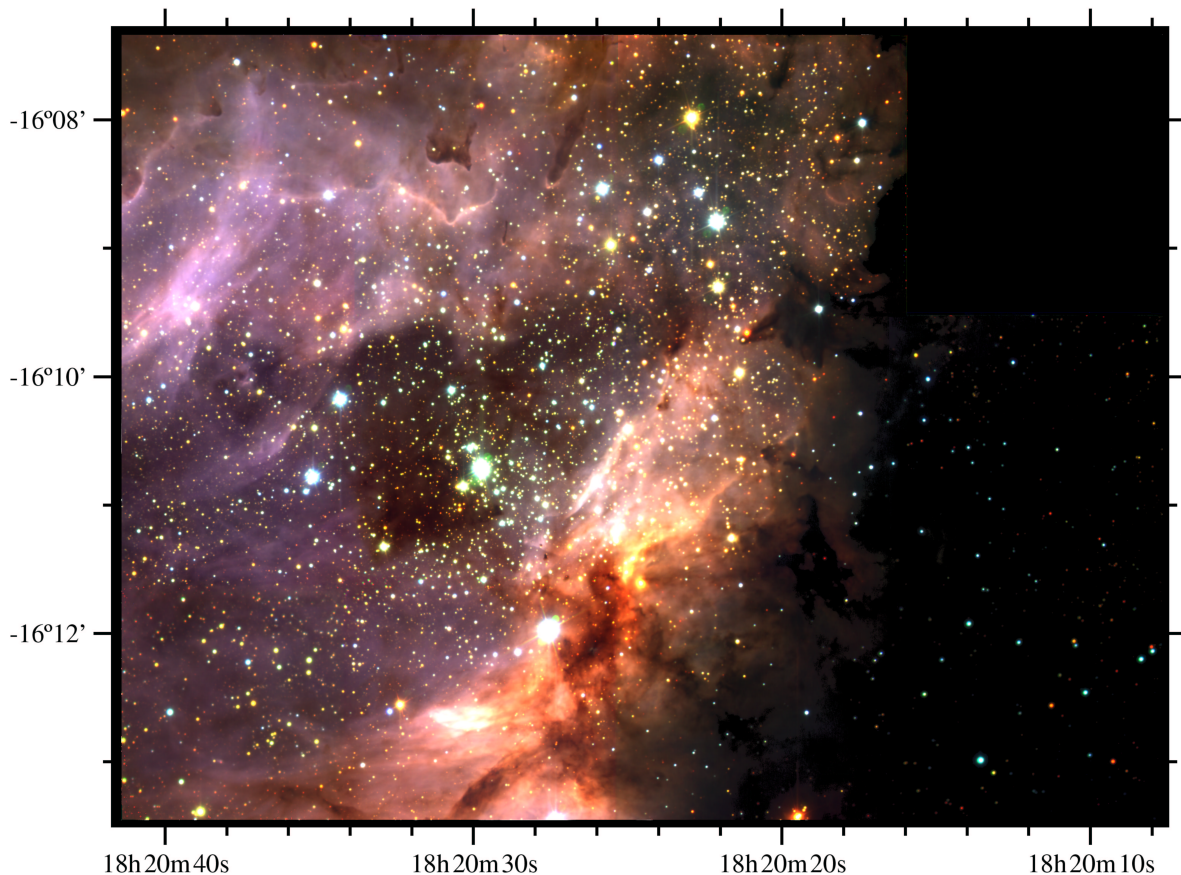


Figure 2.2: ISAAC *JHKs* mosaic of the cluster region in M17. The central position is at RA = 18:20:24.5 and DEC = -16:10:25 (J2000). North is at the top and east to the left; the FoV is $490'' \times 360''$.

JHKs near infrared (NIR) observations were applied at the VLT (UT1). The imaging was carried out in service mode in September 2002 with ISAAC (Moorwood et al. 1998). The pixel resolution was $0''.148$, the effective spatial resolution was $1''.5$ (FWHM). For simplicity *K* is used instead of *Ks*. The *J* filter has leaks in the *K* band and the red edge of the filter is defined by the atmosphere. To prevent contamination an additional blocking filter (*J*+Block, hereafter called *J*) was used.

We used the Aladdin arm which allowed to obtain photometry also for brighter stars due to significantly shorter detector integration times (DITs). In order to cover the cluster area we observed a mosaic of 11 frames. At each position and in each filter 12 object and 12 sky frames were taken with the ISAACLW_img_obs_AutoJitterOffset template. This template allows to obtain sky images in a circle around the initial telescope position and to jitter at each position; sky-throw (i.e. the radius at which sky frames were taken) and jitter box

Filter	DIT [sec]	NDIT object	NDIT sky	Number of AB or BA Cycles	Number of detections
<i>J</i>	0.5	120	59	12	4.990
<i>H</i>	0.5	92	44	12	10.724
<i>K</i>	0.5	70	30	12	18.485

Table 2.1: Selected technical details of the NIR imaging. NDIT is the number of coadded DITs.

width were 600" and 10" respectively. A detailed description of the template can be found in the ISAAC User Manual. Sky frames have been checked for extended emission and sky variability, and were omitted if necessary. The data have been read out in DCR-LB, where the image is the difference between two readouts. The central position is RA = 18:20:25.5 and DEC = -16:10:40 (J2000) and the field size is 6'8 × 8'8. About 95% of the stars have photometric errors ≤ 0.1 mag for $J = 18.9$ mag, $H = 18.3$ mag and $K = 17.2$ mag (see Fig. 2.4). Standard photometric calibration has been achieved with the sources No. 9106, 9116, 9172, 9181, 9185 from Persson et al. (1998). The total number of stars and the corresponding limiting magnitudes are $J = 4990$ (20.9 mag), $H = 10730$ (20.4 mag), $K = 18504$ (20.1 mag); estimates of the completeness limits yield $J = 18.0$ mag, $H = 18.0$ mag and $K = 17.5$ mag (see Fig. 2.3). Fig. 2.2 shows a JHK mosaic of the area providing the so far deepest look into the young cluster.

The natural NIR sky background is dominated by the emission line produced by the OH radical. OH is generated in reactions between H and O₃ in the high atmosphere at an altitude of about 87 km. JHK broad band filters are particularly rich of OH emission lines. Their effect on the astronomical observations has been reviewed by Oliva & Origlia (1992) and Rousselot et al. (2000).

There is significant field distortion in ISAAC images. At the edge, it amounts up to two pixels and in the corners, it amounts up to 2.5 pixels. Therefore the individual fields of the mosaic

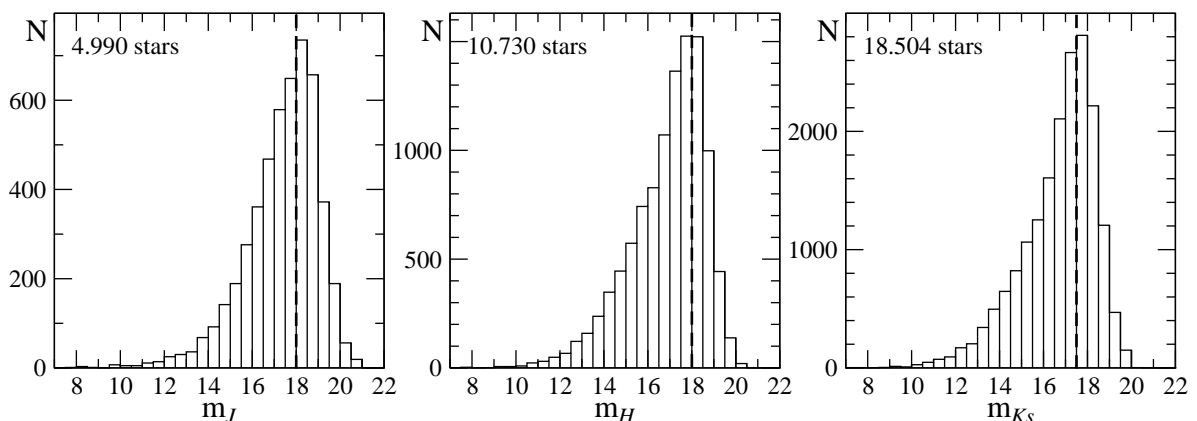


Figure 2.3: Histogram of apparent magnitudes in JHK . Estimated completeness limits are shown by the dashed line.

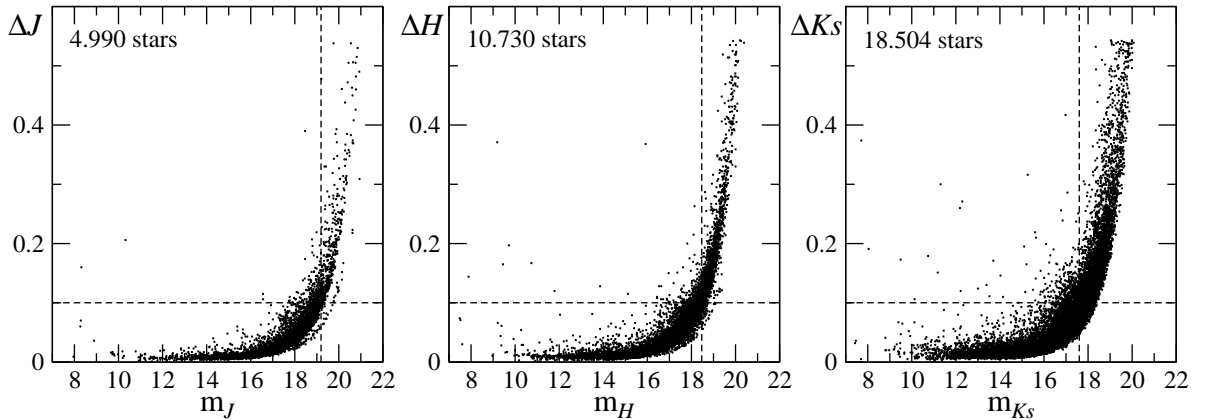


Figure 2.4: Photometric error versus apparent magnitudes for JHK . 95% of the stars left of the vertical dashed line have errors ≤ 0.1 mag.

have been corrected with information provided on the ISAAC home page³ before they were tiled together (see Fig. 2.2). The data were astrometrically calibrated using the 2MASS survey. The data reduction and other image operations (e.g. distortion correction) were performed with IRAF v.2.11.3a. PSF photometry was performed with IRAF/DAOPHOT. The rapidly varying nebular background affects the quality of the photometry and the best results were achieved using the sky fitting algorithm median.

The data were calibrated using photometric standard stars (Persson et al. 1998) (see Tab. 2.2). No transformation equations from ISAAC filters to the Johnson photometric system (Johnson 1966) are available. However, the ISAAC photometric system agrees with the 2MASS photometric system. Conversions between the 2MASS and the Koornneef photometric system (Koornneef 1983a), that combines the SAAO and the Johnson photometric system, were derived by Carpenter (2001) using the 2MASS Second Incremental Data Release. Those transformations have been updated using the All-Sky Release Point Source Catalog and are presented in the Ex-

³http://www.eso.org/instruments/isaac/inst/field_distortion.html

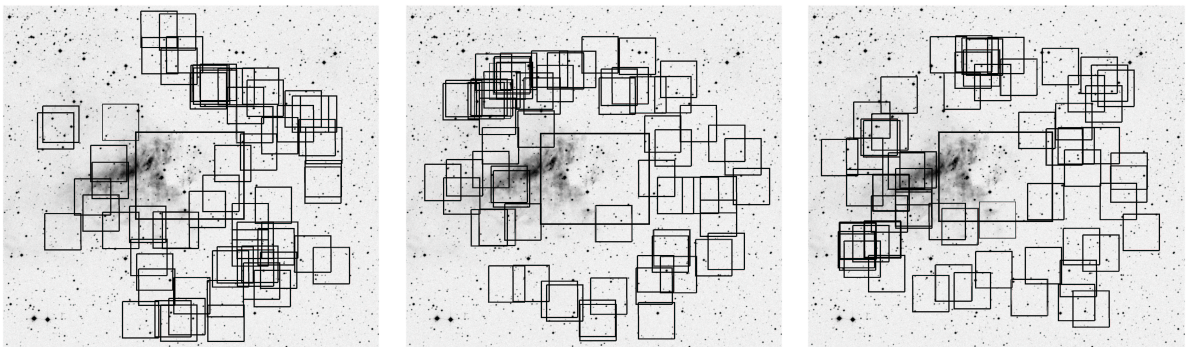


Figure 2.5: Location of the sky fields in JHK (from left to right) superimposed on a DSS I band image. The combined object fields are also indicated. North is at the top and east to the left; the FoV is $31' \times 28'3$.

Table 2.2: Photometric Standard Stars

No.	J [mag]	H [mag]	K [mag]	K_s [mag]	$J-H$ [mag]	$H-K$ [mag]
9106	12.153	11.842	11.772	11.788	0.311	0.070
9116	11.426	11.148	11.077	11.058	0.278	0.071
9172	12.477	12.118	12.026	12.031	0.359	0.092
9181	12.464	12.127	12.095	12.070	0.337	0.032
9185	12.021	11.662	11.586	11.585	0.359	0.076

planatory Supplement to the 2MASS All Sky Data Release and Extended Mission Products VI.4b.

Intrinsic colors and reddening paths have been converted accordingly, instead of the photometric results; otherwise the photometric accuracy would have been degraded and sources with single detections would have been lost at all. The transformation equations are derived from data that spread only from $J-K = 0-1.15$ mag. The present data spans from $J-K = 0-9$ mag while intrinsic colors of main sequence stars range from $J-K = -0.2-1$ mag suggesting that converting the latter one introduces smaller extrapolation errors. Still, the reddening paths, depending on their length, can span a large color range but they agree well with the data. Additional information about ISAAC⁴ are available on the Internet.

2.3 L Band Imaging

L' -band imaging was applied at the ESO VLT. The data was obtained in service mode between May and September 2004 with ISAAC at a central wavelength of $3.78\ \mu\text{m}$ and a bandwidth of $0.58\ \mu\text{m}$. The data have been observed with an imaging template that includes auto-chopping. The pixel resolution was $0''.07$, the effective spatial resolution was $0''.4$ (FWHM). The cluster was covered by a grid of 29 positions around the central position RA = 18:20:29.8 and DEC = -16:10:18 (J2000) resulting in a FoV of $5'.5 \times 5'.6$.

The data reduction and other image operations were performed with IRAF v.2.11.3a by M. Scheyda in the course of his diploma thesis. PSF photometry was achieved with IRAF/DAOPHOT. Again, the rapidly varying nebular background affects the quality of the photometry and the best results were achieved using the sky fitting algorithm median. Photometric calibration was accomplished using the results by Chini & Wargau (1998). The PSF photometry comprises ~ 3200 sources down to a limit of $L = 15.6$ mag. We assume the data to be complete to $L = 13$ mag.

The main results including L -band photometry are displayed in Figures 3.4 to 3.7. The ISAAC L' filter differs from the Johnson L filter. For the same reasons already mentioned in Sect. 2.2 not the data but the intrinsic colors and reddening paths have been converted accordingly. For simplicity L instead of L' is used in the following.

⁴<http://www.eso.org/instruments/isaac/>

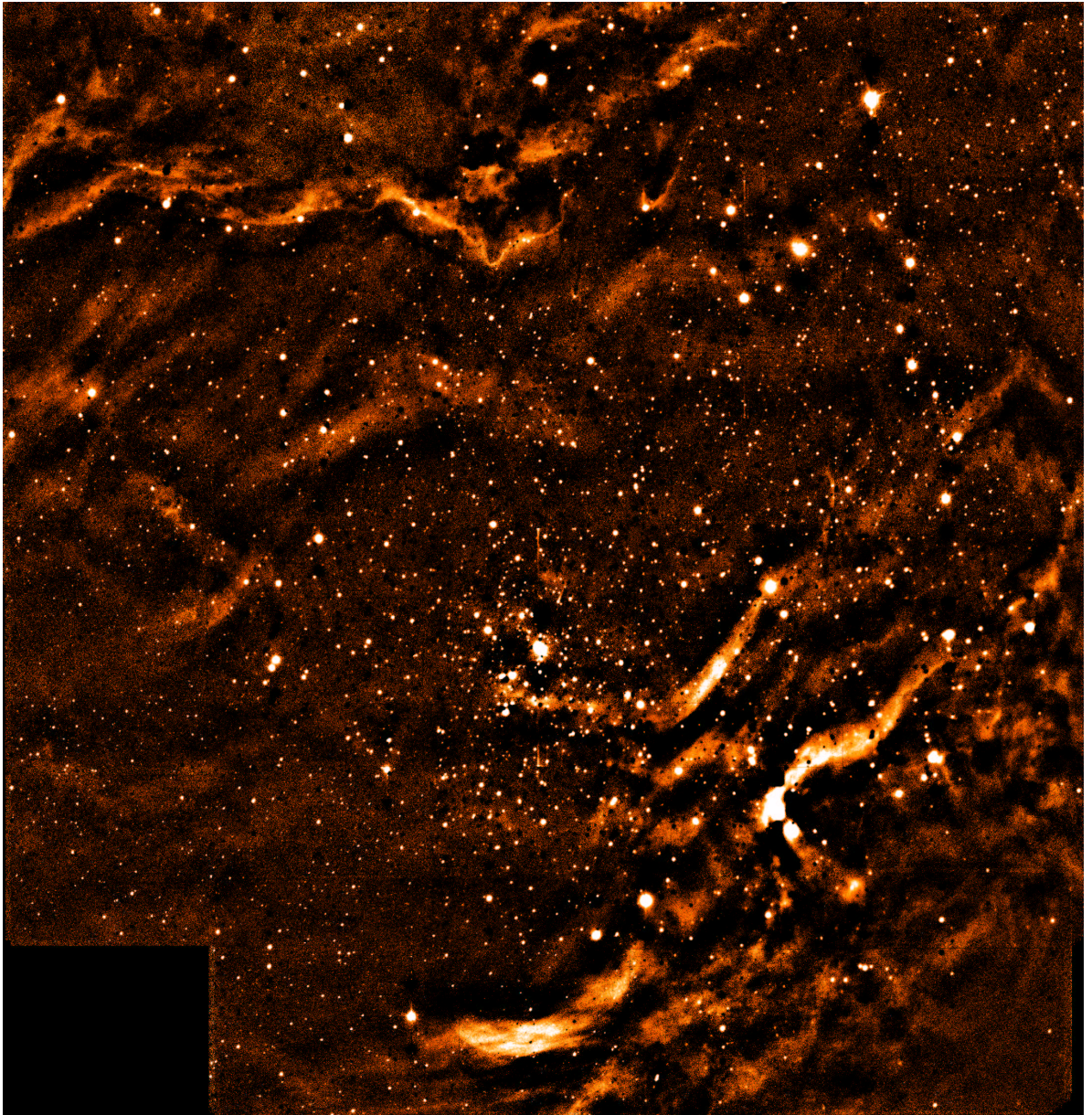


Figure 2.6: ISAAC L -band mosaic of the cluster region in M17. The central position is at RA = 18:20:29.8 and DEC = -16:10:18 (J2000). North is at the top and east to the left; the FoV is $300'' \times 336''$.

2.4 Adaptive Optics $JHKsL'M'$ Imaging

It turned out that a few particular objects of interest required adaptive optics imaging in order to resolve their morphology. For this purpose NAOS/CONICA (NACO) (Lenzen et al. 2003; Rousset et al. 2003) was the perfect instrument.

To improve our ISAAC observations of a huge silhouette disk (see Sect. 4.2.5), we have applied

for director's discretionary time in 2003 and for complementary service mode observations in 2005. The images were centered on RA = 18:20:26.19 and DEC = -16:12:10.4 (J2000). 2003 *K*-band imaging was obtained with a pixel scale of $0.027''$ and a FoV of $28'' \times 28''$. 2005 the disk was imaged in *JHKL'* and *M'*. The pixel scale was $0''.013$ and $0''.027$ for *JHKL* and *L'M'* respectively. The FoV was $14'' \times 14''$ for *JHKM'* and $28'' \times 28''$ for *L'*. For simplicity *KsL'M'* are called *KLM* hereafter.

Another object of special interest was a hyper-compact H II region M17-UC1 (see Sect. 4.2.2). The corresponding data of a region called "Arc", which contains M17-UC1 as well as other interesting sources, was retrieved from the ESO archive. The observations were centered on RA = 18:20:26.2 and DEC = -16:12:10 (J2000). The FoV was $28'' \times 28''$ and $14'' \times 14''$ for *JHKL* and *M* respectively. The pixel resolution was $0.027''$, the limiting magnitudes are $J = 20.6$ mag, $H = 19.3$ mag, $K = 18.4$ mag, and $L = 16.2$ mag.

All data were reduced and analyzed with IRAF and the software package MOPSI (maintained by R. W. Zylka, IRAM, Grenoble, France). Photometric calibration was performed with the aid of our aforementioned ISAAC observations. The astrometry was adjusted by referencing the NACO sources with the detections of the ISAAC data that were astrometrically calibrated using the 2MASS survey. Complementary information about NACO can be found in the Internet⁵.

2.5 Optical Spectroscopy

In order to complement the photometric data of the cluster, we performed optical low-dispersion long-slit and multi-object spectroscopy (MOS) for a total of 403 stars at various wavelengths. Their apparent brightness spans a range from $I = 7.5 - 18$ mag and our optical spectroscopy is almost complete within this magnitude range. Less than a dozen of sources are missing due to the automatic fiber positioning procedure. The stars are distributed homogeneously across the cluster field of Fig. 2.2. In the following, the stellar spectroscopy is separated from the observations devoted particularly to the silhouette disk.

2.5.1 Spectroscopy of the Cluster

EMMI at the ESO NTT

Low-resolution spectroscopy was performed by R. Chini in September 2005 with EMMI (Dekker et al. 1986) at the ESO NTT in low-dispersion long-slit and MOS mode. The slit dimensions of the long-slit and the MOS were $1''.5 \times 8'$ and $1''.0 \times 8''$, respectively; grism 2 provided a wavelength coverage of $\lambda\lambda 3800 - 9200 \text{ \AA}$ with an average spectral resolution of $R \sim 570$. Five different slit positions and two masks were observed providing us with 80 spectra. Standards from Silva & Cornell (1992) have been used to determine stellar temperatures and luminosity classes. Eventually, 74 sources could be classified. Data reduction and analysis was carried out with standard IRAF procedures.

⁵<http://www.eso.org/instruments/naco/>

FLAMES/GIRAFFE/MEDUSA at the ESO VLT

In order to extend the spectroscopic survey to even fainter objects, additional *I*-band MOS spectroscopy has been successfully applied for at the ESO VLT. The observations have been carried out in April and May 2006 with FLAMES using GIRAFFE/MEDUSA (Pasquini et al. 2002); the data was obtained in low resolution mode L881.7 providing a wavelength coverage from $\lambda\lambda 8200 - 9300 \text{ \AA}$ and a spectral resolution of $R \sim 6500$. We observed 4 different fiber allocations each for 1 hour with approximately 80 objects and 25 sky fibers resulting in a total of 320 stellar sources and 100 background positions. The pipeline processed images were further analyzed with IRAF by colleagues from the Astronomical Institute, Bochum (S. Müller and R. Watermann). Spectral classification was accomplished with standards from Bagnulo et al. (2003).

2.5.2 Spectroscopy of the Large Silhouette Disk

A bipolar nebula associated with a huge edge-on disk (see Sect. 4.2.5) has been observed spectroscopically with three different instruments; details are given below. The spectra were obtained to study possible evidence for accretion disk-driven outflows.

EFOSC2 at the ESO 3.6 m

In June 2003 L. Schmidtobreick observed the first spectrum of this nebula with EFOSC2 (Buzzoni et al. 1984) at the ESO 3.6 m. The aperture length was 5', with a width of 1" and a slit orientation perpendicular to the plane of the disk. The spectrum comprises a total wavelength range from $\lambda\lambda 4000 - 9000 \text{ \AA}$ and provide a spectral resolution of $2.8 \text{ \AA pixel}^{-1}$; the accuracy of the wavelengths calibration allows sampling of velocities down to 40 km s^{-1} . Contamination from the H II region has been subtracted by averaging the emission from several offset positions. Details about the ESO 3.6 m-telescope⁶ and EFOSC2⁷ are available in the Internet.

EMMI at the ESO NTT

L. Schmidtobreick took another spectrum of the same object in July 2003 with EMMI at the ESO NTT. The aperture length was 8', with a width of 1" and a slit orientation perpendicular to the plane of the disk. Again, the spectra comprise a total wavelength range from $\lambda\lambda 4000 - 9000 \text{ \AA}$ and provide a spectral resolution of $2.8 \text{ \AA per pixel}$; the accuracy of the wavelengths calibration allows sampling of velocities down to 40 km s^{-1} . Like above, the contamination from the H II region has been removed by subtracting the averaged emission from several offset positions.

UVES at the ESO VLT

Eventually, a last spectroscopic run was performed by R. Chini in July 2004 with UVES (Dekker et al. 2000) at the ESO VLT. The observations were centered on RA = 18:20:26.2 and DEC = -16:12:10 (J2000) and the slit geometry was $0''.3 \times 16''$. The data has been obtained with

⁶<http://www.lis.eso.org/lasilla/Telescopes/360cat/>

⁷<http://www.lis.eso.org/lasilla/sciops/3p6/efosc/>

the Red CCD mosaic with the red filter SHP700 and cross disperser CD#3 yielding a spectral resolution R of 110.000. We chose a non-standard central wavelength of 670 nm. Additional information about UVES ⁸ can be obtained from the Internet.

2.6 Infrared Spectroscopy

We took J - and K -band spectra for 96 and 201 stars, respectively. The J band spectroscopy of the M17 cluster has been obtained during two observing runs in 2005 and 2006 with ISAAC at UT1 in service mode. An $0.6'' \times 120''$ slit was used in short-wavelength medium-resolution mode (SWS1-MR) resulting in a spectral resolution of 5700. The K band spectra were taken with the same instrument; the first session in 2004 was performed in visitor mode, the session in 2005 in service mode. An $0.3'' \times 120''$ slit in short-wavelength low-resolution mode (SWS1-LR) yielding a spectral resolution of 1500.

	slit width	spectroscopy mode	R	Filter
J band spectra	0.6	SWS1-MR	1500	SZ
K band spectra	0.3	SWS1-LR	5700	SK

Table 2.3: Selected technical details of the NIR spectroscopy

The acquisition template "MoveToSlit" is mandatory for short wavelength spectroscopy except for rapid-response observations. It provides the possibility to obtain two images with user-defined offsets in right ascension and declination between each other. The difference of these two images is the actual acquisition image that contains positive and negative stars but no NIR sky background. A drawing of the selected slit is superimposed on the acquisition image and an interactive tool is used to center the slit on certain stars.

The spectroscopic observation have been performed with the template "AutoNodOnSlit" as follows: the telescope was nodded between two positions (A and B) along the slit. At each position 2 or 4 images were obtained depending on the brightness of the objects.

Due to the rapidly varying nebular background on fairly small scales it is not advisable to reduce the data by the standard method. Usually AB pairs are subtracted in order to get rid of the sky background. Unlike the sky background, the nebular background is inhomogeneous and cannot be subtracted by this approach. Therefore the background was fitted during the extraction for each frame individually, and if necessary several times, to optimize the background subtraction. Apart from that, the data have been reduced and analyzed with standard procedures with IRAF v.2.11.3a. Wavelength calibrations were made with arc spectra and OH sky lines (Rousselot et al. 2000) in the K and J band, respectively.

In order to keep the observation effective we decided to go without subsequent telluric standards and flatfields and rely on the standard calibrations. Therefore, residuals of telluric features are present in some of the K band spectra (see Sect. A.3) while some bright spectra show fringing (see Sect. A.2 and A.3).

The selection and spatial distribution of the sources across the field in Fig. 2.2 was fairly arbitrary. We centered one or two of the brighter sources onto the $120''$ slit, while on average two to three additional sources happened to be covered by the same slit position. In this

⁸<http://www.eso.org/instruments/uves/index.html>

way, more than half of the stars entered our IR-sample by pure chance. The IR-sources span an apparent brightness range from $I = 8 - 20$ mag for both the J - and the K -band sources. In summary, both groups (optical + IR) provide a fairly complete magnitude limited sample down to about $I \approx 18$ mag with a uniform field coverage.

2.7 Intrinsic Colors

To interpret the photometric results in terms of color-color and color-magnitude diagrams the adopted intrinsic colors are of crucial importance. They influence the photometric spectral types, the visual extinction, and the crucial question whether a star has infrared excess (IRE).

2.7.1 Dwarf Stars

The intrinsic UBV colors of stars have been reviewed by Schmidt-Kaler (1982). His compilation is based on Schmidt-Kaler (1965), Deutschman et al. (1976), and partly Davis (1977); for F5 - M8 V in addition Gliese & Jahreiß (1980).

Johnson (1966) presented the first $RJJK$ intrinsic colors, based on nearly 1000 stars of all luminosity classes. This pioneering work was followed by a number of contributions: Whittet & van Breda (1980) used 229 stars of luminosity classes II - V and spectral types O6 - A2. Koornneef (1983b) unified previous works. Bessell & Brett (1988) provided data for spectral types B8 - M6 while Bouchet et al. (1991) used 199 stars of all luminosity classes and spectral types B2 - K2. Wegner (1994) used 700 stars of spectral type O5 - B9 and finally Ducati et al. (2001) used a sample of 3946 stars of spectral types B0 - M4 and all luminosity classes. Eventually, the following - partly overlapping - data sets were used in the present work:

M_V	O3 - B3	Crowther (2005)
M_V	B0 - M4	Schmidt-Kaler (1982)
$B-V, V-R, V-I, V-J, V-H, V-K$	B0 - M4	Ducati et al. (2001)
$K-L'$	B8 - M4	Bessell & Brett (1988)

NIR intrinsic colors have been converted to the 2MASS/ISAAC photometric system according to Sec. 2.8; intrinsic colors from Ducati et al. (2001) and Bessell & Brett (1988) have been converted with the equations with the index Koornneef and Bessel & Brett, respectively.

2.7.2 T Tauri Stars

Intrinsic colors of 30 classical T Tauri stars (CTTS) have been derived by Meyer et al. (1997). The locus of CTTS is given by the following equations:

$$J-H = 0.58 \pm 0.11 \times (H-K) + 0.52 \pm 0.06$$

$$H-K = 0.69 \pm 0.05 \times (K-L) - 0.05 \pm 0.04$$

Considering Gaussian error propagation, combination of the above equations yields:

$$\Rightarrow J-H = 0.40 \pm 0.16 \times (K-L) + 0.49 \pm 0.21$$

Weak line T Tauri stars (WTTS) have colors consistent with normal main sequence stars.

2.8 Color Transformations

Color-color diagrams have been used to derive color transformations from Gunn r and i to Johnson R and I .

$$R = r + 0.094 \times (V - J) - 0.036$$

$$I = i + 0.098 \times (V - J) - 0.115$$

Near infrared intrinsic colors and reddening law have been converted to the 2MASS/ISAAC photometric system with the following equations from the Explanatory Supplement to the 2MASS All Sky Data Release and Extended Mission Products VI.4b.

$$(Ks)_{2MASS} = K_{\text{Bessel \& Brett}} + (-0.039 \pm 0.007) + (0.001 \pm 0.005)(J - K)_{\text{Bessel \& Brett}}$$

and

$$(Ks)_{2MASS} = K_{\text{Koornneef}} + (-0.046 \pm 0.005) + (0.036 \pm 0.019)(J - K)_{\text{Koornneef}}$$

$$(J - H)_{2MASS} = (1.019 \pm 0.023)(J - H)_{\text{Koornneef}} + (-0.038 \pm 0.006)$$

$$(J - Ks)_{2MASS} = (0.974 \pm 0.016)(J - K)_{\text{Koornneef}} + (-0.011 \pm 0.006)$$

$$(H - Ks)_{2MASS} = (0.779 \pm 0.052)(H - K)_{\text{Koornneef}} + (0.030 \pm 0.004)$$

↓

$$(K)_{\text{Koornneef}} = (Ks)_{2MASS} + (0.035 \pm 0.035) \times (J - H)_{2MASS} + (-0.047 \pm 0.030)$$

$$(J - H)_{\text{Koornneef}} = (0.981 \pm 0.023) \times (J - H)_{2MASS} + (0.037 \pm 0.006)$$

$$(J - K)_{\text{Koornneef}} = (1.027 \pm 0.016) \times (J - Ks)_{2MASS} + (-0.011 \pm 0.006)$$

$$(H - K)_{\text{Koornneef}} = (1.284 \pm 0.052) \times (H - Ks)_{2MASS} + (-0.039 \pm 0.004)$$

2.9 Transformed Near Infrared Reddening Paths

Like the intrinsic colors, the direction and length of the reddening path play a crucial role for the interpretation of color-color and color-magnitude diagrams. As demonstrated below, the dust inside M17 requires a special reddening law which is characterized by a ratio of total-to-selective extinction $R = 3.9$.

Cardelli et al. (1989) provides an R -dependent reddening law in the Johnson photometric system (Johnson 1966). A_J/A_V , A_H/A_V , and A_{Ks}/A_V have been converted from Cardelli et al. (1989) with $R = 3.9$ according to the above color transformations (see Sec. 2.8). A_H/A_V does not have a unique solution but can result in 0.155 or 0.163; the average was used. $A_{L'}/A_V$ has been calculated from A_H/A_V , A_{Ks}/A_V , and the slope of the data in the $HKKL$ diagram (see Fig. 3.7).

Table 2.4: Reddening Law from Cardelli et al. (1989) with $R=3.9$ and transformed to the 2MASS/ISAAC photometric system

λ	A_λ/A_V	
	Johnson	2MASS/ISAAC
U	1.442	–
B	1.256	–
V	1.000	–
R	0.775	–
I	0.519	–
J	0.306	0.272
H	0.196	0.159
K	0.127	0.106
L	0.052	0.064

Chapter 3

Results

The following sections describe those observational results that concern the cluster in general. The first two parts provide an overview of the photometric properties of the stellar content while the third part addresses the spectroscopic issues.

3.1 Color-Color Diagrams

Color-color diagrams are a potential tool to investigate the properties of stellar photospheres, the interstellar extinction and possible circumstellar emission. A normal stellar photosphere can be approximated by a single blackbody and thus one color is sufficient for its description. However, any deviation from the normal spectral energy distribution due to reddening by dust extinction and/or emission is easily detected when employing additional colors in the framework of TCDs. In this section, the photometric results will be presented in form of various TCDs which are of importance for the detection of circumstellar disks as discussed in Sect. 3.1.8.

Apart from the observed colors for the stars towards M 17, the following diagrams also contain the unreddened colors of main sequence star for comparison. Considering Sect. 2.7 and Sect. 2.8 the corresponding data have been taken from Schmidt-Kaler (1982) and Crowther (2005) for absolute V -magnitudes and $B - V$ while the other colors come from Ducati et al. (2001); the latter ones differ significantly from those by Koornneef (1983b).

3.1.1 Diagrams of the Form $V - \lambda$ vs. $B - V$

TCDs of the form $V - \lambda$ vs. $B - V$ have the property that the locus of the unreddened main sequence and the reddening vector fall onto each other. Therefore, they provide a sensitive method to detect deviations from this expected locus. Possible reasons for deviations may be strong photospheric lines, circumstellar emission and an abnormal reddening law. Age and age spread of a cluster also strongly effect the locus of the stars; isochrones from Siess et al. (2000) reveal that low-mass PMS stars may be mistaken as IRE sources or lead to an erroneous adoption of an abnormal reddening law.

Fig. 3.1 shows six diagrams of the form $V - \lambda$ vs. $B - V$, where λ comprises the wavebands *RIJHKL*. The magenta curve denotes the locus of unreddened main-sequence stars (Ducati et al. 2001), the dashed and solid green lines are the normal (Rieke & Lebofsky 1985) and abnormal (Sect. 4.1.5) reddening vector. The abnormal reddening vector has been tied to

the normal one at an assumed foreground extinction of 2 mag (see Sect.4.1.5). Each diagram contains a different numbers of stars: The $V - R$ vs. $B - V$ diagram is limited by the R band sensitivity and the $V - I$ vs. $B - V$ diagram is limited by the B band sensitivity. The combination of optical and NIR data suffers from the different sensitivity levels: Bright optical stars are saturated in the NIR, most IR sources do not have an optical counterpart.

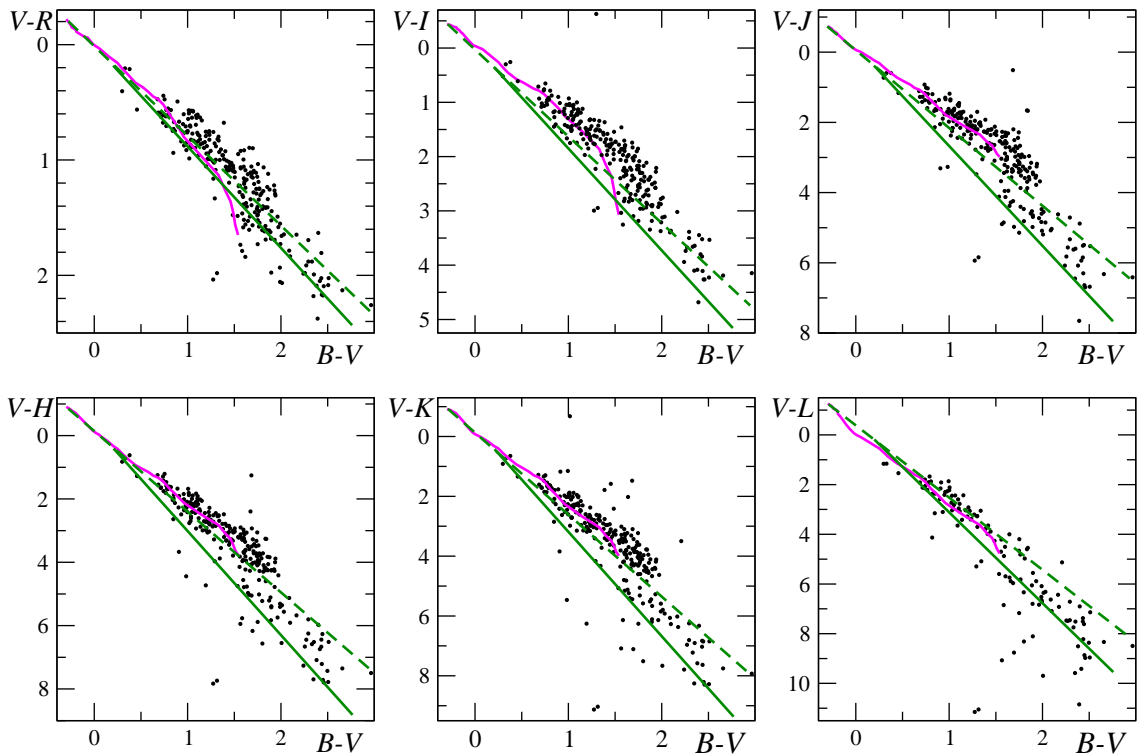


Figure 3.1: TCDs for a sample of 94 to 160 visible stars; the magenta curve represents the locus of unreddened main sequence stars (Schmidt-Kaler 1982; Crowther 2005; Ducati et al. 2001) the green lines denote the reddening paths; dashed for $R = 3.1$ (Rieke & Lebofsky 1985) and solid for $R = 3.9$ (Cardelli et al. 1989).

3.1.2 Diagrams of the Form $I - \lambda$ vs. $V - I$

In diagrams of the form $I - \lambda$ vs. $V - I$ main sequence and reddening vectors are roughly parallel for spectral types earlier than K5. As mentioned in the last section, this provides a sensitive method to detect deviations from the locus of reddened main sequence stars. Fig. 3.2 shows the corresponding TCDs. The green lines correspond to reddening vectors of $A_V = 2$ mag foreground extinction (dashed) and additional $A_V = 10$ mag and $A_V = 5$ mag in M17 (solid) (Sect. 4.1.5). The reddening vectors have been tied to the main sequence in such a way that the space between these lines defines the "allowed" region for main-sequence stars.

3.1.3 The $J - H$ vs. $H - K$ Diagram

TCDs constructed exclusively from NIR colors have been studied by Chini et al. (1992). The comparison of the loci of reddened stars, warm dust of 750 to 2.000 K and black bodies of 1.000

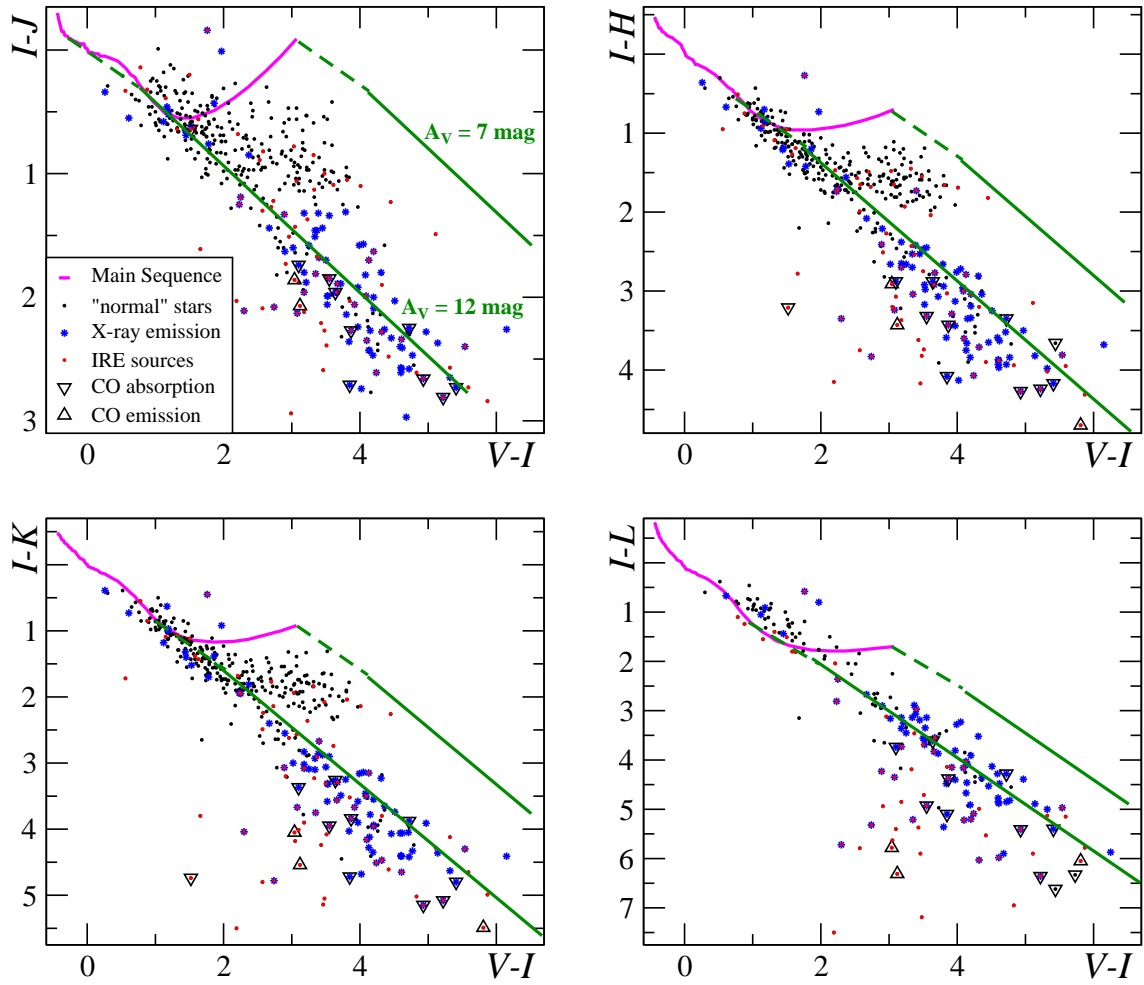


Figure 3.2: The $I - \lambda$ vs. $V - I$ diagrams for optically visible stars; same notation as Fig. 3.1. The green lines denote the reddening vectors with $A_V = 12$ mag and $A_V = 7$ mag, respectively. Red dots correspond to IRE objects which were classified as such in the NIR diagrams of Fig. 3.8. Objects with particular properties are marked by individual symbols.

to 30,000 K showed that the most commonly used JHK diagram has several disadvantages: i) The H -band may be contaminated by emission associated with the formation of molecular hydrogen and the absorption by H^- in cool stellar atmospheres. ii) Emission lines as seen e.g. in T Tauri stars contribute significantly at $1.6 \mu\text{m}$. iii) The reddening path and the locus of dust emission are very similar, making a discrimination between the two effects rather difficult. As shown by Aspin & Barsony (1994) from observational data in the literature, the locus of many T Tauri stars and protostellar objects may fall into the region of normal JHK colors.

Fig. 3.3 shows the JHK diagram for a sample of 4330 stars, whose photometric errors are ≤ 0.1 mag. The magenta curve denotes the unreddened main sequence, the green lines show the reddening vectors appropriate for M 17 as discussed in Sect. 2.9. The observed color range of $J - H \sim 4$ and $H - K \sim 2$ implies that the visual extinction extends over more than 35 mag. 858 (20%) of the objects are above the upper reddening path, which is the region of

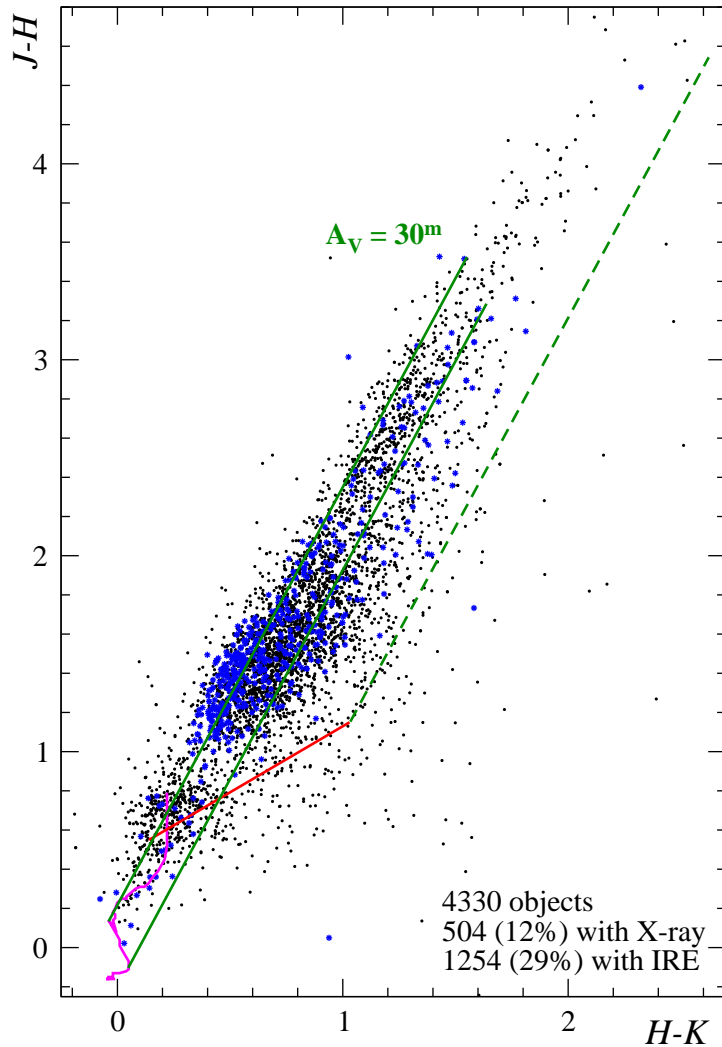


Figure 3.3: The JHK diagram for a sample of 4330 stars. Sources with X-ray emission are marked with blue asterisks. The green lines denote the transformed reddening vectors (Sec. 2.9) for the main sequence (magenta) (Ducati et al. 2001) and T Tauri stars (red) (Meyer et al. 1997) with a length of $A_V = 30^m$ respectively.

giant stars. The fact that several stars with X-ray emission fall into that area, might suggest that they are possibly young objects. 2214 (51%) of the sources are located in the “normal” region between the two leftmost reddening vectors suggesting that they are partly heavily reddened main sequence stars. 1258 (29%) of the sources are located in the “excess” region right of the lower reddening path. Most of them are rather close to the area of reddened main sequence stars i.e. they are likely T Tauri stars; Herbig AeBe stars and protostellar objects are further away from the reddened main sequence stars. The star with the strongest excess has $H - K = 3.56$ and $J - H = 2.53$ (not shown in Fig. 3.3) and resides at the interface between the H II region and the southwestern molecular cloud (M17-SW). This diagram is discussed in more detail in Chap. 4.

3.1.4 The $J - H$ vs. $H - L$ Diagram

Fig. 3.4 shows the JHL diagram for a sample of 2188 stars, whose JHL errors are ≤ 0.1 mag. The magenta curve denotes the unreddened main sequence, the green lines show the reddening vectors appropriate for M17 as discussed in Sect. 2.9. The observed color range of $J - H \sim 4$ and $H - L \sim 3.8$ implies a range visual extinction of more than 35 mag. There are 272 (12%) objects above the upper reddening path in the region of giant stars; again several X-ray sources are among this sample, indicating the youth of those stars. Given the low photometric errors (< 0.1 mag) of the data points in this diagram, their positions have to be taken serious. 898 (41%) of the sources are located in the “normal” region between the two reddening lines suggesting that they are partly heavily reddened main sequence stars. 1018 (47%) sources are located in the “excess” region below the lower reddening path.

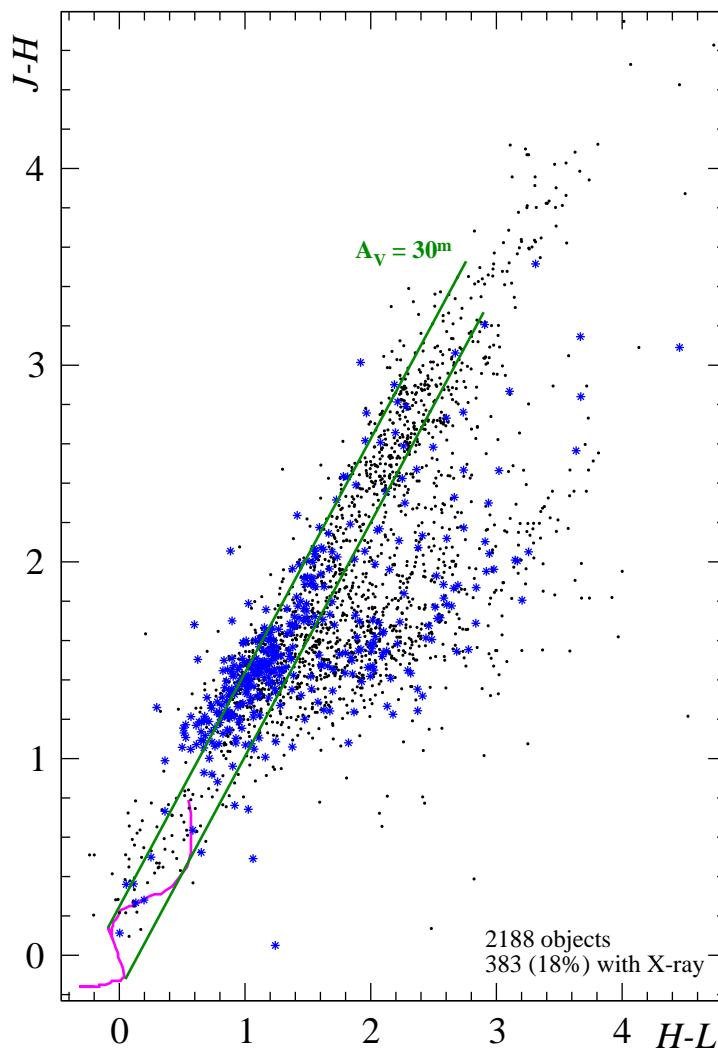


Figure 3.4: Same notation as Fig. 3.3.

3.1.5 The $J - H$ vs. $K - L$ Diagram

Fig. 3.5 shows the $JHKL$ diagram for a sample of 2173 stars, whose $JHKL$ errors are ≤ 0.1 mag. The magenta curve denotes the unreddened main sequence, green lines show the reddening vectors appropriate for M17 as discussed in Sect. 2.9. The observed color range of $J - H \sim 4$ and $K - L \sim 2$ implies a visual extinction of more than 35 mag and 45 mag, respectively; the larger value is obviously contaminated by excess emission. Altogether 161 (7%) stars fall above the upper reddening path, among them a fair fraction of X-ray sources. It is therefore unlikely, that all of them are late-type giant stars. 1126 (52%) sources are located in the “normal” region between the two reddening vectors suggesting that they are partly heavily reddened main sequence stars. 886 (41%) sources are located in the “excess” region below the lower reddening path. This is the region of T Tauri stars, Herbig AeBe stars and protostellar objects.

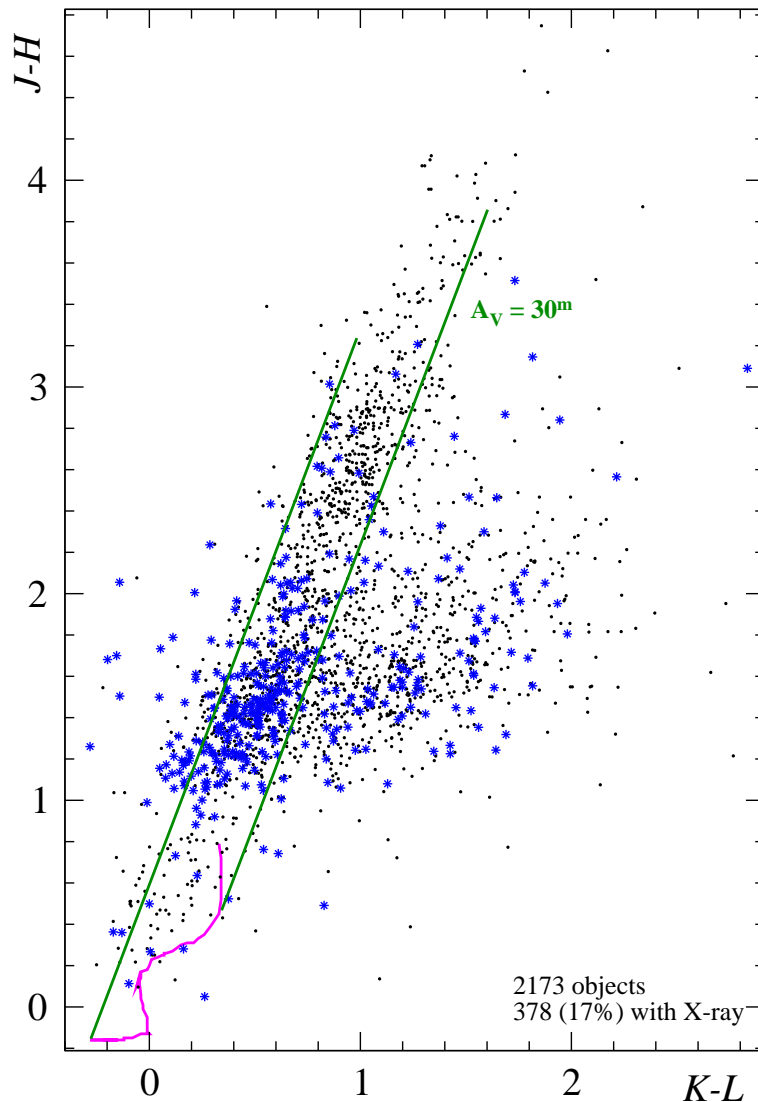


Figure 3.5: Same notation as Fig. 3.3.

3.1.6 The $J - K$ vs. $K - L$ Diagram

Fig. 3.6 shows the $JKKL$ diagram for a sample of 2176 stars, whose JKL errors are ≤ 0.1 mag. The magenta curve denotes the unreddened main sequence, the green lines show the reddening vectors appropriate for M17 as discussed in Sect. 2.9. The observed color range of $J - K \sim 6$ and $K - L \sim 2$ implies a visual extinction of more than 35 mag and 45 mag, respectively; the larger value is obviously contaminated by excess emission. 139 (6%) objects are above the upper reddening path, consistently comprising some X-ray sources. 1143 (53%) of the sources are located in the “normal” region between the two reddening paths suggesting that they are partly heavily reddened main sequence stars. 894 (41%) sources are located in the “excess” region.

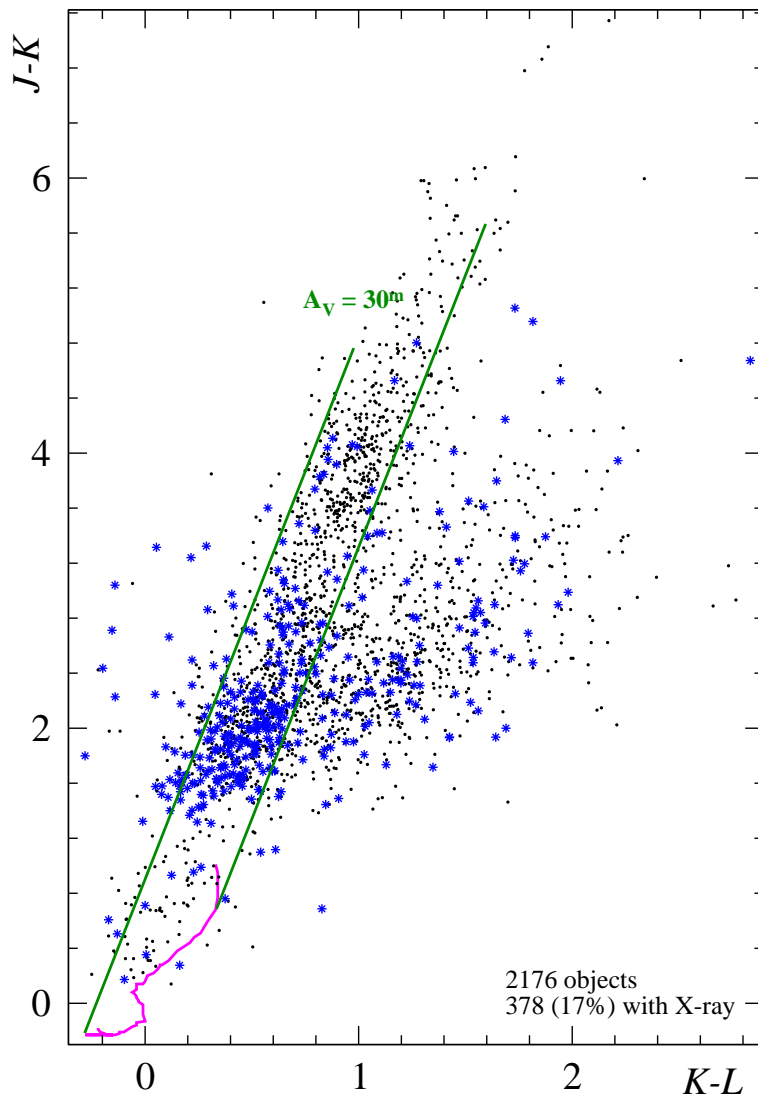


Figure 3.6: Same notation as Fig. 3.3.

3.1.7 The $H - K$ vs. $K - L$ diagram

The last diagram in this series is Fig. 3.7 showing the HKL colors for a sample of 2967 stars; their HKL errors are ≤ 0.1 mag. The magenta curve denotes the unreddened main sequence, the green lines show the reddening vectors appropriate for M17 as discussed in Sect. 2.9, the red line shows the locus of T Tauri stars (Meyer et al. 1997). The observed color range of $H - K \sim 3$ and $K - L \sim 3$ implies a visual extinction of more than 50 mag and 70 mag, respectively. $K - L$ is obviously enlarged by excess emission; $H - K$ is larger than in Fig. 3.3 because this diagram contains stars without J -band detections making it therefore possible to look deeper into the region. Anyway, $H - K$ might also possibly be enlarged by excess emission. Apart from 115 (4%) objects in the region of giant stars, 1474 (50%) of the sources are located in the “normal” region between the two reddening lines suggesting that they are partly heavily reddened main sequence stars. 1378 (46%) sources are located in the “excess” region below the lower reddening path of the main sequence. This diagram is discussed in more detail in Chap. 4.

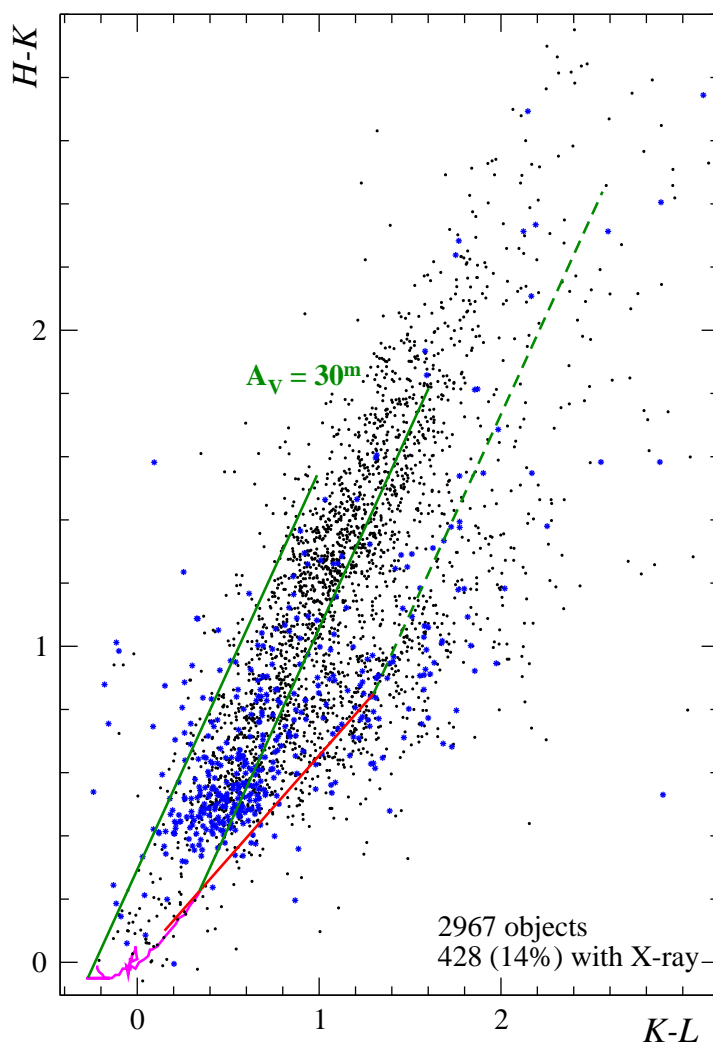


Figure 3.7: Same notation as Fig. 3.3.

3.1.8 Determination of IRE from NIR TCDs

Although the definition of an IRE object seems evident, in practical terms it depends on various assumptions particularly when derived from NIR TCDs. The adopted intrinsic colors are equally important as the slope of the reddening path. The combination of both spans a region in which main sequence stars are located, i.e. between the green lines in Fig. 3.8. Above this stripe, giants, supergiants and massive PMS stars should be located; the latter should share similar color properties as supergiants. Below it is the region of objects with IRE. If a source lies in one or more of the red hatched areas in Fig. 3.8 it has been flagged as an IRE object in the present work. The probability for a true IRE increases with the number of diagrams in which a source is located in the hatched areas.

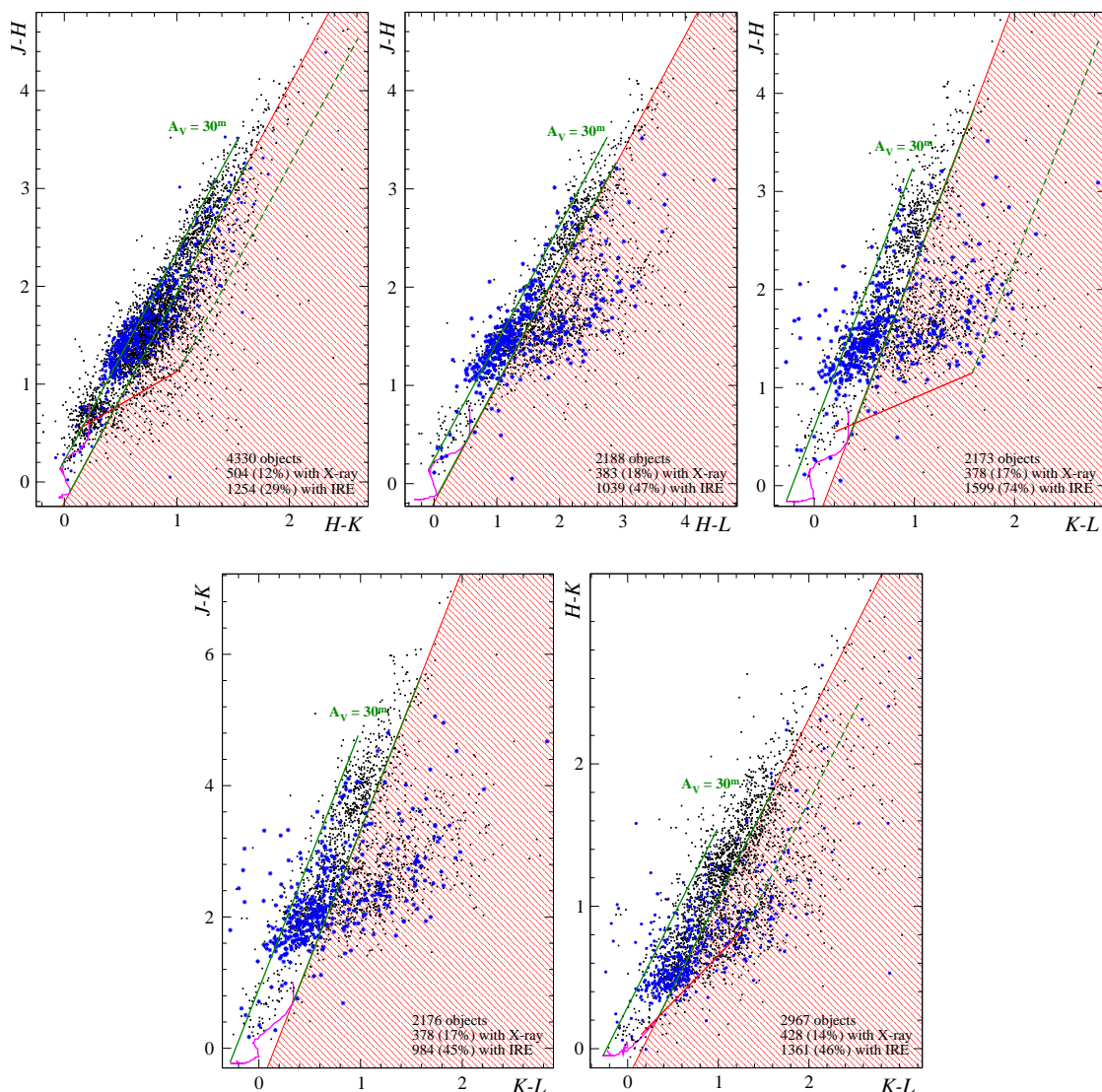


Figure 3.8: Collection of NIR TCDs which have been used to determine IRE (hatched half-planes); same notation as Fig. 3.3.

3.2 Color–Magnitude Diagrams

Color-magnitude diagrams (CMDs), which are equivalent to the Hertzsprung-Russell diagram (HRD), allow – in the case of a main sequence star – to determine both spectral type and reddening. PMS stars can also be traced if their reddening is known. In the case of M17, however, the a priori unknown mixture of stars with differential reddening, IRE due to circumstellar dust and a possible PMS nature does not allow a unique classification. By comparing the results from different CMDs and their combination with the results from the TCDs, the above effects can partly be disentangled. In this section, a number of CMDs will be presented which are of some relevance for the discussion in Chap. 4. A further application of CMDs is the determination of the cluster distance by zero-age main sequence (ZAMS) fitting.

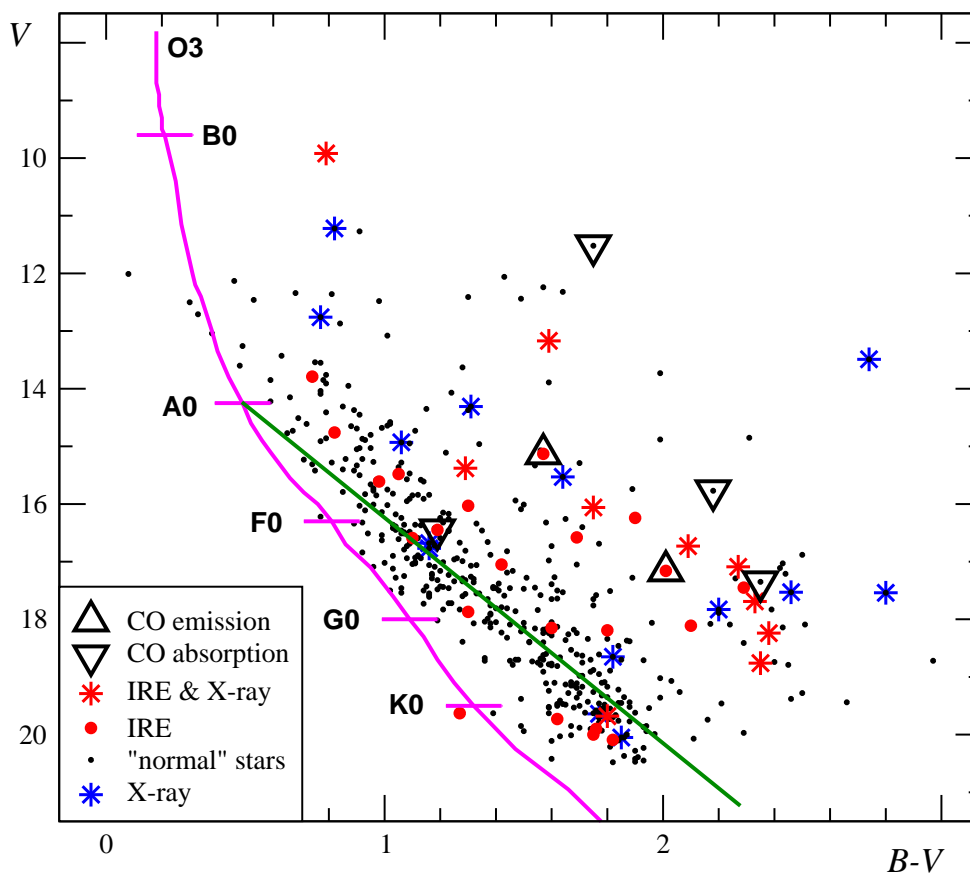


Figure 3.9: The $V/B - V$ CMD for a sample of 483 visible stars. The solid curve (magenta) denotes the locus of main sequence stars from B0 to K5 (Schmidt-Kaler 1982; Ducati et al. 2001) corrected for a normal foreground extinction of 2 mag and a distance modulus of $m - M = 11.6$. The green line denotes the reddening vector for M17 corresponding to $A_V = 7$ mag; it separates spectral types earlier from those that are later than A0.

3.2.1 The V vs. $B - V$ Diagram

For 483 of the optically bright stars whose photometric errors are less than 0.1 mag the classical V vs. $B - V$ diagram is shown in Fig. 3.9. The solid curve (magenta) denotes the locus of the main-sequence from O3 to K5 (Schmidt-Kaler 1982; Ducati et al. 2001), adapted for a distance of 2.1 kpc and a uniform normal foreground extinction of 2 mag. The dereddened version of this diagram will be discussed in Sect. 4. However, objects with special properties have been designated with particular symbols because some of them will disappear in the dereddened version of this diagram (Sect. 4.1.7)

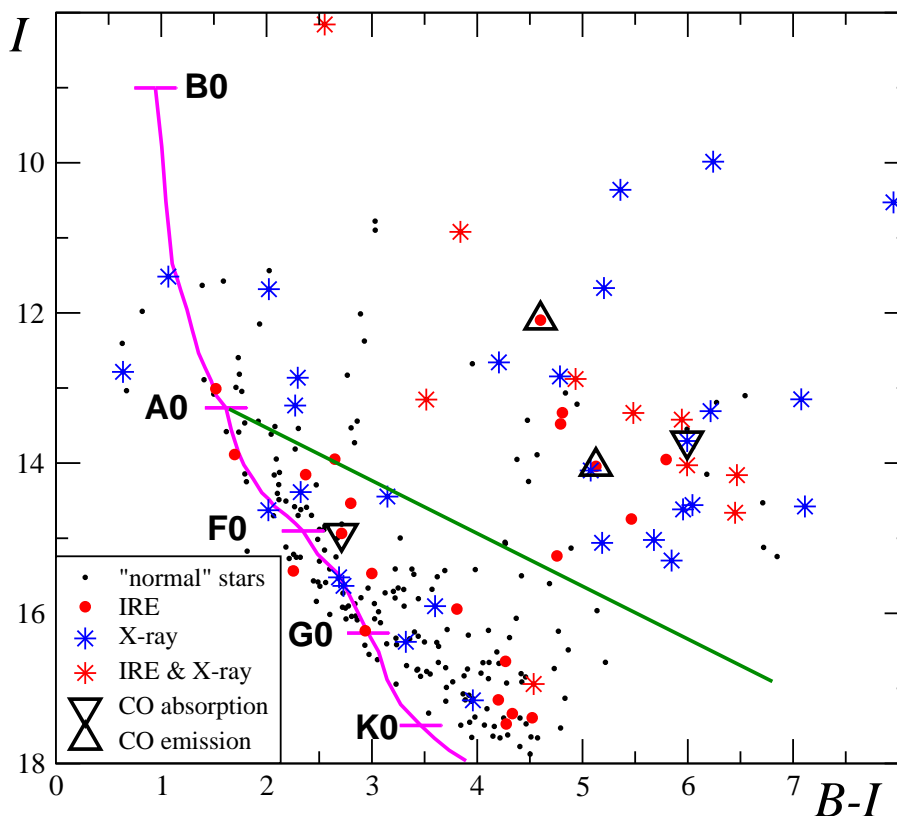


Figure 3.10: The $I/B - I$ CMD for a sample of 251 visible stars; same notation as Fig. 3.9.

3.2.2 The I vs. $B - I$ Diagram

In order to obtain a different view of the above results another optical CMD I vs. $B - I$ has been constructed for 251 stars with photometric errors less than 0.1 mag (Fig. 3.10). The solid curve denotes the locus of the main sequence from B0 to K5 (Schmidt-Kaler 1982; Ducati et al. 2001), adapted for a distance of 2.1 kpc and a uniform normal foreground extinction of 2 mag. As before, the green line denotes the special reddening vector as appropriate for M17 (see Sect. 2.9 and 4.1.5) with a length corresponding to $A_V = 7$ mag. 39 stars lie in the range $I < 15$ mag and $B - I > 4$ mag and could be spectroscopically classified. Apart from the expected OB stars, nine of them are later than G0 and six of those nine show X-ray emission. Apparently the first PMS stars in M17 become visible.

3.2.3 The J vs. $J - H$ Diagram

The J vs. $J - H$ diagram is a potential tool in the present study because it provides a broad view over a large number of stars. Compared to the optical diagrams it contains almost a factor of 30 more stars. Additionally, among all IR diagrams it has probably the lowest contamination by IRE, thus providing a fairly undisturbed view onto the cluster population. It contains 4936 objects and will be discussed in more detail in Sect. 4.1.6.

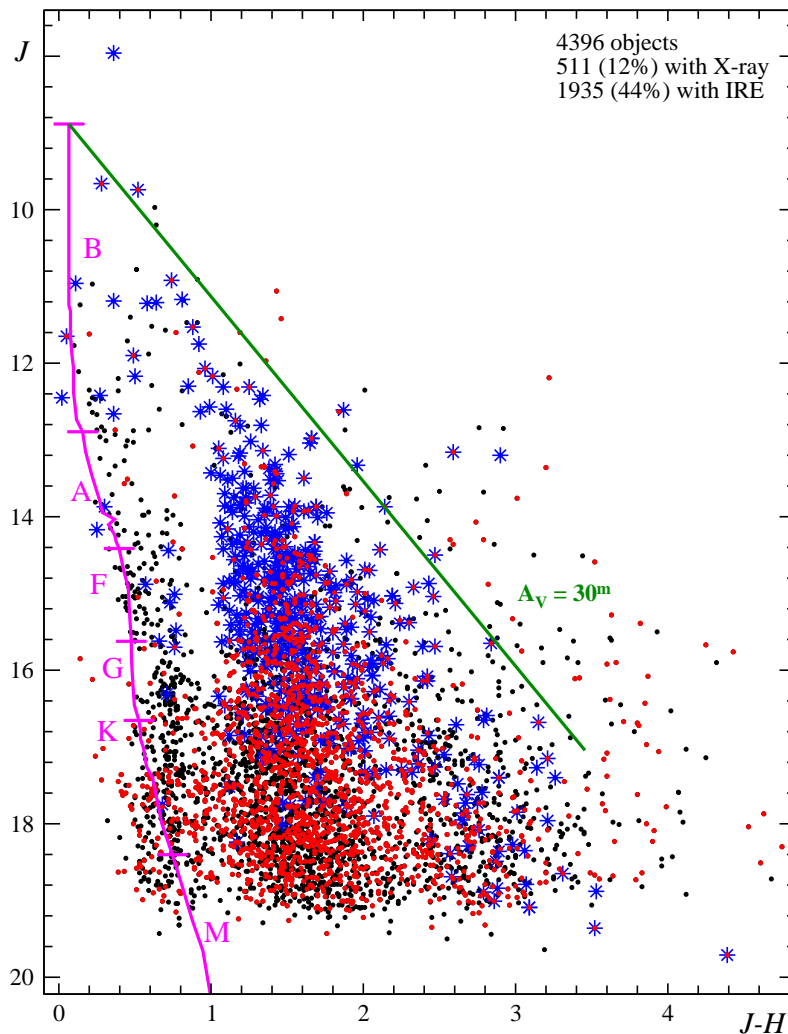


Figure 3.11: J vs. $J - H$ CMD for 4396 stars. The magenta curve corresponds to the ZAMS for a distance of $d = 2.1$ kpc and corrected for a foreground extinction of $A_V = 2$ mag. The reddening vector with a length of $A_V = 30$ mag is shown as a solid green line. Blue asterisks characterize 511 (12%) stars with X-ray emission, red symbols denote 1935 (44%) stars with IRE. The diagram includes only data points with photometric errors less than 0.1 mag at each waveband.

3.2.4 The H vs. $H - K$ Diagram

One consequence of the large extinction in M 17 is the fact that 3733 stars could not be detected in the J band. Therefore, the combination H vs. $H - K$ is the diagram that includes the maximum number of stars of the present investigation; Fig. 3.12 shows 8496 stars.

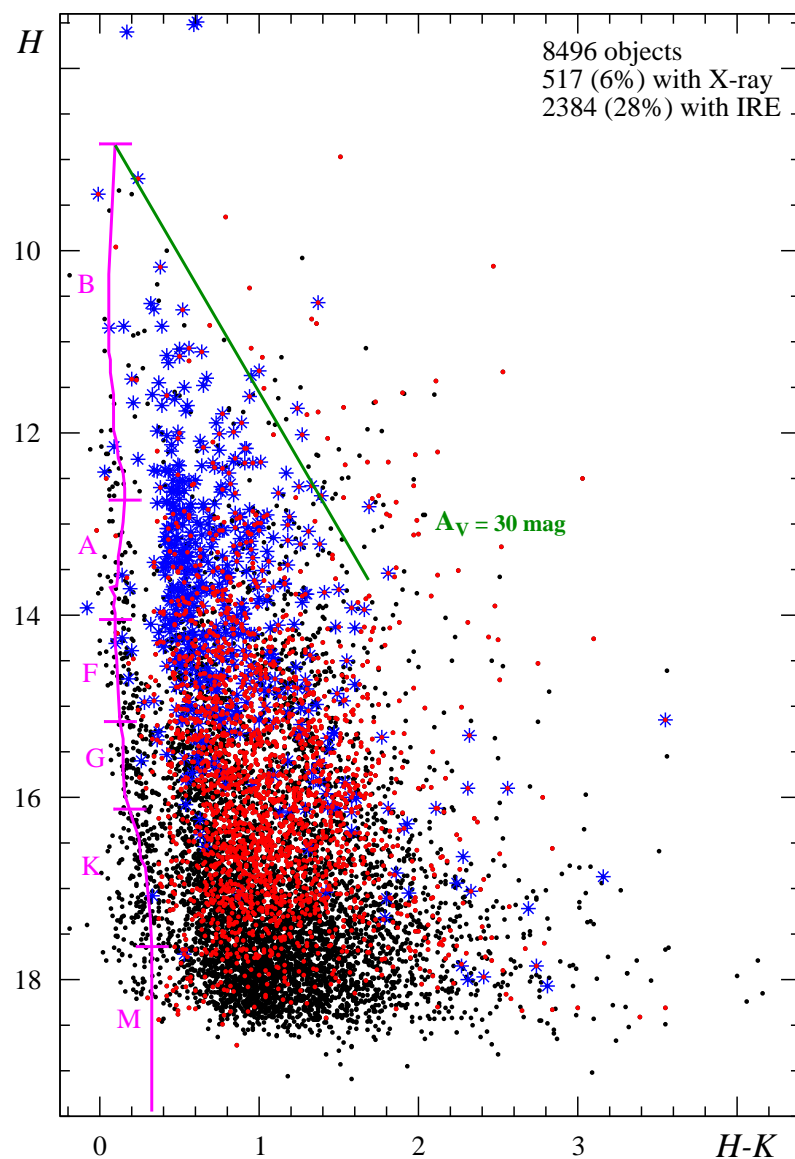


Figure 3.12: The H vs. $H - K$ CMD for 8496 stars; same notation as Fig. 3.11.

A disadvantage of the longer wavebands, however, is that stars with a possible IRE will simulate an object with earlier spectral type and higher extinction. As to be expected, most stars without J measurements (green dots) are either intrinsically faint (later M0) and/or heavily reddened (see Fig. 3.13).

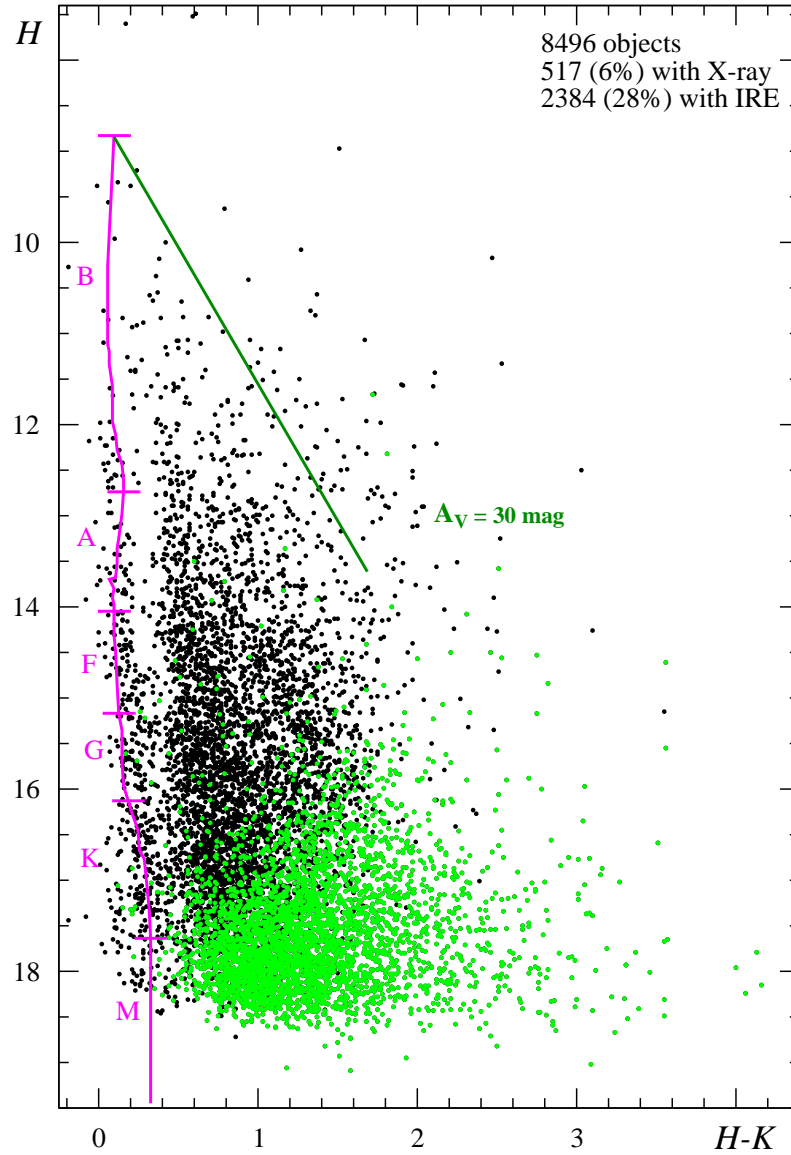


Figure 3.13: Same diagram as Fig. 3.12. Stars that could not be detected in the J -band are marked by green dots.

3.3 Spectra

A spectroscopic classification of stars in M17 is difficult due to the large amount of inter- (and possibly circum-)stellar extinction. Optical studies, particularly in the blue regime, suffer from low intensities, IR studies provide only a few diagnostic lines for classification purposes. Additionally, veiling in both the blue and the IR regime may suppress existing photospheric lines.

3.3.1 Optical Spectra

As explained in Sect. 2 there were two major spectroscopic observing runs at optical wavelengths. A low-resolution campaign comprising the entire wavelength range from $\lambda\lambda 3800 - 9200 \text{ \AA}$ and a medium-resolution run from $\lambda\lambda 8200 - 9300 \text{ \AA}$. Although both data sets have been acquired during the present work (ESO application, observations, service mode preparations), only the first one, including about 80 stars, has been completely reduced and analyzed within the framework of this dissertation. The corresponding spectra are displayed in the Appendix A.1 as long as sufficient S/N could be achieved.

The reduction and analysis of the medium-resolution data for almost 320 stars down to a limiting magnitude of $I \sim 18$ has been performed by an undergraduate student (R. Watermann) during his diploma thesis. This huge amount of data provides the first step toward a statistically meaningful overview about the stellar types in the cluster. Some of those results have also entered the present dissertation. The reduced spectra, however, have not been included in the Appendix.

3.3.2 Infrared Spectra

The results of the fairly unbiased spectroscopic *J*- and *K*-band survey for about 250 stars at a spectral resolution of 5700 and 1500 are shown in the Appendix A.2 and A.3 as long as sufficient S/N could be achieved. The analysis leads to the conclusion that IR spectral classification is almost impossible in such a very young cluster: most *K*-band spectra are featureless as concerns stellar photospheric lines due to veiling from circumstellar dust. Surprisingly, however, about half of the sources show the CO band-head feature at $2.3 \mu\text{m}$ – sometimes in emission but predominantly in absorption (see Sect. 4.1.10). Nevertheless, some dozens of high-mass stars could be classified for the first time. Comparison with existing classification (Hanson et al. 1997) shows good agreement. Those results are summarized in Table 4.2.

Chapter 4

Discussion

The results from Sect. 3 are now analyzed in more detail and are compared with existing data. Many new insights into various aspects of the formation of stars and clusters in general and into the early evolution of massive stars in particular are given. While the first sections describe the properties of the stellar content in a more global way, subregions and objects of particular interest are discussed in the later sections.

4.1 The Young Cluster

While there are extremely detailed studies of the ISM associated with M17 there is relatively sparse information about the stellar content of the region. Starting with the early investigations of a few bright stars (Schulte 1956; Johnson 1973; Kleinmann 1973) there are some limited survey-type studies of the embedded cluster both in the optical/IR and the X-ray regime.

4.1.1 Optical Surveys

Ogura & Ishida (1976) presented *UBV* photometry for about 700 stars in a $30' \times 30'$ field centered at the radio position of M17. Along with 21 low-dispersion spectra they found six heavily reddened O- or possible O-type stars embedded in the central part of the H II region. First evidence for a young embedded cluster came from Beetz et al. (1976) who found more than 100 partly heavily obscured stars by means of *R* and *I*-band imaging. Subsequently, CEN investigated this cluster by *UBVRI* photometry and classified a sufficient number of O-type stars to account for both the ionization and the infrared luminosity of the H II region. The major exciting star was found to be a double O4-type (CEN 1) in the cluster center. Additionally, CEN presented first evidence for a higher-than-normal ratio of total-to-selective extinction ($R = 4.2$) in the region. Since then no further attempts have been made to study the cluster at optical wavelengths.

4.1.2 X-ray Sources

Broos et al. (2007) observed the stellar populations in and around the M17 H II region with *Chandra* (ACIS). The field reveals 886 sources with observed X-ray luminosities between $\sim 29.3 \text{ ergs s}^{-1} < \log L_X < 32.8 \text{ ergs s}^{-1}$. Most of these X-ray sources have stellar counterparts in the IR (see below). By calibrating the X-ray luminosity function to that of the cluster in



Figure 4.1: Large scale ($80' \times 58'$) optical view of the M17 region (Courtesy: Adam Block, NOAO/AURA/NSF). The white contours correspond to the ^{12}CO distribution (intensities in steps of 5 K) for velocities in the range of $17 - 23 \text{ km s}^{-1}$ (Elmegreen et al. 1979). The two local maxima at $T = 35$ and 50 K refer to Cloud A (north) and Cloud B (southwest).

Orion Broos et al. extrapolated a total population of roughly 8000 - 10,000 stars for M17, one-third lying in the central cluster. About 40% of the ACIS sources are heavily obscured with $A_V > 10 \text{ mag}$.

Apart from the central cluster and well-known embedded groups like the UC1/IRS 5, region, the Kleinmann-Wright Object (KWO), and M17-North, Broos et al. describe several concentrations of stars. The most remarkable claim is the finding of a new embedded cluster (designated M17-X). This stellar ensemble is located at $\text{RA} = 18:20:22$ and $\text{DEC} = -16:07:30$ (J2000) northwest of the cluster center and consists of only 14 objects. With a radius of $1.5'$ it comprises a group of previously known bright O stars (CEN 16, 18, 31) and B stars (CEN 8, 9, 74, 75), visible in the upper central region of Fig. 2.2. Opposite to what is described by Broos et al., this group is indeed separated from the rest of the cluster by some dark patches (see Fig. 2.2 and 1.1) suggesting that it is not a new, distinct population.

Broos et al. corroborate the correlation between X-ray and bolometric luminosities of $L_X \sim 10^{-7} L_{\text{bol}}$ on the basis of 14 O and 19 B0-B3 stars. While many O and early-B stars show the

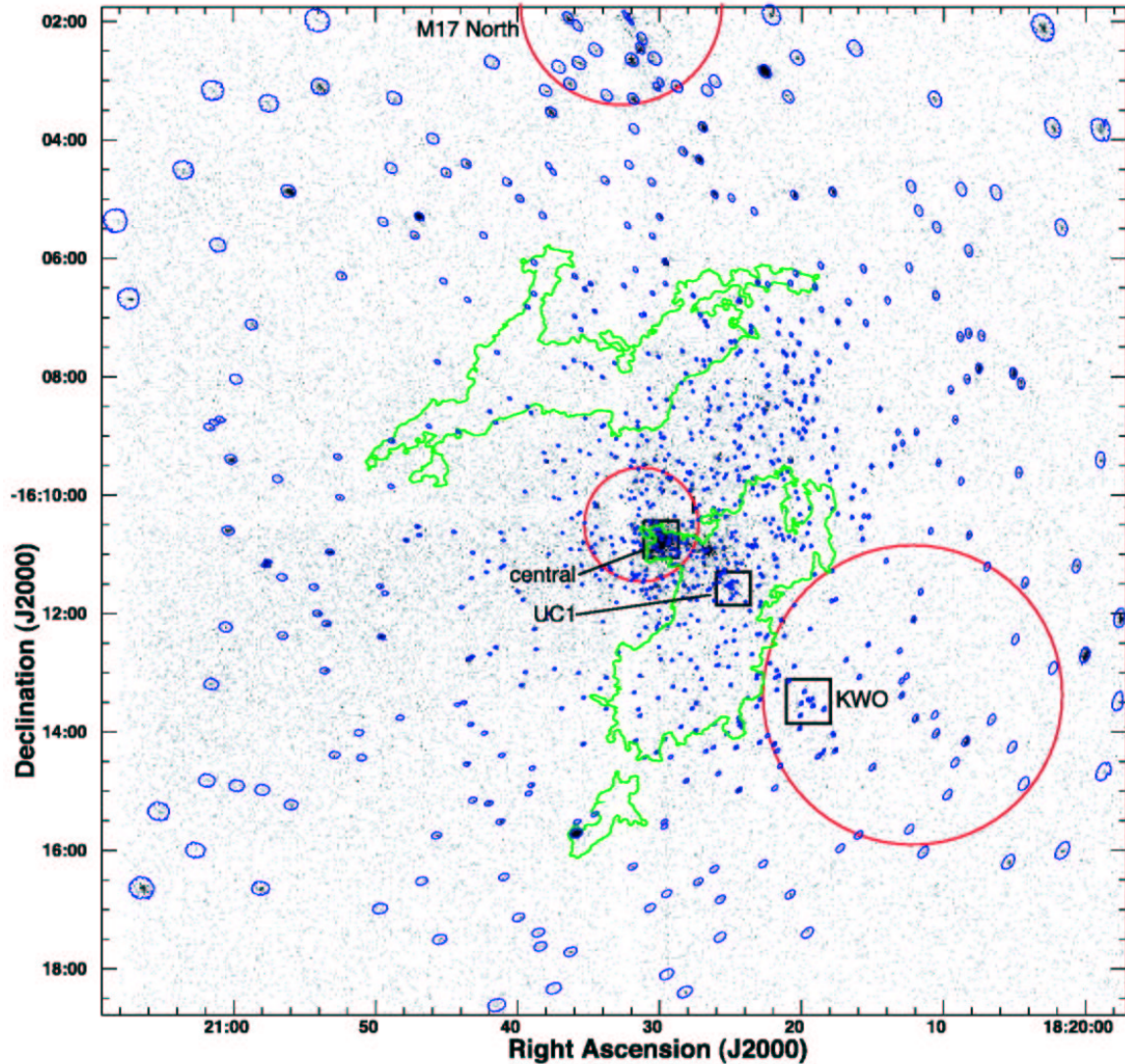


Figure 4.2: *Chandra* ACIS-I binned image of M17 with 886 source extraction regions designed to match the *Chandra* point spread function (PSF) shown in blue (Broos et al. 2007). Green contours outline the $3.6\ \mu\text{m}$ dust emission as detected by *Spitzer* from the Northern and Southern Bar of the H II region. Two circles, reproduced from Fig. 2c in Jiang et al. (2002), outline the central NGC 6618 stellar cluster core and the M17-SW region. A third circle outlines the embedded M17-North region described by Henning et al. (1998). Three small boxes indicate the locations of the major exciting stars (central), a hyper-compact H II region (UC1) and the Kleinmann-Wright Object (KWO).

soft X-ray emission expected from micro shocks in their winds or moderately hard emission that could be caused by magnetically channeled wind shocks, six of these stars exhibit very hard thermal plasma components ($kT > 4\text{keV}$) that may be due to colliding wind binaries. More than 100 candidate new OB stars are found, including 28 X-ray detected intermediate- and high-mass protostar candidates with IREs (see Sect. 4.1.7).

Thirty-nine of the *Chandra* sources show significant X-ray variability with a wide range of flare morphologies, characteristic of X-ray luminous PMS stars. A few sources exhibit random variability not characteristic of T Tauri flares.

The X-ray luminosity function is a tracer of the IMF. However, due to their short (40 ksec) integration time, the existing *Chandra* data do not go down very far in mass. Comparing the *Chandra* sources in M 17 to other star-forming regions (e.g. Orion, NGC 6357, Cep OB3b) shows that the M 17 population of X-ray emitters is similar to these other fields (Broos et al. 2007).

4.1.3 Infrared Surveys

First infrared observations (Kleinmann 1973) revealed two point sources at $2.2\mu\text{m}$, which are coincident with optically visible stars (CEN 1 and CEN 0; see Sect. 4.1.4). Kleinmann & Wright (1973) discovered a further IR source (KWO) in the southwestern molecular cloud which is spatially offset from any other known radio or infrared peaks; this source will be discussed separately in Sect. 4.2.7.

A large NIR map was performed by Lemke & Harris (1981) who covered 50 square arcmin of the nebula and found 10 discrete sources. Five of them were identifiable with known stars. Chini (1982), Chini & Krügel (1985), and Chini & Wargau (1998) observed individual optical stars with apparently large IR excesses (IRE) and discovered further close-by infrared sources. All these measurements used single-channel detectors with partly large ($\sim 10''$) apertures, resulting in poor spatial accuracy with possible bright unknown IR sources inside the aperture; additionally, the beam-switching technique introduced further confusion due to possible unknown sources in the background beam.

With the advent of infrared array detectors the cluster could be observed systematically at *JHK*. Lada et al. (1991) presented first images of a total field of $9' \times 9'$ containing 1109, 2320 and 1305 stars in *J*, *H*, and *K*, respectively. Within an radius of $168''$ around CEN 1 there were more than 350 sources brighter than the completeness limit of $K = 12.8$. Adopting a distance of 2.2 kpc and a visual extinction of 5 – 10 mag for cluster members Lada et al. identified more than 100 OB stars clustering in the obscured portion of the H II region of several parsecs in diameter. Obviously, this estimate, which was purely based on the individual *K*-band brightness, only holds for main sequence stars – an assumption that was not justified by observations. Additionally, the authors claimed that most cluster members display IRE. Although the *K* luminosity function of this cluster must be contaminated by the observed *K*-band excesses (see Sect. 4.1.9) and by possible evolutionary effects, Lada et al. used its slope to state that it is identical to the Salpeter initial mass function. If true, this would imply that the contribution of disk emission is independent of the stellar mass – a fact which is not corroborated observationally either. Actually, observations of IC 348 and the Trapezium cluster show that the disk lifetime appears to be a function of stellar mass (Haisch et al. 2001a), with higher mass stars losing their disks faster than lower mass stars.

Hillenbrand et al. (1993) searched for candidate Herbig Ae/Be stars and conducted a *JHK*

survey within a central $5'.5 \times 5'.5$ field. Their estimated completeness limit was $J = 15$ mag, corresponding roughly to a spectral type of B8. About 10 stars (13% of the entire sample) in the JHK color-color-diagram lie in the excess region and have been suggested to be either i) candidate Herbig Ae/Be stars, i.e. intermediate mass PMS stars surrounded by accretion disks or ii) candidate classical Be stars, i.e. early B stars of unknown evolutionary state surrounded by gaseous circumstellar disks.

The next JHK survey (Hanson et al. 1997) presented positions for 355 IR objects within a $6' \times 6'.2$ field; there is a systematic offset of $1''.9$ between these IR positions and e.g. the ACIS frame (aligned to 2MASS). Photometric limits were $J < 14.7$ mag, $H < 14.1$ mag, and $K < 13.2$ mag. This study was focused at the more massive cluster members and its results are discussed in Sect. 4.1.7 and 4.1.9

Jiang et al. (2002) conducted an extensive JHK survey covering an area of $\sim 14' \times 14'$ with 10σ limiting magnitudes of $J \sim 18.7$ mag, $H \sim 18.2$ mag, and $K \sim 17.5$ mag, and more than 26.000 K -band sources in the entire field. Using a distance of 1.6 kpc they interpreted the IR CMD as to be composed of a congregation of intermediate- to high-mass stars in the central region surrounded by a second generation of younger stars in the nebular bars. However, due to both the non-uniform reddening of the cluster members and the youth of the stars in M17, the position within an NIR CMD is far from being unique. Thus, those classifications are likely to be contaminated by unknown evolutionary effects where PMS stars may simulate earlier spectral types. Eventually, Jiang et al. (2002) postulated a third population of red stars in the southwestern part coinciding with the molecular cloud. Based on the observed $H - K$ colors they argue that these red stars are young stellar objects (YSOs) with intrinsic color excess.

There were also attempts to extend the wavelength coverage to $3.8 \mu\text{m}$: Giard et al. (1994) presented K - and L -band images of the southwestern region with a focus on the interstellar dust grains. As a by-product they listed 7 extremely red objects ($K - L > 3.4$ mag) which were interpreted as young stars in a very early evolutionary stage (see Sect. 4.2.2 and Sect. 4.2.3). A subsequent low-resolution ($5''.6$) JKL survey by Ando et al. (2002) covered a region of $20' \times 20'$ and revealed 38 sources brighter than 7 mag at $3.67 \mu\text{m}$. Among them were 13 known OB stars (see Sect. 4.1.7), two known YSOs and three YSO candidates.

The so far deepest IR view is the $JHKL$ survey presented in this work (Fig. 2.2). The field size at JHK is about $6'.7 \times 8'.9$ and contains 18.504 K -band sources down to a limiting magnitude of 20.1 mag. All 606 ACIS sources contained in this cluster field have IR counterparts. The L -band survey covers a region of $5'.5 \times 5'.7$ and comprises ~ 3700 sources down to a limit of $L = 16.2$ mag.

The JHK TCD (Fig. 4.3) contains 4330 stars toward M17 with photometric errors less than 0.1 mag at each waveband. The sample includes 504 (12%) X-ray sources and 1254 (29%) stars within the IRE region. It shows two concentrations of sources with a pronounced gap at about $0.8 \text{ mag} < J - H < 1.1 \text{ mag}$. If this gap were purely due to extinction it would correspond to about $7 \text{ mag} < A_V < 10 \text{ mag}$. Jiang et al. (2002) report a similar gap in their JHK diagram and interpret the two groups of objects as "*unreddened (foreground) stars and reddened (cluster member and background) stars*".

There is little doubt that most of the heavily reddened stars above the gap belong to the embedded cluster as witnessed by numerous IRE and X-ray sources among this sample. Likewise, there are many sources with the $2.3 \mu\text{m}$ CO band in emission and absorption that share e.g. the same range of visual extinction (see Sect.4.1.9 and 4.1.10). In fact, the "reddest" source in the JHK sample with $H - K = 3.6$ mag is not a background star but it has IRE and shows the CO

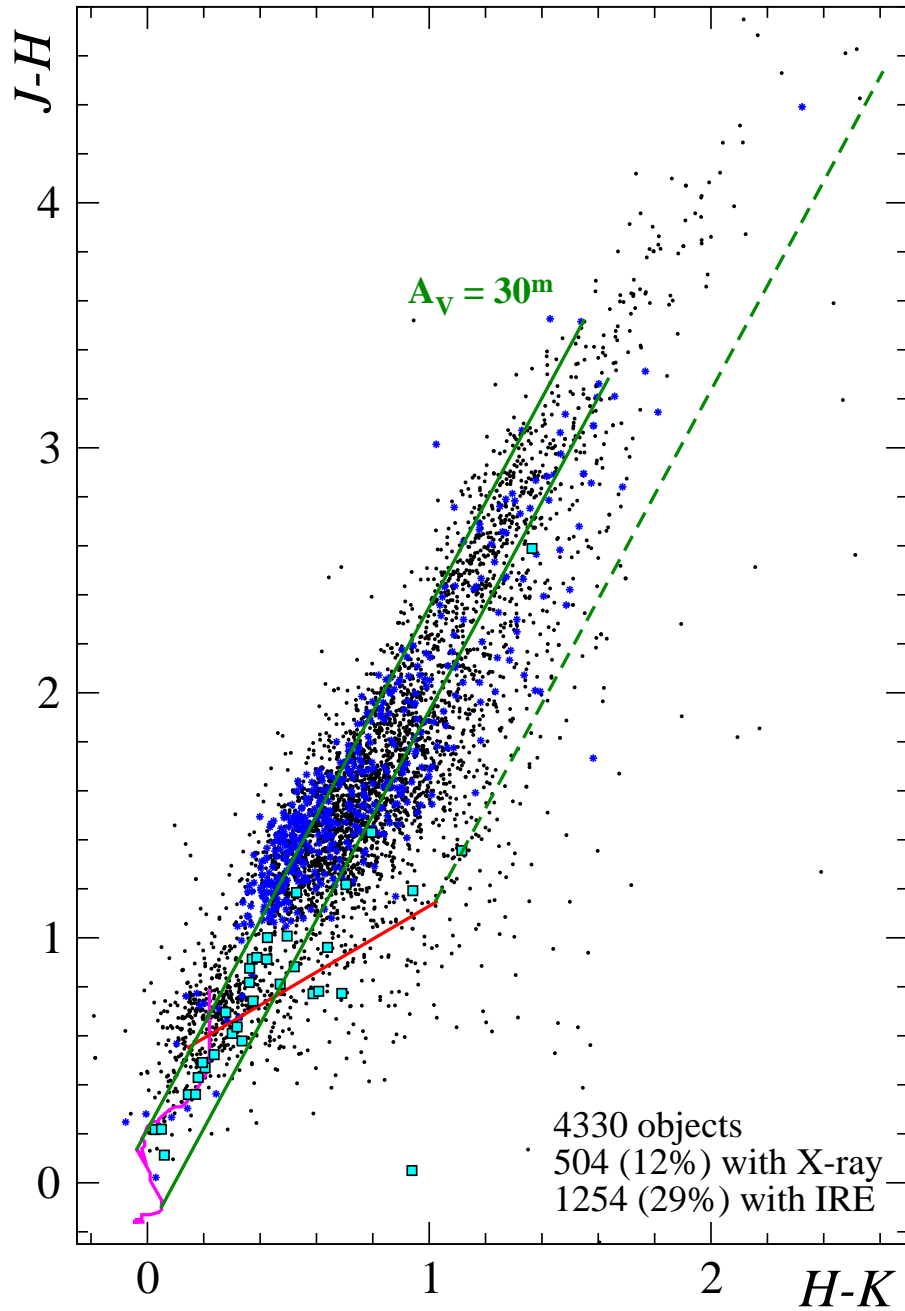


Figure 4.3: JHK diagram of 4330 stars toward M17. The solid magenta curve denotes the locus of unreddened MS stars (Ducati et al. 2001), the red line corresponds to the locus of T Tauri stars (Meyer et al. 1997). Reddening vectors with a length of $A_V = 30^m$ are drawn. Cyan squares refer to spectroscopically classified high-mass stars (see Table 4.2), blue asterisks characterize stars with X-ray emission. Note that some of the massive objects lie in the region of T Tauri stars. The diagram includes only data points with photometric errors less than 0.1 mag at each waveband.

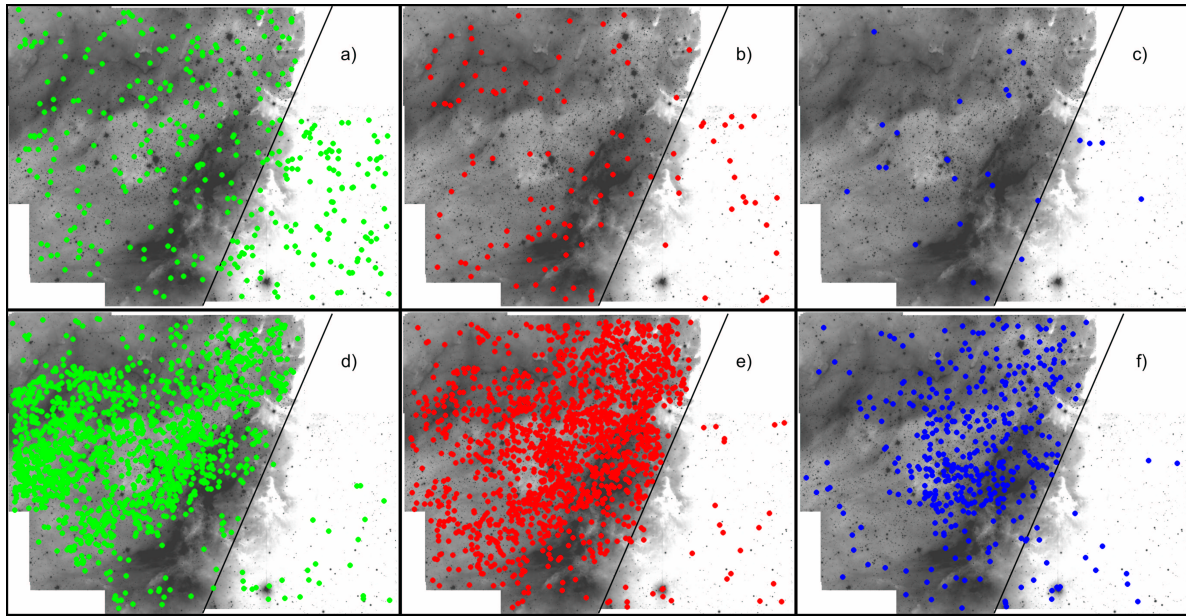


Figure 4.4: Spatial distribution of stars toward M17 grouped according to their position in the JHK diagram (Fig. 4.3). The grey-scale image in the background is the K band mosaic, the straight dotted line separates the H II region from the molecular cloud (Cloud B). **Upper row:** Stars from the less reddened group ($J - H < 0.8$ mag); a) unknown nature (green), b) IRE (red), c) X-ray emission (blue). **Lower row:** Stars from the heavily reddened group ($J - H > 1.1$ mag), same notation as above.

band head feature in emission (Hoffmeister et al. 2006). It seems that the opaque molecular clouds in front and behind the H II region act as a shield between background stars and cluster members. Additionally, Fig. 4.5 suggests that a large fraction of stars with $A_V > 30$ mag – i.e. the most promising background candidates – have IRE and thus are probably cluster members. Broos et al. (2007) estimate a contribution of about 20 (2%) extragalactic sources in the entire ACIS field of which only a few should be detectable in the IR. Given that all X-ray sources have IR counterparts, the contamination by background sources seems to be negligible.

Interestingly, the group of 497 less-reddened objects below the gap, i.e. those with $J - H < 0.8$ mag, contains half of the spectroscopically classified O-type stars of the cluster and a number of further high-mass B-type stars. Simultaneously, 5% of the less-reddened objects show X-ray emission and 24% of them display IRE. Thus, the interpretation by Jiang et al. (2002) that this entire group consists of unreddened (and thus unrelated) foreground stars cannot be valid. Subtracting the 27 X-ray and 118 IRE sources from the 497 stars in the less-reddened group ($J - H < 0.8$ mag), this leaves 352 stars as possible foreground candidates within the JHK diagram. So far 25 of them could be verified as such spectroscopically by their combination of low extinction ($A_V < 1$ mag) and late spectral type (Watermann et al. 2008).

Whether the apparent gap in the TCD in Fig. 4.3 – and as discussed later also in the CMD of Fig. 4.7 – is really due to an absorbing layer that separates both stellar aggregates is not clear at this point. Fig. 4.4 compares the spatial distribution of the two groups: Those 352 "normal" stars of the less reddened group that neither display IRE nor X-ray emission (Fig. 4.4 a) show

Table 4.1: Statistics of sources from the *JHK* diagram

H II region ($N = 3620$)						
$J - H < 0.8$ mag ($N = 340$)			$J - H > 1.1$ mag ($N = 3280$)			Intrinsic colors
normal	IRE	X-ray	normal	IRE	X-ray	
230 (68%)	95 (28%)	22 (6%)	1539 (47%)	1532 (47%)	396 (12%)	(Ducati et al. 2001)
211 (62%)	116 (34%)	22 (6%)	1225 (37%)	1972 (59%)	396 (12%)	(Bessell & Brett 1988)
Cloud B ($N = 226$)						
$J - H < 0.8$ mag ($N = 150$)			$J - H > 1.1$ mag ($N = 76$)			Intrinsic colors
normal	IRE	X-ray	normal	IRE	X-ray	
122 (81%)	23 (15%)	5 (3%)	43 (57%)	33 (43%)	0 (0%)	(Ducati et al. 2001)
141 (76%)	31 (21%)	5 (3%)	36 (47%)	40 (53%)	0 (0%)	(Bessell & Brett 1988)

a fairly homogeneous distribution across the entire field while 145 stars with IRE and/or X-ray emission, seem to prefer locations toward the H II region. "Normal" members of the heavily reddened group show a significantly different distribution: 1539 of them are located in the area of the nebula while only 43 objects are located toward Cloud B. Among the 497 stars of the less-reddened group there is a fair amount of YSOs (24% IRE, 5% X-ray), most of which are located within the H II region. Thus at least a third of them must be regarded as cluster members.

Table 4.1 summarizes the statistics from the sources in the *JHK* diagram in Fig. 4.3 and from their spatial distribution. For that purpose the sample has been divided into "low" and "high" reddening sources according to $J - H < 0.8$ mag and $J - H > 1.1$ mag; the division line between "H II region" and southwestern molecular "Cloud B" has been drawn along the interface in the southwest (see Fig. 4.4). The influence of the adopted intrinsic colors is demonstrated by using values from Ducati et al. (2001) and Bessell & Brett (1988); the latter reference leads to an increase of IRE sources of up to 12%.

The *HKL* TCD (Fig. 4.5) contains 2967 stars toward M 17 with photometric errors less than 0.1 mag at each waveband. The sample includes 428 (14%) X-ray sources and 1361 (46%) stars within the IRE region; for a discussion of the IRE objects see Sect. 4.1.9 The above mentioned gap, which should occur at about $H - K \sim 0.3$ mag, seems to exist but is hardly visible due to the low number of stars in that color region.

Using all information from the *JHKL* data most stars toward M 17 suffer from heavy extinction over a large range ($2 \text{ mag} < A_V < 50 \text{ mag}$). The heavily reddened group comprises about 10.000 objects most of which are likely cluster members; because not all of them were measured at all four wavebands, they do not show up simultaneously in all color-color (Figs. 4.3 and 4.5) and CMDs (e.g. Fig. 4.7). This number is in excellent agreement with the extrapolation by Broos et al. (2007) which predicted 8.000 - 10.000 cluster members. The less-reddened group contains 395 sources without any current signs of youth, i.e. neither X-ray emission nor IRE, which therefore might be foreground stars. Future X-ray observations of higher sensitivity or IR variability studies might reduce this number. One must therefore conclude, that the statistics of this rich cluster is not severely contaminated by unrelated field stars; the numbers above suggest a frequency of $\leq 5\%$.

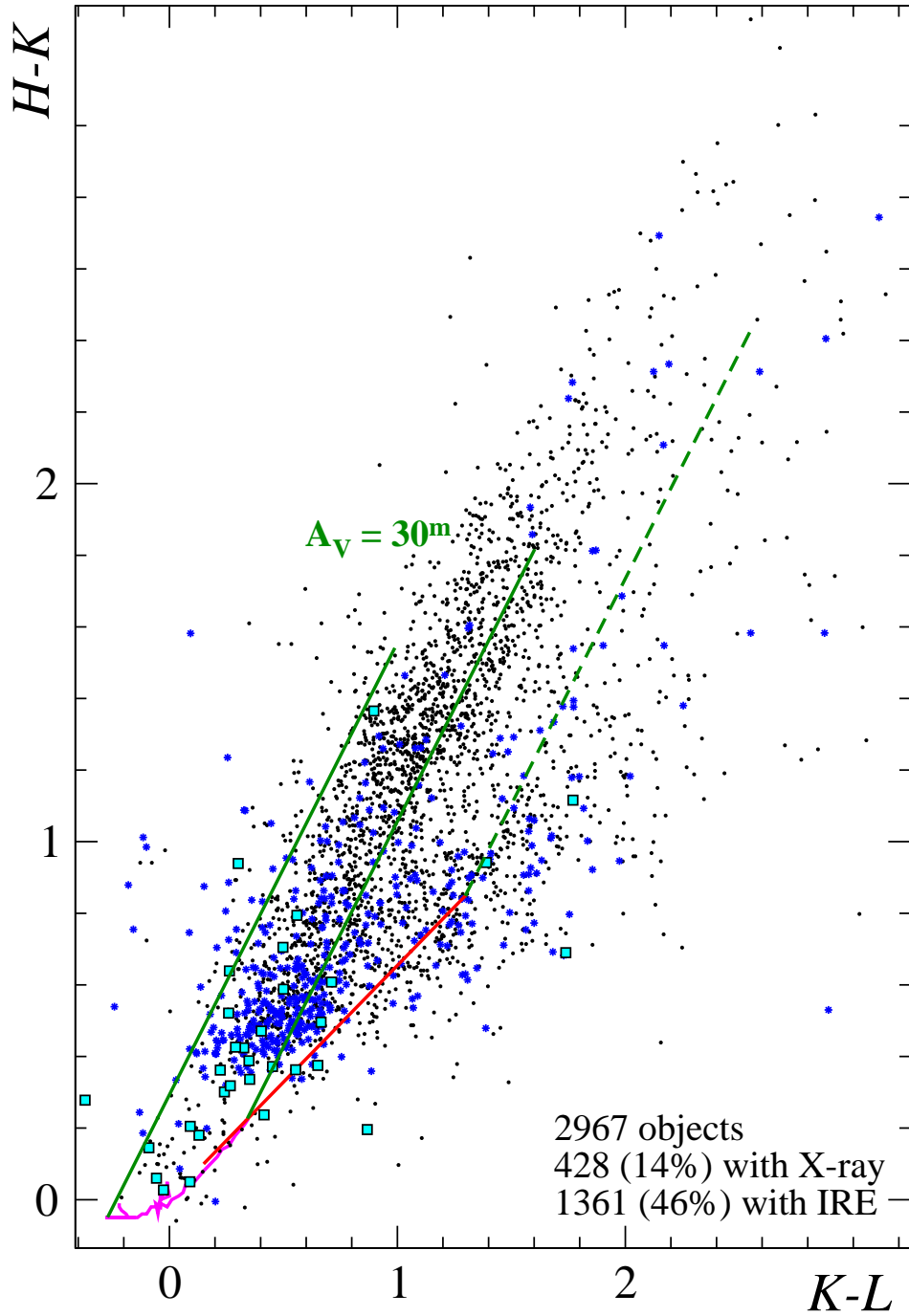


Figure 4.5: HKL diagram of 2967 stars toward M17. The magenta curve denotes the locus of unreddened MS stars (Ducati et al. 2001); the red line corresponds to the locus of T Tauri stars (Meyer et al. 1997). Reddening vectors with a length of $A_V = 30^m$ are drawn. Cyan squares refer to spectroscopically classified high-mass stars (see Table 4.2), blue symbols characterize stars with X-ray emission. The diagram includes only data points with photometric errors less than 0.1 mag at each waveband.

4.1.4 Spectroscopic Surveys

The spectroscopic information for stars in the region has been limited for many decades and was biased toward a few bright stars. Schulte (1956) classified the first early-type star in the region (CEN 2) as O5, confirmed later by Anderson (1970). A second early-type star (CEN 3) was classified as B0 (Pronik 1958), OB⁺ (Stephenson & Hobbs 1961), and eventually as O8.5 V (Crampton et al. 1978). Kleinmann (1973) delivered two additional classifications, viz. K2-5 I for CEN 0, which is most likely not associated with the cluster, and "double O or early B" for CEN 1. Ogura & Ishida (1976) added another early-type star (their No. 345) with a spectral type of O8. Hanson & Conti (1995) and Hanson et al. (1997) provided both infrared and optical spectroscopy with a focus on the ionizing cluster members. They confirmed at least nine O stars and a couple of late-O / early-B stars which were previously identified by the multicolor photometry of CEN.

The spectroscopy of the present work provides new spectral types for 294 stars and thus increases our knowledge of the stellar content of the cluster significantly. As already mentioned, the classification for individual stars is given in the Appendix. Additionally, Tab. 4.2 lists the spectral types for 46 early-type stars which are of crucial importance for the following sections. Finally, for the first time low-mass cluster members could be identified.

4.1.5 The Extinction toward M 17

With the advent of infrared techniques more and more star-forming regions were found to have an unusually high ratio of total-to-selective extinction, i.e. $R = A_V/E_{B-V} > 3.1$. Theoretically this finding was expected due to grain growth in dense and cool dust clouds as originally discussed e.g. by Chini & Krügel (1983) or Cardelli et al. (1989). CEN interpreted their photometric *UBVRI* results as due to an abnormal reddening law in M 17 characterized by $R = 4.2$. Chini & Wargau (1998) have extended the observed wavelength range until $4.8 \mu\text{m}$ and derived an even larger R -value of 4.8 from various color-color-diagrams. Because these R -determinations were based on photoelectric data they may have been contaminated by unknown IR sources within both the observing and the sky aperture; therefore they have to be treated with caution today. However, Hanson et al. (1997) determined individual R -values for 12 OB stars in M 17 by fitting dereddened spectral energy distributions (SEDs) to model atmospheres; they found a range of $2.8 \leq R \leq 5.5$ with an average of $R = 4.1$, corroborating the earlier results by CEN.

If the existence of a higher-than-normal R -value in M 17 is correct, the total extinction along the line of sight must be composed of a normal fraction described by $R = 3.1$ plus a fraction for the dust inside M 17; this division reflects not necessarily the distinction between dust in the foreground and dust in the H II region because the transition between different dust grain populations may also occur within M 17. Campeggio et al. (2007) found an increase of R with A_V for the dark globule CB 107 with $R \sim 3.1$ in the outer parts of the cloud and values up to $R \sim 5$ in the innermost regions. A further grain population might exist in the case of circumstellar disks and shells. Obviously, the separation of these contributions is mandatory but extremely difficult.

Foreground Extinction

There were several attempts to measure the line-of-sight extinction towards M 17 by means of comparing e.g. optically thin radio emission with emission in the visible light or from various line ratios. The lower limits of such attempts should be a reliable indicator for the dust in front of the H II region.

A very early work (Dickel 1968) obtained extinction values toward four positions in the nebula ranging from 4 to 7 mag. Ishida & Kawajiri (1968) produced an extinction map by comparing H α emission with radio maps of Mezger & Henderson (1967) at a resolution of 6'. The visual extinction increases from east to west starting at $A_V = 1$ mag toward the H II region and reaching a maximum of $A_V = 7$ mag toward the central absorbing dust filament.

Chesterman et al. (1982) presented an optical linear polarization map of M 17. The north-eastern portion of the nebula shows a symmetric pattern characteristic of a reflection nebula. Toward the central cluster area measurements are rare due to the high optical depth of the intervening dark patch. Nevertheless, from a few spots significant polarization could be obtained with orientation predominantly north-south; this is in accord with polarization directions found by Schulz et al. (1978) and Schulz et al. (1981). Chesterman et al. (1982) propose that the H II region is seen through a thin cloud of relatively cold dust, aligned by a magnetic field which is intrinsic to the cloud.

Hippelein & Goudis (1986) measured the visual extinction at various locations across M 17 with a beam size of 1'. They compared their own [S III] line data at 9531 Å with those at 18.7 μ m (McCarthy et al. 1979) and at 33.7 μ m (Moorwood et al. 1980) and found good agreement with the maps by Dickel (1968); their maximum extinction toward the dark filament in front of the cluster center was $A_V = 10$ mag. Hippelein & Goudis (1986) estimate the internal extinction within the ionized area to be $A_V \sim 1$ mag.

Glushkov et al. (2005) refined earlier measurements and derived the visual extinction for about 250 spots in the nebula by comparing the H α and 21 cm continuum emission. The A_V values for the eastern, optically bright part of the nebula are 2–6 mag and increase to 7 and 14.5 mag for the western part, which is covered by the dark cloud in front of the cluster center. All these results point toward a minimum extinction between $A_V \sim 1 - 2$ mag located in front of the H II region. This is in fair agreement with Galactic models that predict values of $A_V \sim 2$ mag up to a distance of 2 kpc in the direction of M 17 (Bahcall & Soneira 1980).

Local Extinction

There are various ways to investigate the extinction law. One is to use TCDs where the locus of the unreddened main sequence and the extinction vector are collinear; this method works particularly well for early-type stars whose range of intrinsic colors is considerably small ($\Delta(B-V)_0 < 0.13$ mag between O4 and B3). As explained by Chini & Wargau (1998) reddened early-type stars should be aligned along the reddening path in diagrams of the form $(V - \lambda)$ vs. $(B - V)$ (Fig. 3.1). Therefore, the slope of the linear least-square fit yields the corresponding entries $E_{V-\lambda}/E_{B-V}$ for the extinction law. Obviously, this method is extremely sensitive to IRE because objects with dust emission can steepen the fits at longer wavelengths, simulating larger-than-normal color excess ratios.

A second way to determine the ratio of total-to-selective extinction is to compare the distance modulus $V - M_V$ with the color excess E_{B-V} (Fig. 4.6). This method of "variable extinction" has been introduced by Hiltner & Johnson (1956) and is sensitive to both the distance and

the R -value. It can be applied whenever stars in a stellar aggregate suffer from a large range of extinctions. V is the apparent, M_V the absolute visual brightness as obtained from spectroscopy. To exclude contamination from foreground stars, only spectroscopically classified early-type stars with $A_V > 1.2$ mag were used; simultaneously, this selection omits low-mass PMS objects from the sample. The slope of the linear least square fit corresponds to the ratio of total-to-selective extinction and yields $R = 3.9 \pm 0.2$. This result is a further independent support for a higher-than-normal R -value in M 17 and is based on a unprecedented number of spectroscopically classified early-type stars in the region.

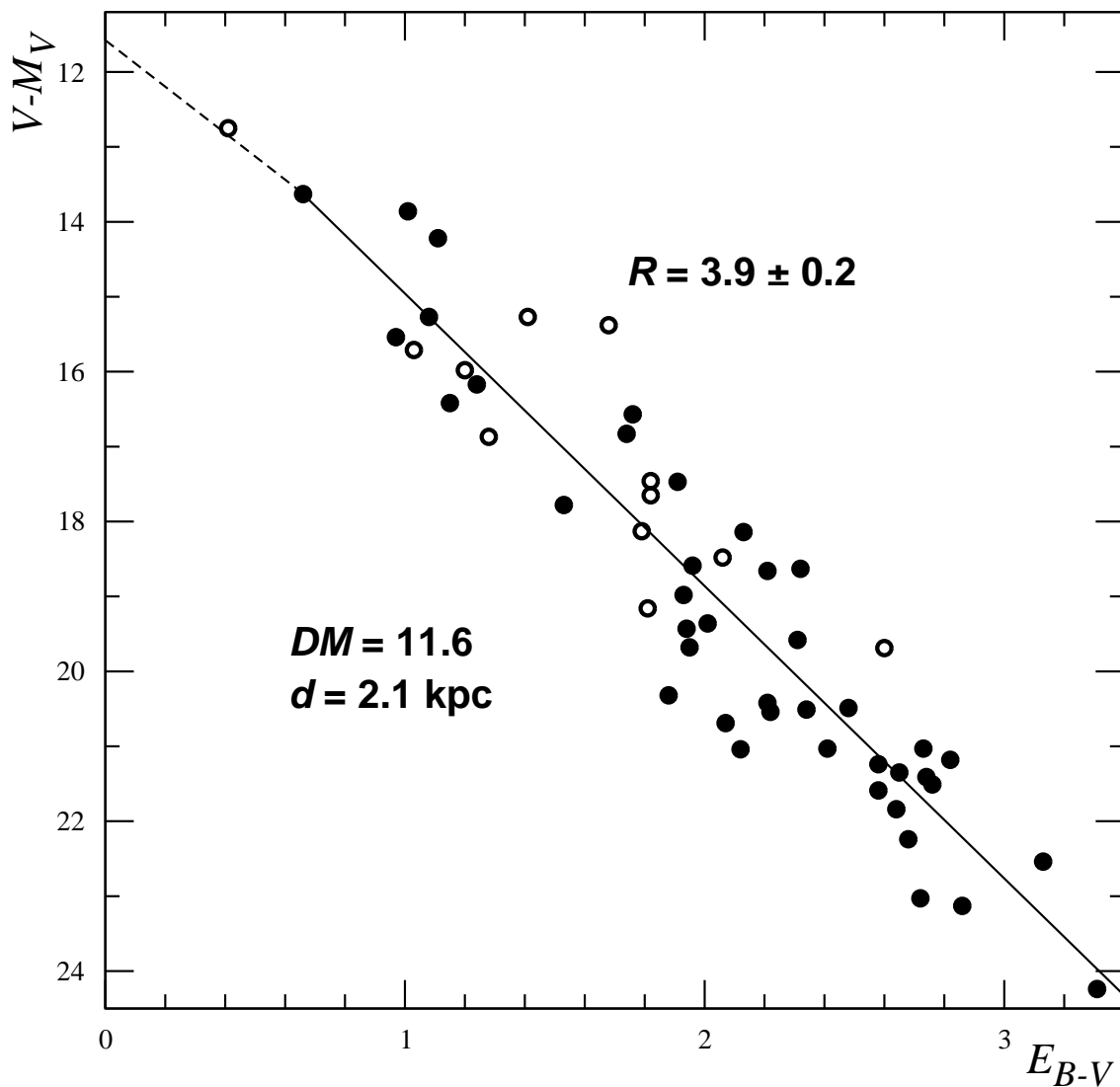


Figure 4.6: Distance modulus vs. color excess for 53 O- and B-type stars in M 17 with $A_V > 1.2$ mag; (●) B3 and earlier, (○) later B3. The fit to the data (solid line) yields $R = 3.9 \pm 0.2$. The dashed line corresponds to the contribution of foreground extinction ($A_V = 2$ mag) with $R = 3.1$.

4.1.6 The Distance toward M 17

Although M 17 is one of the most prominent H II regions in our Galaxy, its distance is still under debate. The various estimates range from 1.3 to 2.9 kpc. This is due to several reasons, among them the galactic longitude which results in large errors for the kinematic distance. From the H109 α recombination line Reifenstein et al. (1970) and Wilson et al. (1970) derived values of $d = 2.1 \pm 1.1$ kpc and 2.3 ± 1.2 kpc, respectively. Churchwell et al. (1990) observed ammonia and water vapor emission from M 17-UC1 and found $d = 2.3$ kpc. Revising the existing data in the literature with the latest values for the galactic rotation curve Russeil (2003) obtained a kinematic distance of 2.4 kpc.

Due to the large extinction of cluster members optical spectrophotometric determinations of the distance were restricted to the brightest stars. From a V_0 vs. $(B - V)_0$ diagram of 51 stars with known spectral type Ogura & Ishida (1976) derived a distance of 1.3 kpc by fitting a ZAMS as the lower envelope to the O- and B-type stars. Most early-type stars, however, were located up to several magnitudes above the ZAMS while three newly identified O-star candidates were below it. It seems, that due to the large field under investigation and the generally low extinction of the stars (only 7 stars have $A_V > 3$ mag) the results of this study were severely contaminated by unrelated field stars.

CEN derived a distance of 2.2 ± 0.2 kpc based on UBV photometry of 19 possible early type candidates. Apart from the general problem of ZAMS fitting for early type stars, the unknown extinction law introduced another source of uncertainty. Nielbock et al. (2001) readdressed this distance determination by excluding IRE objects from the sample of CEN and by using the latest information on the spectral types and the extinction law, which was characterized by $R = 4.8$ at that time. From 16 early type stars Nielbock et al. obtained a mean distance of 1.6 ± 0.3 kpc. This reduced distance, compared to the estimate by CEN, basically resulted from the difference in the R -values used in both papers, i.e. $R = 4.2$ vs. 4.8 and demonstrates the tight dependence between distance and R -value.

Hanson et al. (1997) used the spectra and K -band magnitudes of five O-type stars to determine a distance of $1.3^{+0.4}_{-0.2}$ kpc. While the absolute magnitude calibration at the upper end of the MS has its own difficulties due to the individuality of O-type stars, multiplicity causes an even more severe problem: For example, CEN 3 (\equiv B 98), the star with the lowest distance modulus, has been treated as a single object by Hanson et al.. Our high-resolution JHK imaging, however, shows that within the $3''.6$ aperture used for the photometry quoted by Hanson et al. there are three stars: CEN 3 itself is barely resolved into two (almost) equally bright components at K ; a third, very red star $2''.5$ to the southeast is 0.7 mag fainter than (the double) CEN 3. This explains both the low distance modulus and the low R -value obtained by Hanson et al. for CEN 3. Another example is CEN 18 (\equiv B 260), the star with the second lowest distance modulus. It is a spectroscopic binary with equally bright double Paschen lines, suggesting that the combined K -band brightness of the two components - as used by Hanson et al. - severely underestimate the distance. CEN 37 (\equiv B 174) is also a barely resolved binary in our infrared images. Furthermore, IRE - particularly at K - may introduce problems when using the apparent IR brightness to convert into absolute magnitudes. Finally, given the uncertainties in determining the R -value for individual stars - as attempted by Hanson et al. (1997) - it seems that this low distance estimate of 1.3 kpc, derived from five stars only, three of which are multiple, is based on weak ground.

Povich et al. (2007) obtained a luminosity distance of $1.6^{+0.3}_{-0.1}$ kpc by balancing the integrated

flux in the observed SED with the total bolometric luminosity of all known O and early B stars in the cluster. Obviously this method strongly relies on the completeness of the detected high-mass stars and on their derived spectral types; the latter ones, however, are poorly constrained in some cases. As discussed in Sect. 4.1.7 the number of high-mass stars in M17 is significantly higher than adopted by Povich et al. (2007) thus inevitably increasing their distance estimate. Given the large errors of the kinematic results and the controversy from optical and infrared data on the distance of M17 a new, independent determination seems highly desirable. This has to include the latest results on the reddening law within M17 and a separation between foreground and local extinction. In the following, several methods will be employed to derive the distance for M17. Most data used for these estimates are summarized in Table. 4.2 and are based on those early-type stars.

Method of "Variable Extinction"

The principles of this method have already been outlined in Sect. 4.1.5. In the case of M17 there is the complication that the reddening law is different in the foreground and within the H II region. As a consequence, the transition between normal and special reddening influences the extrapolation to $E_{B-V} = 0$ mag for deriving the distance modulus. Adopting the results from the previous section concerning the foreground extinction of ~ 2 mag one can extrapolate the dashed line in Fig. 4.6 (corresponding to a reddening slope of $R = 3.1$) which starts at $E_{B-V} = 0.65$ mag to $E_{B-V} = 0$ mag. This yields a distance modulus of 11.6 mag corresponding to 2.1 kpc. A different contribution of foreground extinction, say of 3 or only 1 mag, would change this value by ± 0.2 kpc, respectively.

Individual Distance Moduli

The individual distance moduli (DM) of the stars in Table. 4.2 can also be used to calculate a mean distance modulus for this group. The average value for 45 stars is $DM = 11.6 \pm 0.1$ mag equivalent to a distance $d = 2.1 \pm 0.1$ kpc. In this estimate, the above numbers for the amount of foreground extinction ($A_V = 2$ mag) and the special reddening law ($R = 3.9$) for $A_V > 2$ mag have been used.

ZAMS Fitting

Due to the steepness of the ZAMS for the earliest types, ZAMS fitting is not very sensitive for the distance; Fig. 4.7 is such an example. Nevertheless, a combination of a distance of $d = 2.1$ kpc and a foreground extinction of $A_V = 2$ mag places the ZAMS as a lower envelope for most stars within their photometric accuracy of 0.1 mag per waveband. The low-mass K-type stars left of the ZAMS have probably extinctions below the (adopted) foreground limit of $A_V = 2$ mag. For comparison with previous estimates, a distance of e.g. 1.3 kpc, equivalent to a DM of 10.5 mag would shift the main sequence upward by 1.1 mag, thus placing many stars – particularly the A,F and G-types – left of the main sequence. Of course, this could be partly compensated by reducing the foreground extinction correspondingly, however, contradicting the results described in Sect. 4.1.5.

The gap at $0.8 \text{ mag} < (J - H) < 1.1 \text{ mag}$, already noticed in Fig. 4.3, is even more pronounced here, at least for stars brighter than $J \sim 17$ mag. As mentioned before, the stellar group with

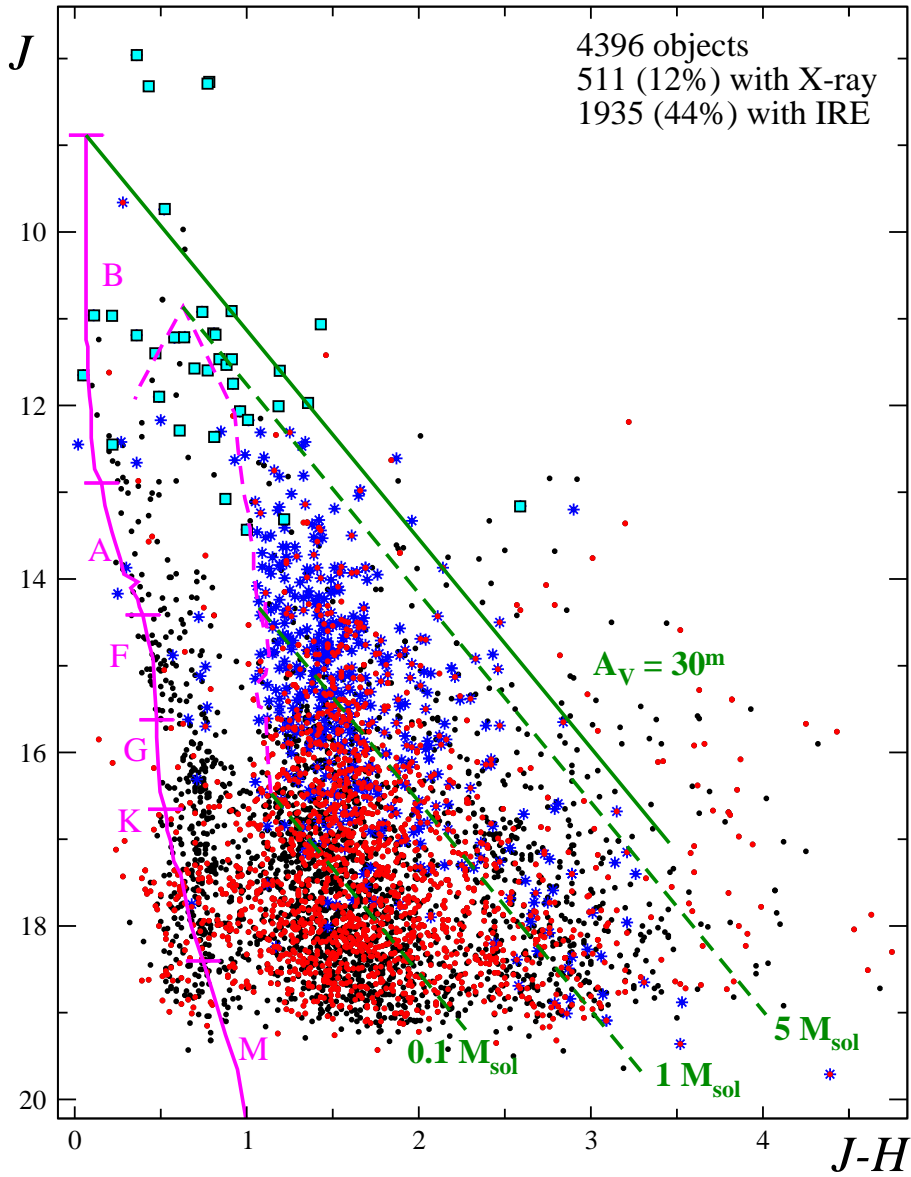


Figure 4.7: J vs. $J - H$ CMD for 4396 stars. The magenta curve corresponds to the ZAMS for a distance of $d = 2.1$ kpc and corrected for a foreground extinction of $A_V = 2$ mag. Within the photometric accuracy it represents the lower-left envelope of most data points; stars leftward of the ZAMS have extinctions less than 2 mag. The dashed curve is a 5×10^5 yrs isochrone (Siess et al. 2000) reddened by 4 mag. Loci of equal mass are indicated by the dashed green lines. The reddening vector with a length of $A_V = 30$ mag is shown as a solid green line. Magenta squares refer to spectroscopically classified high-mass stars (see Table 4.2), blue asterisks characterize 511 (12%) stars with X-ray emission, red symbols denote 1935 (44%) stars with IRE. The diagram includes only data points with photometric errors less than 0.1 mag at each waveband.

lower extinction, coinciding with the ZAMS, contains numerous stars with X-ray emission and IRE and thus is likely to belong to the cluster. The gap is readdressed in Sect. 4.1.11.

Fig. 4.8 shows an optical HR diagram that contains 318 stars which have been classified by their optical spectra. The extinction-corrected visual brightness was derived by splitting the observed E_{B-V} into a foreground and a local fraction as explained above; the intrinsic color $(B - V)_0$ is taken from the spectral type, using the conversion by Schmidt-Kaler (1982). To avoid contamination by unrelated foreground stars only objects with $A_V > 1$ mag have been included. Nearly all early-type stars are X-ray emitters (Broos et al. 2007) while some of them also display IRE probably originating from remnant circumstellar material. A ZAMS for 2.1 kpc is compatible with the data although the steepness of the curve would allow for a much larger range of – preferentially larger – distances.

There are four stars in Fig. 4.8 which are located above the position of an O3 star. Two of them are the components of CEN 1, the major ionizing sources in the field. The northeastern component is located at RA = 18:20:29.89 and DEC = -16:10:44.5 (J2000) and has $V_0 = 4.8$ mag (hereafter referred to as CEN 1a). The brightest star with $V_0 = 4.8$ mag is the southwestern component (hereafter referred to as CEN 1b), located at RA = 18:20:29.81 and DEC = -16:10:45.7 (J2000). CEN 18 is the second brightest star with $V_0 = 5.2$ mag. Eventually, there is CEN 37 with $V_0 = 5.3$ mag. The fact that these stars are brighter than what is expected from their spectral type (cf. Table 4.2) is likely due to their multiplicity. As explained above, CEN 18 is a spectroscopic binary with equally bright double Paschen lines. A reduction by 0.75 mag, as appropriate for a binary with identical components, would shift CEN 18 down into the early O-type region. In the case of CEN 1 a and b both components show double-lined J -band spectra (Sect. 4.2) suggesting that they are binaries themselves. CEN 37 is also a barely resolved binary in our infrared images.

Luminosity Distance

Compared to the study by Hanson et al. (1997) Table 4.2 contains 32 new spectroscopically classified high-mass stars that contribute to the ionization of M 17; the multiple O-stars and hyper compact H II region M 17-UC1 has been omitted from this statistics. Obviously, the considerably increased number of early-type stars requires a revision of the luminosity distance as presented by Povich et al. (2007). These authors obtain a total luminosity of $L_{\text{SED}} = 2.4 \pm 0.3 \times 10^6 L_{\odot}$ from the SED of the nebula by adopting a distance of 1.6 kpc. Using the conversion by Crowther (2005) the luminosity provided by the OB stars in Table 4.2 is $L_{\text{OB}} = 3.8 \times 10^6 L_{\odot}$ at a distance of 2.1 kpc. Taking into account the multiplicity of CEN 1 a and b, CEN 3, 18 and 37 and assuming for simplicity that all of them have an equal-mass companion, the total stellar luminosity would increase to even $5.2 \times 10^6 L_{\odot}$. Scaling the distance in such a way, that L_{SED} equals L_{OB} we obtain a minimum distance of $d_{\text{min}} = 2.0$ kpc (or 2.35 kpc including the four binary O-stars). In summary, all new methods exclude earlier distance estimates significantly below 2 kpc and argue in favor of a distance of $d = 2.1$ kpc.

4.1.7 High-Mass Stars and Energy Balance

So far, two studies were particularly devoted to the high-mass members of the M 17 cluster. Hanson et al. (1997) presented a multi-wavelengths spectroscopic survey of 13 known OB star candidates in the cluster and corroborated or improved their spectral type designations. However, no further massive candidates could be added compared to the early photometric study by CEN. Nielbock et al. (2001) concentrated on the circumstellar environment of some of these massive stars presenting 10 and 20 μm imaging of the area. The SEDs and the morphology of the MIR emission strongly suggested that some massive stars are surrounded by circumstellar dust.

The unbiased spectroscopy of the present study led to the detection of further early-type stars. Table 4.2 summarizes the latest results on massive stars in M 17. The major ionization of M 17 is provided by two O4 V stars in the cluster center. Kleinmann (1973) classified this "anonymous star" as "double O or early B". CEN obtained a double O4 type (CEN 1) but realized that one of the components suffers from larger extinction. A spatially unresolved spectroscopy for both components (Hanson et al. 1997) yielded a combined spectral type of O5 V (optical) and kO3-O4 (*K*- band). The resolved multicolor photometry and spectroscopy of the two components of CEN 1 which are separated by $1''.8$. The photometry indicates that CEN 1a and 1b are reddened by $A_V = 10$ and 13 mag, respectively. If CEN 1 is a physical binary system, this large difference can only be explained by a highly clumped ISM along the line of sight. Another large difference in extinction has been found for the companion of CEN 3 on a scale of $2.5''$.

Despite the increase of known high-mass stars the Lyman continuum flux indicates that further exciting stars must be embedded in the cluster. The number of Lyman continuum photons N_{Lyc}^{**} provided by the known OB stars from Table 4.2 is $1.43 \times 10^{50} \text{ s}^{-1}$ (Crowther 2005); the corresponding value for the nebula is $N_{\text{Lyc}}^{\text{neb}} = 2.4 \times 10^{50} \text{ s}^{-1}$ (Felli et al. 1984), scaled for the minimum distance of $d_{\text{min}} = 2.0 \text{ kpc}$. Using a distance of 2.1 kpc and the conversion by Crowther (2005) an equivalent of eleven O4 V stars is required to excite the nebula. Some of the "missing" early-type stars might exist in the form of unresolved multiple systems along with the known OB stars. Further early-type stars are suggested by the wealth of new photometry data but have to await their spectroscopic confirmation.

Broos et al. (2007) list 143 intermediate- to high-mass X-ray candidates with mass estimates $M > 2.0 M_{\odot}$ (their Tab. 6); some high-mass stars previously cataloged in the literature are also included in this compilation. The mass entries were derived by dereddening the stars in a *J* vs. *J - H* CMD with a normal extinction law and by shifting them onto a 1 Myr isochrone. For 30 stars these mass estimates can now be compared with new spectral types presented here:

- Within this subsample of 30 stars, the masses derived by Broos et al. (2007) are systematically too low. This is partly due to the fact that these authors use a distance of 1.6 kpc. Additionally, if properly dereddened, some stars are located on the ZAMS, i.e. not on the 1 Myr isochrone, thus yielding a higher mass.
- Seven out of these 30 high-mass candidates have late spectral types (F, G, K).
- Ten out of 13 objects, previously proposed to be early-type stars by CEN are indeed high-mass stars.

Table 4.2: High-mass stars in M 17. Extinction and distance modulus have been obtained from optical data whenever available.

Name	J2000		Spectral Type			V	K	A_V	DM
	RA	DEC	opt	K -band	J -band				
H 997	18:20:14.2	-16:14:00	B1 V			15.3	10.7 ²	7.1	11.5
H 1520	18:20:17.5	-16:08:19	B2 V			18.1	10.3	9.2	11.3
CEN 35	18:20:21.5	-16:09:39	O9.5 V	O9.5 Ve	B	17.1	10.1	9.5	11.7
CEN 92	18:20:21.6	-16:11:18	B2 V			20.1	8.8	13.4 ³	9.1
CEN 13	18:20:22.2	-16:10:21	B3 V			12.4	10.7	3.4	10.5
H 3957	18:20:22.5	-16:09:46	B3 V			21.6	11.4	12.3 ³	10.9
CEN 16	18:20:22.7	-16:08:34	O9 V	O9 V	O9.5 I	13.2	9.0	6.9	10.6
CEN 75	18:20:22.8	-16:08:15	B2 V			18.1	11.8	8.6	11.9
CEN 78	18:20:24.0	-16:10:04	B3 V			17.9	11.1	8.5 ³	10.9
CEN 31	18:20:24.4	-16:08:44	O9.5 V	O9.5 V	O9.5 V	15.5	9.2 ²	7.1	12.6
IRS 5	18:20:24.7	-16:11:40		O6 V			9.2	24.0 ³	11.1
M 17-UC1	18:20:24.9	-16:11:35	B0 V				13.1		
CEN 49	18:20:25.3	-16:10:19	B2 V			16.6	9.5	7.0	11.9
CEN 36	18:20:25.3	-16:09:40		O9.5 V	O	17.7	10.5	9.8	12.1
CEN 18	18:20:25.9	-16:08:32	O6 V			13.7	7.8 ²	8.5	10.1
CEN 26	18:20:26.1	-16:11:05	B3 V	B3 V	B	15.3	10.3	6.3	10.6
CEN 48	18:20:26.3	-16:10:16	B3 V	B3 V	O9.5 V	15.1	10.7	6.3	10.2
CEN 52	18:20:26.6	-16:10:23	B0 V			16.7	11.4	7.5	13.2
CEN 51	18:20:26.6	-16:10:03	B3 V		B	17.2	9.5	8.1	10.6
H 6500	18:20:26.7	-16:07:09	B2 V			17.5	8.6 ²	10.4	9.6
B 240	18:20:26.8	-16:07:49	B0 V	O9.5 V		18.2	10.7	9.9	12.3
CEN 23	18:20:27.3	-16:10:25		B3 V	B	14.0	12.2	3.3	12.3
OI345	18:20:27.4	-16:13:32	O6:V ¹			11.3	7.4	4.3	11.9
CEN 46	18:20:27.8	-16:11:02		O9 V	late O I	17.1	9.4 ²	10.2	11.3
CEN 47	18:20:27.9	-16:11:09		O9.5 V	B	16.3	10.6	8.1	12.3
CEN 65	18:20:28.0	-16:10:59		O9 V	O:	16.2	10.1	8.1	12.4
IRS 15	18:20:28.7	-16:12:12	B0.5 V	B0 V	B1 V	16.1	9.8	7.4	12.4
CEN 30	18:20:28.7	-16:09:26	O9 V	O9 V	B1 V	16.7	10.7	8.9	12.2
CEN 55	18:20:29.1	-16:10:54	B0 Ve		early B I	17.3	10.4	9.8	11.5
CEN 42	18:20:29.2	-16:11:11	B2 V			15.7	10.3	7.8	10.4
CEN 59	18:20:29.4	-16:10:56		B0 V	B	17.0	10.0	10.1	10.9
CEN 27	18:20:29.8	-16:11:37	O9 V	O9 V	B	17.2	9.6	10.2	11.3
CEN 1b	18:20:29.8	-16:10:46	O4 V	O4 V	O4 V	14.9	6.9	13.5 ³	10.7
CEN 1a	18:20:29.9	-16:10:44	O4 V	O4 V	O4 V	13.5	6.9	10.2 ³	11.3
CEN 61	18:20:30.2	-16:10:35	O9 V	O ?		16.9	9.0 ²	10.5	10.7
CEN 37	18:20:30.4	-16:10:53	O6 V	O6 V	O6 V	19.3	7.6 ²	14.1 ³	10.2
CEN 25	18:20:30.9	-16:10:08	O7 V	O7 V	O9I	14.9	8.8 ²	8.5	11.1
CEN 28	18:20:31.8	-16:11:38	B2 V	O9 V:		15.4	11.2	5.5	12.3
B 140	18:20:32.9	-16:12:40		B3 V:	B	12.1	10.8	2.0	11.6
CEN 43	18:20:33.1	-16:11:22	O5 V	O4 V	O5 V	17.8	8.1 ²	10.1	12.9
CEN 29	18:20:33.1	-16:10:14	O9 V			17.3	10.4 ²	9.5	12.1
CEN 2	18:20:34.5	-16:10:12	O5 V ¹			11.2	7.5 ²	4.0	12.5
H 12556	18:20:35.2	-16:08:43	B3 V			19.5	12.0	9.2 ³	11.8
CEN 3	18:20:35.4	-16:10:49	O9 V ¹	O9 V	late O I	9.9	7.7	3.8	10.4
CEN 45	18:20:35.6	-16:10:56	B2 V			12.9	10.7	3.7	11.6
B 58	18:20:37.9	-16:07:32	B0: V			16.3	10.2	6.8	13.5

Designations: "CEN" (Chini et al. 1980), "H" present work, "B" (Hanson et al. 1997), "IRS" (Chini & Wargau 1998), "OI" (Ogura & Ishida 1976), "M 17-UC1" (Felli et al. 1984)

Notes: ¹ spectral type from literature, ² photometry from 2MASS, ³ A_V from IR colors, ⁴ spectral type from K -band spectroscopy

This limited statistics indicates that masses derived exclusively from photometry are problematic, in particular when there is highly variable extinction. It is impossible to disentangle uniquely the effects of intrinsic color, reddening, absolute brightness and evolutionary stage from two observable quantities. The assumption of a distinct (common) age for a stellar aggregate enters directly in the mass estimate and may lead to wrong results in the presence of an age spread.

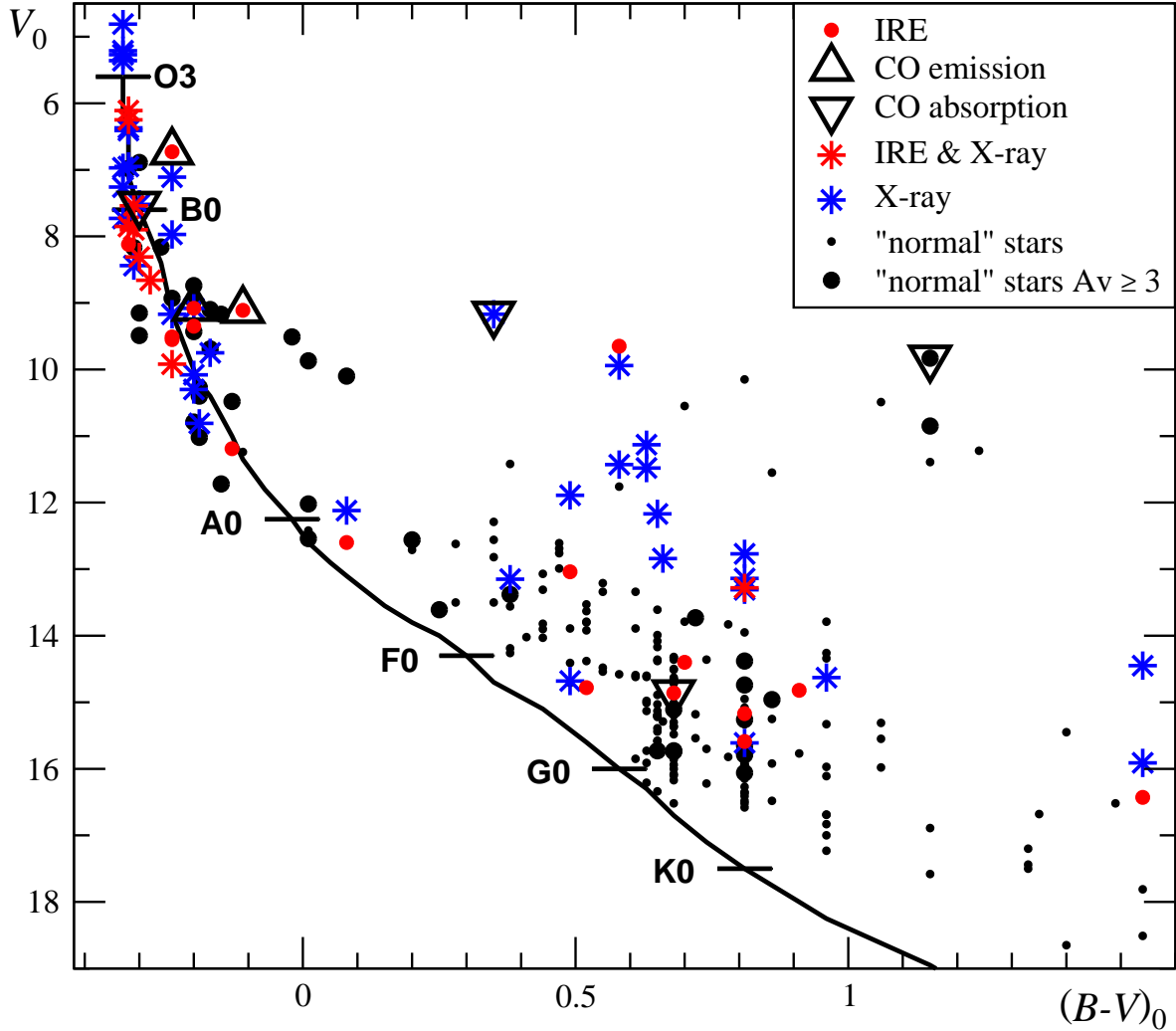


Figure 4.8: Dereddened CMD for 318 spectroscopically classified stars with $A_V > 1$ mag. Blue asterisks denote X-ray emission, red symbols mean IRE. Black dots are normal stars without X-ray emission or IRE; large symbols correspond to $A_V \geq 3$ mag (most likely cluster members), small symbols refer to $A_V > 1$ mag (potential members). Triangles show sources with the $2.3 \mu\text{m}$ CO band head feature (Hoffmeister et al. 2006). The curve is a ZAMS of 2.1 kpc which is compatible with all data points, taking into account the photometric errors of < 0.1 mag at each waveband. Beyond $(B - V)_0 = 0.0$ mag the first spectroscopically classified PMS stars in M 17 become visible.

4.1.8 Low-Mass Stars

The first detections of low-mass stars in M 17 were reported by Broos et al. (2007) who characterized the *Chandra* X-ray sources from their position in the J vs. $J - H$ CMD. With the assumptions explained above ($d = 1.6$ kpc and 1 Myr), the majority of ACIS objects appear to be G and F stars ($0.5M_{\odot} < M < 2M_{\odot}$) reddened by about 3 - 15 mag of visual extinction. Correcting for the difference between 1.6 and 2.1 kpc would shift the stars more into the A - F regime. The age estimate is also uncertain: First, there are 41 X-ray sources to the left of the 1 Myr isochrone in Fig. 6 of Broos et al. (2007), among them 6 IRE sources. Second, the scenario of triggered or sequential SF, often discussed for M 17 (Sect. 4.3) predicts stellar populations of various ages. Dropping also the age assumption and shifting the stars back onto the MS would turn the majority of the ACIS sources even into the B-type range. Thus, a proper spectral classification, preferentially at optical wavelengths, is mandatory.

Among the ~ 400 stars with optical spectra from the present work there is a large number of potential cluster members ($A_V > 1$ mag) with intermediate and low-mass types between A and M, many of which are located ways above the MS (Fig. 4.8). Fig. 4.7 provides further evidence for low-mass stars: Below $J \sim 16$ mag a large number of IRE objects becomes visible. If shifted back onto the ZAMS the majority of them would end up as G or K-type stars. If they should turn out to be PMS stars their masses fall even below $0.5 M_{\odot}$.

4.1.9 IR Excess Objects

Although the definition of an IRE object seems evident, in practical terms it depends on various assumptions particularly when derived from NIR TCDs. Here the adopted intrinsic colors are equally important as the location of the reddening path. The combination of both spans the width of a region in which stars are regarded to be excess-free. MIR observations suffer from this problem to a much lesser extent.

First evidence for the presence of IRE objects was reported by Chini (1982) and Chini & Krügel (1985). The IR emission was interpreted as to arise in cocoons (or tori) of circumstellar dust with temperatures of several 100 K. Chini & Wargau (1998) enlarged the number of IRE sources considerably by observations from 1.2 to $4.8\mu\text{m}$. While the qualitative result, i.e. the existence of circumstellar material is out of question for most of these sources, the early IR photometry has to be treated with caution from today's view. As the data were obtained with single-pixel detectors, there was no information about contaminating objects within the star or sky aperture. Thus, the coincidence of an optically visible (early type) star with a close-by unknown IR source (late type or heavily reddened) is likely to produce an "IRE object", too. Unfortunately, the problem of confusion remains even when using IR array detectors: Lada et al. (1991) found that at a pixel size of $0''.8$ contamination from neighboring stars became a problem for apertures larger than $2''.4$. In their JHK TCD almost all stars (107) identified as cluster members displayed IRE; those were interpreted as to originate from circumstellar disks. Across the total field of view of $9' \times 9'$, the excess sources showed a concentration in the cluster field, i.e. within a radius of $168''$ around CEN 1; within this area, the spatial distribution was fairly homogeneous. Due to the fact that Lada et al. neither give a finding chart nor a table with photometric results, a comparison with other studies is not possible. In view of the more recent results, however, a IRE frequency of almost 100% for the OB stars in M 17 can definitely be excluded.

The JHK TCD presented by Hanson et al. (1997) includes 73 stars in a $6' \times 6'.2$ field with

$J < 14.25$ mag, $H < 13.43$ mag, and $K < 11.0$ mag; about 30% of them lie in the IRE region. As Hanson et al. (1997) remarked themselves the two objects with largest IRE (B139 and B239) have been misidentified. Another IRE object (B339) mentioned by Hanson & Conti (1995) to show "very large NIR excess" has only a small excess in the JHK and the $JHKL$ diagram but no excess in the HKL diagram of this work ($J - H = 4.431$ mag, $H - K = 2.53$ mag and $K - L = 1.93$ mag). Due to the fact that the photometry by Hanson et al. was obtained in a $3''.6$ aperture, contamination from near-by stars could have been a severe problem.

Jiang et al. (2002) also made the attempt to describe the YSOs with IRE by dividing them into two groups – 454 Class I sources and 2798 Class II / Class III sources. This classification was based on the JHK TCD (their Fig. 4b): stars in the reddened "T Tauri region", as outlined by the red line and the dashed reddening vector in Fig. 4.3, were regarded as Class II/III, while stars located right of the dashed line were classified as Class I. Jiang et al. find that the Class II / Class III candidates are distributed all over the field while Class I candidates occur generally in the H II region. The latter result cannot be retraced from the data given in the paper. First, their Table 2 lists 454 Class I sources in "M17" but only 235 are contained in the subregions 1C (20), 1S (97), 1N (115) and 2C (3). Second, Fig. 10 of Jiang et al. which displays the spatial distribution of the Class I sources contains 287 stars, most of which are located in the southern and northern bar.

A comparison between the JHK diagram (Fig. 4.3) and the HKL diagram (Fig. 4.5) shows that the fraction of IRE objects increases from 29% to 46%, using intrinsic colors published by Ducati et al. (2001); those values would transform into 37% and 57%, respectively, when e.g. adopting the intrinsic colors given by Bessell & Brett (1988). The detection rate for L -band sources decreases drastically in the Northern and the Southern bar of M17. This is a consequence of the emission from extended hot interstellar dust and PAHs in the L -band which enhances both the background and the confusion in those regions. Ando et al. (2002) also found that thermal radiation from dust at around 1000 K dominates the emission at L in both the N and S bar.

In order to compare the excess frequency of the M17 cluster with other young clusters, one has to perform the same procedure as proposed by Haisch et al. (2001b) :

- A completeness check for the L -band data yields a limit of $L = 13$ mag for which the detection rate is uniform over the entire field. Due to the higher sensitivity at JHK this limit holds for the remaining wavebands too.
- Selecting only stars brighter than $K = L = 13$ mag to be sensitive to stellar photospheres (i.e. $K - L \sim 0$ mag) reveals a total of 496 stars equivalent to ZAMS spectral types of A4 or earlier.
- The intrinsic colors were taken from Bessell & Brett (1988).

Among the above selected 496 sources there are 308 with IRE, thus leading to an excess frequency of 62% in M17. This number is remarkable in several aspects. First, it only refers to intermediate and high-mass stars earlier than A4, which is unusual in comparison to the other young clusters (see below). Second, Fig. 4.5 shows that the total number of stars with IRE increases toward lower masses: Indeed, 1001 stars with K and $L > 13$ mag yield an (incomplete) IRE frequency of $> 75\%$. In total, the combined IRE frequency is at least 74%.

Haisch et al. (2000) suggest that disks form around the majority of the stars in very young clusters *independent of mass*. Looking in detail into the data of the youngest cluster, however, it seems that the disk fraction is a function of spectral type:

As inferred from the J vs. $J - H$ CMDs constructed from Table 2 in Haisch et al. NGC 2024 contains stars between O and G. The excess frequency as a function of spectral type is 58% (O,B), 69% (A), 76% (F) and 90% (G), i.e. it increases steadily with spectral type. Lada et al. (2000) also claim a mass independence for the Trapezium cluster. There, the excess frequencies increase from 42% (12 O,B,A) to 78% (9 F,G), 82% (87 K) and 81% (177 M); for 62 sub stellar sources the occurrence of IRE decreases to 50%. Eventually, Haisch et al. (2001b) found in IC 348 9 stars of spectral types O, B, A, and F that appear disk-less, while 6 G, 23 K and 42 M stars have a disk fractions of 50%, 52% and 67%, respectively. Thus, in summary, there is a correlation between increasing IRE frequency and spectral type with the OBA types having the lowest IRE fractions.

>From the above formal estimates it seems that M 17 belongs to those young clusters with the highest disk frequency for high- and intermediate-mass stars. In this respect it is comparable to NGC 2024. This issue will be further discussed in Sect. 4.1.11.

4.1.10 CO Band Head Sources

Numerous YSOs display the CO band-heads at $2.3 - 2.4 \mu\text{m}$ in emission. There is consensus that this CO emission originates in extremely dense ($n_{\text{H}} \geq 10^{10} \text{ cm}^{-3}$) and warm ($1500 \text{ K} < T < 4500 \text{ K}$) regions associated with YSOs and is likely a result of the disk accretion process during early stellar evolution. A variety of mechanisms and models have been proposed to explain their precise origin. These include circumstellar disks, stellar winds, magnetic accretion mechanisms, and inner disk instabilities (e.g. Carr 1989; Carr et al. 1993; Chandler et al. 1993; Biscaya et al. 1997). Recently, the CO emission has been used to infer properties of the associated circumstellar disks (Bik & Thi 2004; Blum et al. 2004).

CO band-heads in absorption, in contrast, are typical of the photospheres of cool, mostly evolved stars. Nevertheless, initial surveys of star-forming regions (e.g. Casali & Eiroa 1996) have demonstrated that low-luminosity Class II sources, i.e., stars with flat or decreasing spectral energy distributions, such as T Tauri stars, may also display strong CO absorption features. Sources with steeply rising SEDs (Class I) showed much weaker, or even undetectable, CO absorption. Greene & Lada (1996) also found that the CO bands are much weaker in Class I sources. On the other hand, CO absorption arising from an expanding shell or from an accretion disk has been discussed in the context of FU Orionis objects (Hartmann et al. 2004). Models have shown that variations in the strength and the appearance of the CO feature – either in emission or in absorption – depend on parameters like the stellar temperature, the geometry of the circumstellar material, and the mass accretion rate onto the protostellar object (Carr 1989; Calvet et al. 1991). The weakness or even the absence of any CO feature may therefore be a complex combination of various competing mechanisms.

Within the area covered by the L -band imaging, K -band spectroscopy could be obtained for 201 stars. The spatial coverage of this study is not homogeneous across the region, but focused toward the cluster center and the southwestern interface between the H II region and the molecular cloud. According to the K -band spectra one can divide the sample into four groups (Fig. 4.9): Only 28 stars ("Others") display stellar photospheric absorption lines that can be used for classification. Sixty sources ("Featureless") are lacking any stellar spectral

feature, indicating both the extreme youth of the stellar aggregate and the major role that veiling by circumstellar dust plays during these early phases. Apart from nine stars with the CO band-head in emission ("COES") there are 104 stars which show this feature in absorption ("COAS"). Among these 113 CO sources 109 do not show any further spectral lines. The number statistics of the individual groups is summarized in Table 4.3.

Table 4.3: Statistics of the K -band spectra

Objects	COAS	COES	Featureless	Others
Total	104	9	60	28
IRE	34 (33%)	7 (78%)	32 (53%)	10 (36%)
X-ray	39 (38%)	4 (44%)	19 (32%)	19 (68%)
IRE and X-ray	19 (18%)	4 (44%)	10 (17%)	6 (21%)
IRE and/or X-ray	54 (52%)	7 (78%)	41 (68%)	23 (82%)

Designations: "COAS", CO band-head feature in absorption; "COES", CO band-head feature in emission; "Featureless", objects without any spectral features; "Others", stars with photospheric lines.

Altogether there are 9 (4%) COES; 4 of them – CEN 24 (B275), CEN 49 (B268), CEN 92 (B331), and CEN 93 (B337) – were previously known (Hanson et al. 1997). Among the 104 (52%) COAS there are four sources – CEN 33 (B324), CEN 102 (B305), B22, and B120 – which have been observed by Hanson & Conti (1995); those authors interpreted them as field stars unrelated to M 17. Two other COAS with IRE (B239, B339) were suggested to be high-mass YSOs (Hanson & Conti 1995).

The HKL TCD contains 156 stars with K -band spectroscopy; some of the brighter stars are missing because they were saturated at one of the wavebands. Quite a number of stars are located in the excess region below the reddening path indicating thermal emission from dust in a circumstellar disk and/or envelope. The infrared spectral energy distribution for some of these objects has already been investigated until $20\ \mu\text{m}$ (Chini & Wargau 1998; Nielbock et al. 2001) and corroborates this interpretation. The relative fractions of IRE among the four groups shows a significant trend: IRE is present in 78% of the COES, in 53% of the featureless stars, in 36% of the "Others", and in 33% of the COAS.

Among our K -band spectroscopic sample of 201 stars, there are 81 X-ray sources. The Chandra sources with CO features and with sufficient counts to support spectral fits can be reproduced by a simple thermal plasma model, i.e., there is no need for a flat power law, which is what one would expect if the source were an X-ray binary or a background AGN (Broos et al. 2007). None of these sources is anomalously soft and/or bright with a low absorbing column, so they are unlikely to be foreground field stars; typical A_V values range between 5 and 25 mag, consistent with our $JHKL$ photometry. None of these sources shows X-ray variability within the short (40 ksec) observation. All of them are consistent with being members of the M 17 complex.

There are only four stars with the CO feature that have further spectral lines at shorter wavelengths: B163, which was reported to be featureless by Hanson & Conti (1995), is a COES that shows $\text{Pa}\delta$ and $\text{Br}\gamma$ absorption in our spectrum. If this discrepancy is not due to the low S/N spectrum by Hanson & Conti (1995) we must assume that the source is variable. Additionally, B163 has both X-ray emission and IRE. Another COES with IRE, CEN 93 (Chini et al. 1980), also has $\text{Pa}\delta$ and $\text{Br}\gamma$ in absorption. The COAS CEN 57, with X-ray emission and

IRE shows Pa δ and Br γ absorption, and He I λ 21130 Å in emission. CEN 30, another COAS with X-ray emission, shows Pa δ , He I λ 10311 Å, and Br γ in absorption. In both cases, the infrared spectra are consistent with early B-type stars.

Compared to previous CO band-head studies in star-forming regions, the present survey is the most extensive one; in addition, it is the only one that is fairly unbiased. Casali & Eiroa (1996) suggested from their sample of 44 YSOs in six regions that CO absorption is very common in low-mass YSOs; from their Fig. 2 we estimate the fraction of COAS to be about 50%. Likewise, Casali & Eiroa (1996) argue that Class II sources tend to show CO absorption, while Class I sources are featureless. In the following, we will explore the nature of the M 17 sources in more detail.

In accordance with previous studies the 9 COES are interpreted as YSOs within M 17. Models for the thermal continuum emission from dusty in-falling envelopes around protostars indicate that the envelope emission can exceed the stellar plus disk photospheric emission by almost an order of magnitude (Calvet 1997) thus producing featureless spectra. The veiling of an envelope weakens the CO absorption lines while a disk will only amplify the CO feature. Therefore, the 60 featureless objects are very likely Class I sources within M 17. Those 54 COAS with X-ray emission and/or IRE are also young cluster members, as demonstrated above for the two objects CEN 30 and 57. Only the nature of the 50 remaining COAS is a priori less clear because there is no direct “youth indicator” for classification purposes. However, there are several issues indicating that there might be further YSOs in this group.

The first argument comes from the spatial distribution: most of the COAS are located in the immediate vicinity of other young cluster members and in regions with pronounced nebular emission. This makes it likely that a considerable fraction of them is related to the M 17 cluster. Secondly, the infrared colors of COAS without X-rays are on average redder than for sources with X-ray emission; likewise, their apparent IR-brightness is fainter by one or two magnitudes compared to the other stars in the sample. Given that the scatter of intrinsic *HKL* colors for all luminosity classes is fairly small with respect to the observed colors, one must assume that this large reddening is primarily due to interstellar dust. Thus, all of them have $20 \text{ mag} < A_V < 45 \text{ mag}$, a fact that might explain the non-detections by Chandra and that argues in favor of deeply embedded cluster members, at least for some of them. Finally we want to note that the groups of COES and featureless stars also contain 22% and 32% of objects that neither show X-rays nor IRE; nevertheless, these stars are most likely YSOs. Obviously, the absence of X-ray emission or IRE is no conclusive argument against youth.

The question concerning the mass of these YSOs is very important. To estimate their luminosity we use the *J – H* colors, where contamination by dust emission is likely to be small. Dereddening is achieved by adopting $(J - H)_0 \sim 0.16 \text{ mag}$, the mean intrinsic color of main sequence stars. As the range of intrinsic colors for dwarf and giant stars is sufficiently small ($-0.1 \text{ mag} < (J - H)_0 < 0.3 \text{ mag}$ for types O to K), the dereddening will not be affected much by the stellar temperature. In this way, we obtain absolute magnitudes of $-7.7 \text{ mag} < M_H < 2.6 \text{ mag}$ for the stars at the distance of M 17. This transforms into intermediate to high-mass stars, mostly earlier than A0, adopting main sequence luminosities. Some COAS that can be independently dereddened on the basis of their X-ray spectra corroborate this result: most of them appear to be early B-types; this holds also for the COES.

Figure 4.9 summarizes the major statistical findings in the form of an *H*-band luminosity function, adopting main sequence luminosities. Those 50 COAS that do not show unique youth indicators have been omitted from Fig. 4.9, although there might be further YSOs

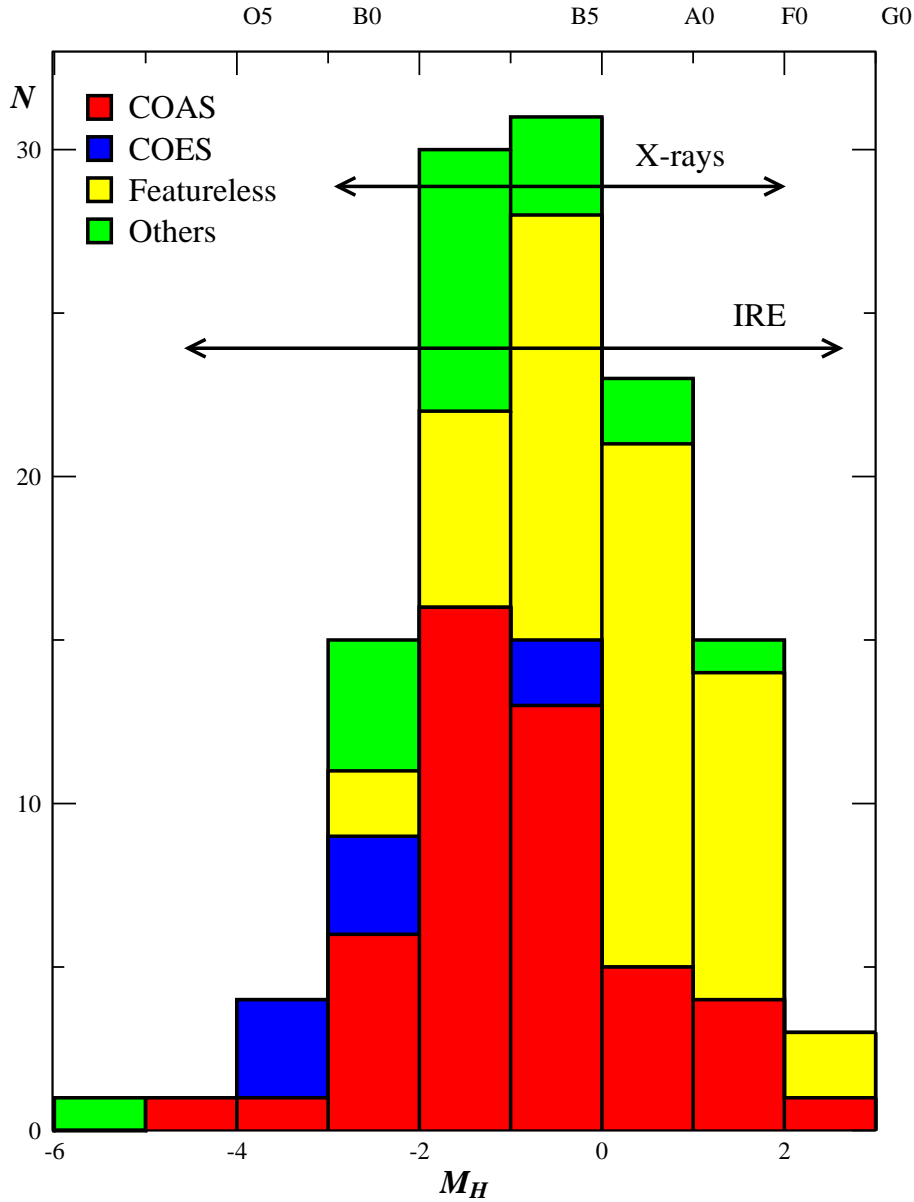


Figure 4.9: H -band luminosity function of probable cluster members in M17. Red: CO absorption, blue: CO emission, yellow: featureless, green: others. The arrows denote the range where stars with X-ray emission or IRE occur.

among them as discussed above. The distribution attains its maximum around B3; there are only 12% A- and 2% F-type stars. The remaining stars have absolute H -magnitudes compatible with intermediate and high mass stars, i.e., earlier than A0. Of course, at the faint end this distribution is influenced by the limiting magnitude of our spectroscopy. The faintest source for which a spectrum could be obtained has an apparent H -band brightness of 17.6 mag. Thus, it follows that we can see stars of, e.g., type A3 only if their visual extinction is below $A_V \sim 25$ mag; types K6 can only be detected with $A_V \leq 5$ mag.

Concerning the individual groups in Fig. 4.9, the featureless objects are basically later than B3, while the COES are earlier than B5. The COAS are distributed across the entire luminosity range. The range $-5 \text{ mag} < M_H < -2 \text{ mag}$ contains 8 COAS that have X-ray emission and/or IRE. This suggests the presence of YSOs with extremely high luminosity.

The above results have assumed the stars to be on the main sequence, although both CO band-heads and IRE indicate pre-main sequence objects. While high-mass stars evolve mainly at constant luminosity and therefore will not alter the overall distribution of spectral types (or masses) in Fig. 4.9, low-mass pre-main sequence objects change their luminosity by more than three orders of magnitude and thus will simulate earlier types and higher masses. Because it is likely that the H -band luminosity function is contaminated by objects of lower masses, these objects must be in an extremely early, i.e., protostellar evolutionary stage (due to their high luminosity).

According to the model by Calvet et al. (1991) the "young" COAS, i.e., those with X-ray emission or IRE, differ from the COES in the sense that either the underlying YSO is cooler or the mass accretion rate is higher. Corroborated by our early-type spectra for CEN 30 and 57, we favor the latter interpretation and identify those COAS as intermediate to high-mass protostars with mass accretion rates above $10^{-5} M_{\odot} \text{ yr}^{-1}$. Sources with featureless spectra may be similar to other hot YSOs like the Herbig Ae/Be star AB Aurigae (Hartmann et al. 1989) and may form a population between the CO emission and absorption sources.

4.1.11 Cluster Age

It is difficult to gauge the age of the youngest star clusters. The comparison of stellar loci with evolutionary tracks requires the precise knowledge of spectral-type, reddening and brightness which is hardly to achieve simultaneously for deeply embedded YSOs. Moreover, it is far from clear whether the ignition of SF in a molecular cloud is coeval for high- and low-mass stars; sequential SF complicates the situation in a large stellar aggregate.

Isochrone Fitting

The most common method is to compare the locus of stars in dereddened HR diagrams and compare it with isochrones. In the case of M 17 one can interpret the gap in Fig. 4.7 in terms of stellar evolution yielding the following results: Stars on the ZAMS, which include some of the exciting stars in the region originate from a first episode of SF in M 17. They have cleared the ISM in their surroundings and thus suffer from only moderate extinction ($A_V = 1 - 3$ mag). Stars beyond the gap are likely due to a second SF epoch and are embedded much deeper into the area. As demonstrated by Figs. 4.4 d - f, however, they are not associated with Cloud B but occur predominantly toward the H II region like the less-reddened stars. Fig. 4.7 shows an isochrone of 5×10^5 years (Siess et al. 2000) and an extinction of 4 mag which serves as a lower envelope for most stars beyond the gap. If true, this would mean that at least a second episode of SF has occurred in the region.

Lifetime of Stellar Disks

An alternative approach is to use the timescale for circumstellar disk dissipation as an indirect probe for the age of a cluster. Obviously, such estimates depend on the method of detecting disks, i.e. generally via K - or L -band excess for ground-based observations or MIR excess as accessible from satellites. Therefore, studies that determine disk frequencies as a function of cluster age have to be compared with caution, depending on how the excess was observed; the influence of intrinsic colors and reddening law has been discussed above. Additionally, a high abundance of nearby O stars might decrease the lifetime of disks considerably.

Haisch et al. (2001b) discuss the lifetimes of circumstellar disks, based on six young clusters that span a range in age of 0.3 – 30 Myr; the corresponding disk fractions started at $3 \pm 3\%$ for NGC 1960 (30 Myr) and raised to $80 \pm 5\%$ for the 1.5 Myr old Trapezium cluster and to $85 \pm 8\%$ for NGC 2024 (0.3 Myr). Analysis indicates that the cluster disk fraction rapidly decreases with increasing cluster age, such that one-half the stars within the clusters lose their disks in ≤ 3 Myr. Moreover, these observations yielded an overall disk lifetime of ~ 6 Myr in the surveyed cluster sample. This was proposed to be the timescale for essentially all the stars in a cluster to lose their disks.

As outlined in Sect. 4.1.9 the occurrence of disks in M 17 is 62% for stars earlier than A4 and increases to more than 75% for later spectral types. This disk frequency places M 17 among the youngest galactic aggregates such as NGC 2024 and the Trapezium cluster.

4.2 Objects of Special Interest

M17 contains numerous sources of interest that are currently under investigation. In the following, a couple of the most spectacular high-mass objects, where substantial observational material has been accumulated in the course of the present work, will be discussed in more detail.

4.2.1 The Major Exciting Binary CEN 1 a and b

From the existing data it is not clear whether the visible components of CEN 1a and 1b form a bound binary system. Their projected distance of ~ 3800 AU fits well into such a picture, the difference in their visual extinctions of about 3 mag might argue against such liaison.

The X-ray counterparts to both stars, are the brightest and most luminous X-ray sources in the cluster with intrinsic total band (0.5 – 8 keV) luminosities $\log L_{t,c} \sim 33.2$ and 33.3 erg s^{-1} , respectively (Broos et al. 2007). Because there is no enhanced X-ray emission between the two stars, there cannot be any strong shock between their winds, as it is expected given their fairly large separation.

Remarkably, both X-ray sources show very similar but yet highly unusual spectra; thermal plasmas in the range $kT = 10 - 13$ keV are not seen even in Wolf-Rayet colliding-wind binaries or in η Carinae. Only the “ γ Cas analogs” (Smith & Balona 2006; Rakowski et al. 2006; Smith et al. 2004) show such hard X-ray spectra, yet M17’s O4 stars do not show the variable light curves typical of these objects. Various model fits (Broos et al. 2007) suggest that CEN 1a and 1b may themselves be massive binaries. In fact, the double Pa δ lines in the J -band spectra of CEN 1 a and b and the double Pa11 line in CEN 1 a with a velocity separation of 240 km s^{-1} argue in favor of such a constellation. It seems that the system forms at least a trapezium of four massive stars. Fig. 4.10 shows the corresponding double lines for CEN 1 a; the K -band spectra of CEN 1 a and 1 b are displayed in the Appendix.

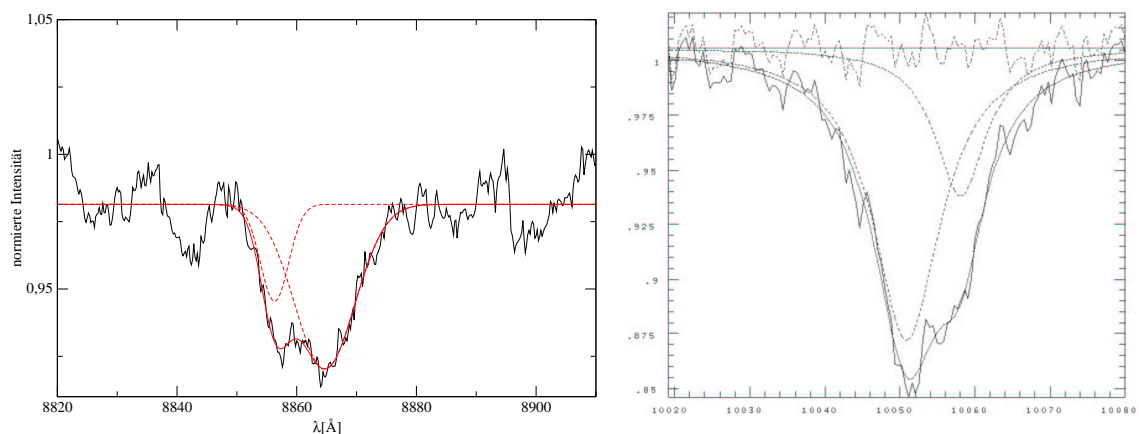


Figure 4.10: P 11 and P δ line for CEN 1 a. The velocity separation is 280 and 240 km s^{-1} , respectively.

4.2.2 M 17-UC1

Massive protostars evolve from hot cores to ultra-compact H II regions and eventually form classical H II regions; however, details of this evolution are far from understood. A few years ago, a new class of exceptionally small and dense objects, so-called hyper-compact H II regions, was discovered. They are believed to represent a transitional stage in early massive stellar evolution. Thus, their understanding is crucial for the formation of massive stars.

M 17-UC1 was discovered as a cometary ultra-compact H II region (Felli et al. 1980, 1984) displaying a shell structure with a diameter of 6.9×10^{15} cm, an estimated electron density in the range $2-6 \times 10^5$ cm $^{-3}$, and an emission measure of $\sim 7 \times 10^8$ pc cm $^{-6}$. The number of stellar Lyman continuum photons of $\simeq 2 \times 10^{47}$ s $^{-1}$ requires a B0 - B0.5 ZAMS star as the ionizing source. Meanwhile, M 17-UC1 was identified as a hyper-compact region (HCH II) with broad (≥ 35 km s $^{-1}$) radio recombination lines and a rising spectral index between 1.4 and 43 GHz (Johnson et al. 1998; Sewilo et al. 2004). While the rising spectral index may be produced by hierarchical clumping in a HCH II, the broad lines may origin from a combination of thermal, turbulent, and electron impact broadening, and large-scale motions such as rotation, expansion, jets, shocks, inflows and disks (Sewilo et al. 2004).

A number of methanol, hydroxyl and water maser sources are located in the vicinity of M 17-UC1 (e.g. Churchwell et al. 1990; Caswell 1997; Walsh et al. 1998; Forster & Caswell 1999). Johnson et al. (1998) observed four H₂O masers in the area – including those two which were previously known. Their projected distances with respect to M 17-UC1 range from ~ 0.08 to 0.38 pc and are thus higher than those found typically between ultra-compact H II regions and maser sources (Hofner & Churchwell 1996).

Within their positional uncertainty of $5''.7$ Harper et al. (1976) detected a strong compact $10.6 \mu\text{m}$ source (IRc2) whose position coincides with that of M 17-UC1. The photometry of IRc2 between 3.5 and $21 \mu\text{m}$ suggested hot dust emission and was assumed to originate entirely from M 17-UC1 (Felli et al. 1984); additionally, IRc2 displayed a strong silicate absorption. When Felli & Stanga (1987) observed M 17-UC1 from 1.25 to $18.1 \mu\text{m}$ they also found an unresolved IR source which they attributed to the ultra-compact H II region. As discussed below, their apertures of $3''.2$ and $7''.2$ included a nearby IR-bright star (B273 in Fig. 4.11) that is responsible for the emission at shorter wavelengths (*JHK*). Furthermore, the maps of Felli et al. at 10.3 and $18.1 \mu\text{m}$ had an E-W flip in their coordinates; as a consequence, the extended MIR emission was erroneously interpreted as to arise from the Arc.

On our images, M 17-UC1 is barely visible in *H*-band with a crude brightness of 17.8 mag. Unlike previous NIR studies, the source could be resolved for the first time into two *K*-band emission blobs, separated by $0''.46$ and a position angle of 126° measured clockwise from north to south. A dark lane separates the two *K*-band nebulae (Fig. 4.11). The south-western emission has an elliptical shape of $0''.9 \times 0''.5$ (3σ contour) and a pronounced peak at RA = 18:20:24.83 and DEC = -16:11:35.0 (J2000) with a FWHM (full width at half maximum) of $0''.19 \times 0''.13$ clearly coinciding with the radio emission. The north-eastern emission at RA = 18:20:24.85 and DEC = -16:11:34.7 (J2000) is more diffuse and has a size of $0''.8 \times 0''.5$. The integrated brightness of both blobs within a radius of 3600 AU is $K = 13.1$ mag, their intensity ratio is 10:1 (SW:NE). At *L* band, the source attains a spherical shape with a radius of $\sim 1''.0$ (3σ contour) and an *L'* brightness of 6.1 mag within 3600 AU.

Kassis et al. (2002) presented maps at 9.8 , 10.5 , 11.7 and $20.6 \mu\text{m}$ and performed radiative transfer code models that describe M 17-UC1 as a ZAMS B0 type star surrounded by a shell of

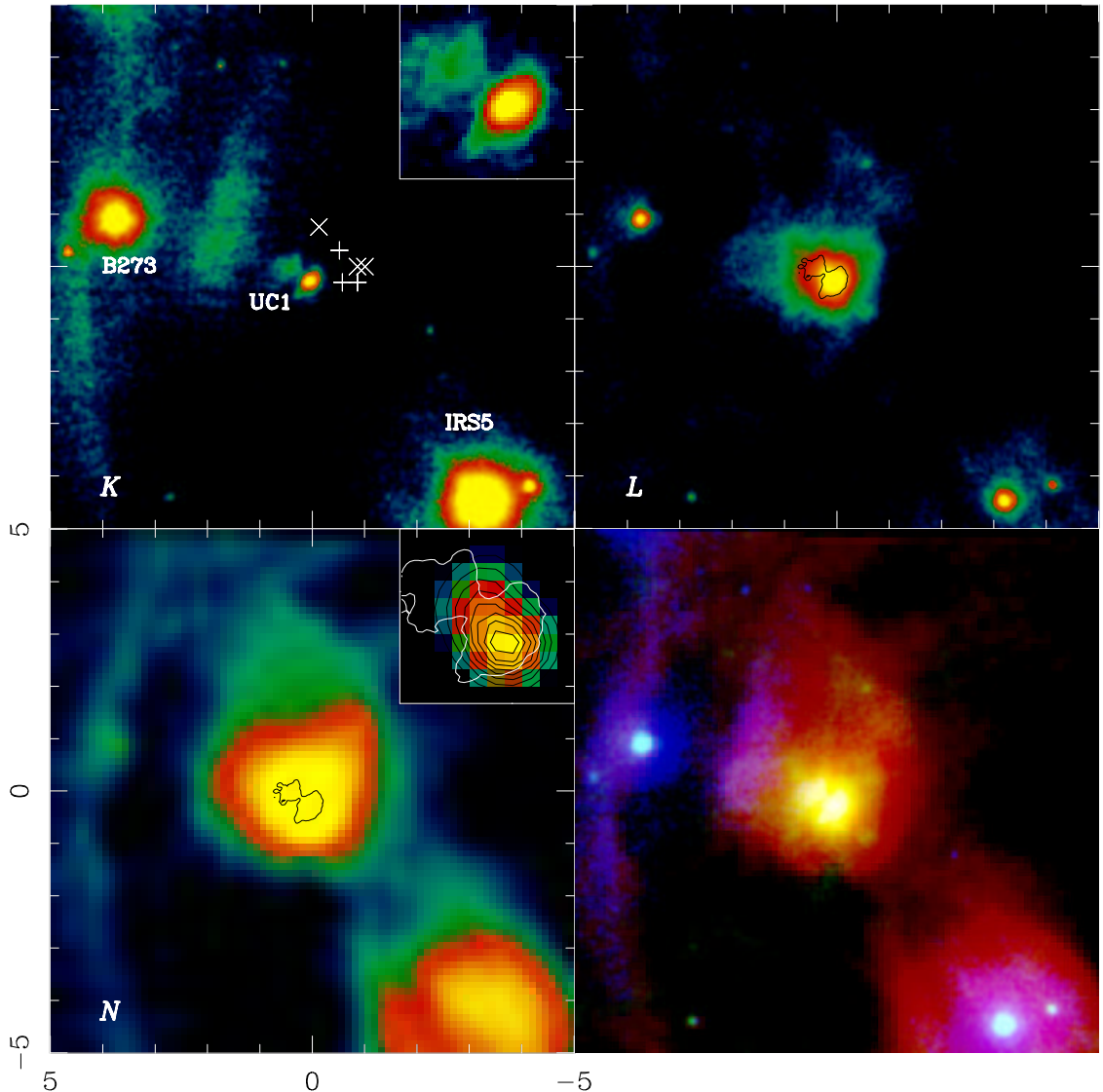


Figure 4.11: M17-UC1 as seen by NACO (K and L and VISIR (SiC/ N) (Nielbock et al. 2007). The central position is RA = 18:20:24.82, DEC = -16:11:34.9 (J2000), the field size is $10'' \times 10''$. The 3σ contour of the K band flux is superimposed on all images. The locations of associated OH (\times) and class II methanol masers ($+$) are indicated in the Ks band image. An enlargement ($1'' \times 1''$) of the source is shown in the upper right corner. The inset in the VISIR image illustrates the intensity distribution across the bright inner emission. Black contours at arbitrary intensity values are shown for enhancement. The lower right panel is a RGB coded composite of the three images (blue: K , green: L , red: N).

$0.6 - 3.4 M_{\odot}$. New N -band data (Nielbock et al. 2007) show a similar – although less resolved – double structure as in the K -band with a FWHM of $0''.7 \times 0''.5$; the brightness maximum is centered on the SW K -band peak (Fig. 4.11). The total circumstellar emission ($\sim 5'' \times 3''$) is relatively complex with a noticeable extent to the northwest.

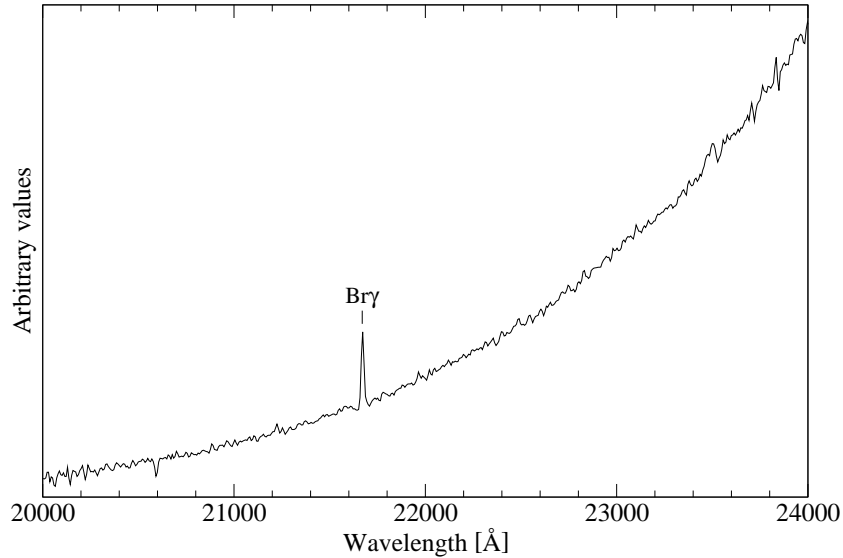


Figure 4.12: *K*-band spectrum of M 17-UC1. Apart from a strongly rising continuum there is only faint and narrow Br γ emission.

The present *K*-band spectrum (Fig. 4.12) of M 17-UC1 includes both nebulae and shows an extremely red continuum caused by hot dust. Apart from the Br γ emission line, which most likely originates from the hyper-compact H II region, the spectrum appears featureless. The *N*-band spectrum displays a deep silicate feature (Fig. 4.13); its existence was already suggested by earlier photometric data (Harper et al. 1976; Kassis et al. 2002) and indicates the presence of cold dust along the line of sight towards M 17-UC1. Using the standard relation for converting optical depth of $\tau \sim 17 \tau_{9.7}$ (Krügel 2003), a visual distance of about 40 mag was inferred. The luminosity between 1.6 and 20 μm corrected for extinction is $1.1 \times 10^4 L_{\odot}$, which is consistent with an early B0 star.

The symmetric absorption pattern of M 17-UC1 in the *K*-band along with the perpendicularly scattered light nebulosities on both sides very much resemble the appearance of young low-mass stars with circumstellar disks (McCaughrean & O'dell 1996; Padgett et al. 1999; Brandner et al. 2000; Grosso et al. 2003). This view is supported by the morphology of theoretically derived synthetic images of protostellar disks presented by Stark et al. (2006). These disks are simulated by varying envelope mass, disk radius and mass, and outflow cavity shape. Among these, suitable representations of the *K*-band image of M 17-UC1 can be found. The fact that class II methanol masers are located in the general direction of the supposed disk gives further evidence. Apart from almost uniformly extended *L*- and *N*-band emission, the disk would be expected to emit strongly in the MIR, too. Nevertheless, there must be cool dust inside the disk as witnessed by the silicate absorption feature. The shape of the central MIR emission elongated perpendicular to the disk orientation is interpreted as scattered light from the central source (inset in lower left panel of Fig. 4.11). Due to the lower optical depth, however, the MIR disk emission is veiled by the silicate absorption and scattered photons. At larger distances from the hyper-compact H II region, a warmer and less dense envelope emits strongly in the MIR. Nielbock et al. (2007) presented complementing radiative transfer model calculations suggesting that M 17-UC1 is surrounded by a disk of cold dust, embedded in an envelope of

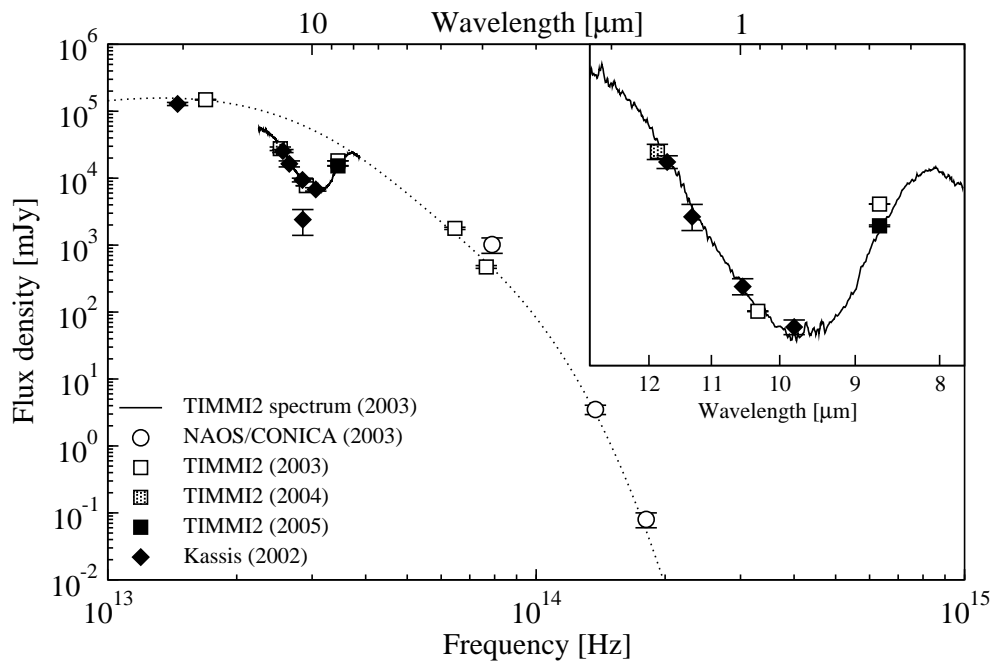


Figure 4.13: SED of M17-UC1. The data were obtained between 1999 and 2006. The solid line is the MIR spectrum of the silicate absorption feature at $9.7 \mu\text{m}$. The inset is a zoom into the spectrum. A continuum fit of two blackbody components with formal color temperatures of $T = 4215$ and 225 K is shown as a dotted line.

warmer dust.

From the results presented here, one must conclude that a circumstellar disk is still present during the HCH II stage and that M17-UC1 is the first example where such a disk could be directly observed.

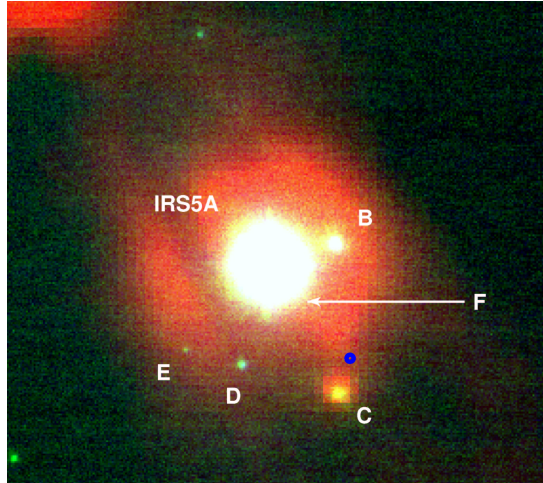


Figure 4.14: IRS 5 and its neighbors as seen by NACO (H and K_s and VISIR (SiC/ N). The central position is RA = 18:20:24.67 and DEC = -16:11:37.9 (J2000), the field size is $10'' \times 10''$. The other bright source in the field is M17-UC1. The locations of an associated H_2O masers is indicated by a blue dot. The image is an RGB coded composite of H , K and N .

4.2.3 IRS 5

This source at RA = 18:20:24.6 and DEC = -16:11:40 (J 2000) was first mentioned by Chini & Wargau (1998) as a bright NIR object 5" southwest of M17-UC1. Subsequent N and Q images showed this source to be equally bright as M17-UC1. In the early MIR map of Felli & Stanga (1987) there is a similar bright source south-east of M17-UC1. This led Nielbock et al. (2001) to suggest that both sources are identical, however, with an erroneous east-west flip of the coordinates in the map by Felli & Stanga. This interpretation was corroborated by Kassis et al. (2002). While the hyper-compact H II region is not visible at J , faint at K but very bright at 1.3 cm, IRS 5 shows rather opposite characteristics, namely being very bright at infrared wavelengths but invisible in the radio continuum. Andriessse & de Vries (1976) found an unresolved MIR object about 20" south of IRS 5 which they identified as a late type cocoon star with a luminosity of at least $400 L_\odot$ and a temperature of 150 K. It is very likely that this source is identical to IRS 5 and that the positional offset is due to the difficulty to unambiguously separate the emission of the stellar source from the high background. The SED indicates that IRS 5 is also still surrounded by a remnant proto-stellar cocoon. From model calculations Kassis et al. (2002) proposed a shell of $70 M_\odot$.

Table 4.4: Photometry of the IRS 5 group

IRS5	J	H	K	L	$J - H$	$H - K$	$K - L$
A	13.15 ± 0.09	10.71 ± 0.24	9.66 ± 0.19	8.08 ± 0.23	2.44 ± 0.25	1.05 ± 0.30	1.58 ± 0.29
B	18.14 ± 0.10	14.42 ± 0.34	13.11 ± 0.34	10.85 ± 0.23	3.72 ± 0.35	1.31 ± 0.45	2.26 ± 0.39
C	> 19.35	17.60 ± 0.35	13.81 ± 0.13	9.36 ± 0.23	> 1.75	3.79 ± 0.37	4.45 ± 0.26
D	> 19.35	16.58 ± 0.34	15.88 ± 0.13	> 15.25	> 2.77	0.70 ± 0.36	< 0.63
E	> 19.35	17.84 ± 0.36	17.12 ± 0.16	> 15.25	> 1.51	0.72 ± 0.38	< 1.78

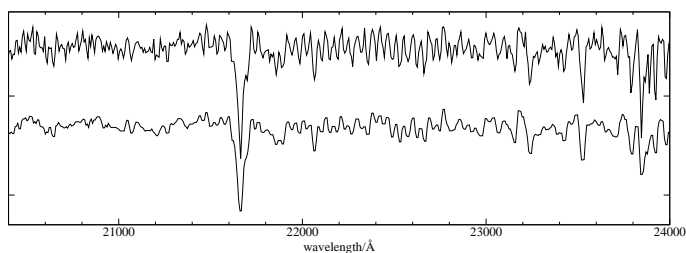


Figure 4.15: Normalized K -band spectrum of IRS 5. The lower version has been binned with a bin size of $\approx 20 \text{ \AA}$ to enhance spectral features. In order to determine a spectral type, the most important features are $\text{Br}\gamma$ (21660 \AA), He I (20590 and 21850 \AA), and He II (21885 \AA). Interestingly the spectrum shows CO absorption lines except for the first band head at 22940 \AA ($2 \rightarrow 0$).

New adaptive optics *HKLN* images of IRS 5 show considerable structure of the source (Fig. 4.14). The main source (A) is accompanied by two red objects (B and C). Component C is the only compact source in the N -band image and coincides with the position of the H_2O maser No. 4 (Johnson et al. 1998) within the positional uncertainties. Subtraction of an average field PSF from component C leaves a ringlike structure on the K -band image that might be an envelope or a face-on disk with a diameter between 230 and 280 AU. $H - K$ colors and lack of further information like X-ray emission or IRE suggest that components D and E might be unrelated stars in foreground of IRS 5. Table 4.4 summarizes the existing point source photometry. The spectral type of IRS 5 could be determined by the present K -band spectroscopy as O6 V (Fig. 4.15). It seems that IRS 5 is another example of an extremely early high-mass star with a circumstellar disk as witnessed by an associated dark lane visible on the L - and N -band image (red channel of Fig. 4.14) that displays the silicate absorption. In Fig. 4.16 the SED of IRS 5 A is presented. The SED is well fitted by two dust components with temperatures of 267 K and 1140 K.

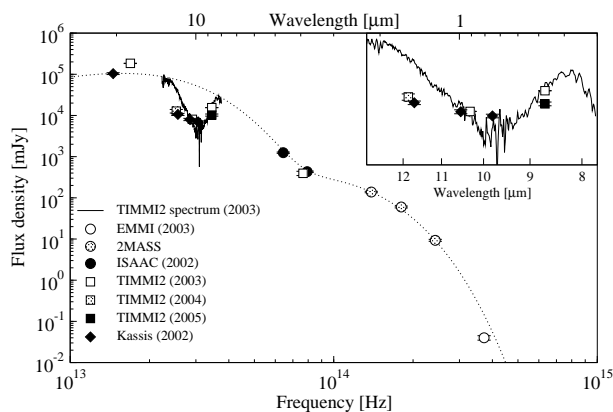


Figure 4.16: SED of IRS 5. The data have been obtained between 2003 and 2005. The solid line is the MIR spectrum of the silicate absorption feature at $9.7 \mu\text{m}$. The inset is a zoom into the silicate feature. The dotted curve is a continuum fit of two blackbody components with temperatures of 267 K and 1140 K, respectively.

4.2.4 IRS 15

Although there is growing evidence that high-mass stars can be formed through accretion from a surrounding disk of gas and dust in the same way like low-mass stars, the question whether the most massive objects are the result of the merging of intermediate-mass stars is not yet settled. In each individual case where a disk seems to surround a high-mass stars the mass of the (proto)star is fairly uncertain. This is because the mass is based on assumptions about the origin of the associated luminosity and/or radio emission; likewise, the problem whether the putative massive star is a single or a multiple object remains doubtful. Thus, the ultimate convincing case of a massive star/disk system, where the stellar mass can be determined uniquely by spectroscopy, has been missing until recently – a consequence of the rapid evolution of these systems and the early destruction of the disk in the vicinity of a massive star.

During the present search for circumstellar material around cluster members spectroscopically classified O- and early B-type stars by were investigated by MIR imaging at 3.7 and 10 μm . Several objects of spectral type O9 to B0 show clear evidence for extended dust emission. The morphology of the circumstellar dust, however, is fairly different, changing from irregular, filamentary shapes to regular features like fan-shaped rims and disk-like ellipses.

One outstanding object is IRS 15 at RA = 18:20:28.7 and DEC = -16:12:12.0 (J2000). It is an optically visible star found to be associated with a strong IRE by Chini & Wargau (1998) and Nielbock et al. (2001). The optical and IR spectra of the present work suggest a spectral type of B0.5 V, corresponding to an effective temperature $T_{\text{eff}} \sim 28.000\text{K}$ and a mass of $26 M_{\odot}$.

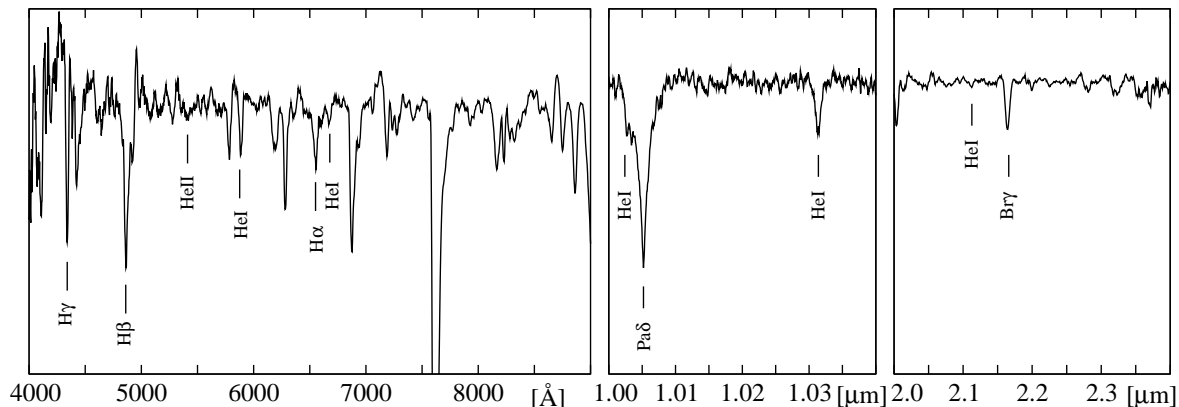


Figure 4.17: Normalized optical and NIR spectra of IRS 5. The most important features for spectral classification are shown. Additionally, in the *K*-band spectrum weak CO absorption lines are present.

Imaging from optical wavelengths to 2.2 μm shows IRS 15 as a point-like object; beyond 2.2 μm extended circumstellar emission becomes increasingly prominent (Fig. 4.18). Eventually, at 10 μm the elliptical nebula attains its largest size. This emission can be modeled by a disk with a scale height ratio of 0.1 an inner radius of 130 AU, an outer radius of 10.000 AU and 0.1 μm -sized silicate dust particles. Chini et al. (2006) obtained a density distribution which displays a flattening in its inner part. Compared to standard accretion disk models a substantial fraction of the inner disk must have been already eroded. Their model requires a total dust mass of $5 \times 10^{-4} M_{\odot}$.



Figure 4.18: *KLN* image of IRS 15 - a spectroscopic B0.5 V star. The central position is at RA = 18:20:28.7 and DEC = -16:12:12 (J2000). North is at the top and east to the left; the field of view is $14'' \times 14''$. At $10 \mu\text{m}$ the disk has a total projected size of $17,400 \times 12,500$ AU (lowest 3σ intensity contour) and is seen under an angle of about 53 degrees with respect to the line of sight.

IRS 15 is very likely a star on the MS which has stopped accretion. Nevertheless, it must be extremely young because the time span during which a massive star can maintain a circumstellar disk that has not yet been completely destroyed by the strong stellar winds must be of the order of a few Myrs. Thus, IRS 15 is a fortunate constellation where the newly-born massive star is already optically visible while its circumstellar disk (or envelope) is not yet dispersed and still glowing at infrared wavelengths. This configuration represents the final evolutionary stage in massive SF.

4.2.5 The Silhouette Disk

Probably one of the youngest stages of massive SF can be found in the SW interface of the H II region and the molecular cloud. In the ISAAC *JHK* mosaic (Fig. 2.2) a huge opaque silhouette was discovered against the background of the nebular emission. The most obvious morphological components of the system are two triangular-shaped dust lanes that are apparent at infrared wavelengths. Fig. 4.19 shows high-resolution 1.6 and 2.2 μm images, which suggest that the morphology of the silhouette resembles a flared disk, seen nearly edge-on, and is associated with an optically visible hourglass-shaped nebula perpendicular to the disk plane. The disk has a diameter of about 20,000 AU, which is by far the largest circumstellar disk detected to date. Although there are a small number of candidates for massive YSOs, some of which are associated with outflows (Greenhill et al. 1998; Marti et al. 1993; Hofner et al. 2001; Gehrz et al. 1982), the largest circumstellar disk hitherto detected around these objects has a diameter of only 130 AU (Shepherd et al. 2001). NGC 7538S, another potential massive YSO and a site of OH and H₂O masers, is embedded in an elongated cloud core (Sandell et al. 2003). Molecular line studies indicate both rotation and outflow, but the velocity structure of the entire system is extremely confused and there is no direct evidence for a disk. The largest silhouette disk so far is known as 114-426 in Orion and has a diameter of about 1,000 AU; however, its central star is probably a low-mass object rather than a massive protostar.

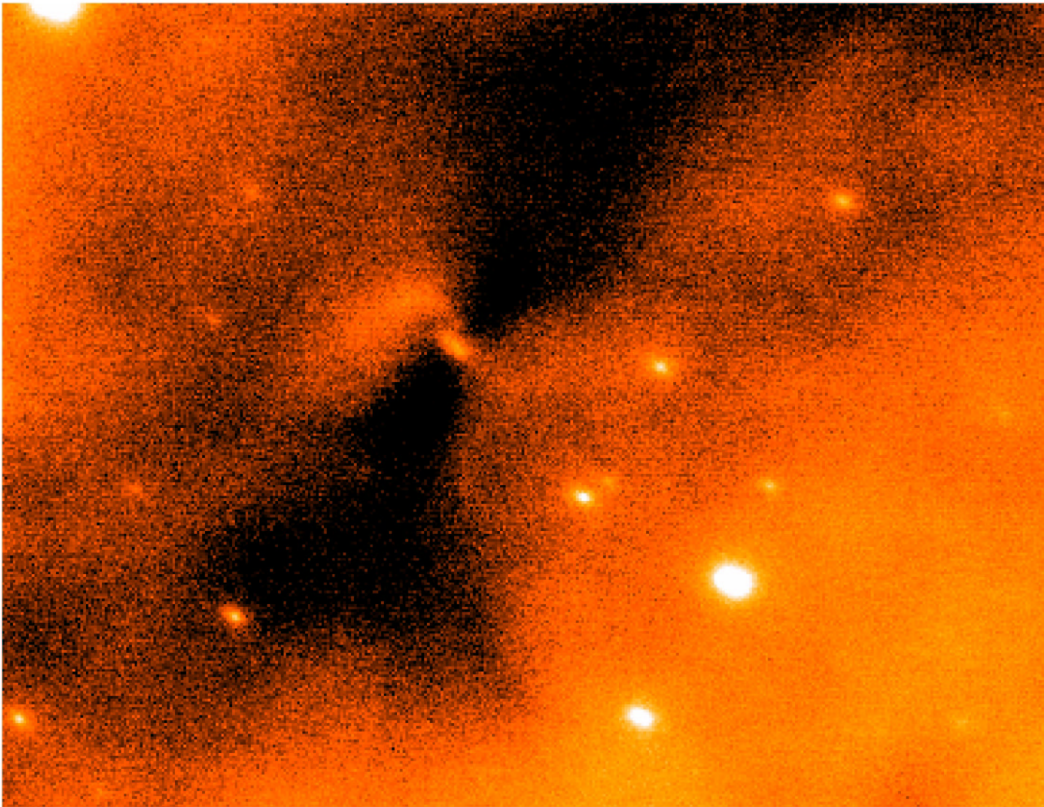


Figure 4.19: Silhouette of the 20,000 AU accretion disk. The 2.2 μm image is centered at RA = 18:20:26.3 and DEC = -16:12:10 (J2000); the FoV is $7'' \times 7''$.

The ^{13}CO data indicate that the disk/envelope system rotates (Chini et al. 2004). However, the disk mass as derived from the molecular emission is still controversial ranging from about $4M_{\odot}$ (Sako et al. 2005) to $110M_{\odot}$ (Chini et al. 2004).

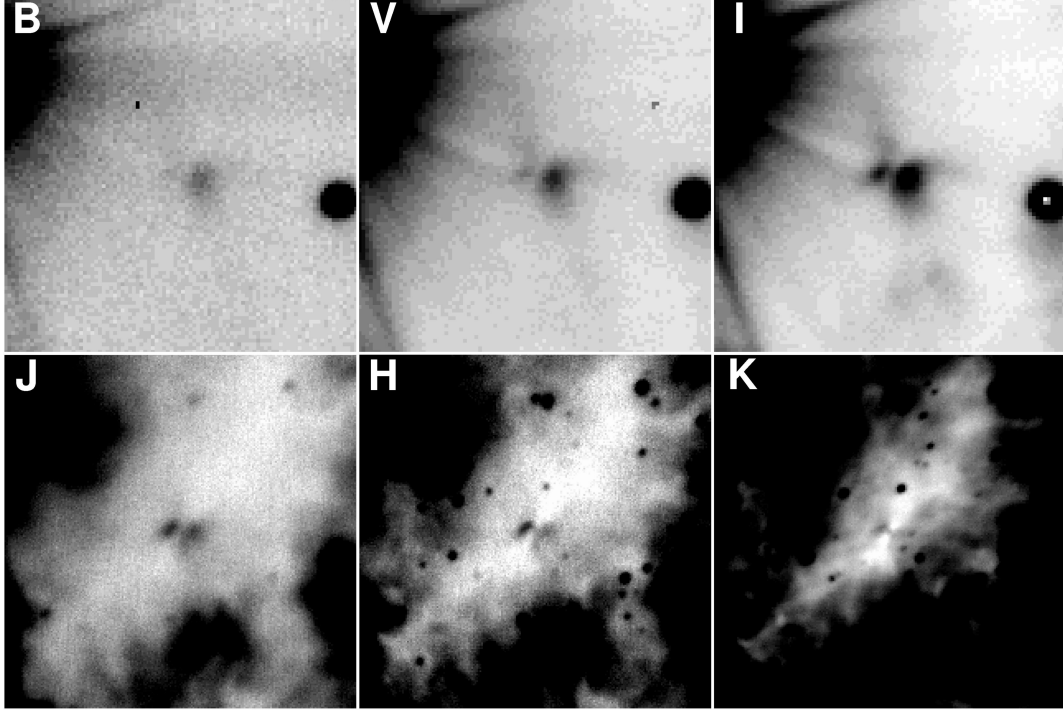


Figure 4.20: Multi-wavelength sequence of the hourglass-shaped reflection nebula. The central position of each frame is at RA = 18:20:26.3 and DEC = -16:12:10 (J2000); the size is always $30'' \times 30''$. The change in morphology and intensity is delineated from the optical to the NIR; the corresponding wavelengths are denoted at the top left of each panel. In the upper row, the nebula is dominated by reflected light from a bipolar cavity; the southwestern (right) lobe is much stronger while the northeastern (left) lobe is obscured by the disk. The lower row is dominated by more compact emission (see also Fig. 4.19).

The second morphological structure that is visible throughout the entire spectral range from 0.4 to $2.2\ \mu\text{m}$ is an hourglass-shaped nebula perpendicular to the plane of the disk; Fig.4.20 shows a sequence of images. Its spectrum is dominated by the emission lines of $\text{H}\alpha$, the Ca II triplet 8498, 8542 and $8662\ \text{\AA}$, and He I $6678\ \text{\AA}$ (Fig. 4.21). In the case of low-mass stars, these lines provide indirect evidence for ongoing accretion from the inner disk onto the star (Muzerolle et al. 1998, 2001). The Ca II triplet was also shown to be a product of disk accretion for both a large sample of T Tauri and Herbig Ae/Be stars (Hamann & Persson 1992). The $\text{H}\alpha$ line is extremely broad and shows a deep blue-shifted absorption as well as an inverse P Cygni profile. Blue-shifted absorption components in permitted lines are typically associated with accretion disk-driven outflows (Hartigan et al. 1995; Calvet 1997); the same is true for forbidden emission lines such as $[\text{O I}] 6300\ \text{\AA}$ and $[\text{S II}] 6731\ \text{\AA}$, which are also present in our spectrum. Numerous permitted and forbidden Fe II lines that are velocity-shifted by $\pm 120\ \text{km s}^{-1}$ are clear signs of high-velocity dissociative shocks with velocities of more than $50\ \text{km s}^{-1}$ (Hartmann et al. 1994).

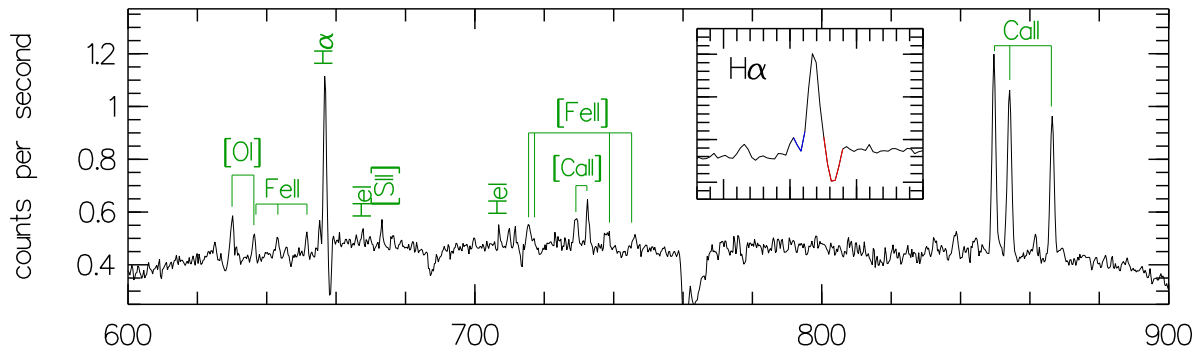


Figure 4.21: Optical spectrum of the bipolar nebula. The slits – oriented perpendicular to the disk plane – had lengths of 5' and 8' and a width of 1". The contamination from the H II region has been subtracted by averaging the emission from several offset positions. The x axis gives the wavelength in nm. The various emission lines in the reflected light indicate evidence for ongoing accretion.

Owing to heavy extinction, the nature of an accreting protostellar object is difficult to infer. For all suggested massive YSOs (see examples above), there is no direct evidence for a (proto)stellar central object; likewise, the origin of the luminosity – typically about 104 solar luminosities – is unclear, and may be due to multiple objects or even embedded clusters. The new disk in M17 is the only system that exhibits a central object at the expected position of the forming star. The 2.2 μm emission is relatively compact (240×450 AU) – too small to host a cluster. One may speculate whether this elongated feature originates from a binary system that is embedded within a common accretion disk. Assuming that the emission is due to direct stellar light, we derive an absolute infrared brightness of $K \approx -2.5$ mag, which would correspond to a main sequence star of about $20 M_{\odot}$. Given the fact that the accretion process is still active, and that models predict that about 30-50% of the circumstellar material can be accumulated onto the central object, it is likely that in the present case a massive protostar is currently being born. Theoretical calculations (Yorke & Sonnhalter 2002) show that an initial gas cloud of 60-120 M_{\odot} may evolve into a star between 33 and 43 M_{\odot} , while the remaining mass is rejected into the ISM.

Steinacker et al. (2006) modeled the optical depth at 2.2 μm and obtained disk masses between 0.03 and 18 M_{\odot} , depending on the assumed distance and the dust model. The nature of the embedded protostar is still unclear. Nielbock et al. (2008) could recently resolve the central elliptical IR emission and found a stellar-like source in the K -band plus a faint jet toward the northeast. Likewise, a faint bent lobe appeared within the SW nebula. Additionally, a collimated jet toward the SW lobe with several H_2 knots was detected by Nürnbergger et al. (2007) corroborating that accretion is going on in this object. The derived accretion rate of $\dot{M} > 10^{-5} M_{\odot} \text{ yr}^{-1}$ and the fact that the disk is by far the largest accretion disk ever discovered indicate the early formation stage of a massive star. Nielbock et al. (2008) derive a conservative lower mass limit of $\sim 2.8 M_{\odot}$ for the protostar.

4.2.6 Extremely Red Objects

Chini (1982) and Chini & Krügel (1985) found seven early B-type stars and one unknown source whose SED between 0.3 and $20\mu\text{m}$ displayed the largest IREs known for optically visible stars at that time. These objects were interpreted as "cocoon stars" with shells or tori of dust of several 100 K. Giard et al. (1994) presented among others K - and L -band images of the Arc region. In their Table 1, seven extremely red ($K - L > 3.5$) sources – different from those of Chini & Krügel (1985) – were listed, among them M17-UC1 and IRS 5. The red colors led Giard et al. (1994) to conclude that this group is in a very early evolutionary stage. The present photometry corroborates that these sources are fairly red, however, the K and L brightness for individual objects differs by more than 2 mag in certain cases. Whether this result is due to variability has to await further observations. Jiang et al. (2002) also discussed a group of very red sources ($H - K \geq 2.4$ mag) for which they could not obtain J -band data. They argue that the majority of these red sources should be YSOs with intrinsic IRE associated with the molecular clouds surrounding the H II region (Fig. 5 of Jiang et al.). The present data – although referring to a smaller field – do not corroborate this interpretation.

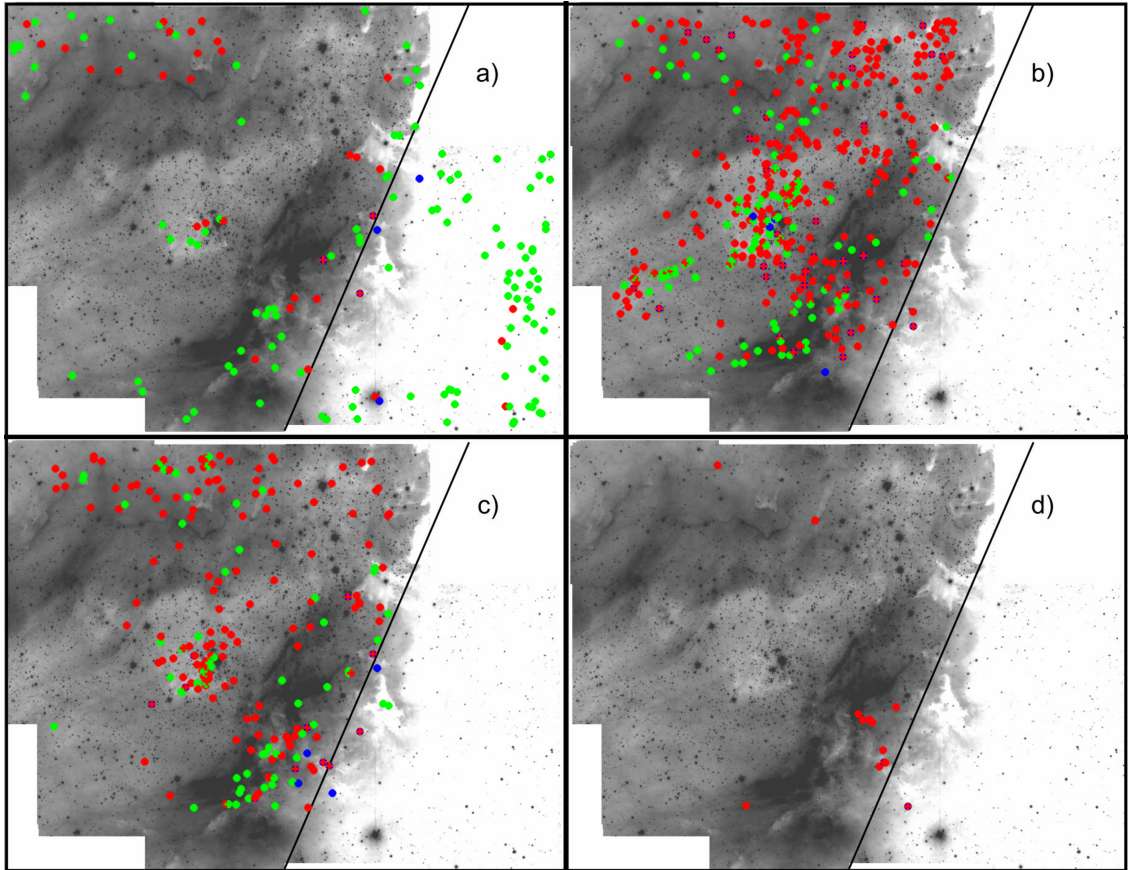


Figure 4.22: Distribution of extremely red objects. **a)** 158 sources with $H - K > 2.4$ mag, **b)** 423 sources with $1.5 \text{ mag} < K - L \leq 2.0$ mag, **c)** 211 sources with $2.0 \text{ mag} < K - L \leq 4.0$ mag, **d)** 13 sources with $K - L > 4.0$ mag. Red symbols correspond to IRE objects, blue symbols denote X-ray sources.

Fig. 4.22 a shows the spatial distribution of 158 sources with $H - K > 2.4$ mag half of which are concentrated southwest of Cloud B. The $JHKL$ data, however, reveal that this red population contains only 20% IRE objects and 2% X-ray emitters, indicating that the majority is not particularly young with intrinsic IRE. Moreover, the few sources with IRE and X-ray among this sample seem to be associated with the H II region and not with the molecular clouds. In fact, there are only three stars with IRE – apart from the Kleinmann-Wright object – outside the H II region. This makes it rather likely that the sources towards the molecular cloud are unrelated background sources shining through the SW edge of Cloud B.

In this work a large number of red objects was found, too; more than half of about 3000 sources in M17 with detections at K and L have colors $K - L > 1.1$ mag with a dozen of sources characterized by extremely red colors of $4 \text{ mag} < K - L < 7 \text{ mag}$. Due to the fact that the JHK and the L observations were obtained at different epochs, variability, if present, could contaminate some of the $K - L$ colors. Given, however, that there are only extremely red and no unusually "blue" sources the photometry seems to be fairly reliable.

If the $K - L$ values of these extremely red sources are due to pure reddening by dust this would imply extinctions A_V of up to 160 mag! Such extreme extinctions typically arise from dense disks or envelopes of deeply embedded protostellar objects and not from the more diffuse dust of a molecular cloud core. If – on the other hand – these red colors are caused by strong IRE emission the sources also must be protostellar in nature and still in the process of forming.

To discriminate between extinction and IRE, these red sources have been examined in the $H - K$ vs. $K - L$ diagram. Fig. 4.23 shows the distribution of $K - L$ colors for 2968 stars of which 52% have IRE. The peak for all sources lies at $K - L \sim 1.1$ mag, the peak for IRE sources is slightly shifted to $K - L \sim 1.3$ mag. In general, the IRE frequency increases with $K - L$. There are 646 objects with $K - L > 1.5$ mag and detections at H . Within the range $1.5 \text{ mag} < K - L \leq 2.0 \text{ mag}$ there are 423 sources of which 77% lie within the IRE region. Among 211 sources with $2.0 \text{ mag} < K - L \leq 4.0 \text{ mag}$ the excess fraction is even 89%. All (13) objects with $K - L > 4 \text{ mag}$ have IRE. Thus it seems that large IREs are responsible for the red colors. The statistics for these red sources are summarized in Table 4.5.

Table 4.5: Statistics of extremely red sources

Color [mag]	H II region ($N = 88/638$)			Cloud B ($N = 70/9$)		
	normal	IRE	X-ray	normal	IRE	X-ray
$H - K > 2.4$	59 (37%)	28 (18%)	3 (2%)	63 (40%)	5 (3%)	3 (2%)
$1.5 \leq K - L < 2.0$	103 (24%)	314 (74%)	39 (9%)	0 (0%)	2 (0.5%)	1 (0.2%)
$2.0 \leq K - L < 4.0$	60 (28%)	143 (68%)	11 (5%)	2 (1%)	2 (1%)	4 (2%)
$K - L \geq 4.0$	0 (0%)	12 (92%)	1 (8%)	0 (0%)	1 (8%)	1 (8%)

To put this extremely red population of M17 in context, it is noteworthy to compare it with other young clusters. In the Taurus population of YSOs, sources with $K - L > 0.4$ mag were classified to have *substantial* IRE; objects with $K - L = 1.5$ mag were even regarded as *protostellar* in nature (Kenyon & Hartmann 1995). In NGC 2024 a broad peak, centered around $K - L \simeq 0.8 - 1.0$ mag appeared in the color distribution, with only a small fraction of the sources having $K - L \geq 2.0$ mag (Haisch et al. 2000). Four sources have $K - L \geq 4.0$ mag, including one source which was detected only at L . In analogy to Taurus, Haisch et al. suggested that 45 sources with $K - L \geq 1.5$ mag are Class I (i.e. protostellar) objects. In the

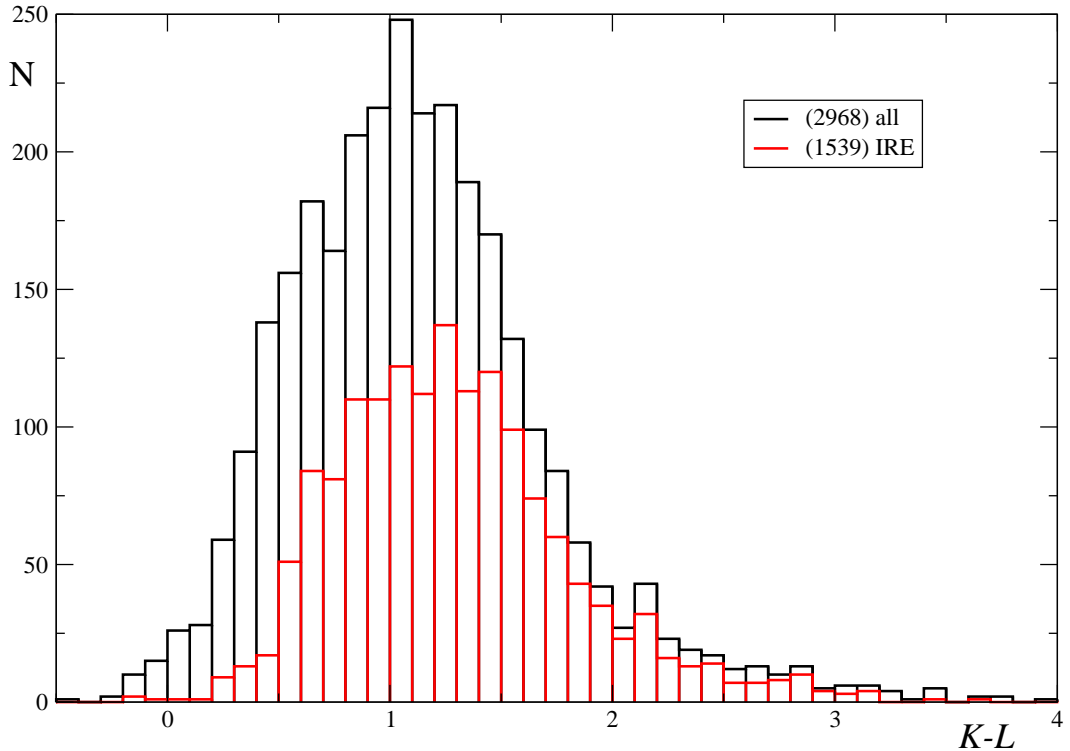


Figure 4.23: $K - L$ color distribution of extremely red objects. Thirteen sources with $4 \text{ mag} < K - L < 7 \text{ mag}$ are not included.

Trapezium cluster (Lada et al. 2000) the color distribution of 603 stars detected in K and L has a broad but prominent peak at $K - L \sim 0.9 \text{ mag}$, very similar to that in NGC 2024. Lada et al. attribute the shift of the peak to relatively large $K - L$ color primarily to IRE emission and to a lesser extent to reddening. It would require about 25 mag of visual extinction to produce a $K - L$ color of 1.0 mag in a naked, disk-less star, but examination of the Trapezium TCDs shows that the vast majority of stars in the cluster have extinctions well under $A_V = 10 \text{ mag}$. As a consequence, Lada et al. identify 78 candidate protostars from their list of sources with $K - L$ colors in excess of 1.5 mag. NGC 3603 contains only 117 IRE objects with $K - L$ generally below 2 mag (Stolte et al. 2004). Eventually in IC 348 there exist no source at all with $K - L > 1.5 \text{ mag}$ (Haisch et al. 2001a). As a consequence, the red population in M 17 is the largest one detected in a young cluster so far; simultaneously, it displays the reddest $K - L$ colors.

The spatial distribution of these extremely red sources is displayed in Fig. 4.22 b-d. The group $1.5 \text{ mag} < K - L \leq 2.0 \text{ mag}$ occurs predominantly in the central cluster and its northwestern extension; further sources are scattered in the northern and SW bar (Fig. 4.22 b). Sources with $2 \text{ mag} < K - L \leq 4 \text{ mag}$ show faint concentrations in the cluster center as well as along the northern bar and SW bar (Fig. 4.22 c). Most of the reddest sources ($K - L > 4 \text{ mag}$) are located in the Arc region and southwest of it (Fig. 4.22 d) – among them M 17-UC1 ($K - L \sim 6.6 \text{ mag}$) and the maser source associated with IRS 5 ($K - L \sim 4.2 \text{ mag}$). Another red source ($K - L \sim 5.2 \text{ mag}$) emerges at the tip of a large trunk in the northwest pointing toward CEN 1.

4.2.7 The KW Object

One of the most famous and simultaneously most puzzling infrared sources of the region was discovered by Kleinmann & Wright (1973) towards the molecular cloud M 17 SW. This strong 10 and 20 μm source with a color temperature of about 200 K was henceforth subject of several investigations and received numerous labels like M 17 IRS, M 17 SW, M 17 IRS1 or the Kleinmann-Wright object (KWO). It is located at RA = 18:20:19.4 and DEC = -16:13:30.0 (J2000); its position relative to the H II region can be inferred from Fig. 4.2.

Tokunaga & Thompson (1979) observed strong Br γ emission from the region, which – in the case of a compact H II region – requires a B0 ZAMS star for its excitation. The observed 1 – 20 μm luminosity of the KW object, however, was a factor of 10 too low. Therefore, they suggested that the Br γ line might be due to the ionization by a small cluster. In contrast, Dyck (1980) concluded from slit scans at 2.2 and 3.8 μm that there is no extended structure and claimed that the KW object is a compact source of less than 0".5 in diameter. Further Br γ studies (Simon et al. 1981) have been interpreted in terms of an optically thick outflow ($\dot{M} > 10^{-6} M_{\odot} \text{ yr}^{-1}$) with a blue-shifted velocity component relative to the ambient medium. The wind hypothesis was put forward by several other authors – among them Persson et al. (1984) ($2.2 \cdot 10^{-6} M_{\odot} \text{ yr}^{-1}$) and Hou et al. (1997) ($1.3 \cdot 10^{-6} M_{\odot} \text{ yr}^{-1}$) – and was supported by the upper limits of the radio emission at 1.3, 6 and 21 cm (Felli et al. 1984). Simon et al. (1983) found variability of the Br α emission and suggested that the region may contain at least an optically thin and an optically thick H II region where the latter is producing the IR line radiation. Eventually, Bunn et al. (1995) speculated that the IR recombination line profiles of the KW object resemble those of a deeply embedded Herbig Be star.

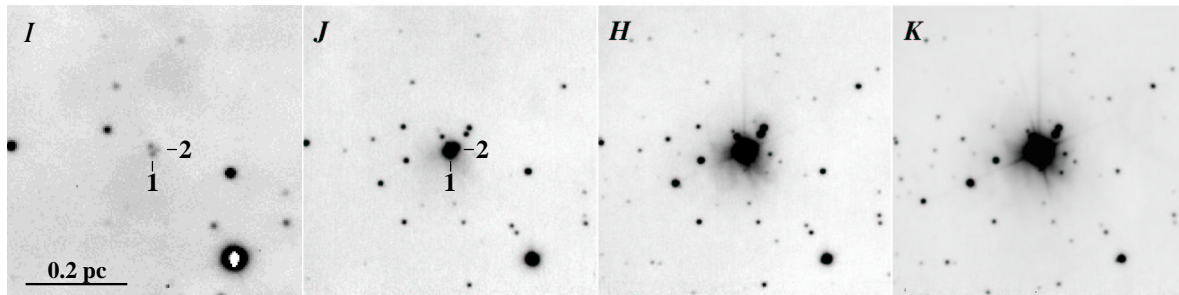


Figure 4.24: *IJHK* imaging of the KW object obtained with EMMI at the NTT and ISAAC at the VLT; the FOV is 55" \times 55".

In the present work the KW object could be resolved into a system of two early B-type stars with a projected separation of 2600 AU (see Fig. 4.24). While the more luminous component (No.1) shows a huge IRE due to circumstellar dust, the fainter one (No.2) displays X-ray emission. The system is deeply embedded ($A_V \sim 24$ mag) in the molecular cloud M 17 SW and associated with an IR reflection nebula. A radiative transfer model of the SED of the IRE object requires a stellar source of $5.1 \cdot 10^3 L_{\odot}$ – equivalent to a B0 star – surrounded by $10 M_{\odot}$ of circumstellar material. The KW object is associated with a small cluster of about 150 red stars. The stellar density within 0.1 pc is $> 2.4 \cdot 10^3 \text{ pc}^{-3}$. From all new evidence it is suggested that the KW object is one of the youngest, most deeply embedded Herbig Be stars known to date.

4.3 Sequential Star Formation?

Much has been speculated about sequential and triggered SF in the M17 region. Basically all arguments were based so far on the relative locations of the H II region and the adjacent Clouds A and B. Elmegreen & Lada (1977) have presented a scheme where subgroups of OB associations drive ionization-front shocks into molecular clouds to trigger the formation of new subgroups. As a consequence one should be able to observe an age gradient along the propagation of the star forming process with loose OB associations at the "old" end and YSOs or protostellar sources at the "young" end. Quantitatively there should be signpost of recent SF in the molecular cloud within 10 - 15 pc from the nearest OB stars. Elmegreen et al. (1979) have suggested that M17 SW is one of those clouds in which sequential SF is under way.

To test this proposition, Jaffe & Fazio (1982) used a FIR survey of the SW giant molecular cloud to investigate the OB SF mechanism in this area. Out of a total of 42 FIR sources they found 13 sources to be associated with the 20 km s^{-1} SW cloud complex. However, there is no evidence for an age gradient along the $\sim 160 \text{ pc}$ extent of M17 SW. The almost regular distribution of compact FIR sources and H_2O masers suggests that these signposts for recent SF are entirely unrelated to the nearby giant H II region and more likely a result of a global spiral shock.

Elmegreen et al. (1988) searched for NIR counterparts of 22 embedded *IRAS* sources and found 20 coincidences. From optical and infrared TCDs they concluded that 13 of them are most likely upper MS or PMS stars with extinctions $A_V \sim 7 \text{ mag}$. This study also yielded no indication for any age gradient along the cloud.

The *JHKL* survey of the present work has covered a small portion ($\sim 25 \text{ arcmin}^2$) of the molecular cloud southwest of M17-UC1. Among the 226 NIR sources detected in this area there are 56 (25%) IRE sources and 5 (2%) X-ray emitters (see Table 4.1). The relative abundances of these youth signatures are significantly below the values of the central cluster and support the idea that SF occurs in all parts of the cloud – independent of the influence by the H II region. However, as shown in Sect. 4.2.6 the youngest sources with largest IRE do not occur in M17 SW.

If there exists triggered SF in the M17 complex, then it occurs on much smaller scales, i.e. at the interface of the H II region with the molecular cloud. The prominent young high-mass objects M17-UC1, IRS 5 and the KW object as well as other sources like B273 or CEN 92 (Hoffmeister et al. 2006) represent a spatially distinct and more recent phase of SF in the Southern bar than the central OB cluster. This might be interpreted as locally triggered SF by the central O stars in the H II region.

4.4 Structure of the Complex

M17 has a complex morphology where neutral and ionized material are mixed along the line of sight. Moreover, HI, H II and molecular gas display various velocity components reflecting the highly dynamical state of the region. Finally, there are thousands of young stars at different evolutionary stages some of which are at the surface of the complex while others are embedded behind more than 40 mag of visual extinction. Therefore, many attempts were made to disentangle the structure of the complex in order to provide a three-dimensional picture of M17.

Combining the kinematic information with the apparent morphology several geometrical models of the M17 complex have been presented. Elliott et al. (1978) confirmed previous results of Goudis & Meaburn (1976) from the analysis of [O III] and [N II] line profiles and support a model proposed by Meaburn (1977), which interprets M17 as composed of a series of partial shells which are neutral on their outsides and ionized on their inside surfaces. In this model, the shells are assumed to be expanding due to the action of the stellar winds.

The most recent model comes from Pellegrini et al. (2007) who modeled an observed line of sight through the gas cloud, including the H⁺, PDR, and molecular layers, in a fully self-consistent single calculation. They concentrated on the SW bar where the PDR is very extended. Pellegrini et al. (2007) show that the observed strong magnetic field inevitably leads to a very deep PDR, because the structure of the neutral and molecular gas is dominated by magnetic pressure, rather than by gas pressure, as previously had been supposed. They also explain a wide variety of observed facts if a hydrostatic geometry prevails, in which the gas pressure from an inner X-ray hot bubble and the outward momentum of the stellar radiation field compress the gas and its associated magnetic field in the PDR. The pressure in the observed magnetic field balances the outward forces, suggesting that the observed geometry is a natural consequence of the formation of a star cluster within a molecular cloud.

All models have in common that they concentrate on the inner, brightest part of the H II region and describe it as a consequence of the formation of a star cluster at the eastern edge of a huge molecular cloud. The OB stars have formed a cavity in such a way that in the northern parts of the molecular cloud are located behind the ionized gas along the line of sight while in the SW parts of the molecular gas lie in front of the H II region. Cloud A (to the north) and B (to the southwest) are considered to be potential sites of new SF. In all models, the H II region is regarded to expand toward the east or southeast.

Fig. 4.25 shows the entire area at 1200 μm obtained with the bolometer array SIMBA at the SEST (data unpublished). It contains the free-free emission from the H II region as well as the dust emission from the associated molecular clouds. Complementary to this is the optical view in Fig. 4.1 which provides the following intuitive views. Firstly, the ionized ISM is much more extended than revealed by any of the radio and IR observations. Secondly, apart from a few small dark blobs, there are three prominent areas of high optical depths which must be located between the H II region and the observer:

- A relatively compact patch in front of the cluster center which obscures in particular the major ionizing source CEN 1 by $A_V \sim 10$ mag.
- A slightly smaller cloud to the southwest of the former which hides the radio maximum and the hyper compact H II region M17-UC1.
- A dark area north (Cloud A) and northwest of the H II region which are part of the huge molecular cloud complex.

The large-scale image of M17 (Fig. 4.1) shows the H II region extending nearly symmetrically out to several tens of parsecs from the central OB cluster. Ionized filaments are not only present in the east, but can be traced toward almost all directions – even to the northwest. There is heavy obscuration to the north and northwest of the brightest part of the nebula and a few extremely dense filaments can be seen in front of the H II region. In contrast, M17 SW (Cloud B) and the associated huge CO cloud (Elmegreen & Lada 1976) is not at all prominent

in Fig. 4.1; the SW molecular cloud - which is believed to lie between the ionized gas and the observer does not stick out as a particularly dark area. The $H\alpha$ emission within this area has a similar intensity like in many other outskirts of the nebula. It seems as if stellar photons may penetrate fairly far into Cloud B. This is in accordance with the finding of a clumpy medium in this region and with the moderate extinction of up to 7 mag (Sect. 4.3). Future studies will have to take into account the large-scale morphology of the area to obtain a complete understanding of M 17.

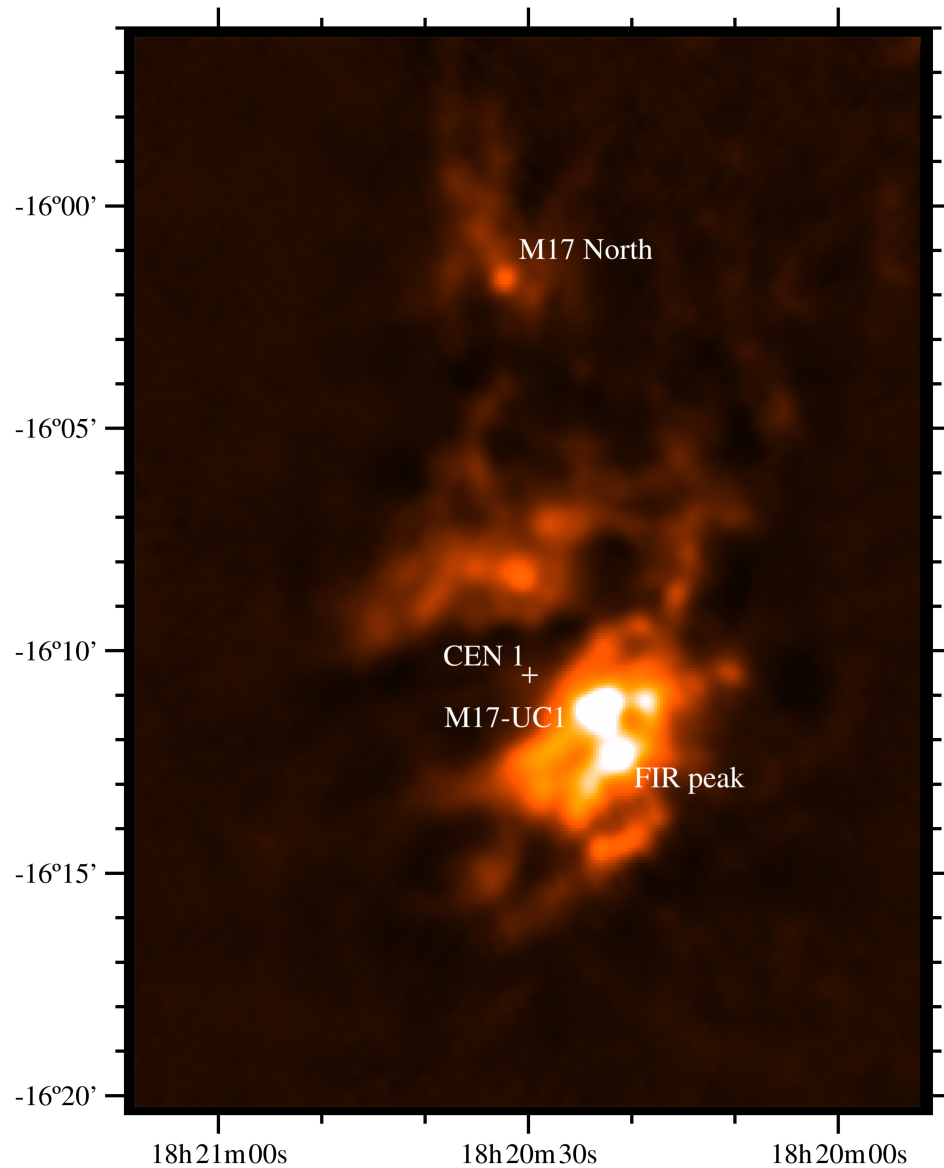


Figure 4.25: The M 17 region at $1200\ \mu\text{m}$ as seen by SIMBA (Chini, priv. comm.); the FOV is $15' \times 20'$, the spatial resolution is $22''$. Only few of the prominent sources are known, among them M 17-North (Henning et al. 1998), M 17-UC1 (Felli et al. 1984) and the FIR peak (Wilson et al. 1979). The cluster center is denoted by a cross at the position of the major exciting O4 binary, CEN 1.

Chapter 5

Summary and Perspectives

This last chapter will give a short summary of what has been achieved so far and what is still missing to complete the picture on the process of massive SF in M17.

5.1 Summary

The present investigation is by far the most extensive study concerning the stellar content of M17. It has improved previous results concerning the distance and the reddening law within M17 and has yielded a reliable estimate on the frequency of circumstellar disks. The improvements over previous investigations are due to i) a higher sensitivity at both optical and infrared wavelengths, ii) a higher spatial and spectral resolution and iii) a large number of extensively studied stars. The major findings are the following ones:

- The M17 cluster consists at least of 8000 young stars. Its distance is 2.1 ± 0.2 kpc, based on an unprecedented number of spectroscopically classified early-type stars. The normal foreground reddening towards M17 is $A_V \sim 2$ mag. Inside the H II region the law of interstellar extinction can be characterized by an R value of 3.9 ± 0.2 . Cluster members suffer from a large range of extinction ($2 < A_V < 50$ mag).
- The number of known, spectroscopically identified early-type stars could be increased by a factor of three, allowing for a more precise energy balance of the region. Simultaneously, for the first time numerous low-mass PMS stars have been detected.
- The presence of circumstellar cocoons and/or disks could be studied as a function of spectral type. It rises from 62% for stars earlier than A4 to $> 75\%$ for later types. The large number of young sources with CO band heads suggests that accretion is still going on. There is an extremely red population of (most likely protostellar) sources which exceeds those of other young clusters in both number and $K - L$ colors.
- Based on isochrone fitting and on arguments about the lifetimes of stellar disks M17 turns out to be one the youngest galactic clusters in the Galaxy with an age of around 500.000 years.
- Sequential star formation seems to occur at the interfaces of the H II region and the adjacent molecular clouds in the north and in the southwest. The youngest sources occur in the *Arc* region, a PDR in the southwest.

- Probably one of the major findings of the present work is the direct discovery of large circumstellar disk (10.000 - 20.000 AU) around several high-mass objects. These comprise various evolutionary stages like an accreting protostar, a hyper-compact H II region and a $26 M_{\odot}$ main sequence star and strongly suggest that the accretion scenario also work for stars above $10 M_{\odot}$.
- As a by-product of this wide-field study, one of the most puzzling IR sources – the Kleinmann-Wright object – was found to be a binary B-type system embedded in a small recently borne cluster located southwest of M17.

5.2 Perspectives

Despite these interesting new results, it is desirable to continue the present work in order to examine three aspects more thoroughly:

- Due to the large range of extinction, a statistically significant IMF could not yet be established. This requires more spectroscopic work in the future.
- There is evidence for a high binary fraction, particularly occurring with high-mass stars. Thus, a spectroscopic multiplicity study is highly desirable.
- The current work provides a rather static view of the star formation process in M17. Comparison with previous data in the literature indicates that variability may be a substantial process (as to expect from the theoretical point of view). Therefore, multi-epoch NIR imaging, as becoming feasible with new wide-field IR devices like HAWK-I at the VLT, seems to be the choice to study the cluster in the future.

Appendix A

Spectroscopic Results

In this chapter the spectroscopic results are presented. Spectra with a low signal to noise ratio have been omitted. Whenever available the following nomenclature has been used: CEN (Chini et al. 1980), IRS (Chini & Wargau 1998), B (Hanson et al. 1997), H (this work). In Table A.1 these results are summarized and complemented by additional information on the visual extinction, excess emission, and the occurrence of X-ray emission and CO band head features. Altogether, the spectral types of 294 stars could be determined. The stars have been ordered by right ascension; in case of equal right ascension the order was made by decreasing declination.

Table A.1: Spectroscopic results for all stars of the present investigation; as far as available visual extinction, IRE (\times), X-ray emission (*), CO emission (Δ), and CO absorption (∇) features are also indicated.

Identifier		RA	Dec	Magnitudes								Other Properties		
H	CEN	18:20:	-16:	<i>B</i>	<i>V</i>	<i>R</i>	<i>I</i>	<i>J</i>	<i>H</i>	<i>K</i>	<i>L</i>	SpT	A_V	IRE, CO, & X-ray
		10.30	13:46.1	16.60	15.61	14.85	13.95	12.34	11.17	10.15		A3	3.0	\times
		10.32	12:09.1	17.71	16.47	15.69	15.16	14.65	14.19	14.10		G2	1.9	
		10.93	08:49.8	17.70	16.59							G3	1.5	
		11.29	14:58.0	17.79	16.59							G3	1.7	
		11.44	06:54.0	21.51	19.62							M4	1.1	
		11.70	14:36.7	17.23	16.34							G3	0.8	
		11.72	08:34.2	21.90	19.74							M4	1.9	
		11.80	12:52.4	20.34	17.54							B2	11.4	*
		11.82	08:03.4	19.45	18.07							G5	2.2	
		12.05	05:38.7	16.31	15.42							F5	1.4	
		12.19	12:07.6	15.94	15.23	14.64	14.14	13.81	13.58	13.53		G2	0.3	
		12.30	06:27.5	15.54	14.65							F8	1.1	
		12.42	09:00.3	20.25	18.38							K0	3.6	
		12.69	11:04.4	19.36	17.99	17.03	16.43	15.72	15.20	15.08		G5	2.2	
		12.69	14:48.6	18.77	17.61							K0	1.1	
		13.35	11:42.3	19.93	18.24	17.13	16.22	15.48	14.75	14.49		K0	2.9	
		13.37	09:20.9	14.86	14.10							F5	1.0	
		13.43	07:59.0	15.65	14.86							F2	1.4	
		13.44	13:03.0	13.02	12.34	11.87	11.63	11.24	11.10	11.06		F3	0.9	
		13.47	07:20.0	16.75	15.61							G8	1.3	
		13.54	11:26.4	17.00	15.91	15.21	14.70	14.15	13.81	13.65		F5	2.0	
		13.82	11:58.7	15.26	14.37	13.87	13.47	13.01	12.69	12.60		G3	0.8	
		13.83	10:35.4	17.67	16.34	15.54	15.00	14.34	13.82	13.70		G5	2.0	

Table A.1 – continued

Identifier		RA Dec [2000]		Magnitudes								Other Properties		
H	CEN	18:20:	-16:	<i>B</i>	<i>V</i>	<i>R</i>	<i>I</i>	<i>J</i>	<i>H</i>	<i>K</i>	<i>L</i>	SpT	<i>A_v</i>	IRE, CO, & X-ray
00997		14.11	13:59.8	16.99	15.29							B1	7.1	
00999		14.12	05:54.7	16.34	15.28							G3	1.3	
01013		14.25	14:35.1	18.46	17.29							G5	1.5	
01028		14.32	06:19.8	15.67	14.68							G6	0.9	
01030		14.34	06:36.0	18.80	17.28							F3	3.9	
01057		14.53	06:51.1	17.03	16.03							G5	1.0	
01142		15.16	10:03.2	14.30	13.54	13.07	12.89	12.53	12.33	12.25		F2	1.3	
01140		15.16	13:51.0	18.68	17.36	16.54	15.93	15.33	14.82	14.60		G5	2.0	
01158		15.28	10:22.6	16.71	15.58	14.95	14.39	13.87	13.56	13.42		F3	2.4	*
01203		15.65	06:13.1	13.96	12.32							K4	1.8	
01213		15.74	08:03.7	18.23	17.07							K0	1.1	
01225		15.91	14:22.9	12.99	12.46							K0	-0.9	
01248		16.29	10:43.0	17.43	16.39	15.51	14.89	14.24	13.84	13.67		F7	1.7	
01255		16.32	07:05.1	18.57	17.26							G3	2.1	
01342		16.75	08:32.2	15.66	14.65	14.08	13.61	13.27	12.84	12.77		F9	1.4	
01369		16.92	12:16.0	20.34	18.63	17.35	16.23	15.80	14.98	14.79		K0	3.0	
01385		16.99	12:24.7	21.21	19.35	17.94	16.93	16.39	15.53	15.40		K0	3.6	
01395		17.03	10:44.6	14.70	13.91	13.36	12.99	12.47	12.23	12.19		G1	0.6	
01413		17.10	08:43.2	19.52	18.14	17.18	16.55	15.88	15.20	15.05		G5	2.2	
01423		17.12	07:35.8	16.77	15.75	15.16	14.70	14.41	13.87	13.79		G5	1.0	
01464		17.33	08:01.6	13.81	12.24	11.32	10.78	9.97	9.34	9.23		K6	1.0	
01485		17.39	10:19.3	13.42	13.04	12.83	12.79	12.45	12.43	12.40		A3	0.9	*
01497		17.43	10:47.0	18.32	17.28	16.45	15.84	15.12	14.67	14.57		G5	1.1	
01520		17.50	08:19.4	20.33	18.09	16.10	14.15	12.01	10.82	10.30		B2	9.2	
01530		17.53	11:11.2	19.12	17.51	16.42	15.43	14.52	13.90	13.69		K8	0.8	
01546		17.58	10:57.4	15.57				12.88	12.59	12.51		G5		
01564		17.63	09:25.4	14.44	13.85							A7	1.2	
01595		17.75	14:04.4	13.53	12.76							F7	0.9	*
01648		17.92	07:59.1	20.08	18.34	17.23	16.44	15.61	14.85	14.70		K0	3.1	
01754		18.18	09:51.8	17.49	16.45	15.88	15.27	14.67	14.28	14.14		G4	1.2	
01772		18.23	06:38.8	16.83	15.85							F9	1.3	
01780		18.27	10:34.1	19.65	18.05	17.13	16.25	15.34	14.76	14.60		K7	0.9	
01817		18.36	09:04.0	18.63	17.19	16.17	15.41	14.83	14.15	13.99		K4	1.2	
01825		18.38	10:49.8	18.46	17.23	16.40	15.73	15.08	14.69	14.56		G8	1.5	
01841		18.42	13:50.4	14.39				13.08	12.64	12.39		F2		
01892		18.53	07:47.6	18.07	16.94	16.12	15.58	15.06	14.56	14.46		K0	1.0	
01981		18.75	09:29.6	13.93	12.44	11.37	10.90	10.32	9.38	9.18		K5	1.1	
02049		18.92	06:18.7	18.02	16.94							G5	1.3	
02054		18.94	10:36.8	17.30	16.24	15.66	15.12	14.42	14.08	13.96		G5	1.2	
02103		19.04	06:35.4	19.65	18.23							K1	1.7	
02161		19.18	12:40.6	14.53	13.79	13.11	13.01	12.87	12.50	12.46	11.91	F7	0.8	×
02265		19.39	06:42.8	18.27	17.09							G3	1.7	
02263		19.40	10:44.9	21.56	19.79	18.54	17.49	16.41	15.83	15.60		M0	1.1	
02525		19.90	07:26.2	18.62	17.34	16.58	16.02	15.39	14.82	14.55		G3	2.0	
02550		19.98	11:52.3	19.88	18.28	17.12	16.38	15.99	15.21	15.03		K7	0.8	
02581		20.04	09:22.9	18.83	17.44	16.76	16.08	15.52	14.96	14.68		G5	2.3	
02863		20.57	12:27.3	20.68	18.98	17.83	16.91	16.48	15.71	15.55		K0	3.0	
02898		20.61	15:02.5	16.41	15.50							G2	0.9	
03032		20.87	11:59.4	20.30	18.61	17.49	16.78	16.41	15.68	15.51		K7	1.1	
03143		21.03	07:25.1	19.25	17.65	16.59	15.81	15.11	14.42	14.24		K0	2.6	
03300	93	21.30	10:40.8					12.63	10.80	9.44	8.03	B7		×, Δ
03325	17	21.33	11:40.4	15.51	14.35	13.70	13.23	12.66	12.29	12.05	12.18	G4	1.5	*

Table A.1 – continued

Identifier		RA	Dec	Magnitudes								Other Properties		
H	CEN	[2000]		B	V	R	I	J	H	K	L	SpT	A _V	IRE, CO, & X-ray
		18:20:	-16:											
03343	34	21.36	09:59.8		18.82	15.93	13.38	10.26	9.72		6.77	K5		▽
03385	35	21.43	09:39.3	19.36	17.09	15.18	13.42	11.53	10.65	10.13	9.87	O9.5	9.6	×, *
03508	92	21.64	11:18.0		20.14	17.19	14.33	11.06	9.63	8.84	8.28	B2		×, △
03827	13	22.19	10:21.2	13.17	12.36	11.75	11.58	10.97	10.75	10.72	10.75	B3	3.4	
03840		22.20	05:43.1	15.81	14.89							F8	1.3	
03889	69	22.32	10:39.0	18.91	17.51	16.45	15.71	14.90	14.42	14.24		K3	1.4	
03917		22.35	05:51.5	17.43	16.36							G5	1.2	
03957		22.45	09:45.9		21.63	18.93	16.04	13.31	12.10	11.39	10.89	B3		×
03970		22.47	15:15.2	21.10	19.32							K0	3.3	
03989	58	22.52	10:11.9	16.61	15.66	14.97	14.49	13.89	13.62	13.46	13.50	G1	1.1	
04108	16	22.70	08:34.3	14.76	13.18	11.87	10.92	9.74	9.21	8.98	8.56	O9	6.9	×, *
04199	75	22.84	08:15.0	20.21	18.11	16.28	14.75	13.08	12.20	11.84	11.29	B2	8.6	×
04252		22.91	05:39.5	17.47	16.27							F5	2.5	
04576		23.47	06:15.3	20.77	19.13							G3	3.4	
04666	94	23.63	10:35.5		20.23	17.88	15.44	12.90	11.77	11.21	10.89	A3		
04680	68	23.65	11:05.6	17.81	16.73	15.83	15.31	14.66	14.28	14.19		G5	1.3	
04779	22	23.85	09:59.2	15.36	14.45	13.79	13.44	12.83	12.55	12.45	12.56	F9	1.1	
04840	78	23.97	10:03.6		17.93	16.04	14.34	12.36	11.55	11.08	10.68	B3		
05071	31	24.37	08:43.6	17.18	15.53							O9.5	7.1	*
05121	32	24.47	09:54.9	17.65	16.45	15.66	14.94	14.30	11.72	10.20		G5	1.6	×, ▽
05198		24.60	11:39.5					13.16	10.57	9.21	8.31	O6		×, *
05332		24.83	11:35.2							13.07	6.48	B0		
05431		25.00	07:42.0	17.69	16.59	15.82	15.44	15.05	14.53	14.35	13.89	F8	1.8	×
05443	24	25.03	10:26.3	16.70	15.13	13.40	12.10	10.23	9.19	8.05	6.32	B8	6.0	×, △
05560	67	25.23	11:12.4	18.33	16.73	15.21	13.95	12.60	11.94	11.57	11.30	B4	6.5	
05564		25.24	12:12.9	17.33	16.03	15.04	14.54	14.33	13.59	13.42	13.03	K2	1.2	×
05593	49	25.29	10:18.7	18.27	16.58	15.01	13.48	11.60	10.41	9.47	8.08	B2	7.0	×
05616	36	25.32	09:39.6	20.02	17.69	15.81	14.03	12.07	11.11	10.47	10.20	O9.5	9.8	×, *
05689	57	25.45	11:15.6	17.95	15.77					9.40	9.11	F2	6.6	▽, *
05706		25.46	10:51.5	19.04	17.83	16.84	15.98	15.22	14.77	14.72		K0	1.3	
05729		25.48	14:23.3	18.95	17.72							G5	1.7	
05762		25.53	09:08.2	19.65	18.15	17.00	16.42	15.89	15.22	15.00		K0	2.2	
05806	95	25.59	08:59.0								6.59	K7		▽
05817	62	25.61	11:19.8	16.65	15.79	15.12	14.63	14.17	13.92	14.00		F7	1.1	*
05894	64	25.73	11:42.0	16.53	15.48	14.59	14.15	13.51	13.07	13.09	12.76	G6	1.1	×
05960	18	25.87	08:32.6	15.72	13.73	11.80	10.36	8.90			7.47	O6	8.5	*
06000	63	25.93	11:26.3	16.51	15.45	14.88	14.40	13.84	13.56	13.57		F8	1.7	
06014	14	25.95	10:52.9	14.56	13.77	13.16	12.82	12.35	12.15	12.14	12.35	F6	1.0	
06074	26	26.04	11:04.6	16.86	15.33	13.84	12.66	11.21	10.58	10.26	9.99	B3	6.3	*
06208	48	26.24	10:16.0	16.63	15.07	13.80	12.68	11.40	10.93	10.72	10.63	B3	6.3	
06345	50	26.45	10:13.5	17.91	16.26	14.73	13.43	11.88	11.29	11.02	10.78	B5	6.6	
06374		26.48	14:40.1	16.15	15.23							G3	0.9	
06401		26.53	12:32.1	20.02	18.06	16.57	15.13	13.33	12.32	11.92	11.49	G7	4.3	
06418		26.55	08:19.4	19.21	17.79	16.71	15.90	14.98	14.48	14.34		K0	1.9	
06416	52	26.56	10:22.9	18.46	16.69	15.12	13.89	12.29	11.68	11.38	11.14	B0	7.5	
06421	51	26.57	10:03.4	19.17	17.16	15.51	14.04	11.97	10.62	9.50	7.73	B3	8.1	×, △
06458	9	26.61	08:46.8	14.58	13.84	13.40	13.08	12.67	12.42	12.36	12.31	F6	0.9	
06476	74	26.64	08:23.0					13.11	12.06	11.57	10.99	A0		×, *
06507		26.70	11:18.5	21.01	19.02	16.96	16.24	14.42	13.61	13.17	12.63	A7	6.5	
06564		26.79	07:44.5	19.34	17.58	16.23	15.07	14.21	13.53	13.34	13.02	K0	3.2	
06577		26.80	07:49.5	20.63	18.25	16.16	14.16	12.17	11.16	10.66	10.00	B0	9.9	×, *
06640		26.89	05:37.1	17.45	16.24							G5	1.6	

Table A.1 – continued

Identifier		RA	Dec	Magnitudes									Other Properties		
H	CEN	[2000]		B	V	R	I	J	H	K	L	SpT	A _v	IRE, CO, & X-ray	
		18:20:	-16:												
06736		27.04	06:20.4	14.07	13.43							F2	0.9		
06916	23	27.35	10:24.9	14.81	14.04	13.42	13.05	12.45	12.23	12.18	12.09	B3	3.3		
06961		27.41	06:39.8	17.16	14.85							K5	4.0		
06980		27.42	10:13.9					15.67	14.07	13.56	12.99	B5			
06962		27.43	13:30.9	12.18	11.27			7.96	7.60	7.43		O6	4.3	*	
06997	41	27.48	10:13.6	19.18	17.28	15.60	14.10	12.30	11.45	11.08	10.74	B5	7.5	*	
07066		27.60	06:11.5	16.74	15.78							G0	1.2		
07181	46	27.76	11:01.9	19.52	17.11	15.06	13.31	11.17	10.36		7.95	O9	10.1	*	
07293	47	27.92	11:08.8	18.16	16.27	14.59	13.22	11.57	10.88	10.60	10.97	O9.5	8.1		
07322	66	27.95	11:42.9	18.85	17.56	16.70	16.04	15.24	14.74	14.61		G5	1.9		
07361	65	28.03	10:58.9	18.14	16.24	14.72	13.33	11.60	10.82	10.13	8.39	O9	8.1	×	
07462		28.13	07:37.8	19.99	18.19	16.59	15.24	13.73	12.97	12.62	12.12	B7	7.0	×	
07470	85	28.16	10:49.3	21.11	18.76	16.58	14.66	12.31	11.07	10.51	9.44	K0	5.5	×, *	
07526		28.23	07:09.4	16.52	15.46							G3	1.3		
07677		28.46	12:21.0	19.67	18.39	17.37	16.62	15.61	15.11	14.98		G5	1.9		
07687	21	28.47	09:05.1	16.33	15.11	14.17	13.53	12.88	12.39	12.27	12.31	F6	2.4		
07702		28.48	14:08.9	15.96	15.05							G5	0.7		
07815		28.67	12:11.8	17.81	16.06	14.33	12.88	10.92	10.18	9.80	9.15	B0.5	7.4	×, *	
07823	30	28.68	09:26.2	18.82	16.73	14.94	13.33	11.65	11.60	10.66	10.36	O9	8.9	×, *	
07885		28.76	06:34.7	20.23	18.37							K1	3.4		
07936		28.86	11:51.5					13.46	12.20	11.60	11.18	A1			
07946	84	28.88	10:42.2	21.69	18.72	16.47	14.58	12.31	11.23	10.79	10.49	G0	8.8	*	
07973	20	28.92	08:15.7	15.84	14.73	13.89	13.54	13.01	12.56	12.42	12.22	K3	0.5		
08092		29.09	07:11.0	18.10	16.40							M0	1.0		
08123	55	29.14	10:54.3	19.70	17.35	15.35	13.71	11.75	10.83	10.44	10.09	B0	9.8	∇, *	
08139	42	29.17	11:10.6	17.63	15.75	14.12	12.85	11.22	10.64	10.30	9.95	B2	7.8	*	
08262	59	29.36	10:55.9	19.47	17.03	15.01	13.19	11.18	10.37	10.00	9.78	B0	10.1		
08299		29.41	12:12.9	20.57	18.14	16.33	14.62	12.63	11.70	11.31	11.02	G0	6.7	*	
08322	96	29.44	09:39.5	21.24	18.79	16.62	14.53	12.15	11.08	10.59	10.19	B6	9.6		
08556	27	29.79	11:37.4	19.65	17.21	15.04	13.10	10.91	10.00	9.58	9.25	O9	10.2		
08575	1b	29.82	10:45.6	18.48	14.89	12.84	10.53	8.27	7.49	6.88	6.17	O4	14.8	*	
08635	1a	29.90	10:44.5	16.23	13.49	11.85	9.99	8.29	7.52	6.93	6.43	O4	11.5	*	
08767		30.10	08:41.9					14.29	13.16	12.59	12.04	B5			
08854	61	30.23	10:35.1	19.38	16.88				9.45		8.77	O9	10.5	*	
08901		30.29	07:10.5	15.99	15.03							G3	1.0		
08987	53	30.43	10:34.7	18.27	16.82	15.74	15.00	14.61	13.97	13.89		K3	1.5		
09000	37	30.44	10:53.1		19.34	16.11	13.10	9.82			7.22	O6		*	
09085		30.54	07:07.9	19.21	18.02							G3	1.7		
09296	25	30.83	10:07.7	16.87	14.88	13.15	11.67	9.79			8.42	O7	8.5	*	
09396		31.00	12:58.9	18.64	17.50	16.64	15.92	15.04	14.63	14.54	14.35	G1	1.7		
09440		31.06	06:57.7	15.62	14.31							K0	1.5	*	
09449		31.08	07:54.7	18.80				14.03	13.31	13.15	12.89	G9			
09454	6	31.09	09:22.0	12.80	12.50	12.10	11.98	11.77	11.68	11.59	11.60	B8	1.3		
09521		31.19	07:53.7	17.57	16.51	15.68	15.25	14.69	14.28	14.20	14.33	G3	1.3		
09585		31.29	07:36.7	20.77	19.09	17.98	16.65	15.68	15.02	14.81		G5	3.4		
09606		31.33	06:03.8	17.57	16.09							G9	2.3		
09757	38	31.57	08:58.7	17.53	16.32	15.44	14.81	14.22	13.71	13.61	13.66	K1	1.1		
09834	99	31.69	09:46.0		19.37	17.06	15.17	13.17	11.98	11.62	11.27	G3		*	
09927		31.80	05:54.3	19.40	18.04							K0	1.7		
09919	54	31.81	09:57.4	18.15	17.12	16.25	15.59	14.87	14.42	14.42	14.34	G8	0.9		
09947	28	31.84	11:38.4	16.67	15.38	14.04	13.15	11.90	11.41	11.21	10.35	B2	5.5	×, *	
09981		31.87	14:16.6	18.38	17.07							K3	1.1		

Table A.1 – continued

Identifier		RA	Dec	Magnitudes									Other Properties		
H	CEN	[2000]		B	V	R	I	J	H	K	L	SpT	A _V	IRE, CO, & X-ray	
		18:20:	-16:												
10273	19	32.31	09:05.6	15.20	14.51	13.92	13.58	13.24	12.97	12.90	12.86	F3	1.0		
10416	79	32.51	10:07.8	22.09	19.44	17.31	15.24	13.11	12.08	11.68	11.36	A0	9.9		
10613		32.79	07:38.5	15.32	14.61	13.98	13.59	13.34	12.97	12.89	12.74	G5	0.1		
10661		32.86	07:26.8	17.12	16.14	15.22	14.70	14.36	13.85	13.69		F3	1.9		
10659		32.87	12:39.6	12.58	12.13	11.56	11.52	10.96	10.85	10.79	10.85	B3	2.1	*	
10684		32.91	11:21.4	19.13	17.58	16.35	15.51	14.54	13.76	13.77	13.63	G5	2.9		
10757		32.99	07:21.1	15.20	14.41							F5	1.1		
10805	43	33.06	11:21.7	20.23	17.83	15.46	13.15	10.18			7.25	O5	10.1	*	
10809	29	33.07	10:13.6	19.54	17.29	15.31	13.55	11.47	10.62		10.07	O9	9.5		
10819		33.08	09:21.8					14.86	13.71	13.21	12.73	M4		*	
10907		33.21	06:05.0	17.45	16.51							G5	0.8		
10906	71	33.22	11:03.1	18.01	16.89	15.93	15.41	14.74	14.28	14.28		G9	1.1		
10918		33.24	12:19.3	18.95	17.72	16.97	16.09	15.26	14.69	14.56	14.57	K0	1.3		
10971		33.30	07:40.5	18.88	17.27	16.08	15.48	14.88	14.16	13.97		K4	1.7		
11082		33.44	15:01.4	13.76	13.26							F2	0.5		
11275		33.69	15:01.1	17.50	16.26							K0	1.3		
11314		33.76	13:05.0		20.78	18.04	15.46	12.81	11.48	10.83	10.46	G2		*	
11508		34.00	12:08.7	20.25	18.08	16.44	15.06	13.46	12.41	12.06	11.91	K0	4.8	*	
11540		34.04	07:33.8	20.98	19.28	18.38	16.87	16.06	15.26	14.97		K5	1.7		
11809		34.41	12:08.8	18.63	17.43	16.38	15.66	15.18	14.44	14.24		K3	0.7		
11854		34.44	06:13.8	15.94	15.03							G5	0.7		
11878	2	34.51	10:11.9	12.04	11.22						7.35	O5	4.0	*	
12098		34.73	06:57.5	20.35	18.79							K0	2.4		
12108	4	34.75	09:41.8	14.08	13.08	12.43	12.15	11.90	11.40	11.17	11.22	G0	1.3		
12225	5	34.89	08:35.4	13.71	12.41	11.32	13.04	10.20	9.56	9.50	9.39	G6	1.9		
12364		35.06	12:48.2	20.36	18.78	17.31	16.81	16.18	15.49	15.25		K0	2.5		
12556		35.25	08:42.7		19.54	17.63	15.24	13.43	12.43	12.01	11.72	B3		*	
12560		35.25	09:17.0		19.30	16.49	13.99	11.42	9.96	9.87	8.86	G0		×	
12649		35.33	14:12.5	15.99	14.93							K3	0.3	*	
12650		35.35	10:25.4					12.35	10.34		8.90	K3			
12704	3	35.40	10:48.0	10.71	9.92	8.99	8.16	8.32	7.89	7.71	7.58	O9	3.8	×, *	
12717		35.40	13:53.3	17.51	16.01							K3	1.7		
12764		35.46	11:30.6	20.70	18.41	16.72	15.02	13.70	12.61	12.16	11.96	K0	5.3	*	
12915	45	35.63	10:55.5	13.71	12.87	12.12	11.68	11.19	10.83	10.69	10.78	B2	3.7	*	
12984		35.70	14:53.1	20.47	18.75							K0	3.0		
13077		35.78	15:02.6	14.82	14.15							A7	1.4		
13125		35.85	13:47.5	13.49	12.06							K0	1.9		
13418		36.17	11:46.2	17.38	16.36	15.66	14.88	14.67	14.14	14.00	13.89	G3	1.2		
13502		36.24	08:16.4	19.32	17.51	16.24	15.06	13.92	13.21	13.03	12.79	M2	1.0		
13516		36.27	10:55.0	15.16	14.31	13.38	12.86	12.17	11.67	11.46	11.42	B4	3.5	*	
13528		36.29	11:34.0					16.12	15.31	14.98	14.79	K0			
13688		36.45	08:20.0	18.47	17.05	16.05	15.47	14.84	14.20	14.10	13.67	K0	1.9	×	
13732		36.50	10:13.4		20.98	18.46	16.66	14.76	13.46	12.86	11.67	M4		×	
13823		36.60	11:56.6	19.56	18.06	16.95	16.33	15.69	15.03	14.78		G5	2.7		
13924		36.66	13:33.0	17.06	15.91							F7	2.0		
13968		36.72	07:52.1	18.21	16.96	16.04	15.52	14.88	14.31	14.20		K0	1.4	*	
14253		36.98	06:41.9	15.40	14.73							A9	1.2		
14402		37.15	10:56.6	16.06	15.31	14.70	14.25	13.95	13.56	13.46	13.52	F3	1.1		
14512		37.24	06:56.2	20.48	18.91							K3	1.9		
14618		37.36	06:32.0	18.22	17.01							K1	1.1		
14686		37.44	09:50.9	18.73	17.05	15.65	14.24	12.80	12.00	11.61	11.34	B7	6.6		
14767		37.52	09:41.6					13.61	11.75	10.94	10.47	K3			

Table A.1 – continued

Identifier		RA Dec [2000]		Magnitudes								Other Properties		
H	CEN	18:20:	-16:	<i>B</i>	<i>V</i>	<i>R</i>	<i>I</i>	<i>J</i>	<i>H</i>	<i>K</i>	<i>L</i>	SpT	<i>A_v</i>	IRE, CO, & X-ray
14763		37.52	12:16.5	15.60	14.58	13.59	12.83	12.20	11.82	11.60		B4	4.2	
14996		37.79	10:60.0	21.14	18.74	17.11	15.30	13.86	12.77	12.42	12.10	M4	2.8	*
15120		37.89	07:32.6	17.90	16.32	14.53	13.07	11.47	10.55	10.18	9.73	B0	6.8	
15259		38.06	11:04.9	19.75	18.15	16.77	15.94	15.27	14.48	14.27	13.91	K0	2.6	×
15434		38.20	05:37.0	17.81	16.46							K0	1.7	
15441		38.23	10:08.5	16.56	15.47	14.62	13.73	13.03	12.54	12.33	12.09	B4	4.5	
15593		38.39	06:28.4	18.14	17.04							G5	1.3	
15720		38.54	08:55.6	19.92	18.26	16.66	15.50	13.98	13.24	12.86	12.63	B6	6.5	
16319		39.20	13:30.6	18.12	17.01							G3	1.4	
16376		39.28	10:28.8	18.68	17.49	16.73	15.90	15.41	14.76	14.47	14.46	G2	1.8	
16379		39.29	11:27.7					15.70	14.94	14.61	14.02	M4		×, *
16514		39.45	09:36.2	16.23	15.27	14.67	14.16	13.98	13.43	13.30	13.24	F8	1.4	
16699		39.62	06:33.5	20.40	18.80							G5	3.1	
16760		39.71	13:12.9		21.72	18.68	15.57	13.32	11.89	11.16		G2		*
16770		39.72	12:54.3	20.18	18.70	17.22	16.75	16.05	15.38	15.06		G5	2.6	
16807		39.77	11:15.2	16.76	15.83	14.99	14.29	13.94	13.34	13.21	12.99	G7	0.7	
17035		40.03	11:32.1	16.49	15.44	14.67	14.13	13.78	13.24	13.06	12.88	F8	1.7	
17049		40.04	08:59.7	16.30	14.96	14.03	13.44	12.87	12.28	12.15	12.17	K3	1.2	
17274		40.30	10:05.7	14.33	13.55	12.99	12.60	12.36	11.97	11.89	11.85	F6	1.0	
17304		40.33	09:40.6	16.25	15.40	14.67	14.12	13.98	13.42	13.31	13.29	F8	1.0	
17728		40.78	10:12.1	15.30	14.07	13.08	12.38	11.71	11.26	11.08	10.95	B5	5.0	
17845		40.92	10:30.9	20.00	18.36	17.24	16.39	15.65	14.88	14.66	14.62	G5	3.3	
18172		41.27	10:14.1	17.50	16.37	15.58	15.02	14.61	14.05	13.92		F7	2.0	
18265		41.38	12:46.9	21.22	19.53							K3	2.3	
18382		41.54	14:59.4	20.08	17.89							A1	8.0	
18493		41.71	10:59.4	16.09	15.22	14.47	13.81	13.57	13.09	12.96		G5	0.6	
18528		41.75	06:50.5	19.76	18.32							K3	1.5	
18534		41.76	14:30.7	20.27	18.70							G5	2.9	
18570		41.83	11:06.7					12.87	10.98	10.21		K2		
18759		42.08	05:48.5	12.09	12.01							A9	-0.6	
18770		42.11	08:08.6	17.91	16.73	15.88	15.25	14.83	14.28	14.13		G2	1.7	
18795		42.14	08:03.1	18.71	17.55	16.70	15.87	15.21	14.56	14.41		G2	1.6	
18929		42.34	13:04.4	18.56	17.29							K5	0.4	
18977		42.41	07:37.6	20.94	19.28	18.39	17.07	16.47	15.70	15.37		K0	2.8	
19056		42.52	12:15.7	17.58	16.51							G2	1.4	
19174		42.69	14:48.3	16.09	15.28							F9	0.8	
19187		42.71	12:35.5	15.75	14.80							K0	0.4	
19189		42.71	14:52.2	15.48	13.89							K1	2.3	
19196		42.74	07:22.1	16.69	15.73	14.96	14.51	14.39	13.72	13.43		G1	1.1	
19224		42.78	10:45.2	16.97	16.01	15.13	14.59	14.24	13.65	13.48		G3	1.0	
19539		43.25	10:44.4	19.93	18.40							K0	2.3	
19563		43.36	11:22.8	18.86	17.46							A1	4.9	
19562		43.36	12:46.5	20.00	17.53							M4	3.1	*
19566		43.40	06:29.6	16.94	16.03							G5	0.7	
19567		43.43	07:41.2	19.30	17.92							K0	1.8	
19576		43.48	10:17.5	18.59	17.54							G2	1.3	
19579		43.50	13:02.0	18.39	17.06							K2	1.3	
19598		43.76	11:46.8	15.79	14.87							G1	1.0	
19626		44.19	15:19.6	18.74	17.58							G5	1.5	
19632		44.25	06:01.9	16.56	15.59							G5	0.9	
19647		44.50	14:15.9	17.45	16.42							G3	1.2	
19693		45.20	08:18.6	15.63	14.61							K0	0.7	

Table A.1 – continued

Identifier		RA	Dec	Magnitudes								Other Properties		
H	CEN	[2000]		<i>B</i>	<i>V</i>	<i>R</i>	<i>I</i>	<i>J</i>	<i>H</i>	<i>K</i>	<i>L</i>	SpT	A_V	IRE, CO, & X-ray
		18:20:	-16:											
19695		45.22	07:02.0	17.35	16.15							G5	1.6	
19701		45.37	06:05.6		20.60							M4		
19713		45.56	06:56.5	17.78	16.69							G7	1.2	
19719		45.66	12:40.0	15.43	14.77							F4	0.8	
19727		45.92	08:50.6	15.22								F8		
19762		46.57	11:41.9	20.87	19.09							A8	5.5	
19778		46.80	12:09.5	14.81	14.22							A1	1.8	
19779		46.81	08:14.7	18.58	16.98							K4	1.7	
19801		47.20	10:12.5	18.99	17.45							A1	5.4	
19810		47.28	14:12.3	16.96	15.84							G3	1.5	
19813		47.33	08:26.1	19.45	18.05							K3	1.4	

A_V values have been calculated from $B - V$ and the intrinsic colors of main sequence stars (Schmidt-Kaler 1982). In case $E_{B-V} \leq 0.65$ mag (corresponding to a foreground extinction of $A_V = 2$ mag) only the normal reddening law, and if otherwise a combination of normal and abnormal reddening law was applied. Negative A_V values are caused by uncertainties in the spectral types.

A.1 Optical Spectroscopy

Optical spectroscopy obtained with EMMI at the NTT. The continuum is normalized to unity.

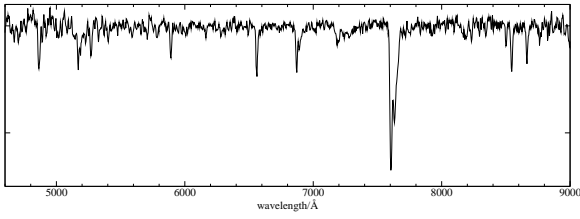


Fig. A.1: H 1342, **F9**

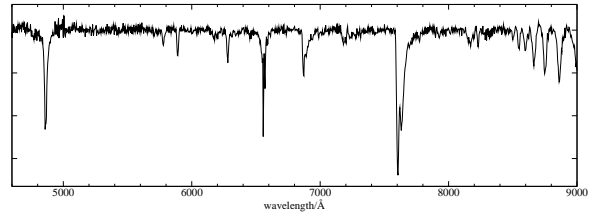


Fig. A.1 cont.: B 86 (H 13516), **B4**

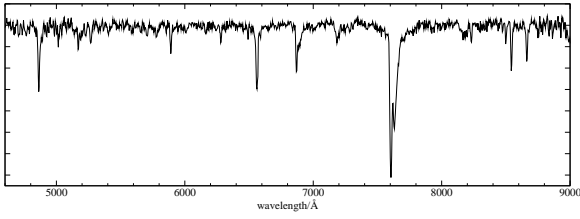


Fig. A.1 cont.: H 880, **F5**

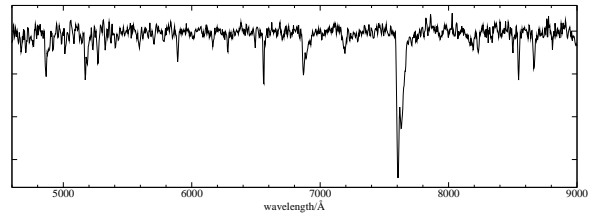


Fig. A.1 cont.: H 1546, **G5**

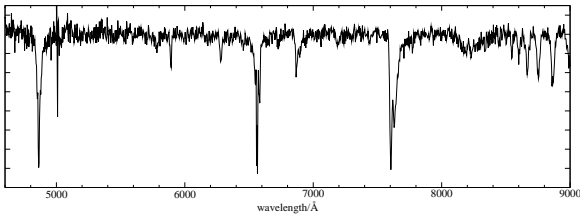


Fig. A.1 cont.: B 56 (H 15441), **B4**

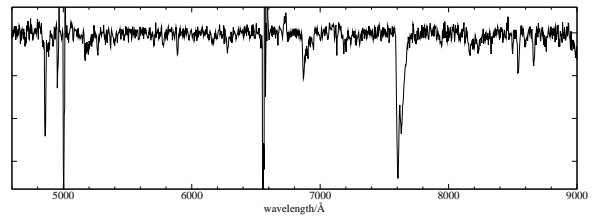


Fig. A.1 cont.: H 14402, **F3**

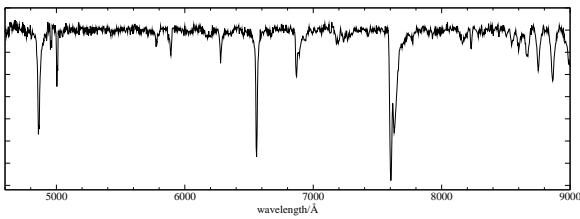


Fig. A.1 cont.: B 33 (H 17728), **B5**

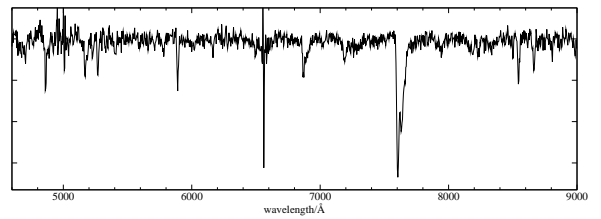


Fig. A.1 cont.: H 18493, **G5**

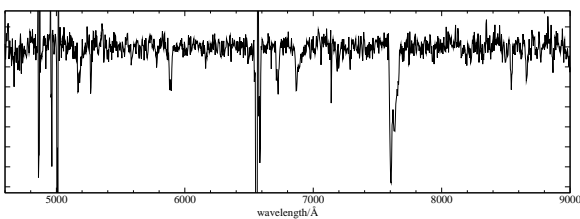


Fig. A.1 cont.: H 18172, **F7**

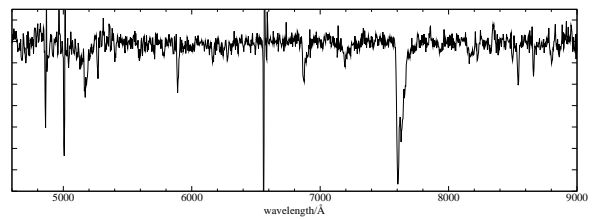


Fig. A.1 cont.: H 16807, **G7**

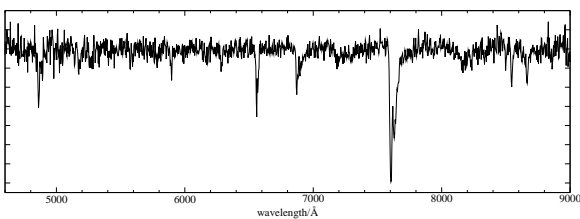


Fig. A.1 cont.: H 1248, **F7**

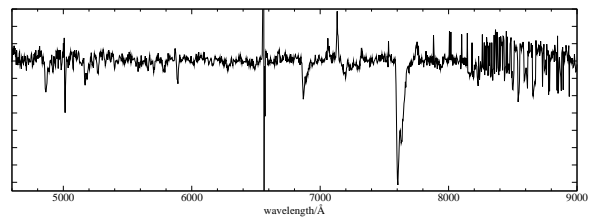


Fig. A.1 cont.: CEN 62 (H 5817), **F5**

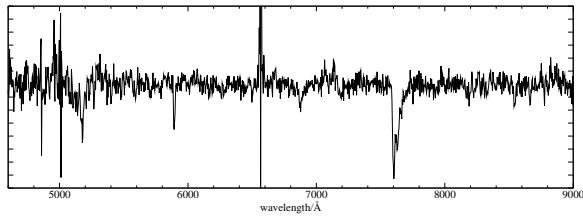


Fig. A.1 cont.: H 11809, **K4**

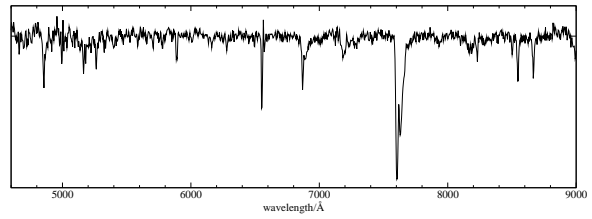


Fig. A.1 cont.: CEN 4 (B 109, H 12108), **G0**

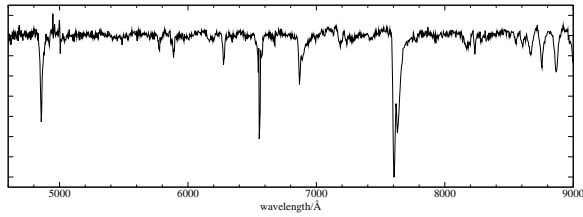


Fig. A.1 cont.: B 67 (H 14763), **B4**

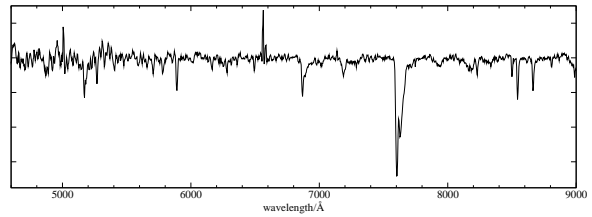


Fig. A.1 cont.: CEN 5 (B 107, H 12225), **G6**

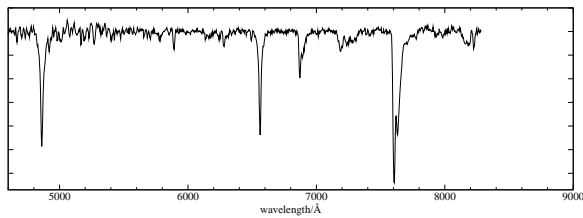


Fig. A.1 cont.: B 140 (H 10659)

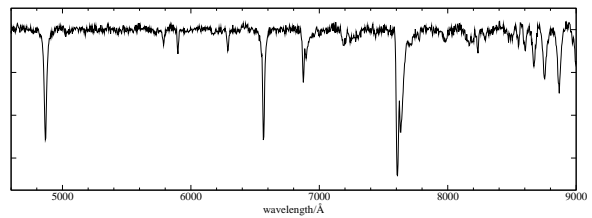


Fig. A.1 cont.: CEN 6 (H 9454), **B8**

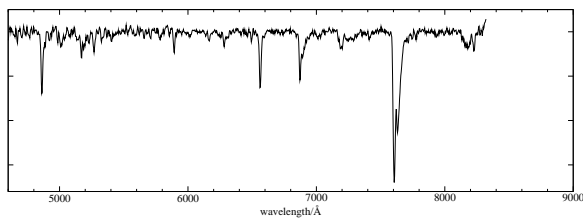


Fig. A.1 cont.: H 2161, **F7**

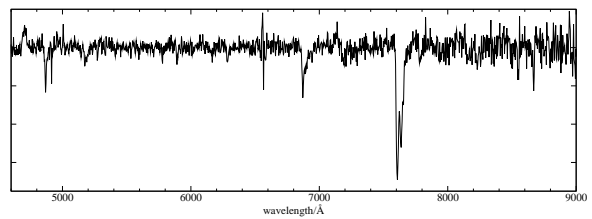


Fig. A.1 cont.: CEN 13 (B 319, H 3827), **B3**

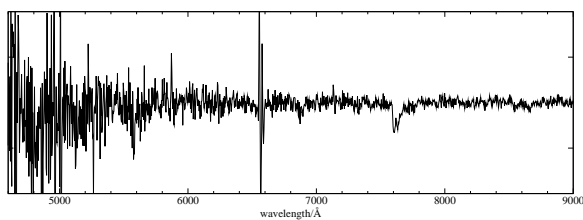


Fig. A.1 cont.: CEN 101 (B 206, H 7942)

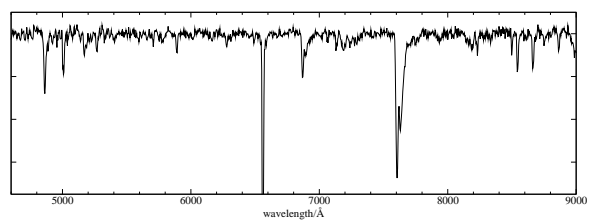


Fig. A.1 cont.: CEN 14 (H 6014), **F6**

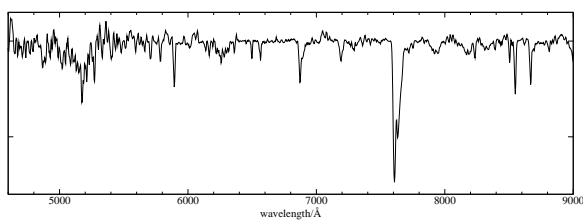


Fig. A.1 cont.: CEN 0 (B 232, H 7096)

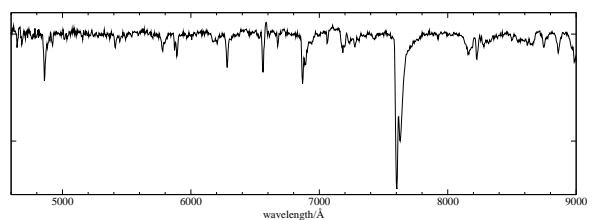


Fig. A.1 cont.: CEN 16 (B 311, H 4108), **O9**

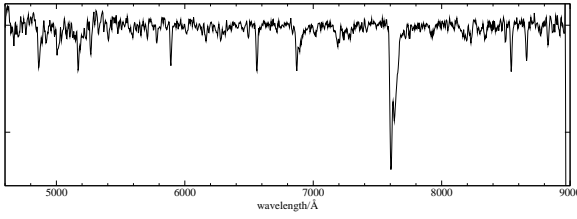


Fig. A.1 cont.: CEN 17 (B 336, H 3325), **G4**

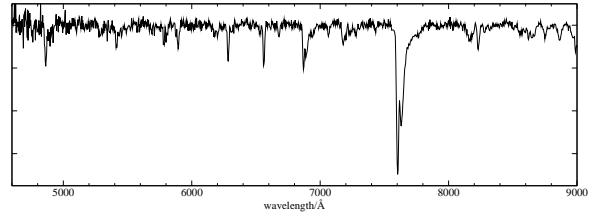


Fig. A.1 cont.: CEN 25 (B 164, H 9296), **O7**

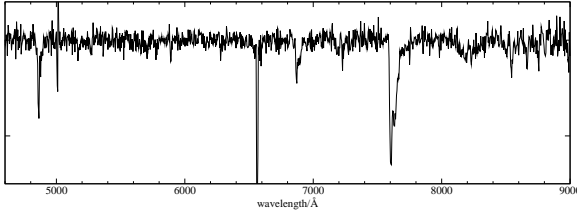


Fig. A.1 cont.: CEN 19 (H 10273), **F3**

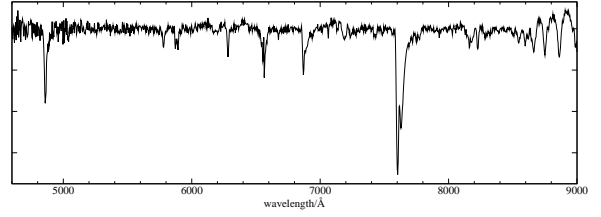


Fig. A.1 cont.: CEN 26 (B 253, H 6074), **B3**

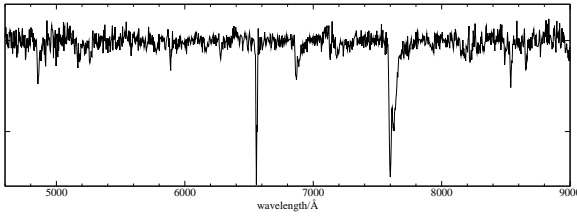


Fig. A.1 cont.: CEN 21 (B 216, H 7687), **F6**

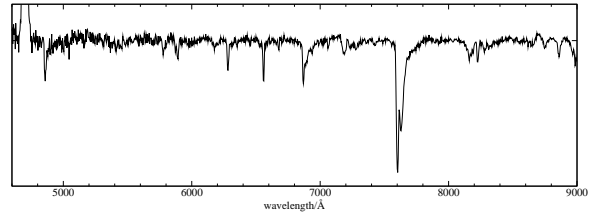


Fig. A.1 cont.: CEN 31 (B 289, H 5071), **O9.5**

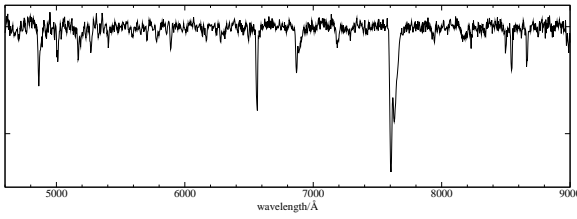


Fig. A.1 cont.: CEN 22 (H 4779), **F9**

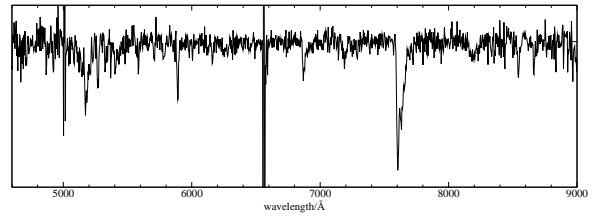


Fig. A.1 cont.: CEN 38 (H 9757), **K1**

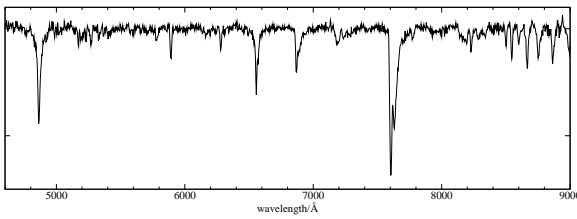


Fig. A.1 cont.: CEN 23 (H 6916)

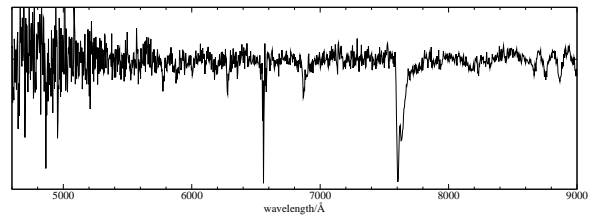


Fig. A.1 cont.: CEN 41 (B 234, H 6997), **B5**

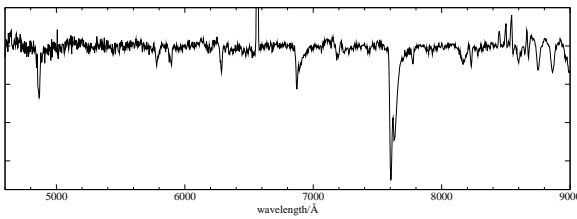


Fig. A.1 cont.: CEN 24 (B 275, H 5443), **B8**

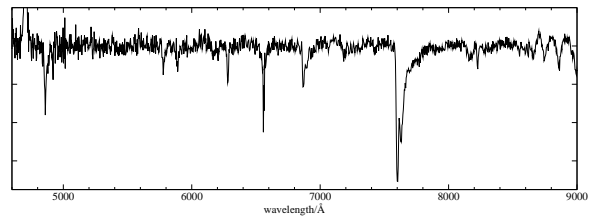


Fig. A.1 cont.: CEN 42 (B 205, H 8139), **B2**

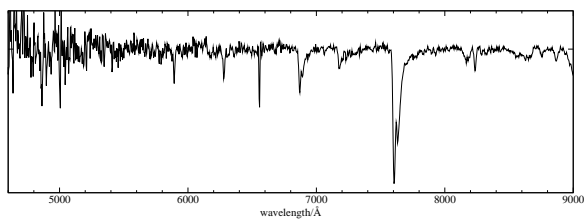


Fig. A.1 cont.: CEN 43 (B 137, H 10805), **O5**

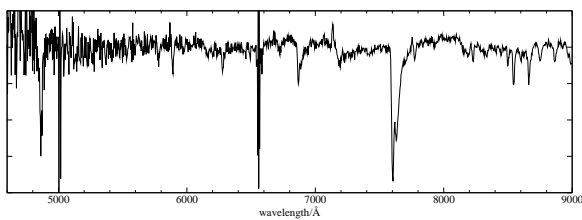


Fig. A.1 cont.: CEN 57 (B 269, H 5689), **F2**

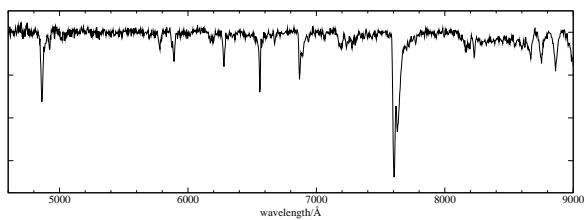


Fig. A.1 cont.: CEN 45 (B 93, H 12915), **B2**

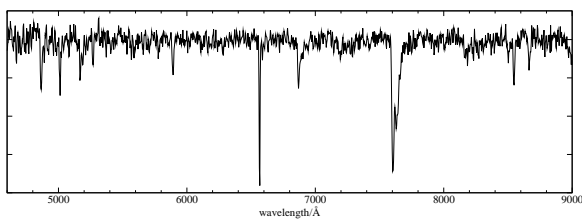


Fig. A.1 cont.: CEN 58 (H 3989), **G1**

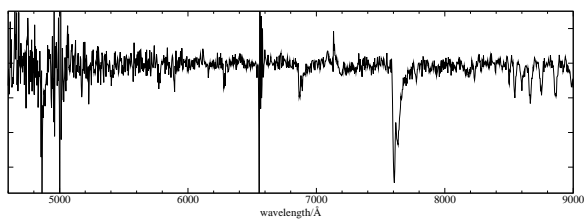


Fig. A.1 cont.: CEN 47 (B 227, H 7293)

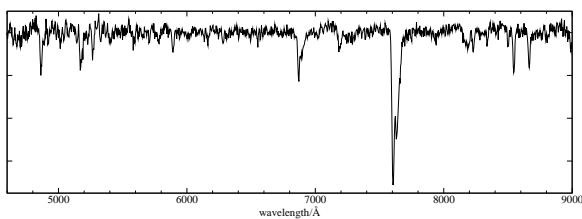


Fig. A.1 cont.: CEN 63 (H 6000), **F8**

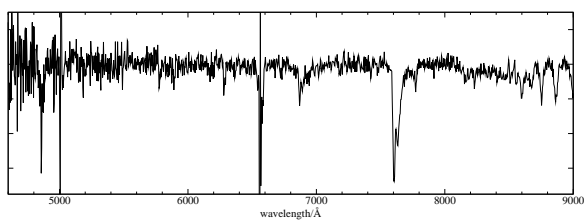


Fig. A.1 cont.: CEN 49 (B 268, H 5593), **B2**

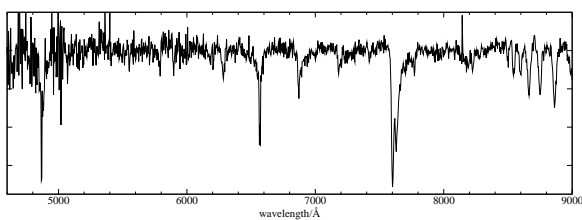


Fig. A.1 cont.: CEN 65 (B 226, H 7361)

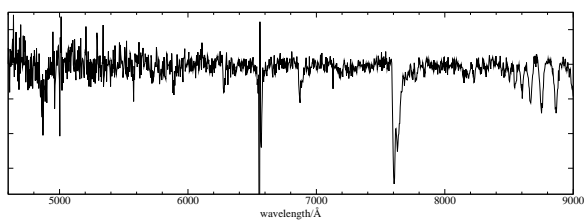


Fig. A.1 cont.: CEN 50 (H 6345), **B5**

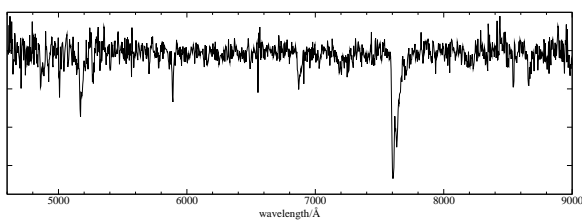


Fig. A.1 cont.: CEN 71 (H 10906), **G9**

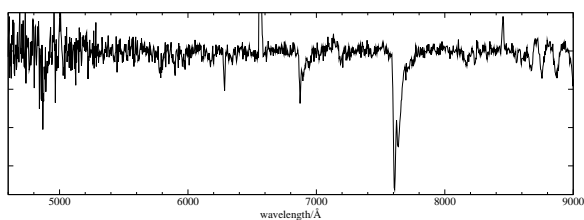


Fig. A.1 cont.: CEN 51 (B 243, H 6421), **B3**

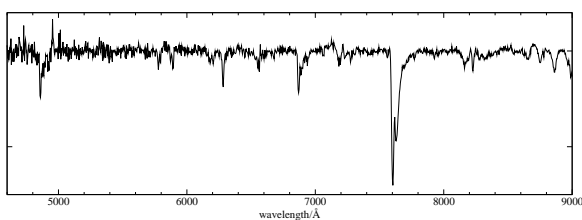


Fig. A.1 cont.: IRS 15 (B 215, H 7815), **B0.5**

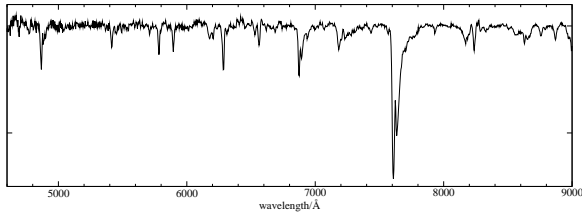


Fig. A.1 cont.: CEN 1 (B189, H 8575/8635),
O4

A.2 *J* Band Spectroscopy

J band spectroscopy of stellar sources obtained with ISAAC at the VLT. The continuum is normalized to unity.

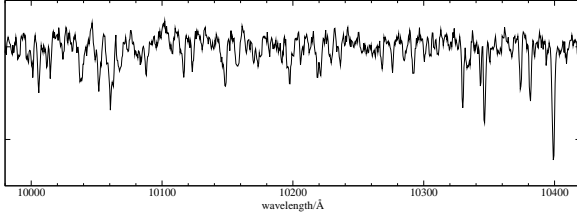


Fig. A.2: CEN 10 (B 320, H 3793)

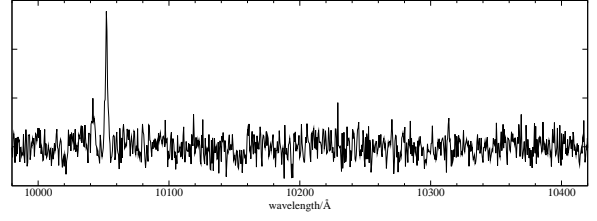


Fig. A.2 cont.: H 4534

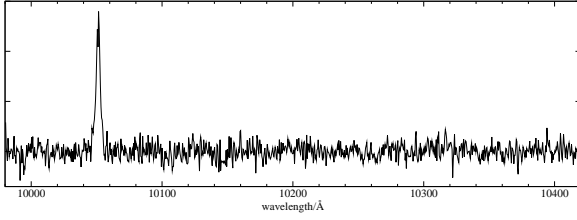


Fig. A.2 cont.: H 3276

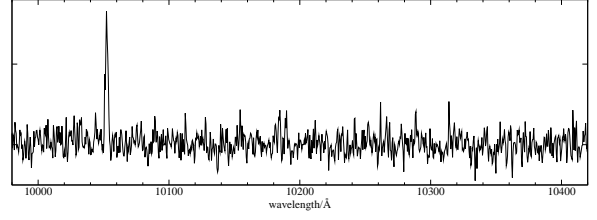


Fig. A.2 cont.: CEN 22 (H 4779)

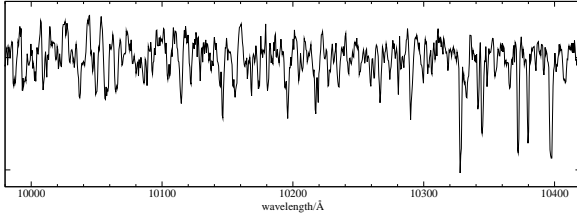


Fig. A.2 cont.: CEN 33 (B 324, H 3767)

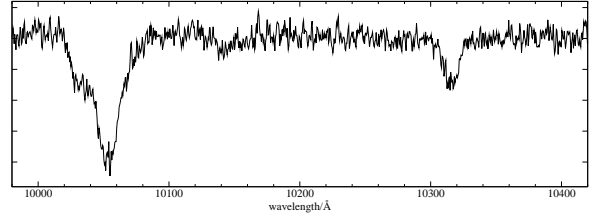


Fig. A.2 cont.: CEN 48 (B 248, H 6208), **O9.5**

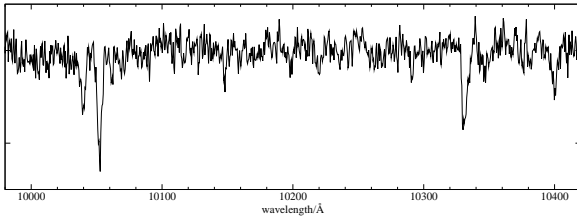


Fig. A.2 cont.: CEN 34 (B 358, H 3343)

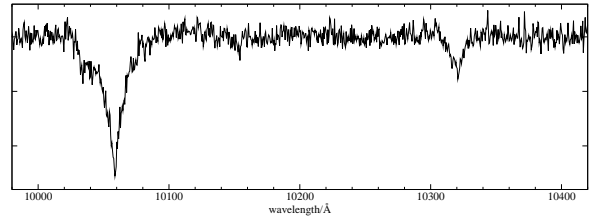


Fig. A.2 cont.: IRS 15 (B 215, H 7815), **B1**

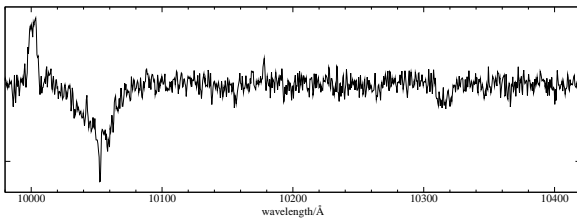


Fig. A.2 cont.: CEN 35 (B 333, H 3385), **B**

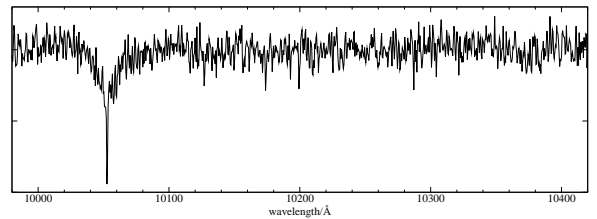


Fig. A.2 cont.: CEN 74 (B 245, H 6476)

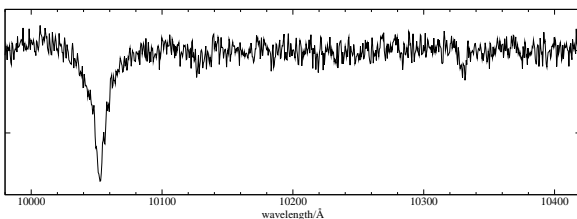


Fig. A.2 cont.: CEN 23 (H 6916), **B**

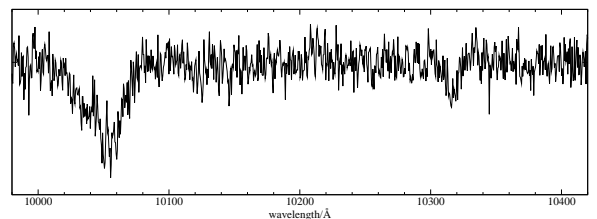


Fig. A.2 cont.: CEN 30 (B 213, H 7823), **B1**

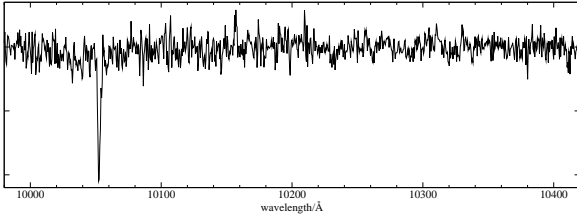


Fig. A.2 cont.: B 314 (H 3957)

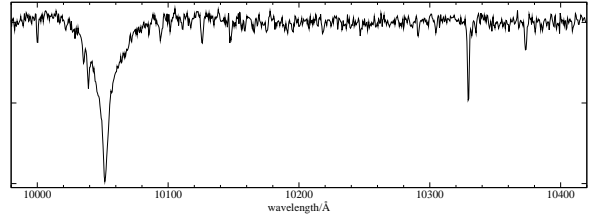


Fig. A.2 cont.: B 140 (H 10659), **B**

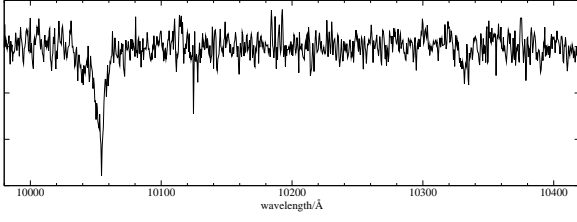


Fig. A.2 cont.: CEN 46 (H 7181), **late O**

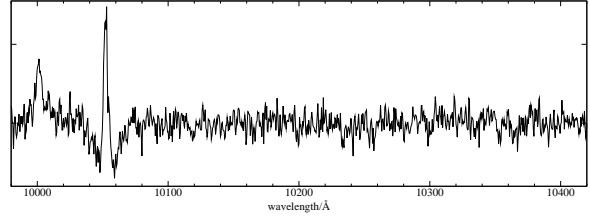


Fig. A.2 cont.: CEN 24 (B 275, H 5443)

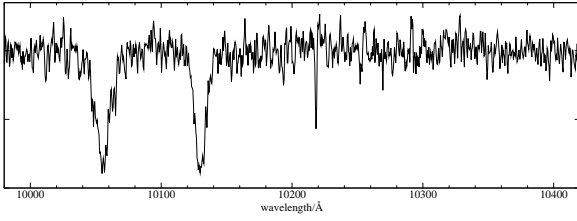


Fig. A.2 cont.: CEN 43 (B 137, H 10805), **O5**

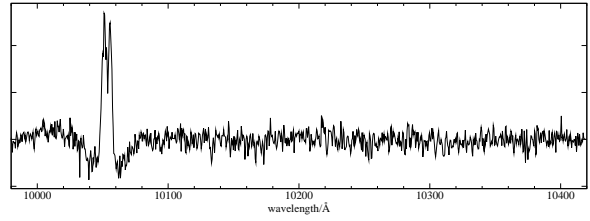


Fig. A.2 cont.: CEN 51 (B 243, H 6421), **B**

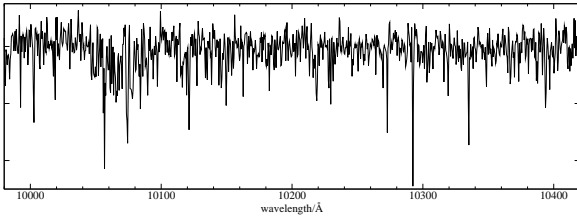


Fig. A.2 cont.: CEN 28 (B 150, H 9947)

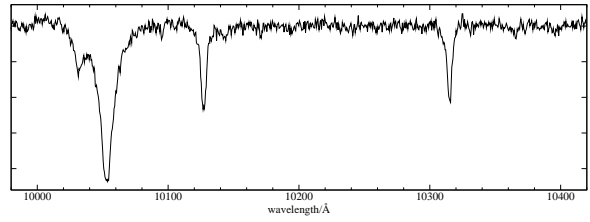


Fig. A.2 cont.: CEN 16 (B 311, H 4108), **O9.5**

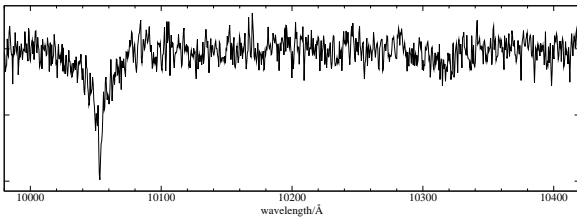


Fig. A.2 cont.: CEN 27 (B 197, H 8556), **B**

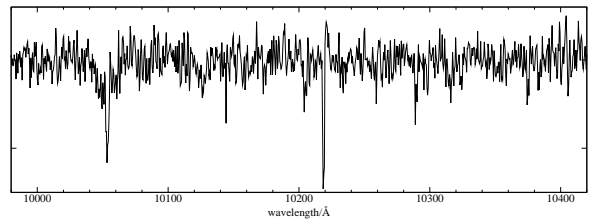


Fig. A.2 cont.: CEN 31 (B 289, H 5071), **O9.5**

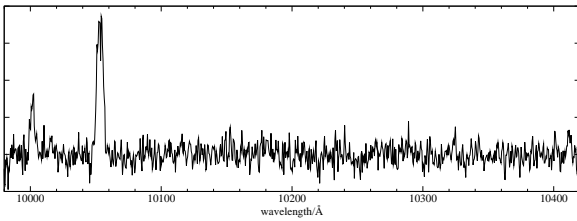


Fig. A.2 cont.: B 168 (H 9396)

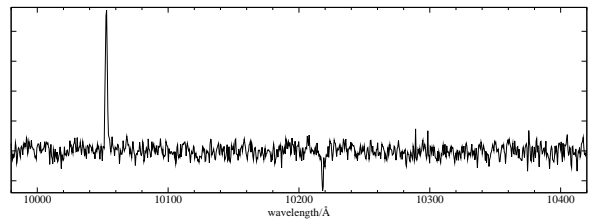


Fig. A.2 cont.: H 7206

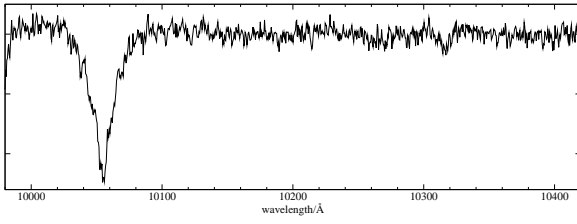


Fig. A.2 cont.: CEN 26 (B 253, H 6074), **B**

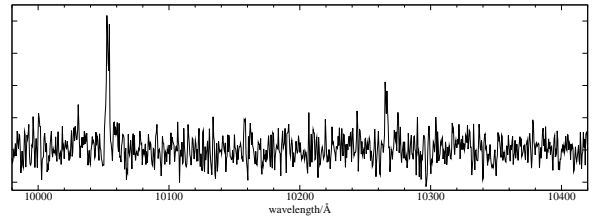


Fig. A.2 cont.: B 313 (H 3982)

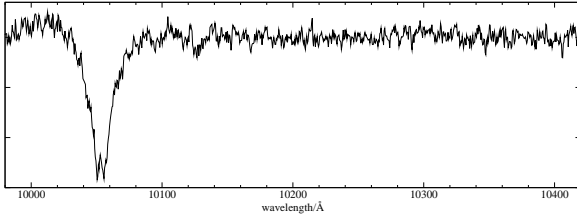


Fig. A.2 cont.: CEN 65 (B 226, H 7361), **O:**

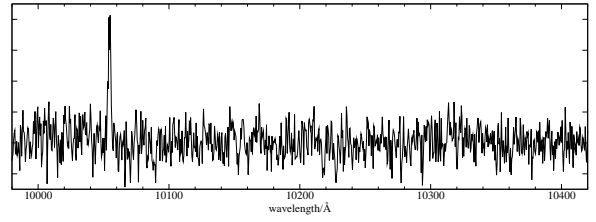


Fig. A.2 cont.: H 4262

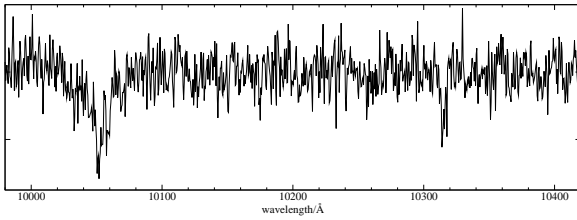


Fig. A.2 cont.: CEN 59 (B 203, H 8262), **B**

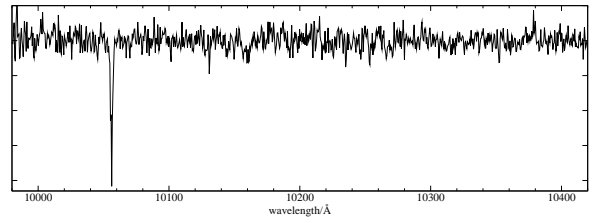


Fig. A.2 cont.: H 7062

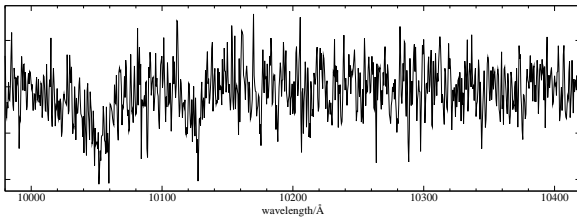


Fig. A.2 cont.: CEN 37 (IRS 21, H 9000), **O6**

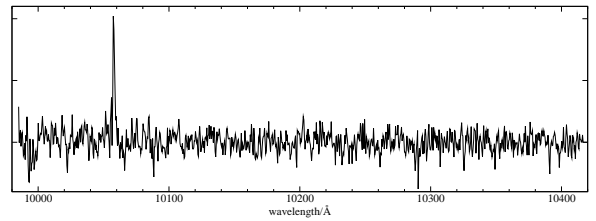


Fig. A.2 cont.: H 7554

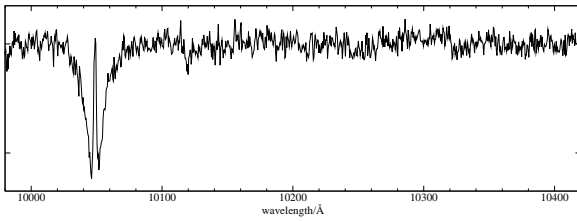


Fig. A.2 cont.: CEN 47 (B 227, H 7293), **B**

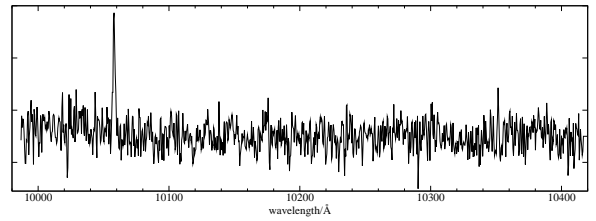


Fig. A.2 cont.: H 7995

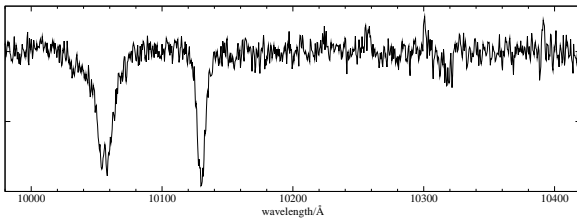


Fig. A.2 cont.: CEN 25 (B 164, H 9296), **O9**

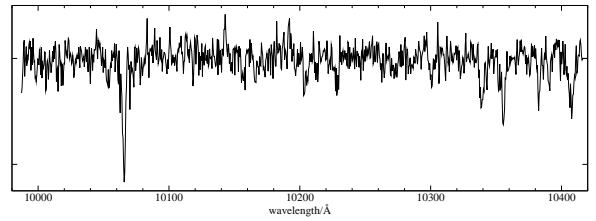


Fig. A.2 cont.: CEN 101 (B 206, H 7942)

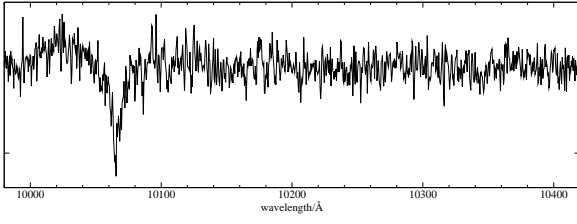


Fig. A.2 cont.: IRS 23 (B 163, H 9370)

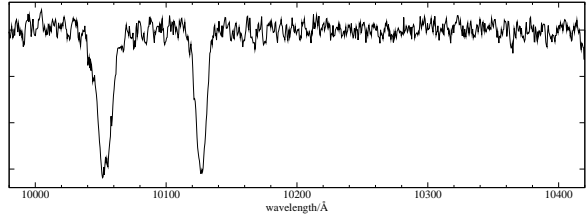


Fig. A.2 cont.: CEN 1b (H 8575), O4

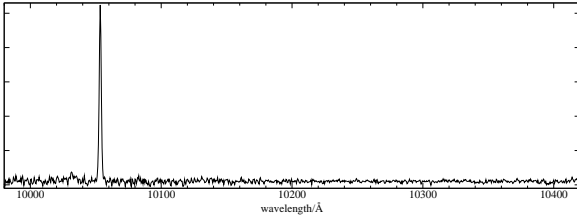


Fig. A.2 cont.: IRS 37 (B 91, H 13300)

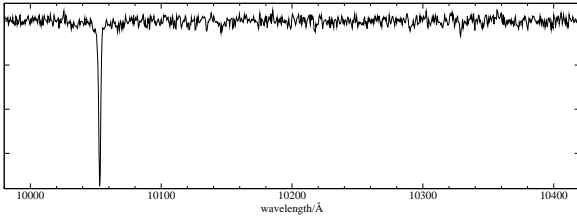


Fig. A.2 cont.: B 46 (H 16566)

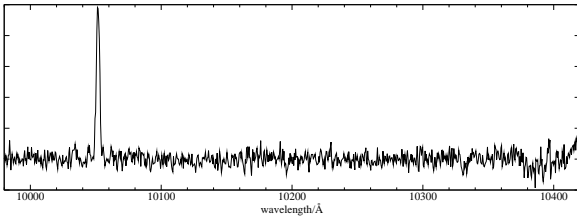


Fig. A.2 cont.: H 7113

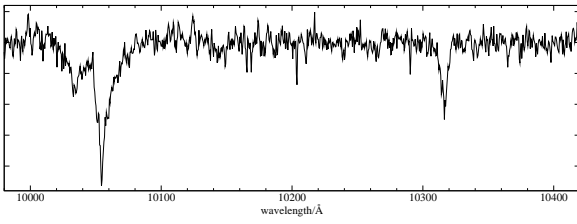


Fig. A.2 cont.: CEN 55 (H 8123), early B

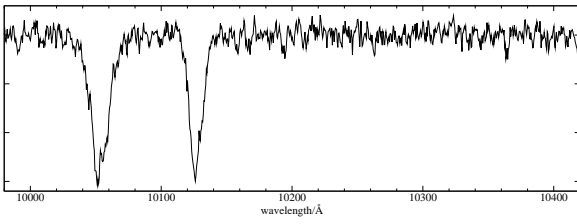


Fig. A.2 cont.: CEN 1a (H 8635), O4

A.3 *K* Band Spectroscopy

K band spectroscopy of stellar objects obtained with ISAAC at the VLT. The continuum is normalized to unity.

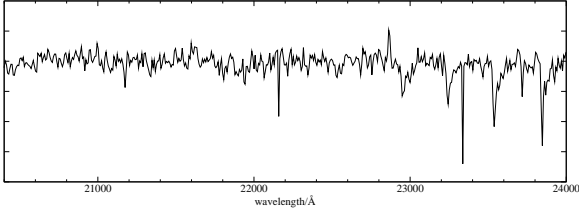


Fig. A.3: CEN 0 (B 232, H 7096)

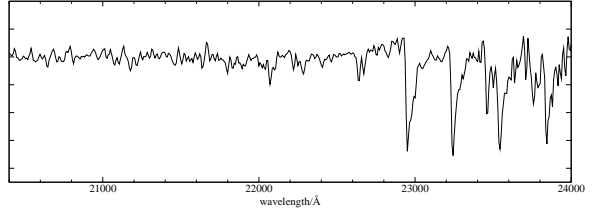


Fig. A.3 cont.: IRS 9 (B 249, H 6221)

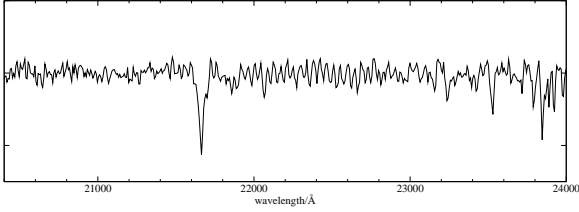


Fig. A.3 cont.: IRS 5 (B 284), **O6**

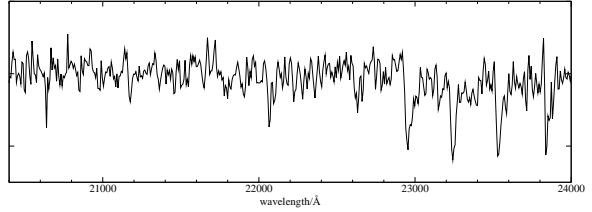


Fig. A.3 cont.: H 4920

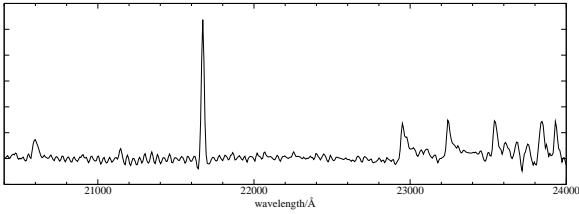


Fig. A.3 cont.: CEN 92 (IRS 2, B 331, H 3508)

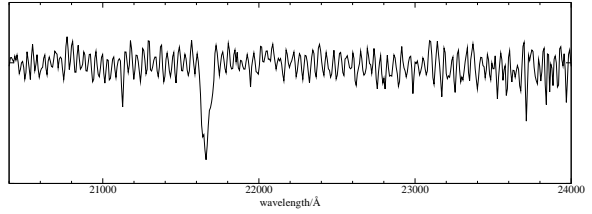


Fig. A.3 cont.: CEN 16 (B 311, H 4108), **O9**

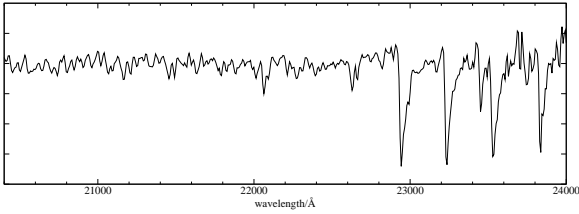


Fig. A.3 cont.: CEN 95 (IRS 8, B 266, H 5806)

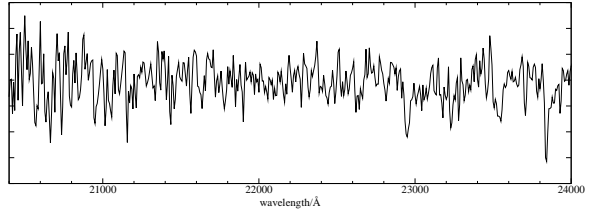


Fig. A.3 cont.: H 9224

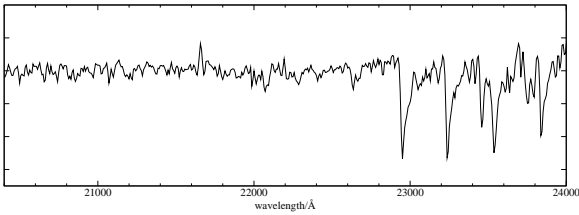


Fig. A.3 cont.: IRS 6 (B 280, H 5351)

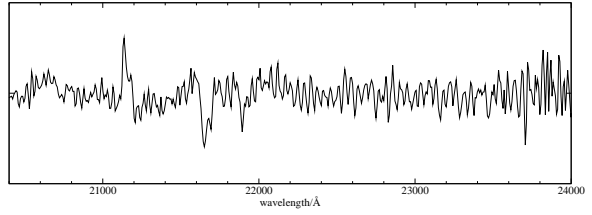


Fig. A.3 cont.: CEN 1a (H 8635), **O4**

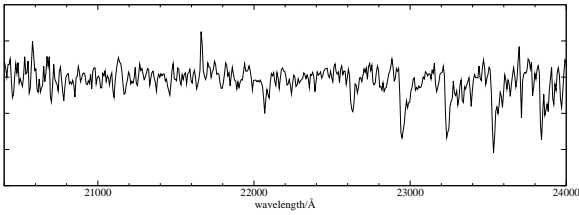


Fig. A.3 cont.: H 7206

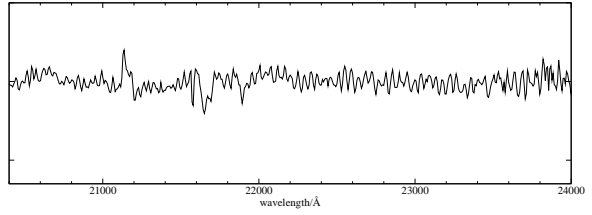


Fig. A.3 cont.: CEN 1b (H 8575), **O4**

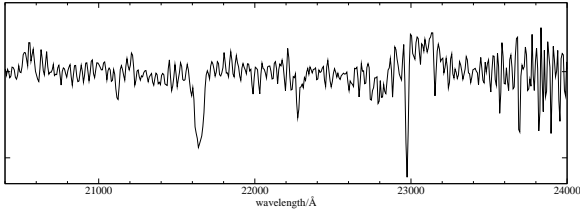


Fig. A.3 cont.: CEN 59 (B 203, H 8262), **B0**

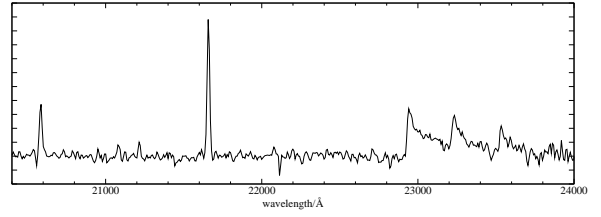


Fig. A.3 cont.: H 3276

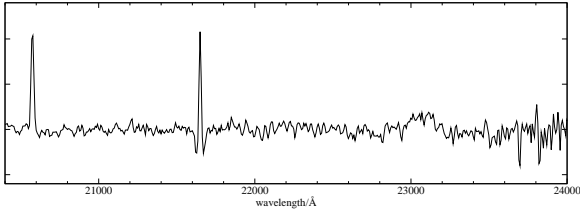


Fig. A.3 cont.: CEN 26 (B 253, H 6074), **B3**

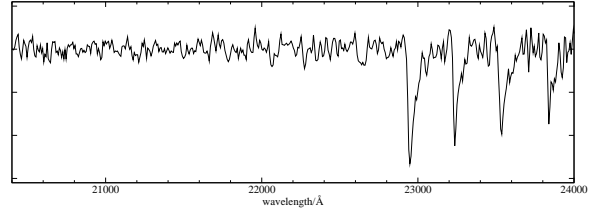


Fig. A.3 cont.: CEN 34 (B 358, H 3343)

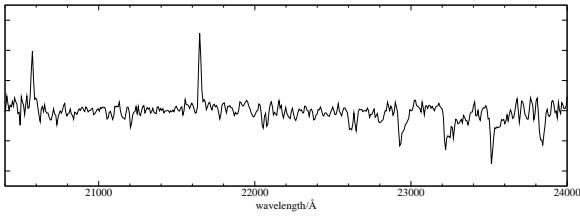


Fig. A.3 cont.: B 291 (H 4982)

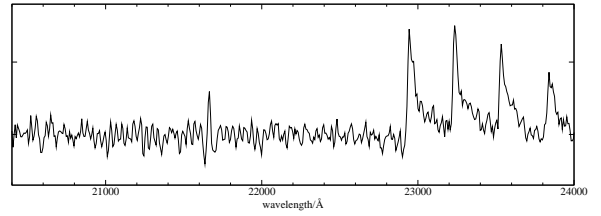


Fig. A.3 cont.: CEN 93 (IRS 1, B 337, H 3300)

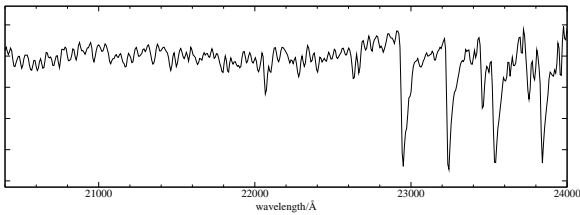


Fig. A.3 cont.: CEN 102 (B 305, H 4264)

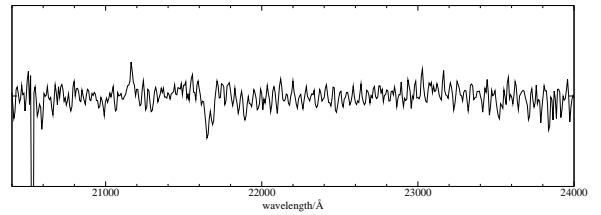


Fig. A.3 cont.: CEN 61 (B 181, H 8854), **O**

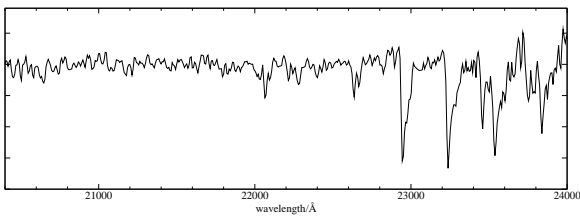


Fig. A.3 cont.: IRS 3 (B 318, H 3900)

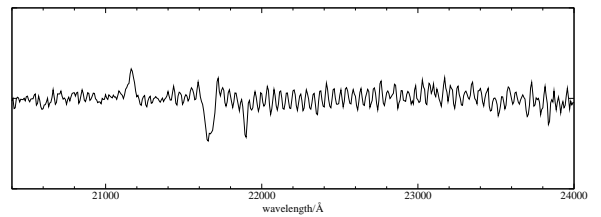


Fig. A.3 cont.: CEN 37 (IRS 21, H 9000), **O6**

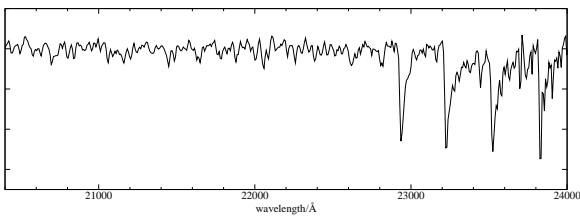


Fig. A.3 cont.: CEN 33 (B 324, H 3767)

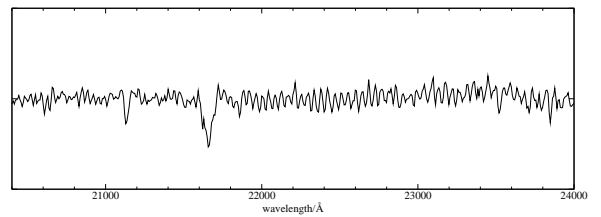


Fig. A.3 cont.: B 173 (H 9109)

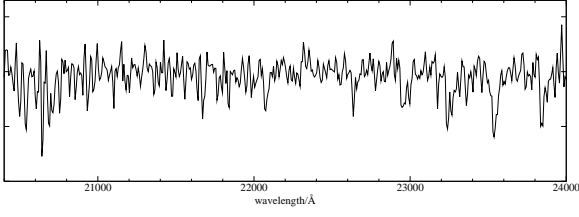


Fig. A.3 cont.: H 9335

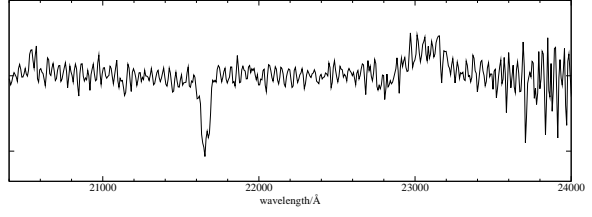


Fig. A.3 cont.: CEN 48 (B 248, H 6208), **B3**

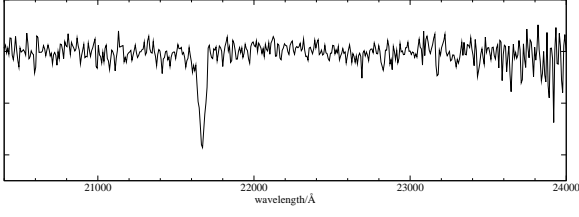


Fig. A.3 cont.: CEN 23 (H 6916), **B3**

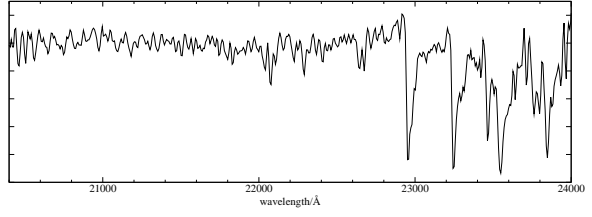


Fig. A.3 cont.: B 339 (H 3195)

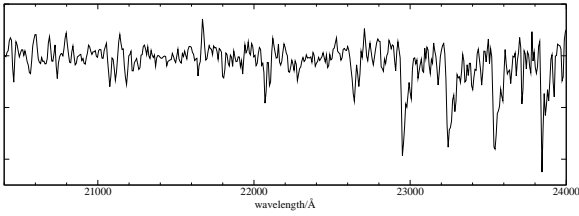


Fig. A.3 cont.: H 6900

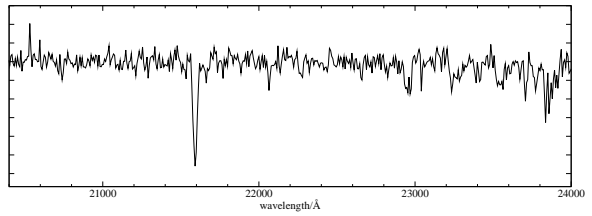


Fig. A.3 cont.: H 2885

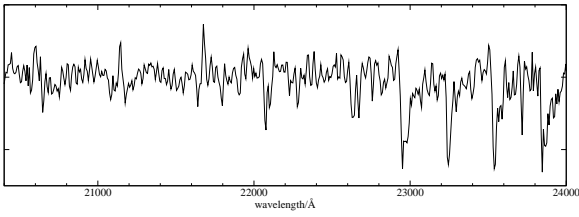


Fig. A.3 cont.: H 5695

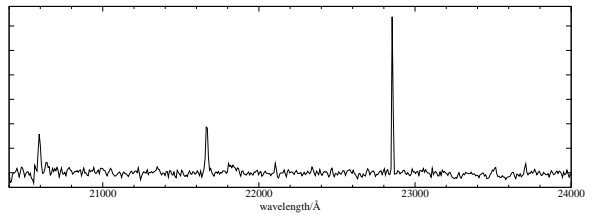


Fig. A.3 cont.: H 2674

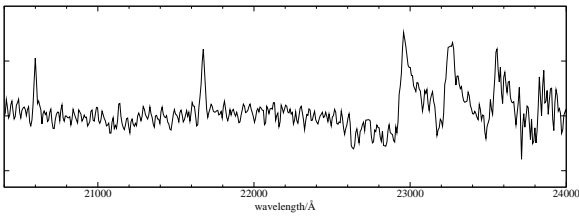


Fig. A.3 cont.: H 5664

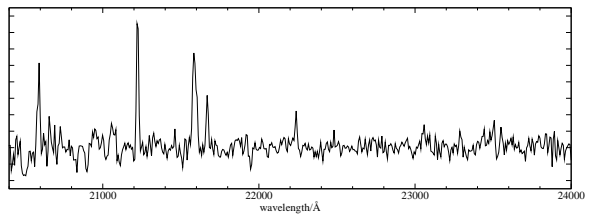


Fig. A.3 cont.: H 2560

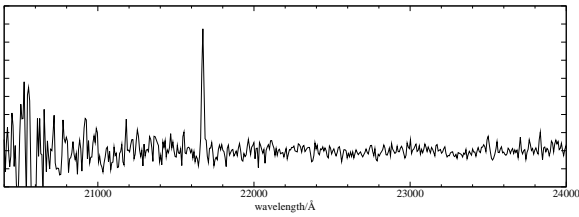


Fig. A.3 cont.: M17-UC1 (H 5332)

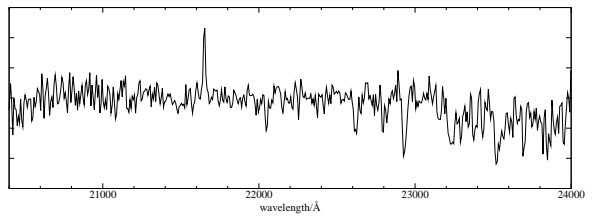


Fig. A.3 cont.: H 7995

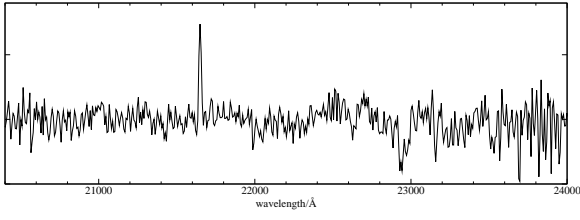


Fig. A.3 cont.: H 7554

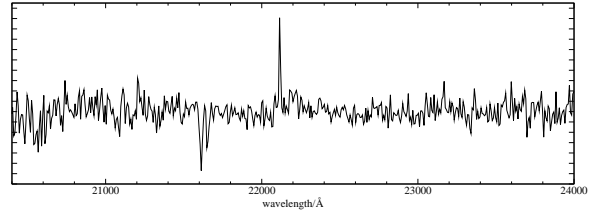


Fig. A.3 cont.: H 8020

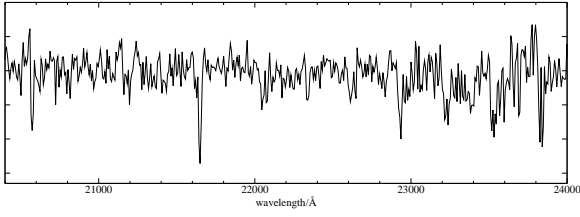


Fig. A.3 cont.: H 7062

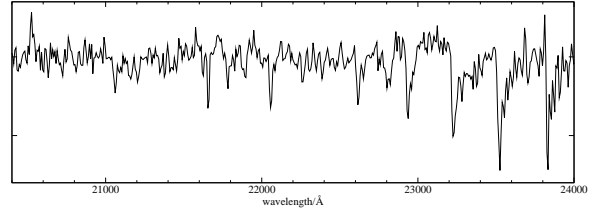


Fig. A.3 cont.: CEN 101 (B 206, H 7942)

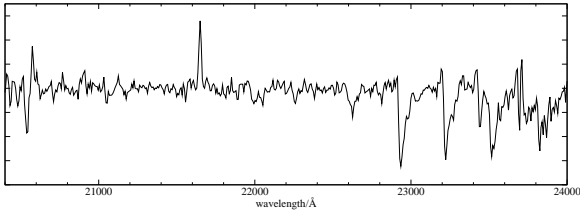


Fig. A.3 cont.: IRS 10 (B 246, H 3793)

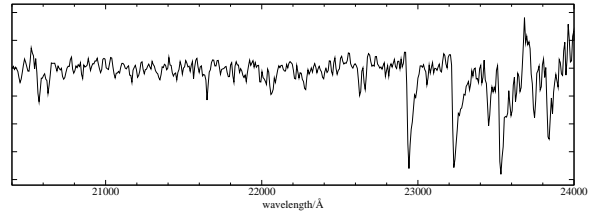


Fig. A.3 cont.: B 46 (H 16566)

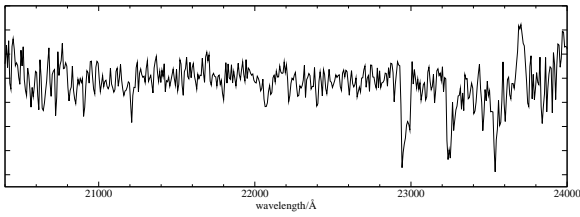


Fig. A.3 cont.: B 158 (H 5919)

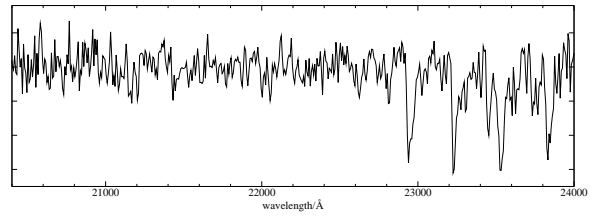


Fig. A.3 cont.: B 59 (H 15211)

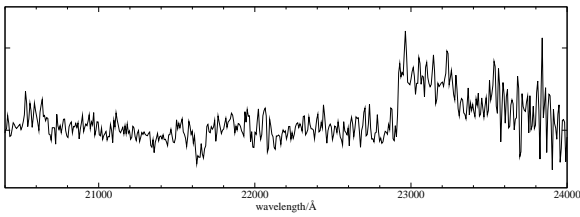


Fig. A.3 cont.: IRS 23 (B 163, H 9370)

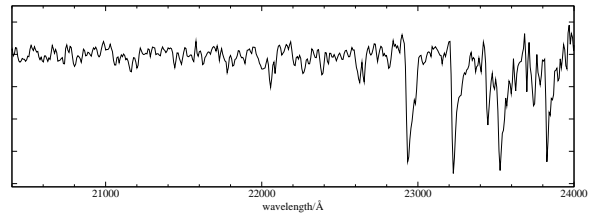


Fig. A.3 cont.: B 73 (H 14421)

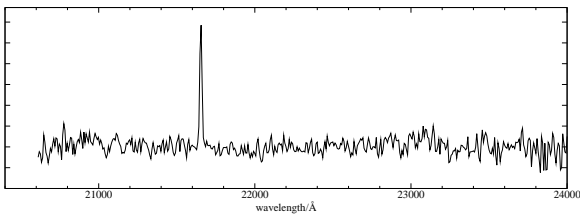


Fig. A.3 cont.: H 9283

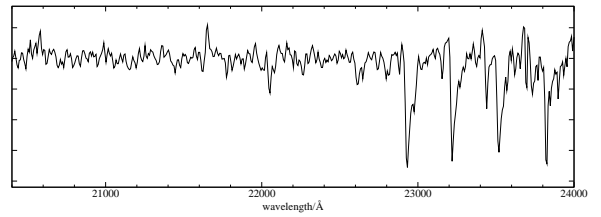


Fig. A.3 cont.: IRS 37 (B 91, H 13300)

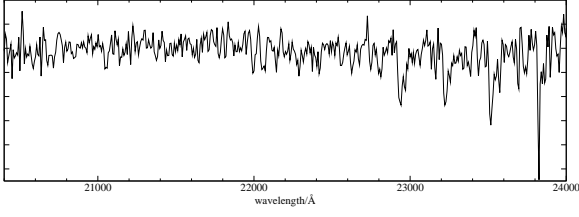


Fig. A.3 cont.: B 122 (H 11560)

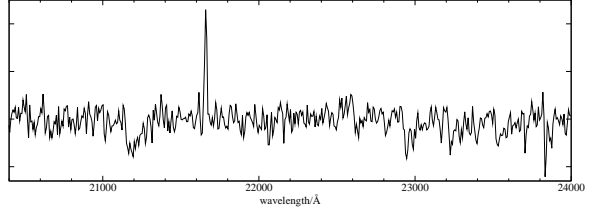


Fig. A.3 cont.: B 286 (H 5202)

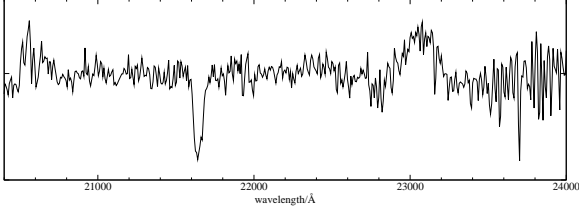


Fig. A.3 cont.: IRS 15 (B 215, H 10659), **B0**

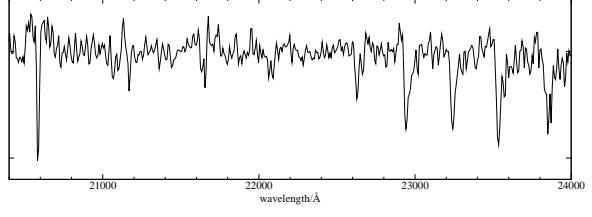


Fig. A.3 cont.: B 273 (H 5468)

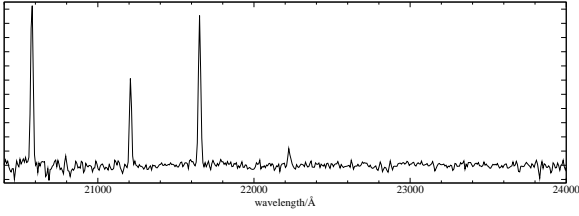


Fig. A.3 cont.: H 7071

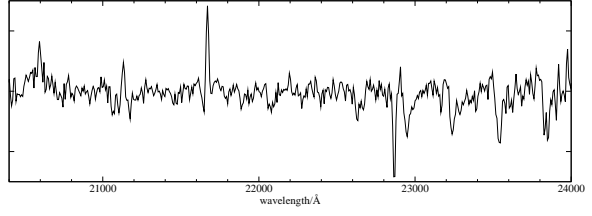


Fig. A.3 cont.: B 279 (H 5344)

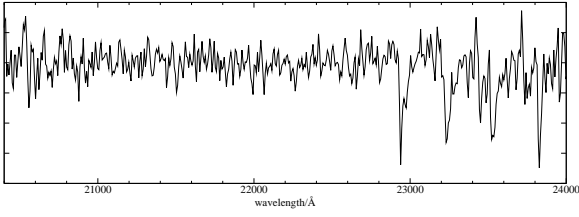


Fig. A.3 cont.: H 5003

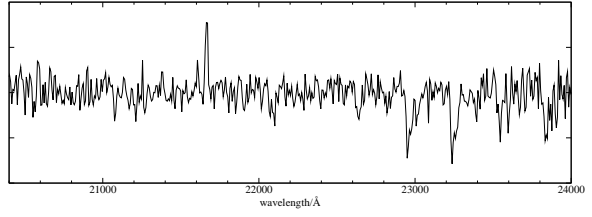


Fig. A.3 cont.: B 291 (H 4982)

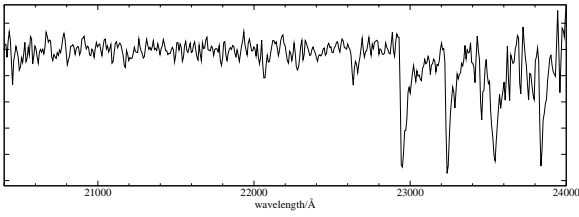


Fig. A.3 cont.: B 274 (H 5479)

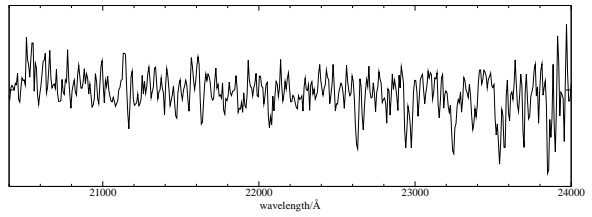


Fig. A.3 cont.: B 312 (H 4013)

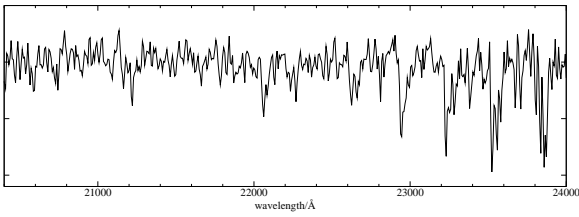


Fig. A.3 cont.: H 5244

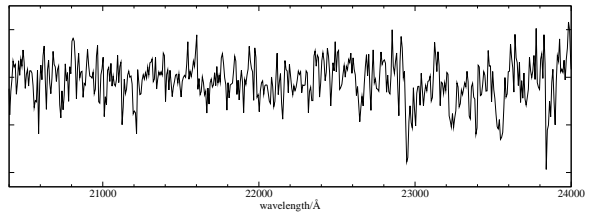


Fig. A.3 cont.: H 3975

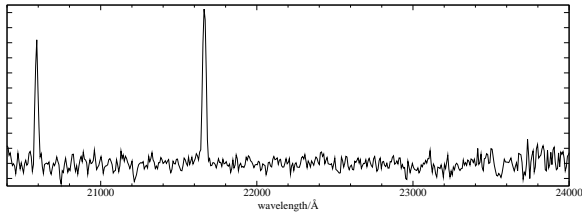


Fig. A.3 cont.: H 3800

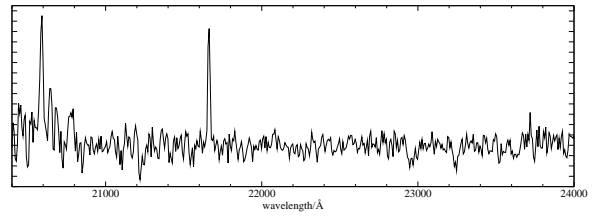


Fig. A.3 cont.: H 5210

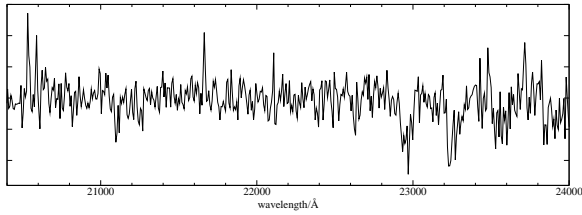


Fig. A.3 cont.: B 285 (H 5176)

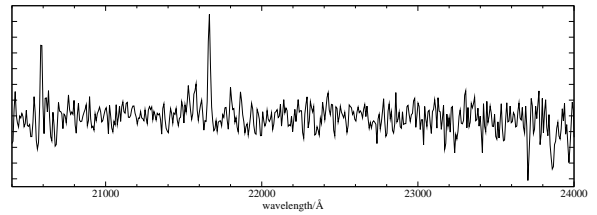


Fig. A.3 cont.: H 4719

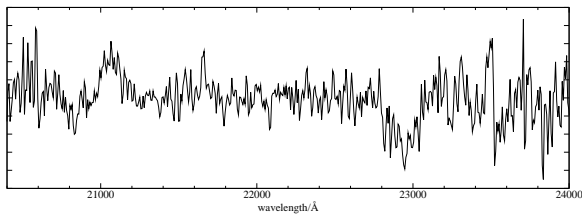


Fig. A.3 cont.: B 330 (H 3568)

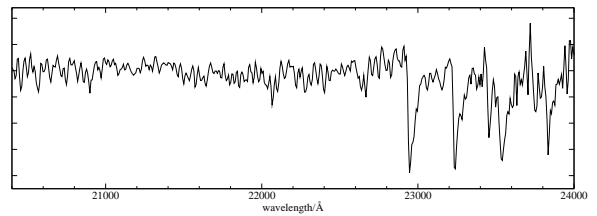


Fig. A.3 cont.: H 1739

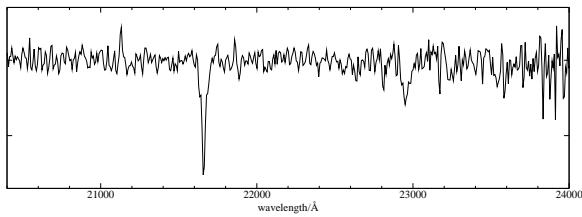


Fig. A.3 cont.: CEN 57 (B 269, H 5689)

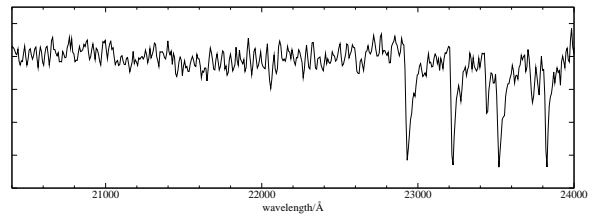


Fig. A.3 cont.: H 1807

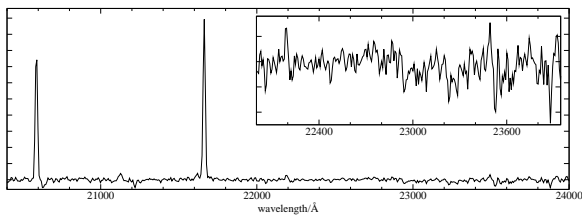


Fig. A.3 cont.: H 5485

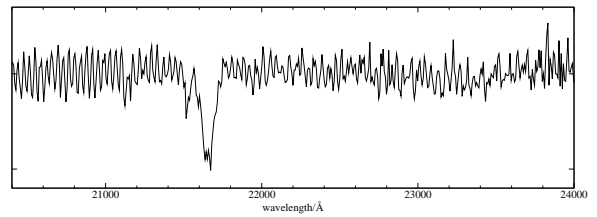


Fig. A.3 cont.: H 1193

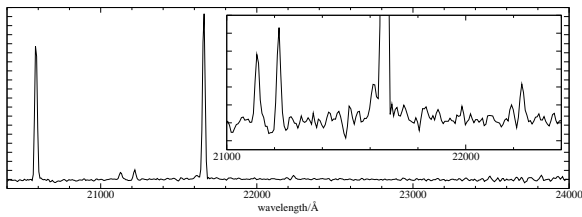


Fig. A.3 cont.: Nebula btwn. B 273 and UC1

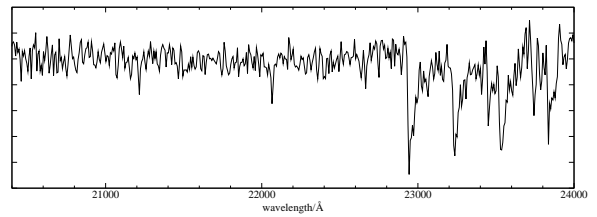


Fig. A.3 cont.: H 19850

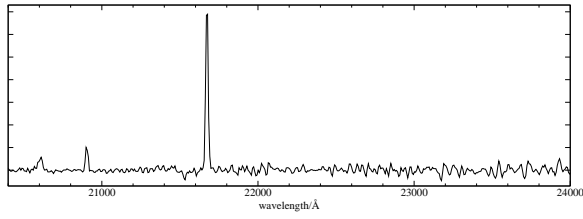


Fig. A.3 cont.: KW object (H 2309)

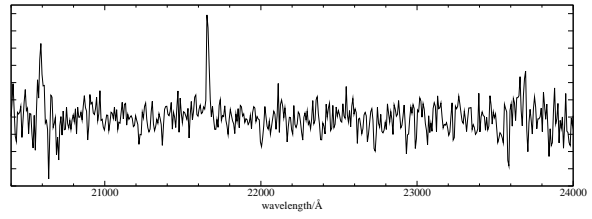


Fig. A.3 cont.: H 4976

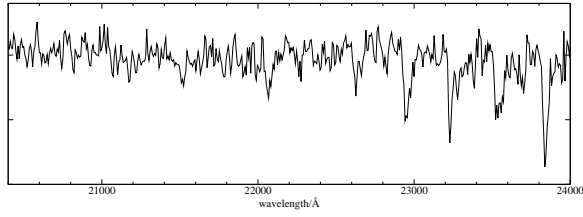


Fig. A.3 cont.: B 335 (H 3382)

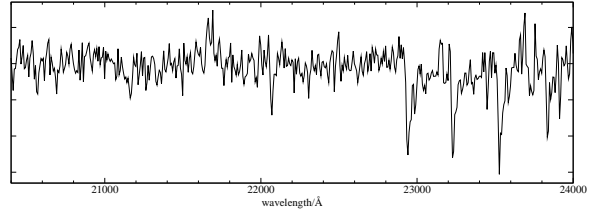


Fig. A.3 cont.: H 5193

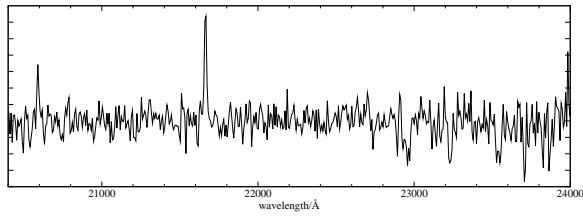


Fig. A.3 cont.: H 6133

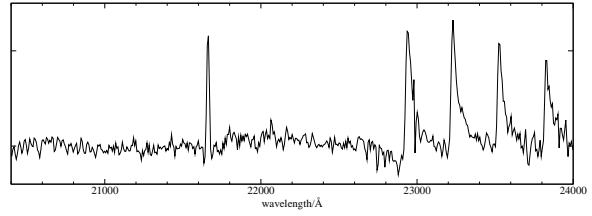


Fig. A.3 cont.: CEN 24 (B 275, H 5443)

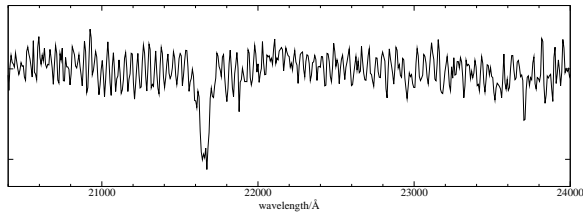


Fig. A.3 cont.: CEN 30 (B 213, H 7823), **O9**

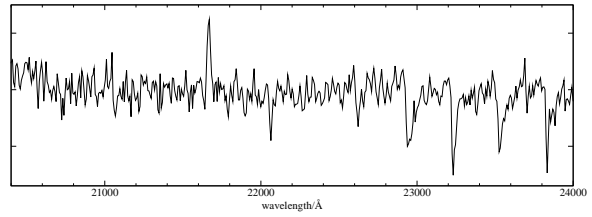


Fig. A.3 cont.: B 262 (H 5896)

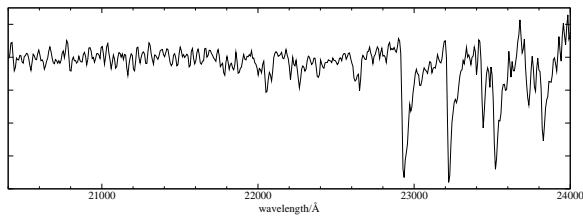


Fig. A.3 cont.: IRS 17 (B 208, H 7900)

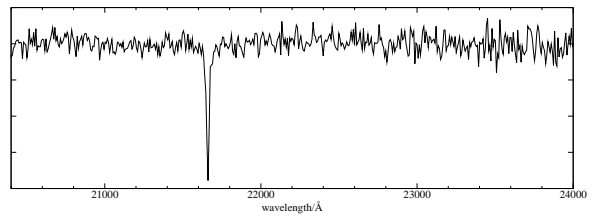


Fig. A.3 cont.: CEN 14 (H 6014)

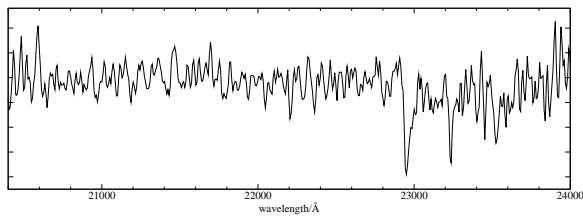


Fig. A.3 cont.: B 191 (H 8603)

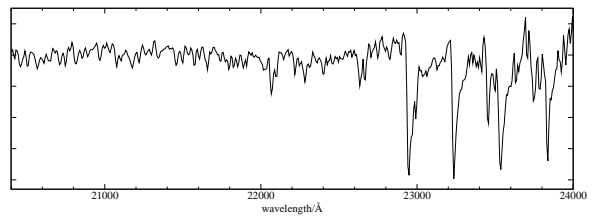


Fig. A.3 cont.: IRS 12 (B 239, H 6691)

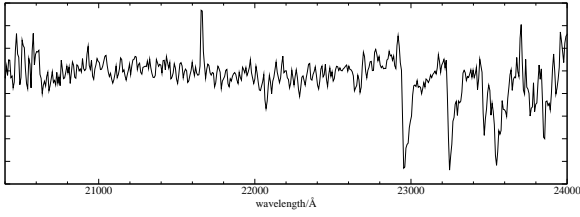


Fig. A.3 cont.: B 339 (H 3195)

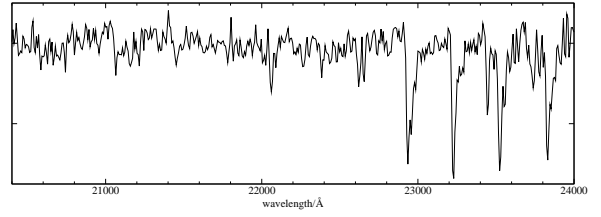


Fig. A.3 cont.: H 7061

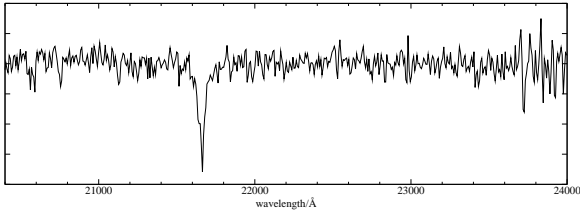


Fig. A.3 cont.: B 314 (H 3957)

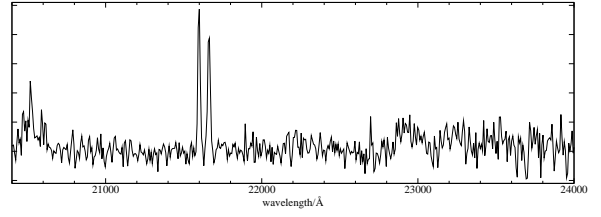


Fig. A.3 cont.: CEN 49 (B 268, H 5593)

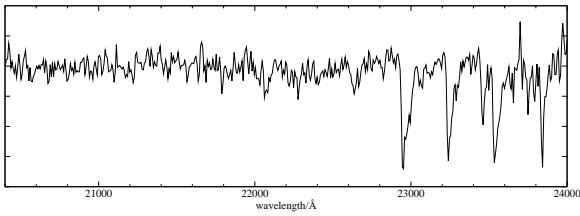


Fig. A.3 cont.: CEN 32 (B 287, H 5121)

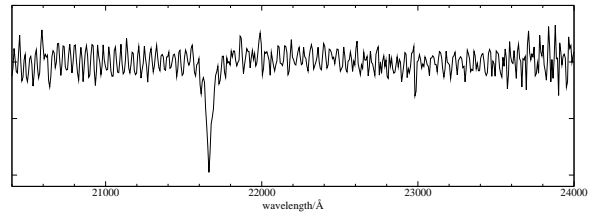


Fig. A.3 cont.: CEN 36 (B 272, H 5616), **O9.5**

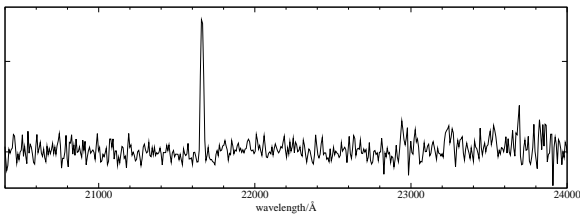


Fig. A.3 cont.: CEN 51 (B 243, H 6421)

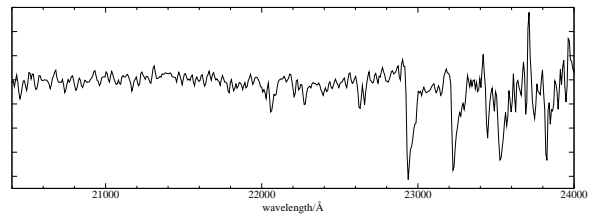


Fig. A.3 cont.: H 10432

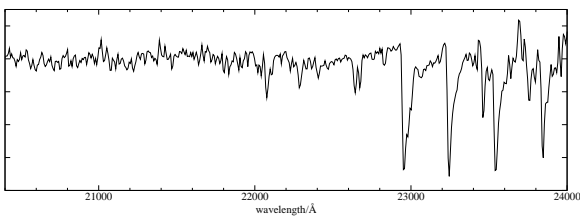


Fig. A.3 cont.: IRS 14 (B 219, H 7570)

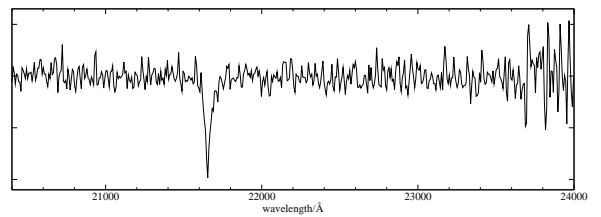


Fig. A.3 cont.: B 140 (H 10659), **B3**

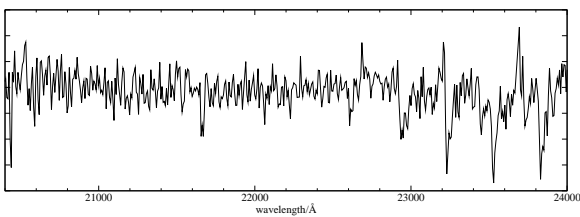


Fig. A.3 cont.: H 6051

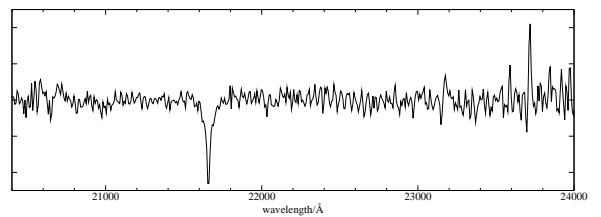


Fig. A.3 cont.: H 8614

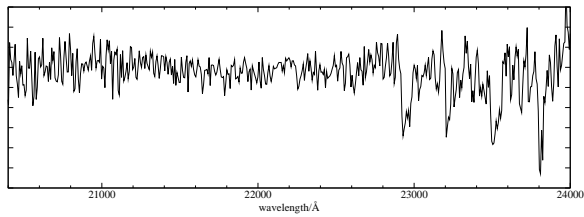


Fig. A.3 cont.: H 8700

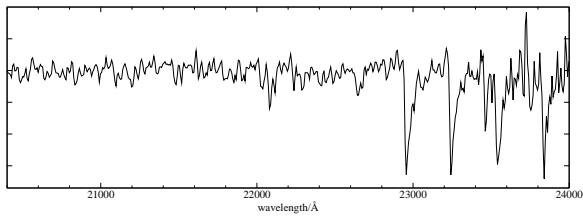


Fig. A.3 cont.: IRS 32 (B 115, H 11751)

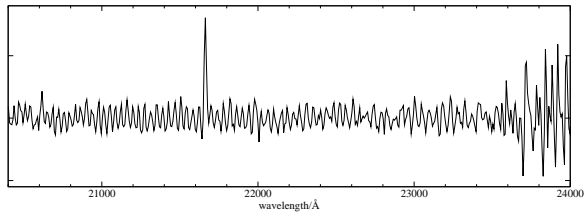


Fig. A.3 cont.: IRS 24 (B 168, H 9342)

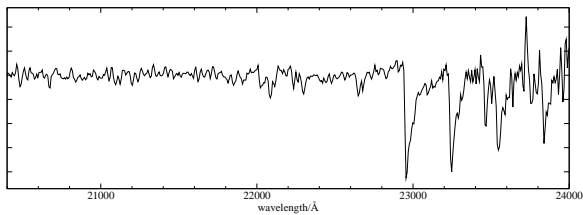


Fig. A.3 cont.: IRS 34 (B 103, H 12554)

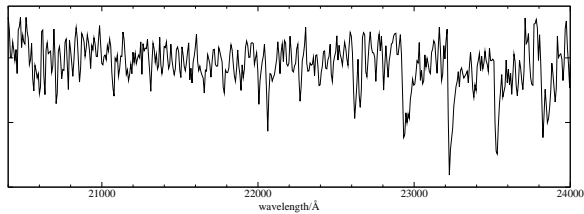


Fig. A.3 cont.: B 74 (H 14395)

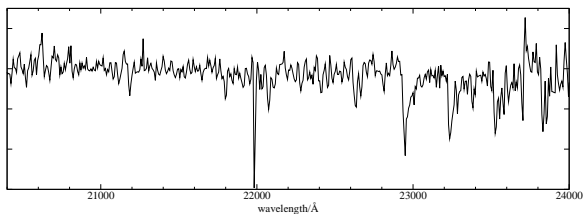


Fig. A.3 cont.: H 9234

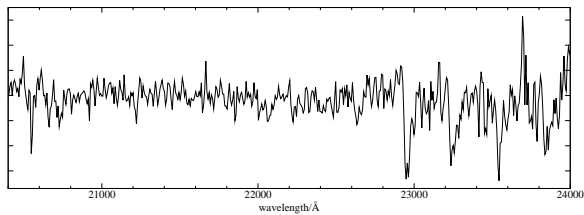


Fig. A.3 cont.: B 29 (H 17879)

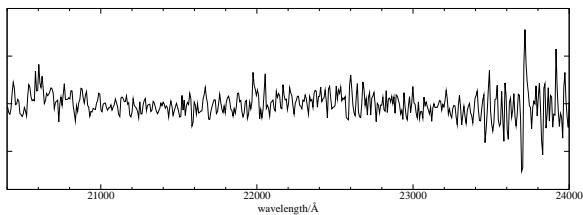


Fig. A.3 cont.: H 9651

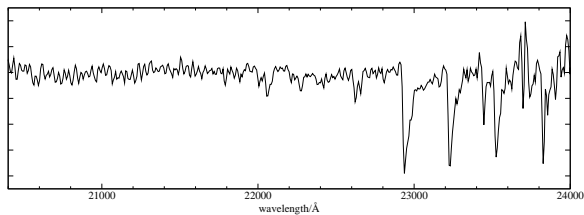


Fig. A.3 cont.: B 17 (H 18809)

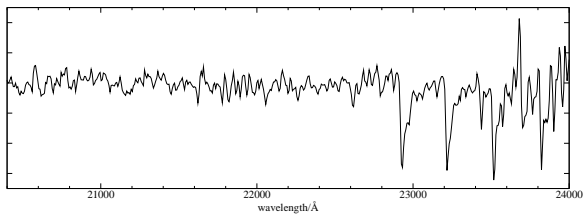


Fig. A.3 cont.: B 143 (H 10382)

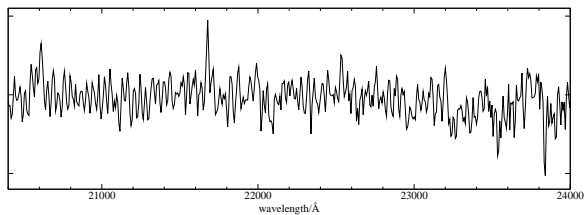


Fig. A.3 cont.: B 165 (H 9316)

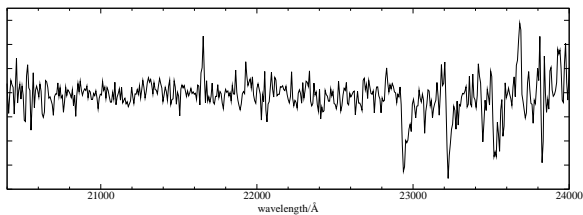


Fig. A.3 cont.: B 88 (H 13319)

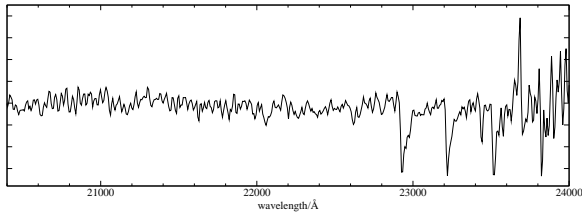


Fig. A.3 cont.: B 51 (H 15894)

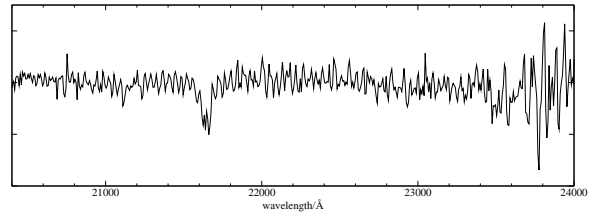


Fig. A.3 cont.: CEN 3 (B 98, H 12704), O9

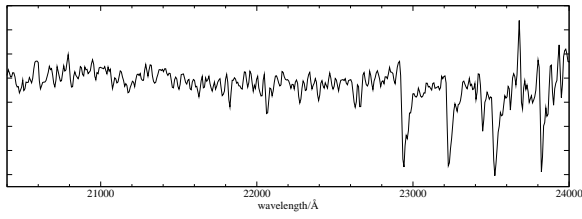


Fig. A.3 cont.: IRS 29 (B 139, H 10609)

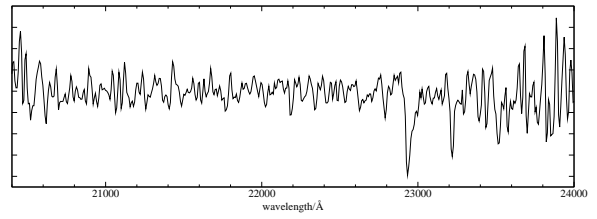


Fig. A.3 cont.: H 12811

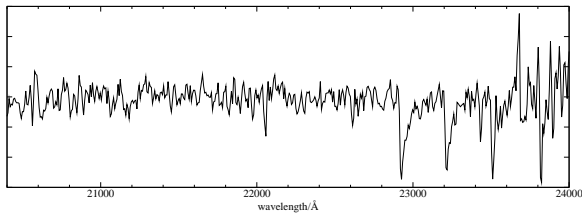


Fig. A.3 cont.: H 11662

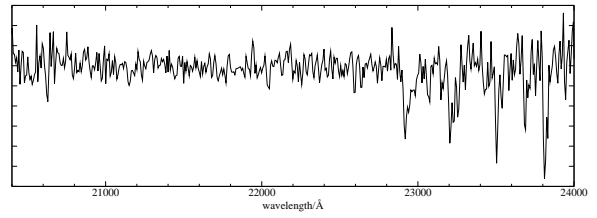


Fig. A.3 cont.: H 13752

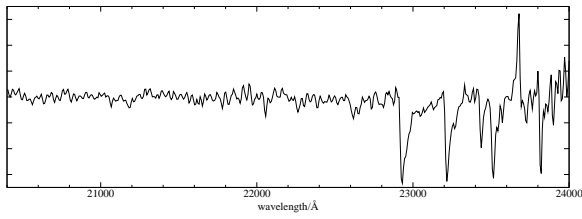


Fig. A.3 cont.: IRS 33 (B 113, H 11810)

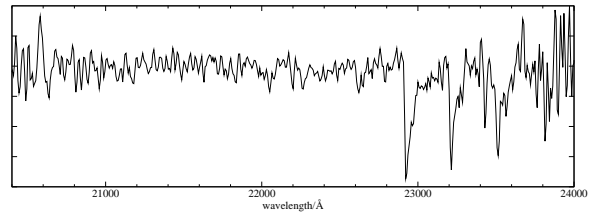


Fig. A.3 cont.: B 72 (H 14599)

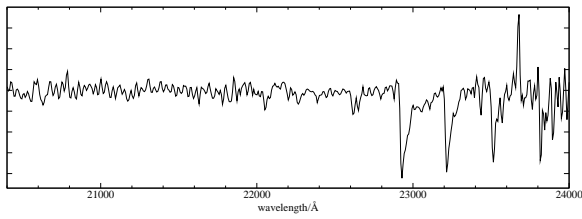


Fig. A.3 cont.: B 47 (H 16365)

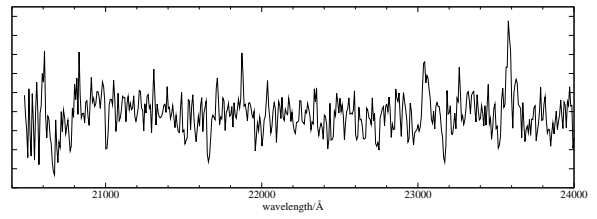


Fig. A.3 cont.: H 4144

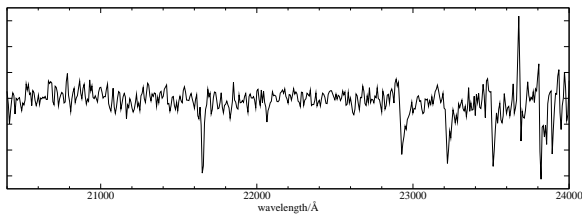


Fig. A.3 cont.: H 16655

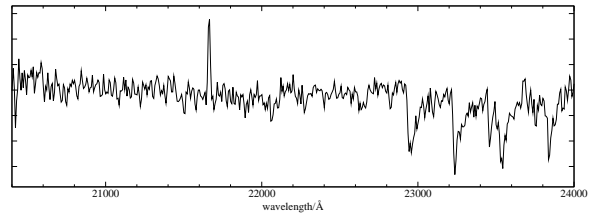


Fig. A.3 cont.: B 307 (H 4244)

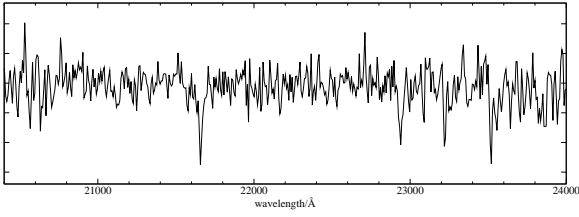


Fig. A.3 cont.: B 288 (H 5100)

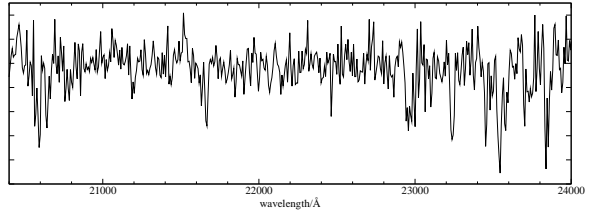


Fig. A.3 cont.: B 75 (H 14213)

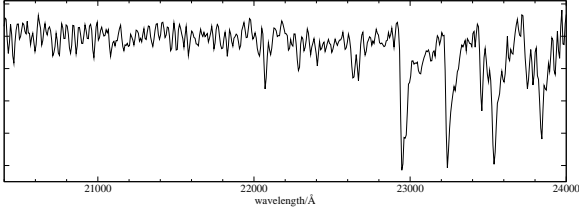


Fig. A.3 cont.: B 332 (H 3477)

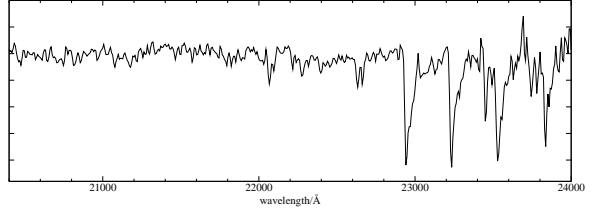


Fig. A.3 cont.: B 60 (H 14926)

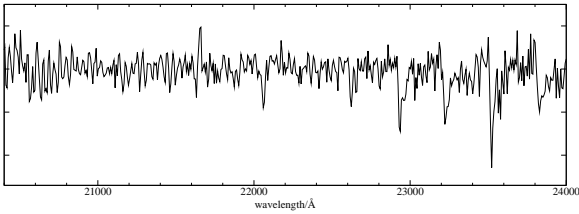


Fig. A.3 cont.: B 310 (H 4130)

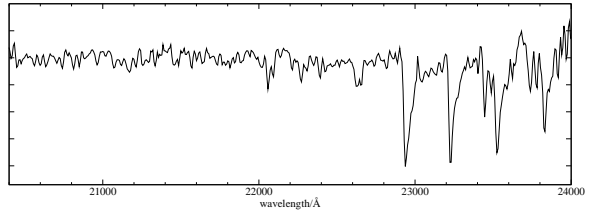


Fig. A.3 cont.: IRS 7 (B 281, H 5283)

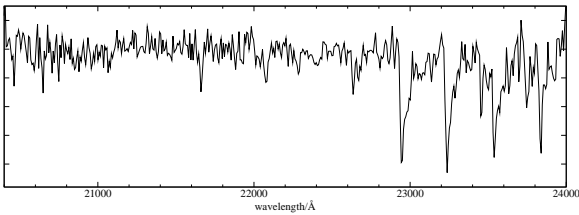


Fig. A.3 cont.: H 4402

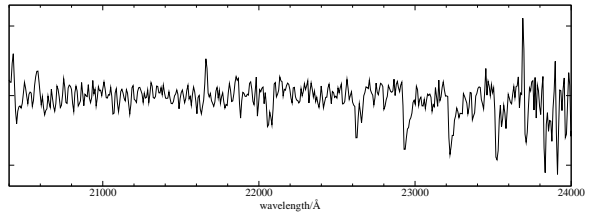


Fig. A.3 cont.: H 4676

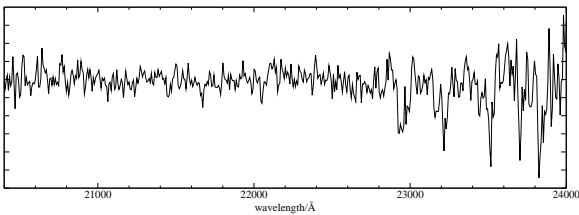


Fig. A.3 cont.: H 11802

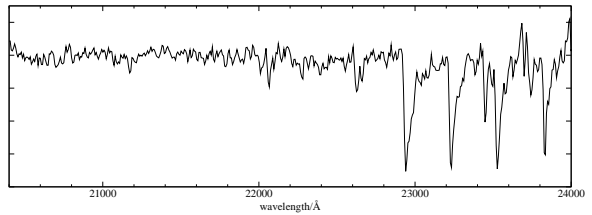


Fig. A.3 cont.: B 81 (H 13854)

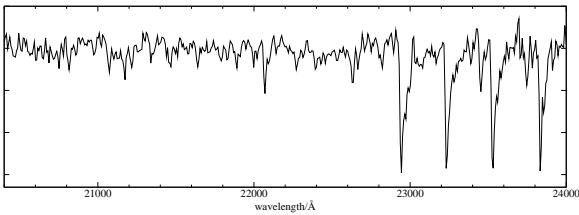


Fig. A.3 cont.: B 82 (H 13652)

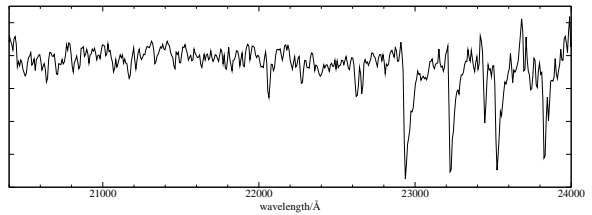


Fig. A.3 cont.: B 54 (H 15602)

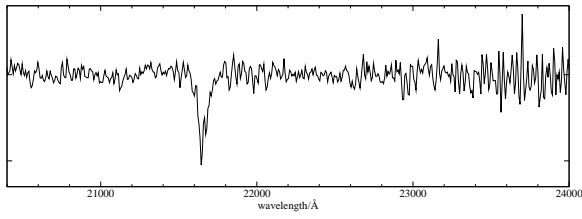


Fig. A.3 cont.: H 11910

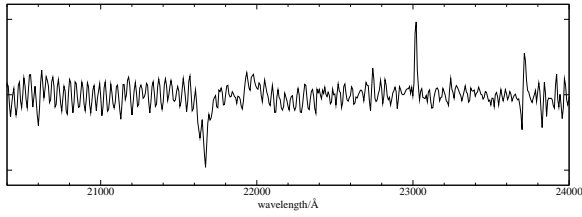


Fig. A.3 cont.: CEN 25 (B 164, H 9296), **O7**

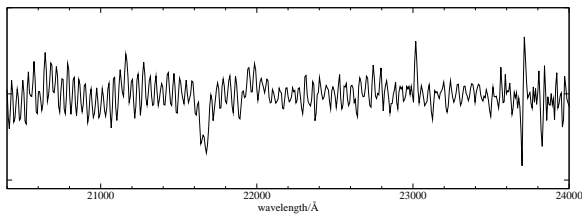


Fig. A.3 cont.: CEN 43 (B 137, H 10805), **O4**

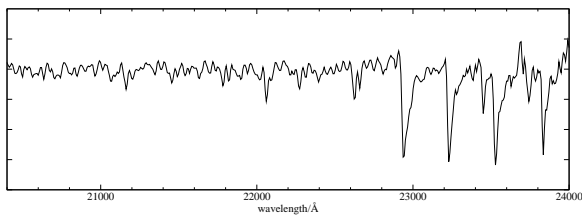


Fig. A.3 cont.: CEN 10 (B 320, H 3793)

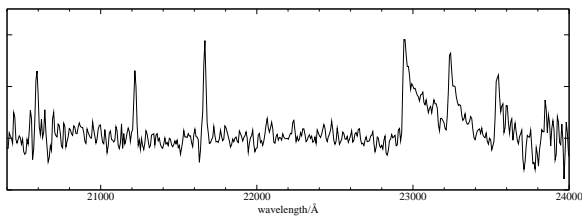


Fig. A.3 cont.: B 353 (H 2382)

Appendix B

Abbreviations

CMD(s)	Color–Magnitude Diagram(s)
CTTS	Classical T Tauri Stars
DIT	Detector Integration Time
EFOSC2	ESO Faint Object Spectrograph and Camera 2
EMMI	ESO Multi-Mode Instrument
ESO	European Organization for Astronomical Research in the Southern Hemisphere
FoV	Field of View
FWHM	Full-width Half-maximum
HCH II	Hyper-compact H II (Region)
HR(D)	Hertzsprung–Russell (Diagram)
IR	Infrared
IRAF	Image Reduction and Analysis Facility
IRE	Infrared Excess
ISAAC	Infrared Spectrometer and Array Camera
ISM	Interstellar Medium
KWO	Kleinmann-Wright Object
M 17-SW	Southwestern Molecular Cloud
MOS	Multi-object Spectroscopy
MS	Main Sequence
NACO	NAOS–CONICA (Nasmyth Adaptive Optics System with Near-Infrared Imager and Spectrograph)
NIR	Near Infrared
NTT	New Technology Telescope
PDR(s)	Photodissociation Region(s)
PMS	Pre-Main Sequence
PSF	Point Spread Function
SAAO	South African Astronomical Observatory
SED	Spectral Energy Distribution
SF	Star Formation
TCD(s)	Two–Color Diagram(s) (i.e. Color–Color Diagram)
UVES	Ultraviolet and Visual Echelle Spectrograph
VLT	Very Large Telescope
WTTS	Weak-line T Tauri Stars
YSO(s)	Young Stellar Object(s)
ZAMS	Zero-age Main Sequence

Bibliography

- Anderson, C. M.: 1970, *Astrophys. J.* **160**, 507
- Ando, M., Nagata, T., Sato, S., Mizuno, N., Mizuno, A., Kawai, T., Nakaya, H., and Glass, I. S.: 2002, *Astrophys. J.* **574**, 187
- Andriessse, C. D. and de Vries, J. S.: 1976, *Astron. Astrophys.* **46**, 143
- Aspin, C. and Barsony, M.: 1994, *Astron. Astrophys.* **288**, 849
- Bagnulo, S., Jehin, E., Ledoux, C., Cabanac, R., Melo, C., Gilmozzi, R., and The ESO Paranal Science Operations Team: 2003, *The Messenger* **114**, 10
- Bahcall, J. N. and Soneira, R. M.: 1980, *Astrophys. Lett.* **44**, 73
- Bally, J., Moeckel, N., and Throop, H.: 2005, in A. N. Krot, E. R. D. Scott, and B. Reipurth (eds.), *Chondrites and the Protoplanetary Disk*, Vol. 341 of *Astronomical Society of the Pacific Conference Series*, pp 81–+
- Baraffe, I., Chabrier, G., Allard, F., and Hauschildt, P. H.: 2002, *Astron. Astrophys.* **382**, 563
- Bate, M. R.: 2000, *Monthly Notices Roy. Astron. Soc.* **314**, 33
- Beetz, M., Elsaesser, H., Weinberger, R., and Poulakos, C.: 1976, *Astron. Astrophys.* **50**, 41
- Bessell, M. S. and Brett, J. M.: 1988, *Publ. of the Astron. Soc. of the Pacific* **100**, 1134
- Bik, A. and Thi, W. F.: 2004, *Astron. Astrophys.* **427**, L13
- Biscaya, A. M., Rieke, G. H., Narayanan, G., Luhman, K. L., and Young, E. T.: 1997, *Astrophys. J.* **491**, 359
- Blum, R. D., Barbosa, C. L., Daminieli, A., Conti, P. S., and Ridgway, S.: 2004, *Astrophys. J.* **617**, 1167
- Bouchet, P., Schmider, F. X., and Manfroid, J.: 1991, *Astron. Astrophys. Suppl.* **91**, 409
- Brandner, W., Sheppard, S., Zinnecker, H., Close, L., Iwamuro, F., Krabbe, A., Maihara, T., Motohara, K., Padgett, D. L., and Tokunaga, A.: 2000, *Astron. Astrophys.* **364**, L13
- Broos, P. S., Feigelson, E. D., Townsley, L. K., Getman, K. V., Wang, J., Garmire, G. P., Jiang, Z., and Tsuboi, Y.: 2007, *Astrophys. Lett.* **169**, 353

- Bunn, J. C., Hoare, M. G., and Drew, J. E.: 1995, *Monthly Notices Roy. Astron. Soc.* **272**, 346
- Buzzoni, B., Delabre, B., Dekker, H., Dodorico, S., Enard, D., Focardi, P., Gustafsson, B., Nees, W., Paureau, J., and Reiss, R.: 1984, *The Messenger* **38**, 9
- Calvet, N.: 1997, in B. Reipurth and C. Bertout (eds.), *IAU Symp. 182: Herbig-Haro Flows and the Birth of Stars*, pp 417–432
- Calvet, N., Patino, A., Magris, G. C., and D’Alessio, P.: 1991, *Astrophys. J.* **380**, 617
- Campeggio, L., Strafella, F., Maiolo, B., Elia, D., and Aiello, S.: 2007, *Astrophys. J.* **668**, 316
- Cardelli, J. A., Clayton, G. C., and Mathis, J. S.: 1989, *Astrophys. J.* **345**, 245
- Carpenter, J. M.: 2001, *Astron. J.* **121**, 2851
- Carr, J. S.: 1989, *Astrophys. J.* **345**, 522
- Carr, J. S., Tokunaga, A. T., Najita, J., Shu, F. H., and Glassgold, A. E.: 1993, *Astrophys. J. Lett.* **411**, L37
- Casali, M. M. and Eiroa, C.: 1996, *Astron. Astrophys.* **306**, 427
- Caswell, J. L.: 1997, *Monthly Notices Roy. Astron. Soc.* **289**, 203
- Chandler, C. J., Carlstrom, J. E., Scoville, N. Z., Dent, W. R. F., and Geballe, T. R.: 1993, *Astrophys. J. Lett.* **412**, L71
- Chesterman, J. F., Warren-Smith, R. F., and Scarrott, S. M.: 1982, *Monthly Notices Roy. Astron. Soc.* **200**, 965
- Chini, R.: 1982, *Astron. Astrophys.* **110**, 332
- Chini, R., Elsässer, H., and Neckel, T.: 1980, *Astron. Astrophys.* **91**, 186
- Chini, R., Hoffmeister, V., Kimeswenger, S., Nielbock, M., Nürnberger, D., Schmidtobreick, L., and Sterzik, M.: 2004, *Nature* **429**, 155
- Chini, R., Hoffmeister, V. H., Nielbock, M., Scheyda, C. M., Steinacker, J., Siebenmorgen, R., and Nürnberger, D.: 2006, *Astrophys. J. Lett.* **645**, L61
- Chini, R. and Krügel, E.: 1983, *Astron. Astrophys.* **117**, 289
- Chini, R. and Krügel, E.: 1985, *Astron. Astrophys.* **146**, 175
- Chini, R., Krügel, E., and Wargau, W. F.: 1992, *Astron. Astrophys.* **265**, 45
- Chini, R. and Wargau, W. F.: 1998, *Astron. Astrophys.* **329**, 161
- Churchwell, E., Walmsley, C. M., and Cesaroni, R.: 1990, *Astron. Astrophys. Suppl.* **83**, 119
- Crampton, D., Georgelin, Y. M., and Georgelin, Y. P.: 1978, *Astron. Astrophys.* **66**, 1

- Crowther, P. A.: 2005, in R. Cesaroni, M. Felli, E. Churchwell, and C. M. Walmsley (eds.), *Massive Star Birth: A Crossroad of Astrophysics*, Vol. 227 of *Proceedings IAU Symposium*, p. 389, IAU, Cambridge University Press
- Davis, R. J.: 1977, *Astrophys. J.* **213**, 105
- Dekker, H., Delabre, B., and Dodorico, S.: 1986, in D. L. Crawford (ed.), *Instrumentation in astronomy VI; Proceedings of the Meeting, Tucson, AZ, Mar. 4-8, 1986. Part 1*, pp 339–348
- Dekker, H., D’Odorico, S., Kaufer, A., Delabre, B., and Kotzlowski, H.: 2000, in M. Iye and A. F. Moorwood (eds.), *Proceedings of the SPIE Vol. 4008, Optical and IR Telescope Instrumentation and Detectors*, pp 534–545
- Deutschman, W. A., Davis, R. J., and Schild, R. E.: 1976, *Astrophys. Lett.* **30**, 97
- Dickel, H. R.: 1968, *Astrophys. J.* **152**, 651
- Ducati, J. R., Bevilacqua, C. M., Rembold, S. B., and Ribeiro, D.: 2001, *Astrophys. J.* **558**, 309
- Dyck, H. M.: 1980, *Astron. J.* **85**, 891
- Elliott, K. H., Meaburn, J., and Terrett, D. L.: 1978, *Monthly Notices Roy. Astron. Soc.* **184**, 527
- Elmegreen, B. G. and Lada, C. J.: 1976, *Astron. J.* **81**, 1089
- Elmegreen, B. G. and Lada, C. J.: 1977, *Astrophys. J.* **214**, 725
- Elmegreen, B. G., Lada, C. J., and Dickinson, D. F.: 1979, *Astrophys. J.* **230**, 415
- Elmegreen, D. M., Phillips, J., Beck, K., Thomas, H., and Howard, J.: 1988, *Astrophys. J.* **335**, 803
- Felli, M., Johnston, K. J., and Churchwell, E.: 1980, *Astrophys. J. Lett.* **242**, L157
- Felli, M., Massi, M., and Churchwell, E.: 1984, *Astron. Astrophys.* **136**, 53
- Felli, M. and Stanga, R.: 1987, *Astron. Astrophys.* **175**, 193
- Forster, J. R. and Caswell, J. L.: 1999, *Astron. Astrophys. Suppl.* **137**, 43
- Gehrz, R. D., Grasdalen, G. L., Castelaz, M., Gullixson, C., Mozurkewich, D., and Hackwell, J. A.: 1982, *Astrophys. J.* **254**, 550
- Giard, M., Bernard, J. P., Lacombe, F., Normand, P., and Rouan, D.: 1994, *Astron. Astrophys.* **291**, 239
- Gliese, W. and Jahreiß, H.: 1980, *Astron. Astrophys.* **85**, 350
- Glushkov, Y. I., Esipov, V. F., and Kondrat’Eva, L. N.: 2005, *Astronomy Reports* **49**, 36
- Goudis, C. and Meaburn, J.: 1976, *Astron. Astrophys.* **51**, 401

- Greene, T. P. and Lada, C. J.: 1996, *Astron. J.* **112**, 2184
- Greenhill, L. J., Gwinn, C. R., Schwartz, C., Moran, J. M., and Diamond, P. J.: 1998, *Nature* **396**, 650
- Grosso, N., Alves, J., Wood, K., Neuhäuser, R., Montmerle, T., and Bjorkman, J. E.: 2003, *Astrophys. J.* **586**, 296
- Haisch, Jr., K. E., Lada, E. A., and Lada, C. J.: 2000, *Astron. J.* **120**, 1396
- Haisch, Jr., K. E., Lada, E. A., and Lada, C. J.: 2001a, *Astron. J.* **121**, 2065
- Haisch, Jr., K. E., Lada, E. A., and Lada, C. J.: 2001b, *Astrophys. J. Lett.* **553**, L153
- Hamann, F. and Persson, S. E.: 1992, *Astrophys. Lett.* **82**, 285
- Hanson, M. M. and Conti, P. S.: 1995, *Astrophys. J. Lett.* **448**, L45+
- Hanson, M. M., Howarth, I. D., and Conti, P. S.: 1997, *Astrophys. J.* **489**, 698
- Harper, D. A., Low, F. J., Rieke, G. H., and Thronson, Jr., H. A.: 1976, *Astrophys. J.* **205**, 136
- Hartigan, P., Edwards, S., and Ghandour, L.: 1995, *Astrophys. J.* **452**, 736
- Hartmann, L., Hewett, R., and Calvet, N.: 1994, *Astrophys. J.* **426**, 669
- Hartmann, L., Hinkle, K., and Calvet, N.: 2004, *Astrophys. J.* **609**, 906
- Hartmann, L., Kenyon, S. J., Hewett, R., Edwards, S., Strom, K. M., Strom, S. E., and Stauffer, J. R.: 1989, *Astrophys. J.* **338**, 1001
- Henning, T., Klein, R., Launhardt, R., Lemke, D., and Pfau, W.: 1998, *Astron. Astrophys.* **332**, 1035
- Hillenbrand, L. A., Strom, S. E., Merrill, K. M., and Gatley, I.: 1993, in J. P. Cassinelli and E. B. Churchwell (eds.), *Massive Stars: Their Lives in the Interstellar Medium*, Vol. 35 of *Astronomical Society of the Pacific Conference Series*, pp 141–+
- Hiltner, W. A. and Johnson, H. L.: 1956, *Astrophys. J.* **124**, 367
- Hippelein, H. H. and Goudis, C.: 1986, *Astron. Astrophys.* **155**, 6
- Hoffmeister, V. H., Chini, R., Scheyda, C. M., Nürnberger, D., Vogt, N., and Nielbock, M.: 2006, *Astron. Astrophys.* **457**, L29
- Hofner, P. and Churchwell, E.: 1996, *Astron. Astrophys. Suppl.* **120**, 283
- Hofner, P., Wiesemeyer, H., and Henning, T.: 2001, *Astrophys. J.* **549**, 425
- Hou, J.-L., Jiang, D.-R., and Fu, C.-Q.: 1997, *Astron. Astrophys.* **327**, 725
- Ishida, K. and Kawajiri, K.: 1968, *Publ. of the Astron. Soc. of Japan* **20**, 95

- Jaffe, D. T. and Fazio, G. G.: 1982, *Astrophys. J. Lett.* **257**, L77
- Jappsen, A.-K., Klessen, R. S., Larson, R. B., Li, Y., and Mac Low, M.-M.: 2005, *Astron. Astrophys.* **435**, 611
- Jiang, Z., Yao, Y., Yang, J., Ando, M., Kato, D., Kawai, T., Kurita, M., Nagata, T., Nagayama, T., Nakajima, Y., Nagashima, C., Sato, S., Tamura, M., Nakaya, H., and Sugitani, K.: 2002, *Astrophys. J.* **577**, 245
- Johnson, C. O., Depree, C. G., and Goss, W. M.: 1998, *Astrophys. J.* **500**, 302
- Johnson, H. L.: 1966, *Ann. Rev. Astron. Astrophys.* **4**, 193
- Johnson, H. M.: 1973, *Astrophys. J.* **182**, 497
- Kassis, M., Deutsch, L. K., Campbell, M. F., Hora, J. L., Fazio, G. G., and Hoffmann, W. F.: 2002, *Astron. J.* **124**, 1636
- Kennicutt, R. C.: 2005, in R. Cesaroni, M. Felli, E. Churchwell, and M. Walmsley (eds.), *Massive Star Birth: A Crossroads of Astrophysics*, Vol. 227 of *IAU Symposium*, pp 3–11
- Kennicutt, Jr., R. C.: 1998, *Ann. Rev. Astron. Astrophys.* **36**, 189
- Kenyon, S. J. and Hartmann, L.: 1995, *Astrophys. Lett.* **101**, 117
- Kleinmann, D. E.: 1973, *Astrophys. and Space Science* **13**, 49
- Kleinmann, D. E. and Wright, E. L.: 1973, *Astrophys. J. Lett.* **185**, L131+
- Klessen, R. S., Ballesteros-Paredes, J., Vázquez-Semadeni, E., and Durán-Rojas, C.: 2005, *Astrophys. J.* **620**, 786
- Koornneef, J.: 1983a, *Astron. Astrophys. Suppl.* **51**, 489
- Koornneef, J.: 1983b, *Astron. Astrophys.* **128**, 84
- Krügel, E.: 2003, *The physics of interstellar dust*, IoP Series in astronomy and astrophysics, Bristol, UK: The Institute of Physics, 2003.
- Kudritzki, R. P.: 2002, *Astrophys. J.* **577**, 389
- Lada, C. J., Depoy, D. L., Merrill, K. M., and Gatley, I.: 1991, *Astrophys. J.* **374**, 533
- Lada, C. J., Muench, A. A., Haisch, Jr., K. E., Lada, E. A., Alves, J. F., Tollestrup, E. V., and Willner, S. P.: 2000, *Astron. J.* **120**, 3162
- Landolt, A. U.: 1992, *Astron. J.* **104**, 340
- Larson, R. B.: 1969, *Monthly Notices Roy. Astron. Soc.* **145**, 271
- Larson, R. B.: 2005, *Monthly Notices Roy. Astron. Soc.* **359**, 211
- Lemke, D. and Harris, A. W.: 1981, *Astron. Astrophys.* **99**, 285

- Lenzen, R., Hartung, M., Brandner, W., Finger, G., Hubin, N. N., Lacombe, F., Lagrange, A.-M., Lehnert, M. D., Moorwood, A. F. M., and Mouillet, D.: 2003, in M. Iye and A. F. M. Moorwood (eds.), *Instrument Design and Performance for Optical/Infrared Ground-based Telescopes. Proceedings of the SPIE, Volume 4841*, pp 944–952
- Mac Low, M.-M. and Klessen, R. S.: 2004, *Reviews of Modern Physics* **76**, 125
- Marti, J., Rodriguez, L. F., and Reipurth, B.: 1993, *Astrophys. J.* **416**, 208
- McCarthy, J. F., Forrest, W. J., and Houck, J. R.: 1979, *Astrophys. J.* **231**, 711
- McCaughrean, M. J. and O'dell, C. R.: 1996, *Astron. J.* **111**, 1977
- Meaburn, J.: 1977, in H. van Woerden (ed.), *Topics in Interstellar Matter*, Vol. 70 of *Astrophysics and Space Science Library*, pp 81–88
- Meyer, M. R., Calvet, N., and Hillenbrand, L. A.: 1997, *Astron. J.* **114**, 288
- Mezger, P. G. and Henderson, A. P.: 1967, *Astrophys. J.* **147**, 471
- Moorwood, A., Cuby, J.-G., Biereichel, P., Brynnel, J., Delabre, B., Devillard, N., van Dijsselmond, A., Finger, G., Gemperlein, H., et al.: 1998, *The Messenger* **94**, 7
- Moorwood, A. F. M., Baluteau, J.-P., Anderegg, M., Fitton, B., Coron, N., and Biraud, Y.: 1980, *Astrophys. J.* **238**, 565
- Muzerolle, J., Calvet, N., and Hartmann, L.: 2001, *Astrophys. J.* **550**, 944
- Muzerolle, J., Hartmann, L., and Calvet, N.: 1998, *Astron. J.* **116**, 455
- Nielbock, M., Chini, R., Hoffmeister, V. H., Scheyda, C. M., and Steinacker, J.: 2008, *Monthly Notices Roy. Astron. Soc.* , submitted
- Nielbock, M., Chini, R., Hoffmeister, V. H., Scheyda, C. M., Steinacker, J., Nürnberger, D., and Siebenmorgen, R.: 2007, *Astrophys. J. Lett.* **656**, L81
- Nielbock, M., Chini, R., Jütte, M., and Manthey, E.: 2001, *Astron. Astrophys.* **377**, 273
- Nürnberger, D. E. A., Chini, R., Eisenhauer, F., Kissler-Patig, M., Modigliani, A., Siebenmorgen, R., Sterzik, M. F., and Szeifert, T.: 2007, *Astron. Astrophys.* **465**, 931
- Ogura, K. and Ishida, K.: 1976, *Publ. of the Astron. Soc. of Japan* **28**, 35
- Oliva, E. and Origlia, L.: 1992, *Astron. Astrophys.* **254**, 466
- Padgett, D. L., Brandner, W., Stapelfeldt, K. R., Strom, S. E., Terebey, S., and Koerner, D.: 1999, *Astron. J.* **117**, 1490
- Padoan, P. and Nordlund, Å.: 2002, *Astrophys. J.* **576**, 870
- Palla, F. and Stahler, S. W.: 1993, *Astrophys. J.* **418**, 414

- Pasquini, L., Avila, G., Blecha, A., Cacciari, C., Cayatte, V., Colless, M., Damiani, F., de Propriis, R., Dekker, H., di Marcantonio, P., Farrell, T., Gillingham, P., Guinouard, I., Hammer, F., Kaufer, A., Hill, V., Marteau, M., Modigliani, A., Mulas, G., North, P., Popovic, D., Rossetti, E., Royer, F., Santin, P., Schmutzer, R., Simond, G., Vola, P., Waller, L., and Zoccali, M.: 2002, *The Messenger* **110**, 1
- Pellegrini, E. W., Baldwin, J. A., Brogan, C. L., Hanson, M. M., Abel, N. P., Ferland, G. J., Nemala, H. B., Shaw, G., and Troland, T. H.: 2007, *Astrophys. J.* **658**, 1119
- Persson, S. E., Geballe, T. R., McGregor, P. J., Edwards, S., and Lonsdale, C. J.: 1984, *Astrophys. J.* **286**, 289
- Persson, S. E., Murphy, D. C., Krzeminski, W., Roth, M., and Rieke, M. J.: 1998, *Astron. J.* **116**, 2475
- Povich, M. S., Stone, J. M., Churchwell, E., Zweibel, E. G., Wolfire, M. G., Babler, B. L., Indebetouw, R., Meade, M. R., and Whitney, B. A.: 2007, *Astrophys. J.* **660**, 346
- Pronik, I. I.: 1958, *Izvestiya Ordena Trudovogo Krasnogo Znameni Krymskoj Astrofizicheskoj Observatorii* **20**, 208
- Rakowski, C. E., Schulz, N. S., Wolk, S. J., and Testa, P.: 2006, *Astrophys. J. Lett.* **649**, L111
- Reifenstein, E. C., Wilson, T. L., Burke, B. F., Mezger, P. G., and Altenhoff, W. J.: 1970, *Astron. Astrophys.* **4**, 357
- Rieke, G. H. and Lebofsky, M. J.: 1985, *Astrophys. J.* **288**, 618
- Rousselot, P., Lidman, C., Cuby, J.-G., Moreels, G., and Monnet, G.: 2000, *Astron. Astrophys.* **354**, 1134
- Rousset, G., Lacombe, F., Puget, P., Hubin, N. N., Gendron, E., Fusco, T., Arsenault, R., Charton, J., Feautrier, P., Gigan, P., Kern, P. Y., Lagrange, A.-M., Madec, P.-Y., Mouillet, D., Rabaud, D., Rabou, P., Stadler, E., and Zins, G.: 2003, in P. L. Wizinowich and D. Bonaccini (eds.), *Adaptive Optical System Technologies II. Edited by Wizinowich, Peter L.; Bonaccini, Domenico. Proceedings of the SPIE, Volume 4839*, pp 140–149
- Russeil, D.: 2003, *Astron. Astrophys.* **397**, 133
- Sako, S., Yamashita, T., Kataza, H., Miyata, T., Okamoto, Y. K., Honda, M., Fujiyoshi, T., Terada, H., Kamazaki, T., Jiang, Z., Hanawa, T., and Onaka, T.: 2005, *Nature* **434**, 995
- Sandell, G., Wright, M., and Forster, J. R.: 2003, *Astrophys. J. Lett.* **590**, L45
- Schmidt-Kaler, T. H.: 1965, *Landolt-Börnstein, New Series, Group VI, Vol1, Stars and Star Clusters*, Springer, New York
- Schmidt-Kaler, T. H.: 1982, *Landolt-Börnstein, New Series, Group VI, Vol2b, Stars and Star Clusters*, Springer, New York
- Schulte, D. H.: 1956, *Astrophys. J.* **123**, 250

- Schulz, A., Lenzen, R., Schmidt, T., and Proetel, K.: 1981, *Astron. Astrophys.* **95**, 94
- Schulz, A., Proetel, K., and Schmidt, T.: 1978, *Astron. Astrophys.* **64**, L13
- Sewilo, M., Churchwell, E., Kurtz, S., Goss, W. M., and Hofner, P.: 2004, *Astrophys. J.* **605**, 285
- Shepherd, D. S., Claussen, M. J., and Kurtz, S. E.: 2001, *Science* **292**, 1513
- Siess, L., Dufour, E., and Forestini, M.: 2000, *Astron. Astrophys.* **358**, 593
- Silva, D. R. and Cornell, M. E.: 1992, *Astrophys. Lett.* **81**, 865
- Simon, M., Felli, M., Massi, M., Cassar, L., and Fischer, J.: 1983, *Astrophys. J.* **266**, 623
- Simon, M., Righini-Cohen, G., Cassar, L., and Fischer, J.: 1981, *Astrophys. J.* **251**, 552
- Smith, M. A. and Balona, L.: 2006, *Astrophys. J.* **640**, 491
- Smith, M. A., Cohen, D. H., Gu, M. F., Robinson, R. D., Evans, N. R., and Schran, P. G.: 2004, *Astrophys. J.* **600**, 972
- Stark, D. P., Whitney, B. A., Stassun, K., and Wood, K.: 2006, *Astrophys. J.* **649**, 900
- Steinacker, J., Chini, R., Nielbock, M., Nürnberger, D., Hoffmeister, V., Huré, J.-M., and Semenov, D.: 2006, *Astron. Astrophys.* **456**, 1013
- Stephenson, C. B. and Hobbs, R. W.: 1961, *Astron. J.* **66**, 186
- Stolte, A., Brandner, W., Brandl, B., Zinnecker, H., and Grebel, E. K.: 2004, *Astron. J.* **128**, 765
- Tokunaga, A. T. and Thompson, R. I.: 1979, *Astrophys. J.* **229**, 583
- Walsh, A. J., Burton, M. G., Hyland, A. R., and Robinson, G.: 1998, *Monthly Notices Roy. Astron. Soc.* **301**, 640
- Watermann, R., Hoffmeister, V. H., Chini, R., and Scheyda, C. M.: 2008, *Astrophys. J.* , submitted
- Wegner, W.: 1994, *Monthly Notices Roy. Astron. Soc.* **270**, 229
- Whittet, D. C. B. and van Breda, I. G.: 1980, *Monthly Notices Roy. Astron. Soc.* **192**, 467
- Wilson, T. L., Fazio, G. G., Jaffe, D., Kleinmann, D., Wright, E. L., and Low, F. J.: 1979, *Astron. Astrophys.* **76**, 86
- Wilson, T. L., Mezger, P. G., Gardner, F. F., and Milne, D. K.: 1970, *Astron. Astrophys.* **6**, 364
- Yorke, H. W. and Sonnhalter, C.: 2002, *Astrophys. J.* **569**, 846
- Zinnecker, H., McCaughrean, M. J., and Wilking, B. A.: 1993, in E. H. Levy and J. I. Lunine (eds.), *Protostars and Planets III*, pp 429–495

Curriculum Vitae

Personal Data

Name Vera H. Hoffmeister
Date of Birth May 2nd, 1978
Place of Birth Munich, Bavaria, Germany
Nationality German

Education

School

1984 - 1985:
Grundschule am Mariahilfplatz, Munich
1985 - 1988:
Rolandschule, Oberhausen
1988 - 1997:
Heinrich-Heine-Gymnasium, Oberhausen

Study

1997 - 2002:
Physics and Astronomy at the Ruhr-Universität-Bochum

Diploma

2002 - 2003:
“The Young Cluster in M 17 - Reddening, Distance, IMF and the Occurrence of Circumstellar Disks” at the Astronomisches Institut der Ruhr-Universität-Bochum

Thesis

2003 - present:
“The Formation of Massive Stars” at the Astronomisches Institut der Ruhr-Universität-Bochum